Versuchsanstalt für Wasserbau
Hydrologie und Glaziologie
der Eidgenössischen
Technischen Hochschule Zürich

Mitteilungen 202

Estimating basal properties of glaciers and ice streams from surface measurements

Mélanie Raymond

Zürich, 2007

Herausgeber: Prof. Dr.-Ing. H.-E. Minor

Zitiervorschlag für VAW-Mitteilungen:

Raymond M., ed. (2007)

Estimating basal properties of glaciers and
ice streams from surface measurements

VAW-Mitteilung 202, Versuchsanstalt für Wasserbau,
Hydrologie und Glaziologie (VAW), ETH Zürich, Zürich

Im Eigenverlag der
Versuchsanstalt für Wasserbau,
Hydrologie und Glaziologie
ETH Zürich
CH-8092 Zürich

Tel.: +41 - 44 - 632 4091
Fax: +41 - 44 - 632 1192
e-mail: info@vaw.baug.ethz.ch

Zürich, 2007

ISSN 0374-0056

“L’essentiel du cierge n’est point la cire qui laisse des traces,
mais la lumière.”

Antoine de Saint-Exupéry, Citadelle

The thesis is dedicated to Suzanne Furrer

Preface

Inverse methods deal with the problem of estimating a physical quantity through indirect measurements. Determining the shape of the bedrock underneath an ice stream using measurements of surface velocities is an example of such a problem. In general, there is no single solution to such an inverse problem. Often a certain set of solutions can, however, be excluded, and certain solutions can be judged to be more likely than others. In the past, these basic aspects of inverse modeling have been ignored in most glaciological work. Instead of providing a probability function that describes the probability of any given solution, most, if not all, work done so far in this field have presented one single solution as the solution to the problem.

In this context, M. Raymond gives nice and timely demonstration of the utilization of the Bayesian inversion method to find a solution to a key glaciological inverse problem. For the first time, estimates of both basal topography and basal slipperiness underneath ice streams (fast glaciers within an ice sheet) are derived from surface topography and surface velocity measurements using formal inverse methods. She determines these quantities using both synthetic data and real data from Rutford Ice Stream, West Antarctica. Importantly, she takes full account of measurements and interpolation errors through the use of corresponding covariance matrixes, and also states clearly the retrieval error estimates.

In the first part of the thesis, M. Raymond analyses the influence of basal disturbances on the surface topography and surface flow field (forward problem in the steady-state), by taking into account both the non-linear rheology of glacier ice and any finite amplitude effects. This is a completely new aspect, which was never treated before. In the second part of her thesis, M. Raymond introduces the nonlinear Bayesian inversion approach. The results obtained for the Rutford Ice Stream in Antarctica are impressive and show the great potential in the field of glaciology of the methodology adopted. It should be emphasized, that she first inferred basal properties from surface measurements without letting the surface evolve with time. This is a ‘snapshot’ approach used so far in all other treatments of this problem. However, comparison between measured and calculated rates of surface elevation changes revealed large and significant differences. Therefore, in a second step, the surface topography was allowed to evolve until rates of changes were compatible with measurements. Hence she could determine basal conditions that are consistent with all surface observations. This again is indeed a novel approach, never treated so far in glaciology.

Zurich, September 2007 Prof. Dr. H.-E. Minor

Contents

List of Figures

List of Symbols

The main symbols used are defined here. Others which are defined and used only sporadically may not be listed. Vectors are denoted by bold face italic letters (e.g. $\boldsymbol{d}$) and matrices by bold uppercase letters (e.g. $\mathbf{C}$). Subscripts are defined at the end of the table. In Chapters 2 and 3 dimensional variables are denoted with a tilde and non-dimensional without. The quantities in square brackets represent the respective typical values chosen for non-dimensionalization of the variables.

Symbol	Meaning	Units
Chapter 2 **Chapter 3**		
$\tilde{A}$	rate factor	$a^{-1}\,Pa^{-n}$
$\tilde{b}$	bedrock elevation	m
b	non-dimensional bedrock elevation; $b = \tilde{b}/[\tilde{h}^{(0)}]$	$-$
$\Delta\tilde{b}$	amplitude of bedrock perturbation	m
Δb	non-dimensional amplitude of bedrock perturbation	$-$
$\tilde{C}$	sliding coefficient	$m\,a^{-1}\,Pa^{-m}$
$\tilde{C}^{(0)}$	mean basal slipperiness	$m\,a^{-1}\,Pa^{-m}$
$C^{(0)}$	non-dimensional mean basal slipperiness, slip ratio	$-$
ΔC	fractional amplitude of basal slipperiness perturbation	$-$
$\tilde{g}$	acceleration due to gravity	$m\,s^{-2}$
$\tilde{h}$	ice thickness	m
$[\tilde{h}^{(0)}]$	typical mean ice thickness	m
h	non-dimensional ice thickness; $h = \tilde{h}/[\tilde{h}^{(0)}]$	$-$
$\tilde{k}$	wave number	m^{-1}
m	sliding law exponent	$-$
n	flow exponent	$-$
$\tilde{p}$	pressure	Pa
p	non-dimensional pressure; $p = \tilde{p}/[\tilde{\tau}_b]$	$-$
q	non-dimensional ice flux	$-$
Δq	non-dimensional ice flux perturbation	$-$
$\tilde{s}$	surface elevation	m
s	non-dimensional surface elevation; $s = \tilde{s}/[\tilde{h}^{(0)}]$	$-$
Δs	non-dimensional surface perturbation	$-$
$\tilde{t}$	time	a
t	non-dimensional time; $t = \tilde{t}/[\tilde{h}^{(0)}/\tilde{u}_d]$	$-$

Symbol	Meaning	Units
$\tilde{u}$	horizontal velocity	$m\,a^{-1}$
u	non-dimensional horizontal velocity; $u = \tilde{u}/[\tilde{u}_d]$	–
Δu	non-dimensional horizontal velocity perturbation	–
$\tilde{u}_b$	basal sliding velocity	$m\,a^{-1}$
$\tilde{u}_d$	surface-parallel deformational velocity	$m\,a^{-1}$
$[\tilde{u}_d]$	typical mean surface-parallel deformational velocity	$m\,a^{-1}$
$\tilde{v}_i$	components of the velocity vector $\tilde{\boldsymbol{v}} = (\tilde{u}, \tilde{w})$	$m\,a^{-1}$
$\tilde{w}$	vertical velocity	$m\,a^{-1}$
w	non-dimensional vertical velocity; $w = \tilde{w}/[\tilde{u}_d]$	–
Δw	non-dimensional vertical velocity perturbation	–
$\tilde{x}, \tilde{z}$	space coordinates	m
x, z	non-dimensional space coordinates; $(x, z) = (\tilde{x}, \tilde{z})/[\tilde{h}^{(0)}]$	–
Δz	non-dimensional vertical elevation perturbation	–
α	surface slope	–
$\tilde{\dot{\epsilon}}_{ij}$	components of the strain rate tensor	a^{-1}
$\tilde{\lambda}$	wavelength	m
λ	non-dimensional wavelength; $\lambda = \tilde{\lambda}/[\tilde{h}^{(0)}]$	–
$\tilde{\rho}$	ice density	$kg\,m^{-3}$
$\tilde{\sigma}_{ij}$	components of the Cauchy stress tensor	Pa
σ_{ij}	non-dimensional components of the Cauchy stress tensor	–
$\tilde{\sigma}_{ij}^{(d)}$	components of the Cauchy deviatoric stress tensor	Pa
$\tilde{\tau}$	effective shear stress	Pa
τ	non-dimensional effective shear stress; $\tau = \tilde{\tau}/[\tilde{\tau}_b]$	Pa
$\tilde{\tau}_b$	basal shear stress	Pa
$[\tilde{\tau}_b]$	typical mean basal shear stress	Pa
τ_b	non-dimensional basal shear stress; $\tau_b = \tilde{\tau}_b/[\tilde{\tau}_b]$	–
$\tilde{\tau}_0$	crossover stress	Pa
$\mathcal{T}$	non-dimensional transfer function	
$\mathcal{T}_{\mathcal{SB}}$	bedrock-to-surface topography transfer function	–
$\mathcal{T}_{\mathcal{SC}}$	basal slipperiness-to-surface topography transfer function	–
$\mathcal{T}_{\mathcal{UB}}$	bedrock-to-horizontal surface velocity transfer function	–
$\mathcal{T}_{\mathcal{UC}}$	basal slipperiness-to-horizontal surface velocity transfer function	–
$\mathcal{T}_{\mathcal{WB}}$	bedrock-to-vertical surface velocity transfer function	–
$\mathcal{T}_{\mathcal{WC}}$	basal slipperiness-to-vertical surface velocity transfer function	–

Chapter 4
Chapter 5
Chapter 6

A	rate factor	$d^{-1}\,Pa^{-n}$
A_0	constant rate factor	$d^{-1}\,Pa^{-n}$
b	vertical position of bedrock	m
$\dot{b}$	accumulation rate	$m\,d^{-1}$

Symbol	Meaning	Units
$\boldsymbol{b}$	bedrock topography vector	m
$\boldsymbol{b}_{\mathrm{prior}}$	prior bedrock topography vector	m
Δb	variation of b about mean bedrock elevation	m
C	sliding coefficient	$m\,a^{-1}\,Pa^{-m}$
$\boldsymbol{C}$	basal slipperiness vector	$m\,a^{-1}\,Pa^{-m}$
$\boldsymbol{C}_{\mathrm{prior}}$	prior basal slipperiness vector	$m\,a^{-1}\,Pa^{-m}$
ΔC	fractional variation of C about mean basal slipperiness	–
$C^{(0)}$	slip ratio, mean basal slipperiness	–
$\mathbf{C}$	covariance matrix	
$\mathbf{C}_{\mathbf{B}}$	covariance matrix for the uncertainties in bedrock	m^2
$\mathbf{C}_{\mathbf{C}}$	covariance matrix for the uncertainties in basal slipperiness	$m^2\,a^{-2}\,Pa^{-2m}$
$\mathbf{C}_{\mathbf{D}}$	covariance matrix for the noise in the data	
$\mathbf{C}_{\mathbf{M}}$	covariance matrix for the model parameters	
$\mathbf{C}_{\mathbf{s}}$	covariance matrix for the noise in surface topography	m^2
$\mathbf{C}_{\mathbf{u}}$	covariance matrix for the noise in horizontal velocity	$m^2\,d^{-2}$
$\mathbf{C}_{\mathbf{w}}$	covariance matrix for the noise in vertical velocity	$m^2\,d^{-2}$
$\boldsymbol{d}$	data vector	
$\mathbf{F}$	discrete Fourier transform matrix	–
g	acceleration due to gravity	$m\,s^{-2}$
$\mathbf{g}$	vector-valued forward function	
h	ice thickness	m
J	cost function	
$\boldsymbol{k}$	wave number vector	m^{-1}
$\mathbf{K}$	Fréchet derivatives matrix	
l	correlation length	m
$\boldsymbol{m}$	model parameters vector	
$\boldsymbol{m}_{\mathrm{prior}}$	a priori model parameter vector	
$\hat{\boldsymbol{m}}$	retrieved model parameter vector	
n	flow exponent	–
m	sliding law exponent	–
N	number of discretization points	–
P	probability density function	
s	vertical position of surface	m
Δs	variation of surface about mean value	m
$\boldsymbol{s}$	vector of surface topography	m
$\Delta\boldsymbol{s}$	vector of residuals between observations and model	m
t	time	d
T	temperature	$^\circ\,C$
u	horizontal velocity	$m\,d^{-1}$
$\boldsymbol{u}$	vector of horizontal velocity	$m\,d^{-1}$
Δu	variation of horizontal velocity about mean	$m\,d^{-1}$
$\Delta\boldsymbol{u}$	vector of residuals between observations and model	$m\,d^{-1}$
u_b	basal sliding velocity	$m\,d^{-1}$
u_c	centerline velocity	$m\,d^{-1}$
u_d	surface-parallel deformational velocity	$m\,d^{-1}$
$\boldsymbol{v}$	velocity vector	$m\,d^{-1}$

Symbol	Meaning	Units
w	vertical velocity	$m\,d^{-1}$
$\boldsymbol{w}$	vector of vertical velocity	$m\,d^{-1}$
Δw	variation of vertical velocity about mean	$m\,d^{-1}$
$\Delta \boldsymbol{w}$	vector of residuals between observations and model	m
W	ice stream width	m
x, z	space coordinates	m
α	surface slope	$-$
ϵ	measurement error	
$\dot{\epsilon}_{ij}$	components of the strain rate tensor	d^{-1}
∇_m	gradient with respect to m	
ρ	ice density	$kg\,m^{-3}$
σ	standard deviation of error	
σ_{ij}	components of the Cauchy stress tensor	Pa
τ	effective shear stress	Pa
τ_b	basal shear stress	Pa
τ_0	crossover stress	Pa

Subscripts

B	properties of bedrock
b	basal properties
C	properties of basal slipperiness
d	deformational
D	data
M	model parameters
s	properties of the surface
u	properties of horizontal velocity
w	properties of vertical velocity

Superscripts

H	Hermitian transpose
T	transpose
(0)	zeroth order quantity

Abstract

This thesis introduces a nonlinear Bayesian inference approach to estimate the basal properties of glaciers and ice streams from measurements of surface topography and surface velocities. A prerequisite to make inferences on the nature of basal conditions indirectly from surface measurements is the understanding of the relationship between basal conditions and surface fields.

In the first part of this thesis, the influence of basal disturbances on the steady-state surface topography and on surface velocities as well as on the velocity fields of glaciers and ice sheets is investigated numerically. This is done for finite-amplitude basal perturbations in both bed topography and basal slipperiness using a non-linear ice rheology and a non-linear sliding law. The effects of varying the exponent n in Glen's flow law on transfer characteristics are mainly quantitative, and do not affect qualitative aspects of the transfer amplitudes and phase shifts such as the number of maxima and inflection points when plotted as a function of wavelength. The effects of nonlinear rheology on the velocity fields consists primarily in a concentration of the anomalous flow near the base and in a reduction of the horizontal velocity perturbation near the surface.

The second part of the thesis is devoted to the inverse problem. We introduce a nonlinear Bayesian inversion approach to estimate both basal topography and basal slipperiness beneath ice streams from surface topography and surface velocities measurements. The inverse procedure is based on an iterative Newtonian optimization of a cost function involving a forward step solved with a numerical finite-element model. The first order forward model derivatives needed for inversion are approximated with linear transfer functions. This approximation is attractive as it greatly enhances the numerical efficiency of the method by sparing the time-consuming evaluation of the numerical derivatives. Using synthetic data generated with a forward finite-element model, we show that the inversion procedure gives accurate estimates of the basal perturbations. The inversion procedure is then used to estimate the basal properties along a flow line of Rutford Ice Stream, West Antarctica. The basal properties we compute for Rutford ice stream are consistent both with the surface observations and the radar measurements of bedrock topography.

Résumé

Cette thèse introduit une approche d'inférence bayésienne non-linéaire pour estimer les propriétés basales de glaciers et fleuves de glaces à partir de mesures de la topographie de surface et de vitesses de surface. Une condition préalable pour pouvoir inférer la nature des conditions basales indirectement à partir de données de surface est de comprendre la relation entre conditions basales et champs de surface.

Dans la première partie, l'influence de perturbations basales sinusoïdales sur la topographie stationnaire de la surface et les vitesses de surface ainsi que sur le champs des vitesses internes du glacier est étudiée à l'aide d'un modèle numérique. Ceci nous permet d'examiner les effets de perturbations basales d'amplitudes finies du lit glaciaire et du glissement basal pour une rhéologie non-linéaire de la glace et une loi de glissement non-linéaire. Les résultats montrent que les caractéristiques de transfert sont affectées de manière principalement quantitative lorsque l'exposant n de la loi de Glen est varié. Les effets d'une rhéologie non-linéaire sur le champs des vitesses consistent principalement en une concentration du flux anormal proche de la base et une réduction de la perturbation de vitesse horizontale proche de la surface.

La seconde partie est dédiée au problème inverse. Nous introduisons une approche d'inférence bayésienne pour estimer la topographie du lit glaciaire et le glissement basal sous les fleuves de glaces à partir de mesures de topographie de surface et de vitesse de surface. La procédure inverse est basée sur une optimisation itérative newtonienne d'une fonction de coût comprenant un pas direct, résolu avec un modèle numérique d'éléments finis. La dérivée première du problème direct nécessaire à l'inversion est approximée avec des fonctions de transferts linéaires. Cette approximation permet d'augmenter l'efficacité numérique de la méthode et d'éviter l'évaluation d'une dérivée numérique coûteuse. Dans un premier temps, la procédure d'inversion est testée avec des données simulées à l'aide du modèle numérique. Les expériences montrent que la procédure d'inversion converge rapidement et permet d'obtenir des inférences précises. Dans un second temps, la méthode d'inversion est utilisée pour estimer les propriétés basales le long d'une ligne de flux sur le fleuve de glace du Rutford, dans l'Antarctique ouest. Les propriétés basales inférées sont consistantes avec les mesures radars pour la topographie du lit glaciaire et les observations de surfaces.

Chapter 1

Introduction

In this chapter, we introduce the general framework of the thesis, followed by a description of its aim and outline.

1.1 General Framework

Background

Fast flowing ice streams are dominant features of the flow regime and drainage system of the West Antarctic Ice Sheet (henceforth WAIS) (Figure 1.1). They determine the flux of ice flowing from the interior towards the coast. These ice streams account for most of the ice discharge from the ice sheet (Bentley and Giovinetto, 1990; Bamber et al., 2000). Changes in flow speed or geometrical configurations of these ice streams affect the mass-balance of the ice sheet and can have significant effect on global sea level. Recently, some ice streams showed drastic changes in flow behavior. The lower region of Ice Stream C, Siple Coast, shut down about 150 years ago (Retzlaff and Bentley, 1993). Ice Stream B, decelerated by 23 % during the period 1974-1997 (Joughin et al., 2002). These changes caused the region to switch from a negative (thinning) to positive (thickening) mass balance (Joughin and Tulaczyk, 2002). Changes in ice-stream boundaries as revealed by radar and recorded in the Ross Ice Shelf (Fahnestock et al., 2000) further demonstrate the large temporal variability in the position and dynamics of ice streams. This variability is too fast to be caused by temporal variations in accumulation rates or air temperatures. Some ongoing changes in basal control on the flow and position of ice-stream boundaries represent the most likely explanation.

The WAIS ice streams are remarkable in that they achieve high flow velocities ($\sim$ 300 m yr^{-1}) despite small gravitational driving stress ($\sim$ 1-30 kPa). Under these conditions, the high velocities arise from effective basal lubrication. In many cases, extensive and fine-grained tills contribute to the extreme lubrication (Alley et al., 1987, e.g). In the absence of significant resistance from the bed, ice stream motion is mainly restrained by friction from the sides (Whillans et al., 2001). Further, distributed short scale bedrock undulations or spatial variations in resistance to basal sliding ('sticky spots') may support part of the driving stress on localized regions (Alley, 1993). These spots are thought to play an important control on the flow of some fast flowing ice streams. Understanding the basal conditions under ice streams is thus important to predicting the future ice discharge from the ice streams and the resulting sea-level rise.

The basal conditions under ice streams have been examined using seismic measurements (Blankenship et al., 1986) and radar (Gades et al., 2000) or by direct access through boreholes (Kamb, 2001). Control and inverse methods have also been developed to estimate the basal conditions indirectly from surface measurements. MacAyeal (1992) and Joughin et al. (2004) applied control methods to estimate the basal shear stress under the Ross ice streams and the northeast Greenland Ice Stream (Joughin et al., 2000) from surface ice velocity data. Thorsteinsson et al. (2003) inferred both basal topography and basal lubrication at the bed of Ice Stream E from observations of surface elevation and surface velocities based on the linearized perturbation theory of the transmission of basal disturbances to the ice surface by Gudmundsson (2003).

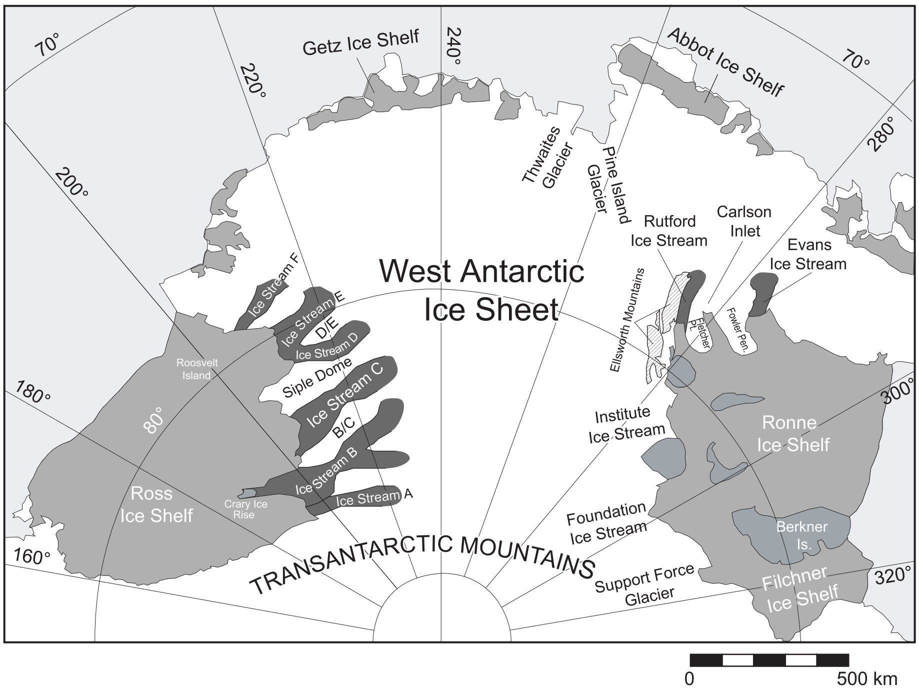

Figure 1.1: The West Antarctic Ice Sheet (modified from (Fahnestock and Bamber, 2001)). Ice streams are in dark gray, ice shelves in gray and oceans in light gray. Ice rises and inter-stream ridges as well as other grounded ice are shown in white. Ice Streams A to F flow into the Ross Ice Shelf, while Rutford and Evans Ice Streams flow into the Ronne Ice Shelf. Active ice streams move at velocities of some 0.3 to 1 km a year.

Motivation and Approach

Surface topography and surface velocities of glaciers and ice streams reflect to some extent the shape of the underlying bed and the basal resistance to basal sliding. Gudmundsson (2003) shows that the transmission of basal variability to the surface of glaciers and ice streams increases when the mean basal motion is large compared to motion from internal ice deformation. Thus, ice streams that move predominantly by basal motion should be best suited for the estimation of basal properties from surface measurements.

In this thesis, we introduce a nonlinear Bayesian inversion approach to determine both basal topography and basal lubrication beneath ice streams. This involves the construction of a forward model encapsulating our understanding of the physics of the relationship between basal and surface properties. In this thesis, we relate surface and basal conditions with a two-dimensional finite-element model using Glen's flow law and solving the full momentum balance equations for which acceleration terms are neglected. The model also calculates the transient evolution of the free surface. This allows us to consider both the non-linearity of the constitutive law for ice and nonlinear finite-amplitude effects set up by the basal perturbations.

In Bayesian inference, the inverse problem is of statistical nature and the solution to the inverse problem is a so called a posteriori probability density function for the model parameters, i.e bedrock topography and basal slipperiness (Figure 1.2). In the case where the forward function is nonlinear, as our finite element model, there exist no explicit solution for the inversion and the solution of the inverse problem must be sought by some optimization technique. This is accomplished by a nonlinear Gauss-Newton procedure (e.g. Rodgers, 2000). This procedure involves the determination of the first order derivatives of the forward function. These are approximated by analytical linear transfer functions. This approximation is attractive as it greatly enhances the numerical efficiency of the method by sparing the time-consuming evaluation of the numerical derivatives.

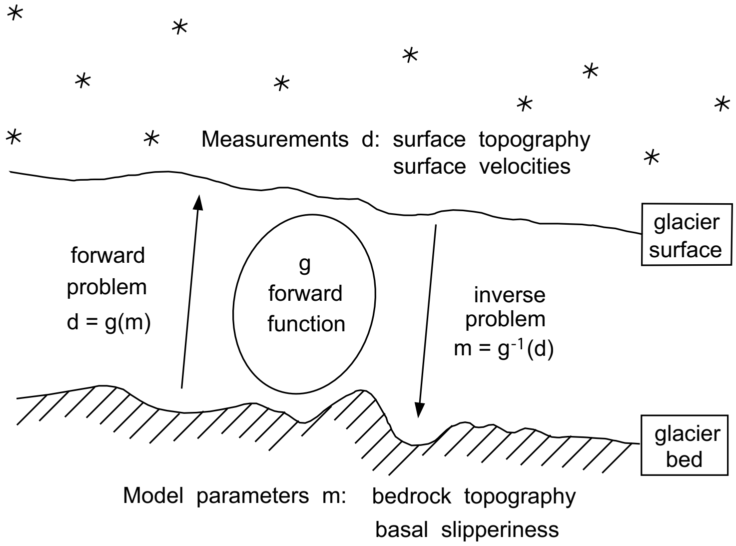

Figure 1.2: Relation between surface measurements and model parameters.

The proposed inverse procedure differs significantly from previous inverse modeling work on ice streams. Thorsteinsson et al. (2003) inversion's approach using the theory of glacier flow perturbations by Gudmundsson (2003) as forward function is inherently restricted to small variations about the mean conditions as the perturbation theory relies on a number of small-amplitude assumptions about the strength of the perturbations. These limitations are overcome by the proposed method.

1.2 Aim of this Thesis

The main objectives are (i) to investigate the nonlinear forward transfer of basal disturbances to the surface of glacier and (ii) to introduce a nonlinear Bayesian inference approach to determine the basal properties of glaciers and ice streams from surface measurements. In a first step, the inversion procedure is applied to synthetic data. This permits to explore the capabilities and limitations of the inversion. In a second step, the inverse procedure is applied to a flowline of Rutford Ice Stream, West Antarctica.

1.3 Thesis outline

This thesis is divided into two independent and self-contained parts. The first part of the thesis is concerned with the non-linear forward problem. **Chapter 2** describes the transfer characteristics of finite-amplitude basal disturbances to the surface of glaciers and ice sheets. The influence of basal disturbances on the steady-state surface topography and on surface velocities of glaciers is investigated numerically in two dimensions for perturbations in bed topography and basal slipperiness using a non-linear ice rheology. In **Chapter 3**, the influence of these perturbations on the flow field of glaciers is examined.

The second part of the thesis deals with the non-linear inverse problem. **Chapter 4** introduces the method of Bayesian inference. **Chapter 5** illustrates the application of Bayesian inversion to synthetic data in which glacier surface data are inverted for bedrock topography and basal slipperiness. **Chapter 6** presents inversion results for the Rutford ice stream, West Antarctica. Finally, **Chapter 7** gives general conclusions.

Part I

Forward problem

Chapter 2

On the relationship between surface and basal properties on glaciers, ice sheets, and ice streams.

This chapter is published under the same title in the Journal of Geophysical Research, with co-author G. H Gudmundsson from the British Antarctic Survey, Cambridge, UK.

Abstract

The influence of basal disturbances on the steady-state surface topography and on surface velocities of glaciers and ice sheets is investigated numerically. This is done for finite-amplitude basal perturbations in both bed topography and basal slipperiness using a non-linear ice rheology and a non-linear sliding law. The effects of varying the exponent n in Glen's flow law on transfer characteristics are mainly quantitative, and do not affect qualitative aspects of the transfer amplitudes and phase shifts such as the number of maxima and inflection points when plotted as functions of wavelength. In particular, the well-known maximum in bed-to-surface transfer amplitude for a Newtonian medium at sufficiently high slip ratios (ratio between mean sliding velocity and mean ice deformational velocity) also forms for $n > 1$. Transfer amplitudes generally become smaller with increasing n for wavelengths less than about three times the mean ice thickness (h). For larger wavelengths the situation is reversed and transfer amplitudes increase with n. For active ice streams, characterized by high basal slipperiness, low surface slopes ($< 0.5°$), and $n = 3$, topographic transfer amplitudes are generally large (> 0.5) and fairly constant for all wavelengths longer than about 3 to 5 h. With increasing n and decreasing surface slope the lower limit of wavelengths over which horizontal stress gradients can be ignored increases markedly. Perturbation solutions for Newtonian medium are found to give an accurate description of the transfer characteristics for bedrock amplitudes up to 50 $\%$ ice thickness and for fractional amplitudes of slipperiness perturbations up to 0.5.

2.1 Introduction

In this paper we describe the transfer characteristics of finite-amplitude basal disturbances to the surface of glaciers and ice sheets. We use a non-linear numerical model to investigate the steady-state relationship between bed and surface along a flow line when transverse effects can be ignored. Two types of sinusoidal basal disturbances are considered: 1) bedrock undulations, and 2) spatial variations in basal slipperiness. For both types of disturbances, the transfer amplitudes and phase shifts are calculated over a large range of wavelengths using a modified form of Glen's flow law.

There are two different types of non-linear effects encountered in this problem: rheological nonlinearities, and finite amplitude effects, i.e., the effects of the amplitude of the basal perturbations on the bed-to-surface transfer, both of which have hitherto not been addressed to the level attempted here. The effects of stress disturbances set up by basal topography on the effective viscosity distribution of ice have, for example, not been addressed by previous authors in their analyses of the bed-to-surface transfer of basal disturbances through a non-linear medium (Hutter et al., 1981; Hutter, 1983; Balise, 1987; Jóhannesson, 1992), with the exception of Hindmarsh (2004) who included first-order effective viscosity effects in his perturbation approach to this problem. Furthermore, by focusing on the (linear) sensitivity of the surface to basal perturbations, all previous authors (e.g., Hutter, 1983; Balise and Raymond, 1985; Reeh, 1987; Whillans and Johnsen, 1983; Jóhannesson, 1992; Gudmundsson, 2003) have not considered any finite-amplitude effects. Our numerical approach to this problem allows us to deal with both types of non-linearities. We estimate the strength of finite-amplitude effects and describe how non-Newtonian rheology modifies bed-to-surface transfer.

We consider variations in basal properties over both short and long scales with respect to mean thickness, but short compared to the overall span of the ice sheet. This allows us to consider the glacier geometry as corresponding to a uniformly inclined plane slab of constant thickness on which (finite) perturbations in bed and surface are superimposed. Examples of recent theoretical studies dealing with the effects of basal topography for scales much greater than the typical ice thickness and at the same time much shorter than the horizontal span of an ice sheet can be found in Morland (2001) and Schoof (2003).

Understanding the relationship between basal conditions and surface fields is of considerable practical interest as it allows, at least in principle, inferences on the nature of basal conditions to be made directly from surface observations. Due to the non-linear nature of this problem, it is difficult to give a full description of the transfer characteristics. In the linear case, the relationship between bed and surface can be completely described in terms of surface and bed amplitude ratios and phase shifts, given as functions of wavelength. In the non-linear case, the effect of an arbitrary basal disturbance is, on the other hand, no longer just a sum of the effects of its individual sinusoidal components. We emphasize that for the problem to be linear it is not sufficient that the medium is linear; finite amplitude effects must also be absent. On the other hand, the problem can be approximately linear, despite the rheology being non-linear. If, for example, perturbations in deviatoric stresses are small compared to the unperturbed effective stress distribution, the problem can be expected to remain nearly linear even when the effective viscosity depends on the state of stress. The term 'nearly-linear' is here used for problems which are non-linear, but which can be solved by linearization around some state of reference. Although not limited to do so by our method, we focus our attention to a large extent on situations where both the effects of stress perturbations on the effective viscosity and finite amplitude effects are small enough for the problem in this sense to remain nearly linear. The strength of non-linear effects is estimated, and appropriate transfer-function representation of the relationship between bed and surface are given for those sets of parameters for which the problem is found to be nearly linear.

The most widely used rheological model for glacier ice, Glen's flow law, is a power law. This power-law model is unrealistic in both the high and the low strain-rate limits. For a uniform flow down an inclined plane, this rheological model predicts an effective viscosity distribution approaching infinity at the surface. As a consequence one can expect, and below this will be shown to be the case, the surface response to be a strongly non-linear function of basal amplitude. The problem can be made moderately non-linear by enforcing an upper limit to the effective stress as done for example by Hutter (1983) through the addition of a linear term to Glen's flow law. Alternatively, the reference state can be modified by adding a uniform non-zero longitudinal strain-rate across the thickness as done by Jóhannesson (1992) or by assuming the flow to be quasi-uniform as done by Hindmarsh (2004). In a fully non-linear treatment as presented here, there is no need to enforce an upper limit to the effective viscosity either by modifying the flow law or by introducing a uniform longitudinal strain rate. The disturbances in flow set up by the basal perturbations give, on their own account, rise to a finite near surface viscosity.

The structure of the paper is as follows. We start by determining the strength of finite-amplitude effects on the bed-to-surface transfer as a function of amplitude for both linear and non-linear medium. We then quantify the strength of finite-amplitude effects, determine the range of basal amplitudes for which they can effectively be ignored, and determine in absolute terms the range of validity of small-amplitude perturbation theories. Subsequently we focus on cases were the geometrical non-linearities play a minor role, and investigate how the bed-to-surface transfer is affected by non-Newtonian rheology. The effects of surface slope are briefly discussed.

2.2 Finite-Element Ice-Flow Model

We consider flow down an infinite plane with a mean inclination α. In the $(\tilde{x}, \tilde{z})$ Cartesian frame, the $\tilde{x}$-axis and $\tilde{z}$-axis are parallel and perpendicular to the mean slope, respectively. $\tilde{s}(\tilde{x}, \tilde{t})$ defines the surface and $\tilde{b}(\tilde{x})$ the base of the glacier with $\tilde{b}(\tilde{x}) \leq \tilde{z} \leq \tilde{s}(\tilde{x}, \tilde{t})$. Dimensional variables are denoted with a tilde, non-dimensional without. Figure 2.1 illustrates the geometry of the ice-flow problem. Two-dimensional plane-strain calculations are performed using four-node, isoparametric, quadrilateral Hermann elements. A mixed Lagrangian-Eulerian approach is employed in determining the position of the steady-state surface (Leysinger Vieli and Gudmundsson, 2004). The field equations to be solved describe the conservation of mass for incompressible materials

$$\tilde{v}_{i,i} = 0 \tag{2.1}$$

and the conservation of angular and linear momentum

$$\tilde{\sigma}_{ij} = \tilde{\sigma}_{ji} \qquad \text{and} \qquad \tilde{\sigma}_{ij,j} + \tilde{\rho}\tilde{g}_i = 0, \tag{2.2}$$

where $\tilde{v}_i$ are the components of the velocity vector, $\tilde{\sigma}_{ij}$ the components of the Cauchy-stress tensor, $\tilde{g}$ the acceleration due to gravity and $\tilde{\rho}$ the density of ice. A nonlinear flow law relating deviatoric stresses and strains (Glen, 1955; Steinemann, 1958) is extended following Hutter (1983) with a linear term to avoid the singularity in viscosity in the flow law as the deviatoric stress goes to zero

$$\tilde{\dot{\epsilon}}_{ij} = \tilde{A}(\tilde{\tau}^{n-1} + \tilde{\tau_0}^{n-1})\tilde{\sigma}_{ij}^{(d)}. \tag{2.3}$$

In this equation, $\tilde{\dot{\epsilon}}_{ij}$ and $\tilde{\sigma}_{ij}^{(d)}$ are the strain rate and deviatoric stress tensors, respectively, $\tilde{\tau}$ is the effective shear stress, $\tilde{A}$ is a temperature-independent rate factor, and n is the stress exponent. The parameter $\tilde{\tau_0}$ is the *cross-over stress* at which the linear and exponential terms contribute equally to the total strain rate. Currently $\tilde{\tau_0}$ is not well constrained through measurements and could be somewhere within the range $0 < \tilde{\tau_0} < 50\,\mathrm{kPa}$ (Pettit and Waddington, 2003). Compared to typical basal stresses on ice streams and glaciers of a few tens of kPa and about 100 kPa, respectively, this is a fairly large range.

A sliding relation of the form

$$\tilde{u}_b = \tilde{C}(\tilde{x})\tilde{\tau}_b^m, \tag{2.4}$$

is adopted, where $\tilde{u}_b$ is the sliding velocity tangential to the bed, $\tilde{C}(\tilde{x})$ the sliding coefficient, and $\tilde{\tau}_b$ the bed parallel shear stress. In the numerical model, sliding is introduced by adding a uniform thin layer to the base of the glacier. The rheological properties of this layer are suitably chosen so that the resulting velocity at the upper boundary corresponds to Equation (2.4). This is a convenient and often used method of introducing basal motion in finite element models (e.g., Schweizer and Iken, 1992). This approach is not strictly equivalent to Eq. (2.4), because surface-parallel deviatoric stresses can be present within this layer. Below, it will be shown that these differences are, however, small.

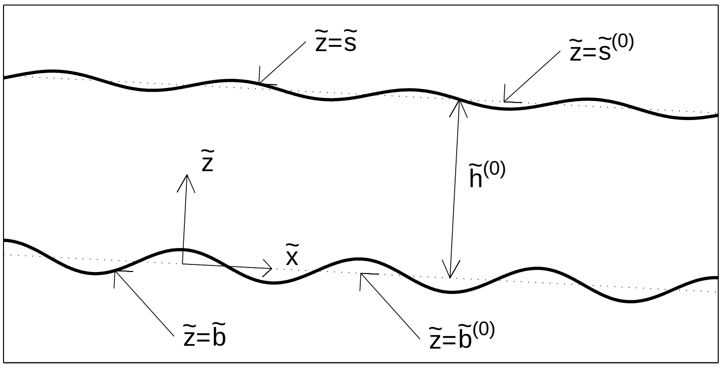

Figure 2.1: Illustration of the glacier geometry and coordinate system. Bedrock perturbation and corresponding surface reaction are shown as a black line. The dashed lines show the undisturbed plane slab geometry. The superscript (0) indicates average values over the whole computational domain.

2.2.1 Boundary Conditions

Periodic boundary conditions are imposed along the glacier upstream and downstream boundaries. Hence, the considered flow section is repeated infinitely in x-direction. The upper surface $\tilde{s}(\tilde{x}, \tilde{t})$ is stress free and its time-dependent evolution governed by the kinematic boundary condition

$$\tilde{s}_{\tilde{t}} + \tilde{u}\tilde{s}_{\tilde{x}} = \tilde{w} \qquad \tilde{z} = \tilde{s}(\tilde{x}, \tilde{t}). \tag{2.5}$$

The mass flux across the upper surface is therefore set to zero. The length of the model is equal to the wavelength of the basal disturbance. Sinusoidal perturbations in bedrock topography $\mathcal{B}$ are introduced by writing $\tilde{b}(\tilde{x}) = \tilde{b}^{(0)} + \Delta\tilde{b}\cos(\tilde{k}\tilde{x})$, where $\tilde{b}(\tilde{x})$ describes the basal topography, $\tilde{b}^{(0)}$ stands for the mean bedrock elevation, $\Delta\tilde{b}$ is the amplitude of the bedrock perturbation, $\tilde{k} = 2\pi/\tilde{\lambda}$ the wave number. Similarly, perturbations in basal slipperiness ($\mathcal{C}$ perturbations) are written as $\tilde{C}(\tilde{x}) = \tilde{C}^{(0)}(1 + \Delta C\ \cos\tilde{k}\tilde{x})$ where $\tilde{C}^{(0)}$ is the mean basal slipperiness, and ΔC is the fractional amplitude of the slipperiness perturbation. Note that the total amplitude of the basal slipperiness perturbation is given by the product $\tilde{C}^{(0)}\Delta C$, and that the fractional slipperiness amplitude (ΔC) is equal to the ratio of the total amplitude of the basal slipperiness perturbation ($\tilde{C}^{(0)}\Delta C$) to the mean value of the basal slipperiness perturbation ($\tilde{C}^{(0)}$). The superscript (0) indicates here average values over the whole computational domain. This notation is used because when comparing numerical results with relevant perturbation theories, these correspond to zeroth order quantities.

2.2.2 Non-dimensionalization

The variables are non-dimensionalized by choosing their typical values. For example, spatial scales are non-dimensionalized with a typical thickness. We will write $\psi = \tilde{\psi}/[\tilde{\psi}]$; the quantities in square brackets represent the respective typical values, and those without tilde are the corresponding dimensionless quantities. The spatial variables $\tilde{x}, \tilde{z}, \tilde{s}, \tilde{b}$, the velocity components $\tilde{u}, \tilde{w}$, the time $\tilde{t}$, the stress $\tilde{\sigma}$ and pressure $\tilde{p}$ are non-dimensionalized as follows,

$$\begin{aligned} (x, z, s, b) &= (\tilde{x}, \tilde{z}, \tilde{s}, \tilde{b})/[\tilde{h}^{(0)}] \\ (u, w) &= (\tilde{u}, \tilde{w})/[\tilde{u}_d] \\ t &= \tilde{t}/[\tilde{h}/\tilde{u}_d] \\ (\tau, \sigma, p) &= (\tilde{\tau}, \tilde{\sigma}, \tilde{p})/[\tilde{\tau}_b] \end{aligned}$$

where $[\tilde{h}^{(0)}]$ is a typical mean ice thickness, $[\tilde{u}_d]$ a typical contribution of internal deformation to the surface-parallel velocity, $[\tilde{\tau}_b] = \tilde{\rho}\tilde{g}\tilde{h}\sin(\alpha)$ a typical bed parallel shear stress. The kinematic boundary condition is invariant under this set of scalings. In dimensionless form, the rate factor A reads $A = (\frac{2}{n+1} + \frac{\tilde{\tau}_0{}^{n-1}}{\tilde{\tau}_b^{n-1}})^{-1}$. The sliding law has the form $u_b = C\tau_b^m$ with $C = \tilde{C}[\tilde{\tau}_b^m/\tilde{u}_d]$. In scaled units, the glacier thickness is equal to unity and the mean surface parallel deformational velocity $u_d = 1$.

2.3 Algorithm

At each time step the velocity field is first calculated by solving (2.1), (2.2), and (2.3) together with the boundary conditions corresponding to either one of the two perturbation problems considered. For $n \neq 1$ the effective viscosity distribution is updated and a new solution calculated. This is repeated until the maximum change of the velocity at some node divided by the maximum velocity of the whole domain is less than 10^{-4}. Then the kinematic boundary condition (2.5) is integrated forward in time with an unconditionally stable implicit Crank-Nicholson finite difference scheme. This procedure is continued until a steady-state has been reached, which is judged to be the case as soon as the change in vertical displacement is less than 10^{-7} of the mean thickness. In all numerical experiments performed, calculations started from an undisturbed plane-slab geometry and continued until a steady-state had been reached. We have not investigated the possibility of a multi-valued geometry-flux relationship predicted for this problem by Schoof (2004), and therefore can neither confirm nor rule out the possibility that our steady-state geometries may depend on the initial geometry chosen.

2.4 Results

For the two types of basal perturbations considered, the relationship between surface topography and velocities depends on a number of parameters. For a bedrock ($\mathcal{B}$) perturbation, the ratio between basal amplitude and mean thickness ($\Delta b/h$) is an important non-dimensional number. For a basal slipperiness perturbation ($\mathcal{C}$), the fractional amplitude of the perturbation (ΔC) plays a similar role. Other parameters affecting the solution are the ratio of amplitude to wavelength ($\Delta b/\lambda$ and $\Delta C/\lambda$), mean surface slope (α), mean basal slipperiness ($C^{(0)}$), and stress exponent n. In transient runs, the rate factor (A) affects the time scale, but otherwise has no effect on the results. In calculations done for non-Newtonian medium, the cross-over stress (τ_0) is a further model parameter.

Numerical results are mostly presented in the form of transfer functions, describing the effect of the basal perturbations on the surface topography and surface velocities. The transfer functions give the transfer amplitude and the relative phase shift as a function of wavelength for sinusoidal perturbations. The transfer amplitude is the ratio between surface and basal perturbation amplitudes and describes how much from the basal perturbation is transmitted to the surface. It is sometimes also referred to as amplitude ratio. The relative phase shift gives the relative phase shift of the surface field with respect to the basal perturbation. Both transfer amplitudes and phase shifts are described by complex numbers. The transfer functions $\mathcal{T}$ are denoted with a two letter suffix. The first suffix relates to the effect and the second one to the cause. $\mathcal{T}_{\mathcal{SB}}$, for example, is the transfer function that describes a change in the surface topography caused by a perturbation in bedrock topography, whereas $\mathcal{T}_{\mathcal{UC}}$ is the transfer function describing a change in horizontal surface velocity caused by a spatial variation in the basal slipperiness. As discussed above, this method of presenting the results is only useful if the response is nearly linear, that is, if the surface fields can be approximated accurately as sinusoidal curves having the same wavelength as the basal perturbation. Non-linear effects introduce multiples of the fundamental wavelength. Such effects can, in principle, be described through higher-order transfer functions (e.g., Gudmundsson, 1997a). We estimate these higher-order effects, and present the results in form of transfer functions of the fundamental wavelength when we judge that these higher-order effects can be ignored.

Numerical results for linear rheology were compared with both steady-state and transient analytical solutions. Figures 2.2a and b shows examples of calculated and analytical surface-to-bed amplitude ratio and phase shift for a Newtonian fluid as a function of time for both sinusoidal bedrock and slipperiness perturbations. The solid line is the analytical solution (Gudmundsson, 2003), which for this set of parameters predicts the surface to oscillate a few times before settling on the steady-state solution (a kinematic surface oscillation). The diamond symbols represent the numerical results. As can be seen the agreement between the numerical and analytical solutions is excellent.

2.4.1 Finite-amplitude effects

$\mathcal{B}$ perturbation

The analytical solution given by Gudmundsson (2003) for a Newtonian medium is correct to first order in Δbk, where k is the wavenumber, and should be accurate whenever $\Delta bk \ll 1$ and $\Delta b/h \ll 1$. One of the properties of the analytical transfer amplitudes is that they always increase in a direct proportion to the size of the basal amplitude. Figure 2.3 shows the percentage difference in transfer amplitude, i.e., $100 \times (abs(\mathcal{T}^c_{\mathcal{SB}}) - abs(\mathcal{T}^a_{\mathcal{SB}}))/abs(\mathcal{T}^a_{\mathcal{SB}})$, where abs is the complex magnitude and the superscripts a and c stand for analytical and numerically calculated, respectively. Also shown is the absolute difference in phase, i.e., $angle(\mathcal{T}^c_{\mathcal{SB}}) - angle(\mathcal{T}^a_{\mathcal{SB}})$, where $angle$ is the complex phase angle. The differences are plotted as functions of bed amplitude for $C^{(0)} = 0$ and for three different wavelengths. As seen in Figure 2.3, the numerical transfer amplitudes increase slower than linearly with increasing bed amplitude, and the percentage difference in transfer amplitude is therefore negative. As expected, the difference between calculated and analytical values increases approximately quadratically as a function of Δb for a given wavelength. We have a high confidence in the correctness of the numerical solution and consider the difference between the analytical and the numerical solutions to be caused by non-linear finite-amplitude effects not accounted for in the analytical perturbation solution. However, these differences are small, smaller in fact than might have been expected on the basis that the analytical solution is only correct to first order in Δbk and only valid for $\Delta b/h \ll 1$. For $\Delta b = 0.5$, or 50$\%$ ice thickness, and $C^{(0)} = 0$, calculated transfer amplitudes are, for example, only about 10 to 20 percent smaller than the analytical values. For $\Delta b = 0.5$ and $\lambda = 5$, $\Delta bk = 0.62 \not\ll 1$, and one could therefore have expected the difference between analytical and numerical values to be larger. This result gives increased confidence in using the analytical solution to calculate flow over finite amplitude bedrock perturbations.

With increasing amplitude of the bedrock perturbation (for a given wavelength), the problem becomes increasingly non-linear and the surface shape starts to deviate from a pure sinusoidal form. In Figure 2.4 the transfer amplitudes for the first three harmonics are shown. As expected, amplitudes of higher order harmonics become progressively stronger with Δbk. Nevertheless, the first-order harmonic agrees well with the theoretical transfer amplitudes (shown as horizontal dashed and solid lines) up to at least $\Delta b = 0.3$, which corresponds to about $\Delta bk = 0.37$ for $\lambda = 5$. Even for large basal sliding velocities ($C^{(0)} = 1000$, Figure 2.4b), higher order harmonics are, for Δbk less than about 0.4, at least 10 times smaller than the fundamental harmonic. Again we find that the analytical solutions seem to give an accurate description of the relationship between bed and surface geometry even up to moderate values for Δbk. As Schoof (2002) has pointed out, stress perturbations associated with any finite sized bedrock perturbation must grow as the basal sliding velocity is increased. It follows that the accuracy of the analytical solution must depend on $C^{(0)}$. This is a well-made point, and stresses the importance of being able to estimate the errors for any given finite value of $C^{(0)}$, something that can only be done through the type of numerical comparison between the analytical theory and

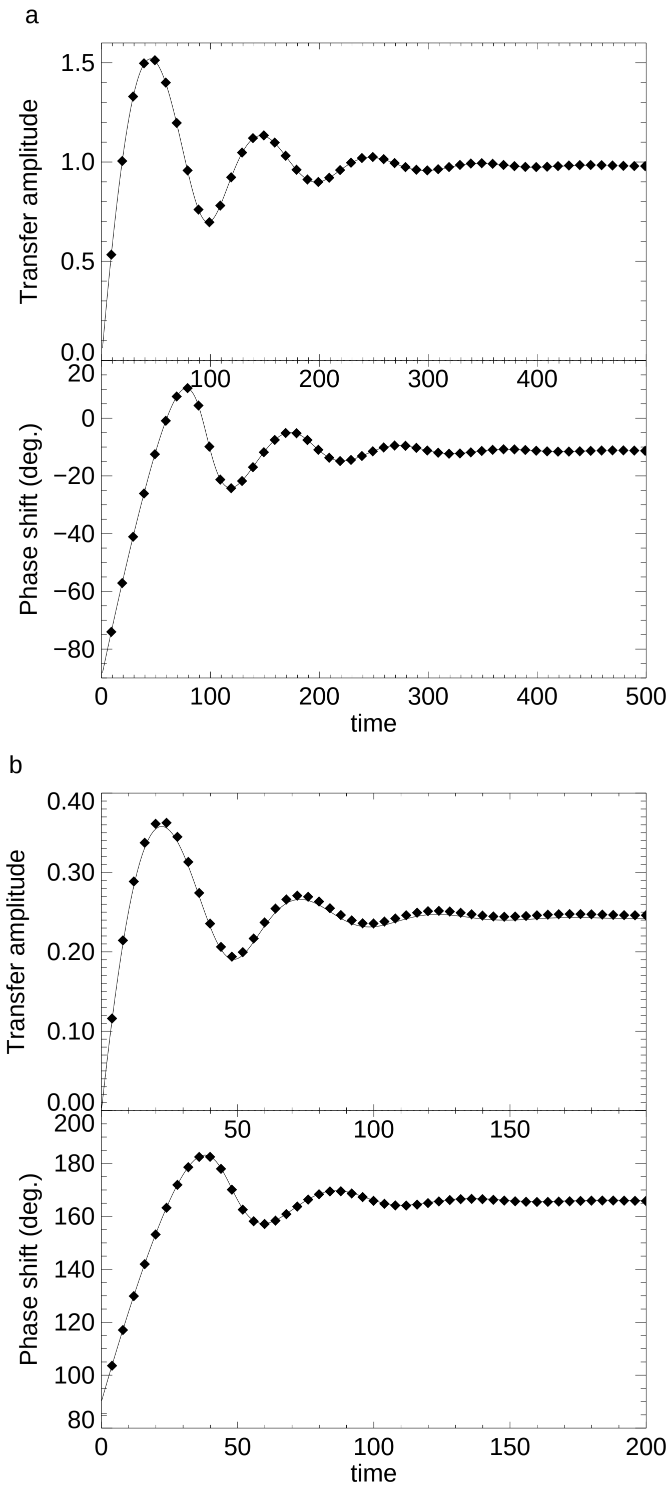

Figure 2.2: Comparison of numerical with analytical amplitude ratios and relative phase shifts as a function of time for a Newtonian rheology ($n = 1$). (a) Flow over a sinusoidal bedrock perturbation with amplitude $\Delta b = 0.05$ and no basal sliding ($C^{(0)} = 0$); (b) Basal sliding perturbation with a fractional slipperiness amplitude $\Delta C = 0.05$, and mean slipperiness $C^{(0)} = 1$. The wavelength is $\lambda = 200$ and the mean surface slope is $\alpha = 3°$. The diamonds are the numerical results and the solid line the analytical solution (Gudmundsson, 2003).

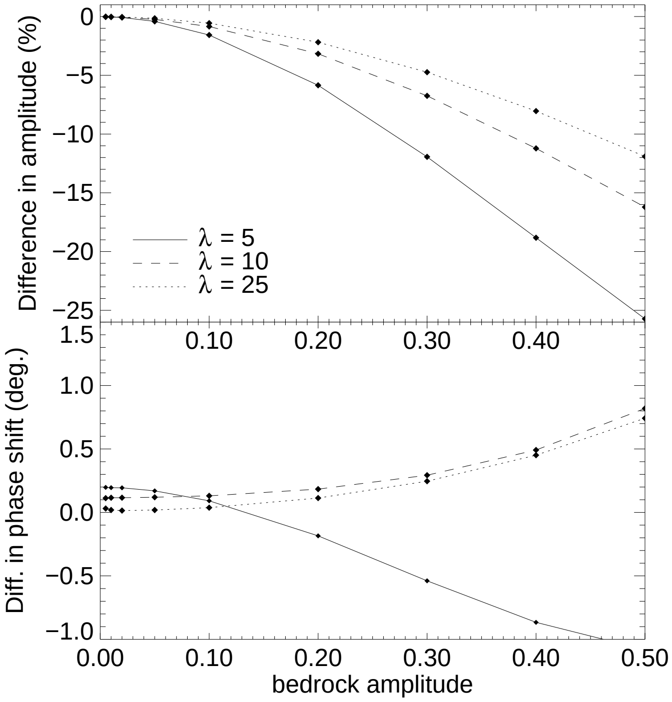

Figure 2.3: Difference between numerical and analytical steady-state amplitude ratios and phase shifts as a function of bedrock amplitude for a sinusoidal bedrock perturbation in the absence of basal sliding ($C^{(0)} = 0$). The medium is Newtonian ($n = 1$), the wavelengths are $\lambda = 5, 10, 25$, and the mean surface slope is $\alpha = 3°$. All curves are linear interpolations of calculated values (diamonds).

numerical calculations done here. Figure 2.4b gives a partial answer to this issue and shows clearly that the theoretical transfer amplitudes are accurate for $C^{(0)} = 1000$ up to about $\Delta bk = 0.2$ or $\Delta b/h = 0.3$. In particular, our results do not support Schoof's (2002) claim, based on scaling analysis, that the analytical solutions can only be used for up to about $\Delta b/h \approx 0.0001$ for $C^{(0)}$ on the order of 1000.

For $n > 1$ finite-amplitude effects are, as we will now show, particularly strong. Figure 2.5 shows the effect of basal amplitude on the bed-to-surface transfer for $n = 3$ and $n = 5$, for various values of the cross-over stress τ_0. Focusing on the curves for $\tau_0 = 0$, it is evident that the slope of the transfer amplitudes and phase shifts, as functions of amplitude, do not approach zero for $\Delta b \rightarrow 0$. The sensitivity of the transfer functions to the basal amplitude, defined as the partial derivative of $\mathcal{T}$ with respect to Δb, is, thus, not zero in the limit $\Delta b \rightarrow 0$. In principle, transfer functions can still be used to describe the bed-to-surface transfer, but they can not be listed independently of Δb. However, more importantly this implies that for $\tau_0 = 0$ the problem can not be linearized because finite-amplitude effects are important irrespectively of how small the basal amplitude is. For a power-law rheology, modifying the geometry of a uniformly inclined slab to include bedrock undulations, however small the amplitude of these undulations may be, causes the effective viscosity near to the surface to go from infinity to some large, but finite, value. It is this singularity of the near-surface effective viscosity in the limit of small bedrock amplitudes which is responsible for the non-zero slopes as $\Delta b \rightarrow 0$ for $\tau_0 = 0$ in Figure 2.5. This singular aspect of power-law rheology is not new and has been discussed before (e.g., Johnson and McMeeking, 1984). As has been pointed out by Hutter (1983), Jóhannesson (1992), and Hindmarsh (2004), to render the problem suitable for linearisation, the reference state must either be modified to include a non-zero surface-parallel deviatoric stress, or, as an alternative, a cross-over stress term must be added to Glen's flow law. These two approaches are physically not equivalent, and which one is more appropriate depends on the particular flow regime of the glacier under study, and the rheological properties of polycrystalline ice at low deviatoric stresses which currently are not well constrained (e.g., Pettit and Waddington, 2003; Duval et al., 2000; Duval, 2003). At low enough deviatoric stresses diffusional flow with $n = 1$ is expected to be the dominant deformation process, but the upper limit of this stress range is not known, and it has not been possible to observe this deformation process in laboratory experiments (Goldsby and Kohlsted, 2001). In glaciers and ice sheets, the effective viscosity of ice at low stresses is determined by the size of the linear term, and the three-dimensional stress configuration. Which of these contributions has a larger effect on the near-surface effective viscosity depends, therefore, not only on the magnitude of the cross-over stress term, but also on various factors affecting the near-surface stress, such as the longitudinal strain-rate which in turn is related to the accumulation rate.

Note that for $\tau_0 = 0$ and $n \neq 1$, finite-amplitude effects are especially pronounced for small basal amplitudes. This behavior, and the general shapes of the curves in Figure 2.5, contrast sharply with what is seen in Figure 2.3 for $n = 1$, where finite-amplitude effects only start to play role for relatively large (about $\Delta b > 0.3$) bedrock amplitudes. The finite-amplitude effects for a power-law medium are presumably particularly strong for small amplitudes rather than large ones because the change in near-surface effective viscosity decreases with increasing amplitude.

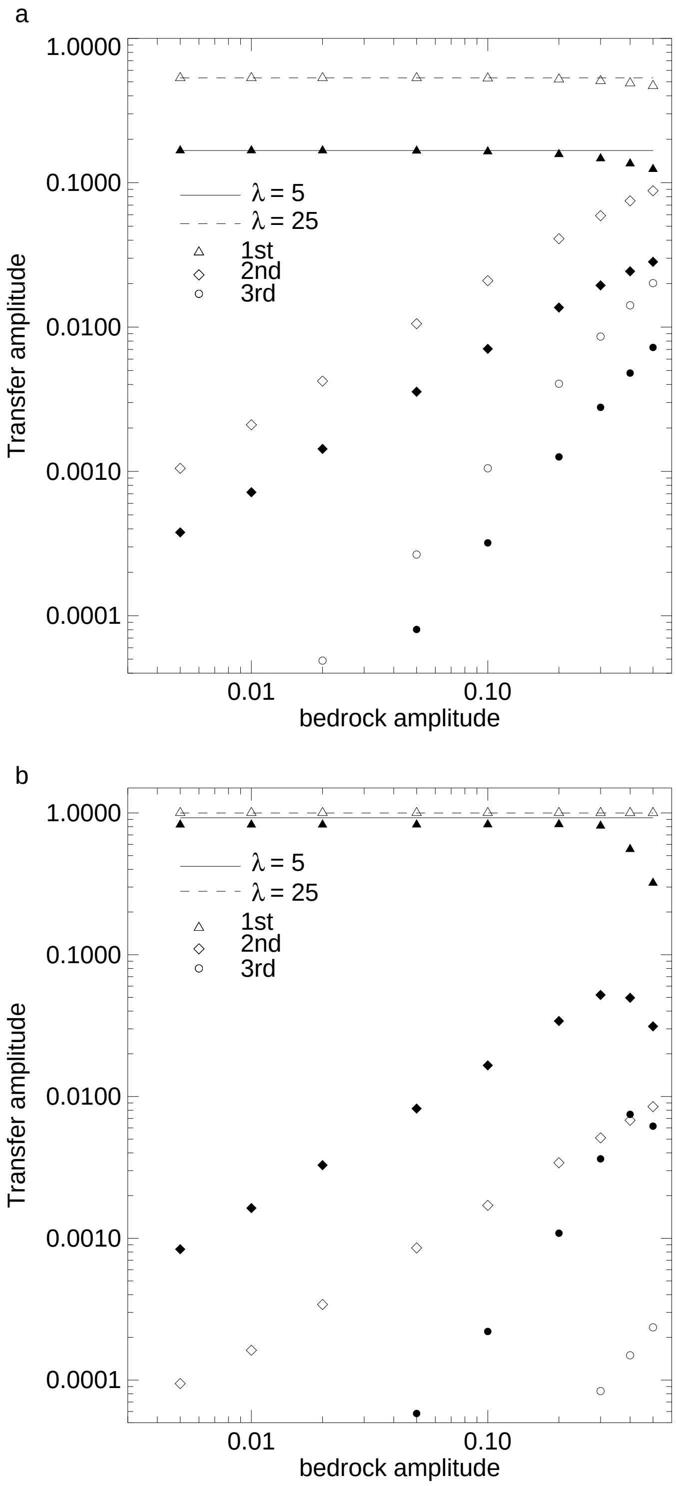

Figure 2.4: Transfer amplitudes of the first (triangles), second (diamonds), and third (circles) harmonics as a function of bedrock amplitude, for wavelengths of 5 (solid lines, solid symbols) and 25 (dashed lines, open symbols), and $C^{(0)} = 0$ (Figure a) and $C^{(0)} = 1000$ (Figure b). The medium is Newtonian. The solid and dashed lines are the theoretical limits for the first harmonic as $\Delta b/\lambda \to 0$. The mean surface slope is $\alpha = 3°$.

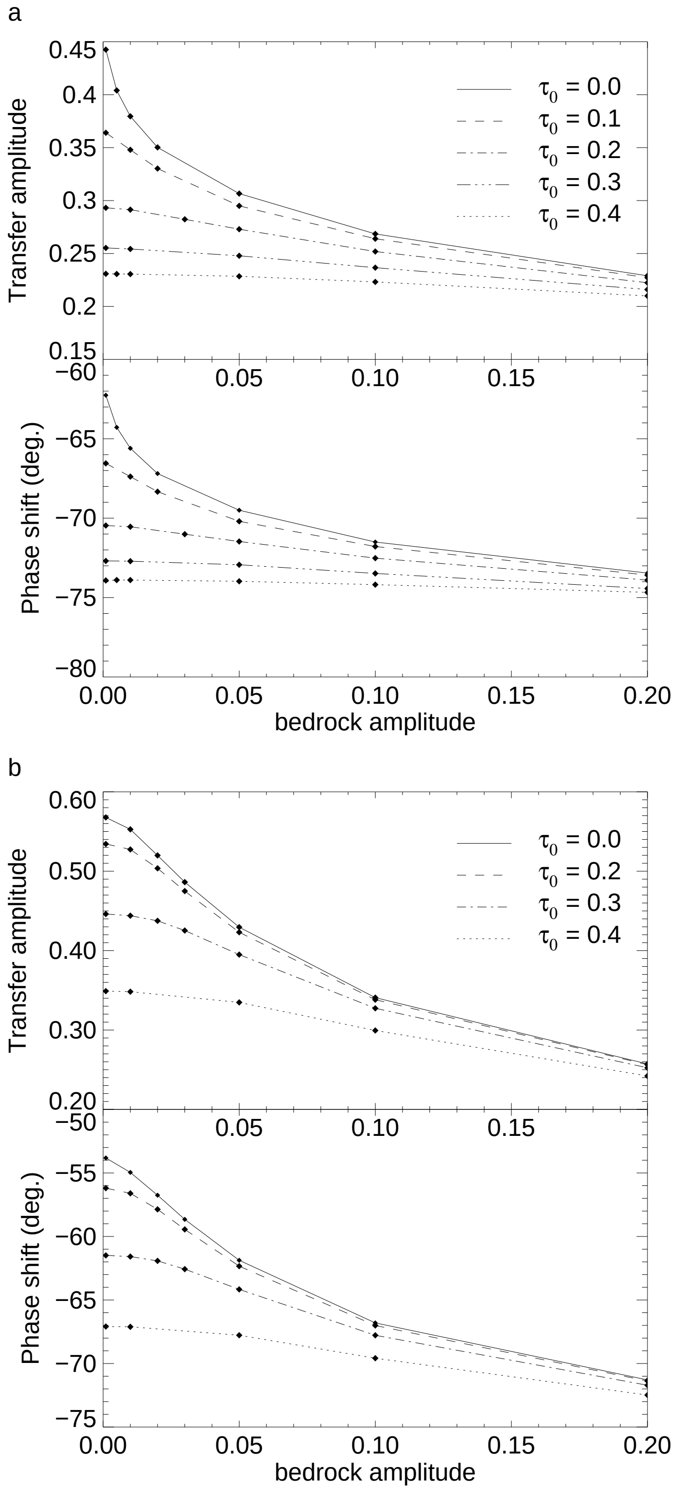

Figure 2.5: Steady-state amplitude ratios and phase shifts for a $\mathcal{B}$ perturbation as a function of the bedrock amplitude Δb for $n = 3$ (a), and $n = 5$ (b), and different values of cross-over stress (τ_0). The wavelength is $\lambda = 10$, $C^{(0)} = 0$, and $\alpha = 3°$. All curves are linear interpolations of calculated values (diamonds).

$\mathcal{C}$ perturbation

In Figure 2.6 the numerically calculated Fourier coefficients of the first, second, and third fundamental harmonics are shown for a slipperiness perturbation as functions of ΔC. This figure corresponds to Figure 2.4 for a bedrock perturbation. Again, the analytical solution valid to first order in ΔCk is represented through horizontal solid and dashed lines. Figure 2.6 shows, as did Figure 2.4 for the bed topography perturbation, that the analytical solution is accurate for a considerably larger range of the perturbation parameter (here ΔC), than the basic assumption of the analytical theory ($\Delta C \ll 1$) might have led one to expect. For $C^{(0)} = 1$, for example, the analytical solution is accurate within a few percent for $\Delta C = 0.2$ for both $\lambda = 5$ and $\lambda = 25$. Even for $C^{(0)} = 1000$, the analytical solution is similarly accurate up to $\Delta C = 0.1$ for both these wavelengths.

Figure 2.7 shows transfer amplitudes and phase shifts for a slippery perturbation as a function of amplitude (ΔC). A similar behavior is observed as in Figure 2.5, which is the corresponding figure for a bedrock perturbation. For $\tau_0 = 0$ finite amplitude effects are important even in the limit $\Delta C \rightarrow 0$, and the slope of the $\tau_0 = 0$ curve does not approach zero in this limit. With increasing τ_0 the picture changes markedly, and for $\tau_0 = 0.3$ the response is effectively linear over the amplitude range shown ($0 \leq \Delta C \leq 0.2$)

Cross-over stress

In the numerical approach used here, the singular behavior of the surface near viscosity as a function of Δb does not pose any fundamental difficulties. Whenever finite-amplitude effects become important, the transfer functions are, however, no longer independent of Δb. As we have seen this happens for all values of Δb for $n > 1$. Clearly this reduces severely the usefulness of the transfer-function representation. Because of this, and more importantly because the finite-amplitude effects at small amplitudes are caused by physically unrealistic aspects of Glen's flow law, we, in the following, only calculate transfer functions for $n > 1$ with $\tau_0 > 0$.

As seen in Figure 2.5 the linearity of the problem with respect to Δb can be regained for $n > 1$ using a relatively modest value of τ_0. For $\tau_0 = 0.3$, for example, the response is effectively linear with respect to Δb over small amplitudes. Using this value for the cross-over stress the contribution of the linear term to the effective viscosity becomes larger than that of the non-linear term (τ^{n-1}) in the uppermost 30 $\%$ of the thickness irrespective of surface slope (a consequence of the decision to scale the stresses with the mean basal shear stress instead of, for example, overburden pressure). Since most of the ice deformation contributing to the forward motion of glaciers and ice sheets takes place below this depth, the mean forward deformational velocity is hardly affected as the cross-over stress is increased from zero to 0.3.

Polycrystalline ice must, as all materials, posses a finite viscosity in limit of vanishingly small stresses. It is however not clear if the near-surface effective viscosity in glaciers and ice sheets is typically determined by the size of the constant viscosity term or by the effects of mean longitudinal deviatoric surface-parallel stress on the effective viscosity. This is an issue that can only be answered through further studies on the rheological properties of polycrystalline ice. In the absence of clear experimental evidence regarding the size of the constant viscosity term we, somewhat arbitrarily, set $\tau_0 = 0.3$, which is the

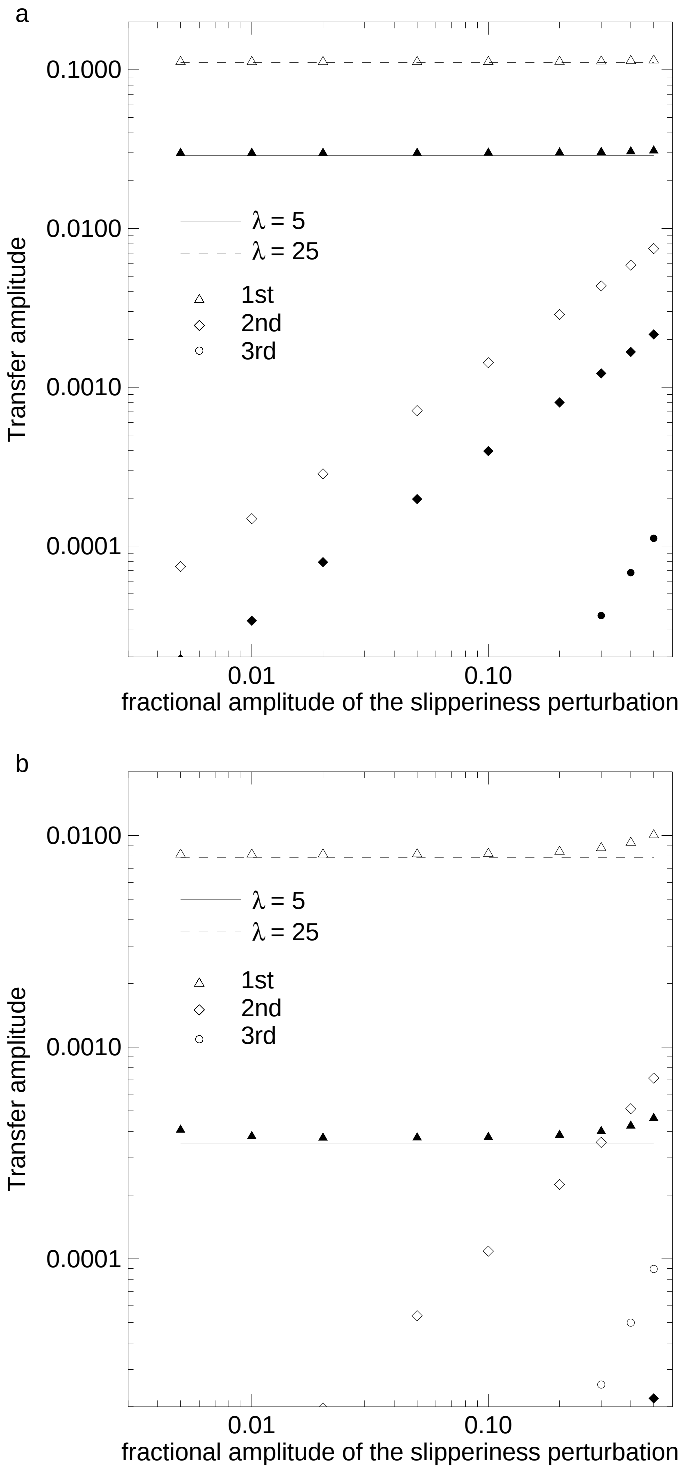

Figure 2.6: Basal-slipperiness-to-surface-topography transfer amplitudes of the first (triangles), second (diamonds), and third (circles) harmonics as functions of the fractional amplitude (ΔC) of the slipperiness perturbation, for wavelengths of 5 (solid lines, solid symbols) and 25 (dashed lines, open symbols), and $C^{(0)} = 1$ (Figure a) and $C^{(0)} = 1000$ (Figure b). The medium is Newtonian. The solid and dashed lines are the theoretical limits for the first harmonic as $\Delta C/\lambda \rightarrow 0$. The mean surface slope is $\alpha = 3°$.

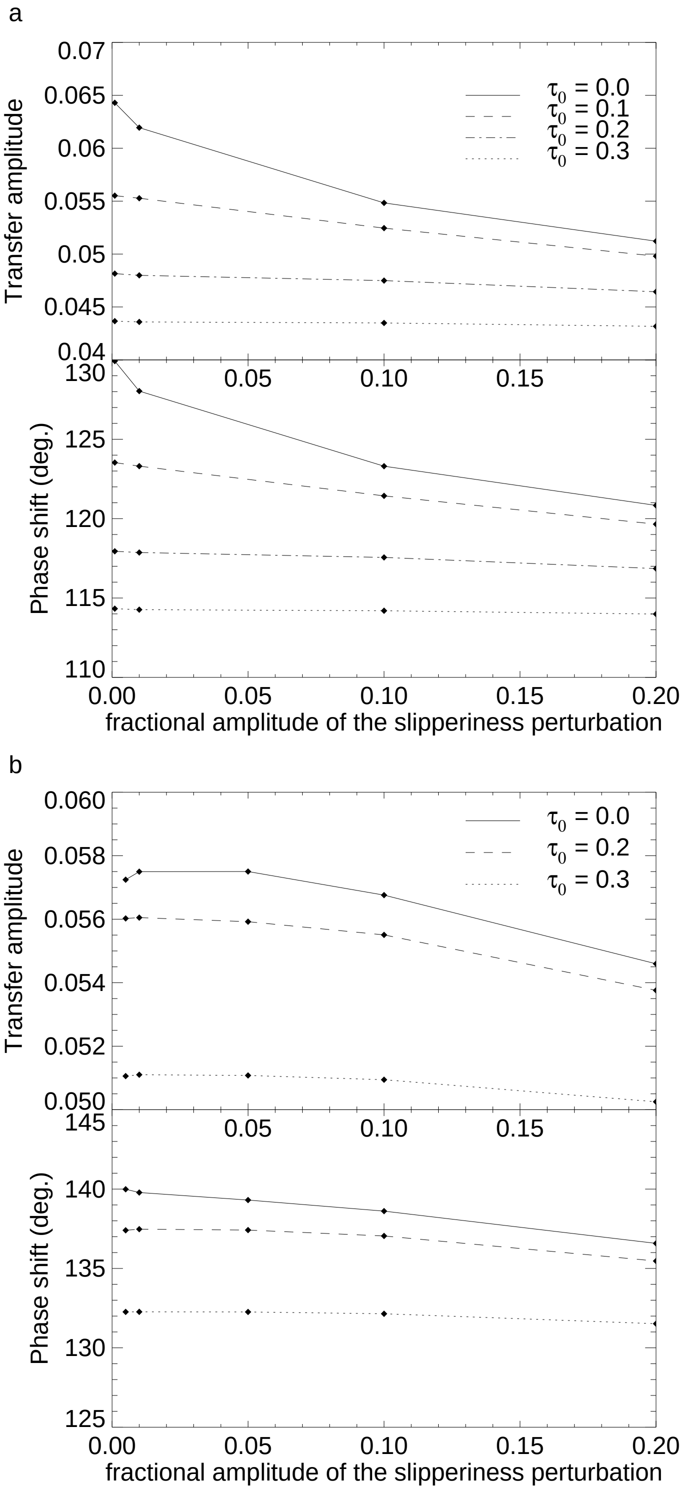

Figure 2.7: Steady-state amplitude ratios and phase shifts for a $\mathcal{C}$ perturbation as a function of ΔC for (a) $n = 3$ and (b) $n = 5$ shown for different values of τ_0. The wavelength is $\lambda = 10$, $C^{(0)} = 1$ and $\alpha = 3°$. All curves are linear interpolations of calculated values (diamonds).

lowest value that, according to Figure 2.5, makes the transfer approximately linear as a function of bedrock amplitude.

Figure 2.8 shows $\mathcal{T}_{S\mathcal{B}}$ (a) and $\mathcal{T}_{SC}$ (b) for different values of τ_0 as a function of wavelength. The bedrock and fractional slipperiness amplitudes were $\Delta b = 0.01$ and $\Delta C = 0.05$, respectively. As can be seen, the effect of τ_0 on the transfer amplitudes varies with wavelength. The effects of non-linear rheology on transfer characteristics will be discussed in detail in the next section, and, as will then become clear, the effect of increasing τ_0 on transfer characteristics is to suppress non-linear rheological effects. This is expected since with increasing τ_0 the thickness of the near-surface layer, where the linear term in the flow law exceeds the non-linear one, increases. Varying τ_0 within the range of 0 to 0.3 does, however, not lead to large quantitative differences in transfer amplitudes and phase shifts. In Figure 2.8 it can, for example, be seen that $\mathcal{T}_{S\mathcal{B}}$ amplitude varies by no more than by about 0.15 and that of $\mathcal{T}_{SC}$ by less than about 0.1.

2.4.2 Surface Topography

$\mathcal{B}$ perturbation

Figure 2.9 shows the amplitude ratio and the phase shift for a non-linear rheology for a $\mathcal{B}$ perturbation in the absence of basal motion (a) and in the presence of significant basal motion ($C^{(0)} = 10$, b). For comparison, the transfer function for a linear Newtonian rheology is also shown (solid lines). Numerical values are represented by diamonds, and for $n \neq 1$ the diamonds are connected by a linear interpolation. For $n = 1$ the (solid) line gives the analytical solution valid for small-amplitudes. How closely the diamonds follow the solid line, thus, gives an estimate of the agreement between numerical and analytical solution. As can be seen the agreement is good. The numerical calculations were done for both $\Delta b = 0.01$ and $\Delta b = 0.05$ and it was tested that finite-amplitude effects could be ignored for this amplitude range (see also Figures 2.3 and 2.5.)

For $C^{(0)} = 10$ (Figure 2.9b) the numerical values are a few percent smaller than the analytical solution for wavelengths in the range from about 5 to 50. This difference is due to the fact that basal motion in the numerical model is simulated by adding a thin basal layer with the right viscosity to give a surface-parallel velocity at its top equal to the required sliding velocity. As stated above, this method of introducing basal motion has often been used in numerical finite-element calculations (e.g., Schweizer and Iken, 1992; Vieli et al., 2000). It is, however, because of surface-parallel stress transmission acting in this basal layer, not strictly equivalent to the use of a sliding law relating basal motion and basal shear stress. Figure 2.9 gives the first quantitative estimate known to us of the differences in flow due to these two different ways of accounting for basal motion. That the differences are so small, or only a few percent, is reassuring, and can be taken as an *a posteriori* justification for all previous uses of this method to simulate a basal sliding law in finite-element models.

As Figure 2.9 shows, the non-linear bed-to-surface topography transfer functions ($\mathcal{T}_{S\mathcal{B}}$) differ from the linear one in a number of ways. Nevertheless, the qualitative features are quite similar. Focusing on Figure 2.9a ($C^{(0)} = 0$, no basal motion), we see that all transfer amplitudes increase monotonically with increasing wavelength, irrespectively of

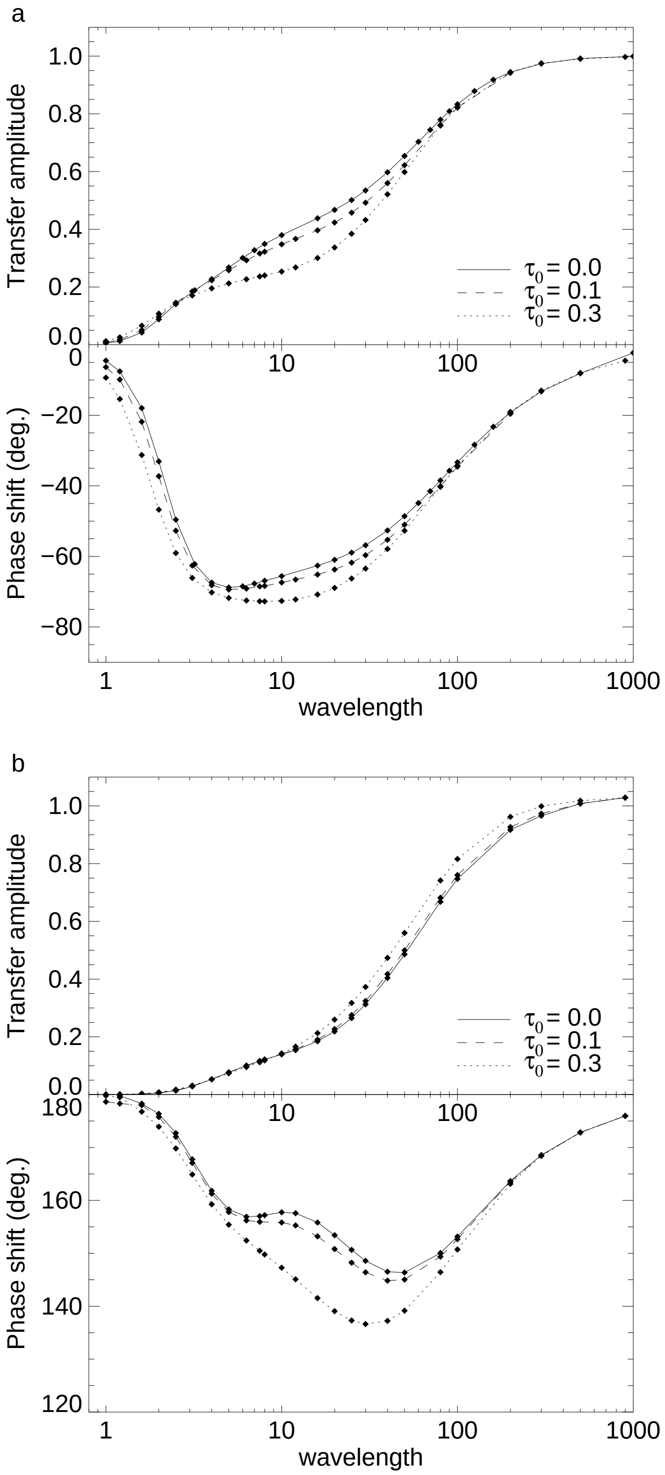

Figure 2.8: $\mathcal{T}_{\mathcal{SB}}$ for $C^{(0)} = 0$ and $\mathcal{T}_{\mathcal{SC}}$ for $C^{(0)} = 10$ as a function of wavelength for $n = 3$ and different values of τ_0. The amplitudes of the bedrock and fractional slipperiness perturbations are $\Delta b = 0.01$ and $\Delta C = 0.05$, respectively. The mean surface slope is $\alpha = 3°$. All curves are linear interpolations of calculated values (diamonds).

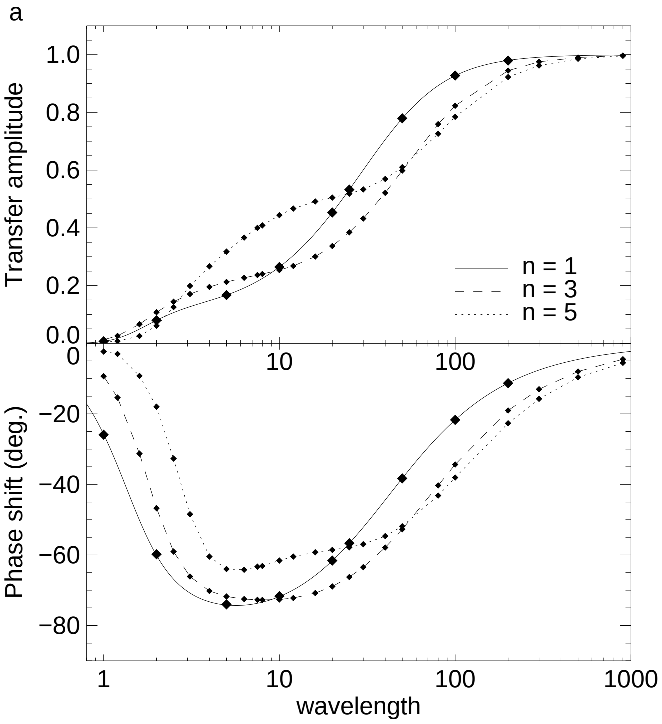

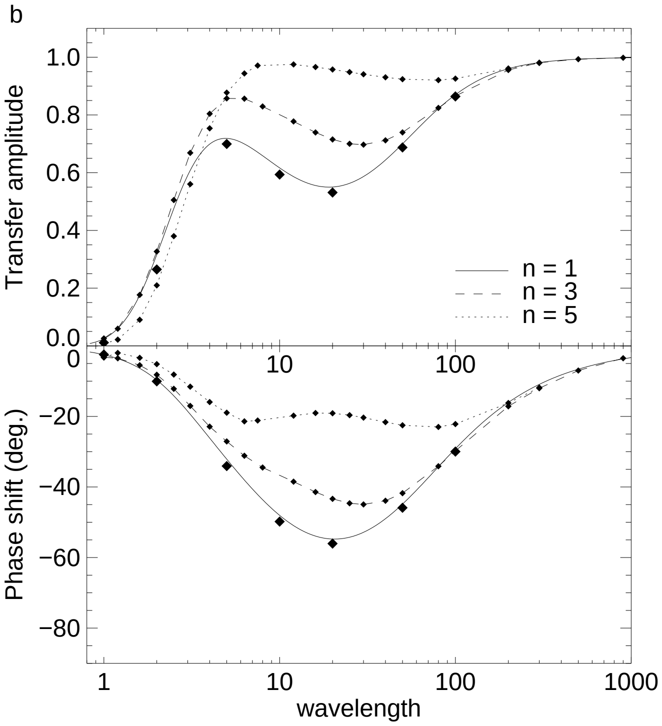

Figure 2.9: Steady-state amplitude ratios and phase shifts for a perturbation in basal topography for $C^{(0)} = 0$ (a) and for $C^{(0)} = 10$ (b). Diamonds indicate calculated values. The solid line is the analytical solution valid for $n = 1$. The dashed and the dotted lines are linear interpolations of calculated values for $n = 3$ and $n = 5$, respectively. The mean surface slope is $\alpha = 3°$. Non-linear calculations were done with $\tau_0 = 0.3$.

the value of n. On the other hand, Figure 2.9b shows that a local maximum is formed in all transfer amplitudes for $C^{(0)} = 10$, again irrespectively of the value of n.

For $C^{(0)} = 0$ no local-maximum in transfer amplitudes is found (Figure 2.9a) a fact also observed by Jóhannesson (1992) in his semi-numerical approach to this problem. This is a fundamental qualitative difference in bed-to-surface characteristics between the non-sliding and the sliding situation. Nevertheless, the same process leading to a local maximum for $C^{(0)}$ sufficiently large seems to be affecting the transfer amplitudes for any value of $C^{(0)}$, even for $C^{(0)} = 0$. It can, for example be observed in Figure 2.9a that, over the range of wavelengths from about 2 to 7 for $n = 1$, and about 2 to 50 for $n = 5$, the transfer amplitudes are larger than one would otherwise expect from the shape of the amplitude curves at both smaller and larger wavelengths. Gudmundsson (2003) gives a simple physical explanation for the appearance of the local maximum in transfer amplitudes, as being the result of a competition between two processes as the wavelength is increased: the increase in the vertical extent of the flow perturbations as measured from the bed-line and the decrease in the strength of the perturbation measured close to the bed as the slope parameter ($\Delta b/\lambda$) becomes smaller.

As seen in Figure 2.9 the effects of non-linear rheology on the transfer characteristics can be either to increase or decrease the transfer amplitudes and relative phase shifts depending on wavelength. It is helpful to distinguish between three ranges of wavelengths: short, intermediate, and large. Over short wavelengths, transfer amplitudes are small (< 0.1) and decrease with increasing n. This range of wavelengths is from 0 to about 2 with the upper range depending on n and increasing with it. Over intermediate wavelengths, transfer amplitudes increase markedly with n and a local maximum in transfer amplitudes is formed for $C^{(0)}$ large enough. Again the upper limit of this range of intermediate wavelengths depends on n and shifts to larger wavelengths with increasing n. For $n = 1$, the range of intermediate wavelengths is from about 2 to 30 and from about 2 to 70 for $n = 3$. The long wavelength range is characterized by a gradual monotonic increase in transfer amplitudes towards unity. Over these long wavelengths, the transfer can be accurately described by a linearized version of the shallow ice approximation (SIA).

One of the qualitative differences between $\mathcal{T}_{S\mathcal{B}}$ transfer amplitudes calculated on the basis of the shallow-ice approximation (SIA) and those calculated by including all deviatoric stress components is the different number of inflection points they exhibit as functions of wavelength. The SIA transfer functions have only one inflection point, and not three as is found when all stress components are included in the calculations. In Figure 2.9, the third inflection point of each curve (from concave to convex), counting from $\lambda = 0$, can be taken as marking the transition to long-wavelengths. Over long-wavelengths, the shallow-ice approximation gives an accurate description of glacier flow. Over all shorter wavelengths the flow is to some extent affected by deviatoric stresses not included in the shallow-ice approximation. As can be seen from Figure 2.9, increasing n has the effect of shifting the third inflection point to higher values. This non-linear effect was first observed by Landon and Raymond (1978) and, as discussed by them, reflects an increase in the range of surface-parallel stress gradients with increasing n.

The lower half of Figures 2.9a and b show relative phase shifts of the surface topography with respect to the bed topography. In the short and the long-wavelength limit, surface undulations are, as expected, always in phase with the bedrock undulations. The phase shifts are within the range of -90 to 0 degrees, with the lower limit of that range increasing (smaller negative numbers) with increasing n. In steady state, the peak of the surface undulation is, thus, always upstream of the bedrock undulation. Note that this statement is not correct for transient flow as Figure 2.2 shows. With increasing n, phase shifts increase over short and intermediate wavelengths, but decrease over long wavelengths.

$\mathcal{C}$ perturbation

The $\mathcal{T}_{SC}$ transfer functions for basal slipperiness perturbations are shown in Figure 2.10 for $C^{(0)} = 1$ (a) and $C^{(0)} = 10$ (b). For ease of comparison, transfer amplitudes are scaled with their respective long-wavelength limits ($C^{(0)}/(n + 1 + 2C^{(0)})$, see Gudmundsson (2004)).

As is the case for the $\mathcal{T}_{SB}$ transfer functions, distinguishing between short, intermediate, and long wavelengths is also useful for $\mathcal{T}_{SC}$. The respective limits of these ranges of wavelengths, and the general effect of n on transfer amplitudes, are found to be the same for both the $\mathcal{T}_{SB}$ and the $\mathcal{T}_{SC}$ transfer amplitudes. Note that there is no local maximum seen in the amplitudes of the $\mathcal{T}_{SC}$ transfer functions in Figure 2.10. In most other aspects, however, there are strong similarities between Figure 2.10 and 2.9: the number of inflection points is the same in all curves, all amplitudes decrease over short and increase over intermediate wavelengths with n, and the lower-limits of the long-wavelength ranges shifts to larger wavelengths with increasing n for both $\mathcal{T}_{SB}$ and $\mathcal{T}_{SC}$. Note however also that, over intermediate wavelengths, an increase in $C^{(0)}$ has a very different effect on $\mathcal{T}_{SC}$ than on $\mathcal{T}_{SB}$. Not only is no local maximum formed with increasing $C^{(0)}$, transfer amplitudes in fact become smaller with increasing $C^{(0)}$. This quantitative aspect of the transfer amplitudes shown in Figure 2.10, however, depends on them being scaled with their respective long-wavelength limits. If that is not done, the long-wavelength limit increases with $C^{(0)}$ and with it the transfer amplitudes over the intermediate range as well.

The lack of a local maximum and reduction in transfer amplitudes over intermediate wavelengths with increasing $C^{(0)}$ (when scaled with their respective long-wavelength limits), appear to be the most fundamental differences between $\mathcal{T}_{SC}$ and $\mathcal{T}_{SB}$ transfer amplitudes. The net effect is to make the transition from weak to strong bed-to-surface transfer sharper with increasing n for high (> 5) values of $C^{(0)}$. Note that the phase shifts shown in the lower half of Figures 2.10a and b are, within the accuracy of the calculation, related to those in 2.9 through $\phi_{SC} = \pi + \phi_{SB}$, as is expected theoretically (Gudmundsson, 2003).

Influence of surface slope

Figure 2.11a shows the effect of surface slope on the $\mathcal{T}_{SB}$ transfer function. Figure 2.11b is the corresponding figure for $\mathcal{T}_{SC}$. Increasing mean surface slope results in larger bed-to-surface amplitudes and relative phase shifts. The same monotonic increase in transfer amplitudes is predicted by analytical expressions for transfer amplitudes valid for long-wavelengths and arbitrary n (see Equation (4.4.6) in Jóhannesson (1992)). Generally the lower-limit of the long-wavelength range becomes larger with decreasing surface slope, and the position of the third inflection point shifts to higher values of λ. Since the long-wavelength range corresponds to those wavelengths where the shallow-ice approximation is valid, this implies that its applicability to problems of glacier flow is markedly more limited for ice sheets with low than high surface slopes.

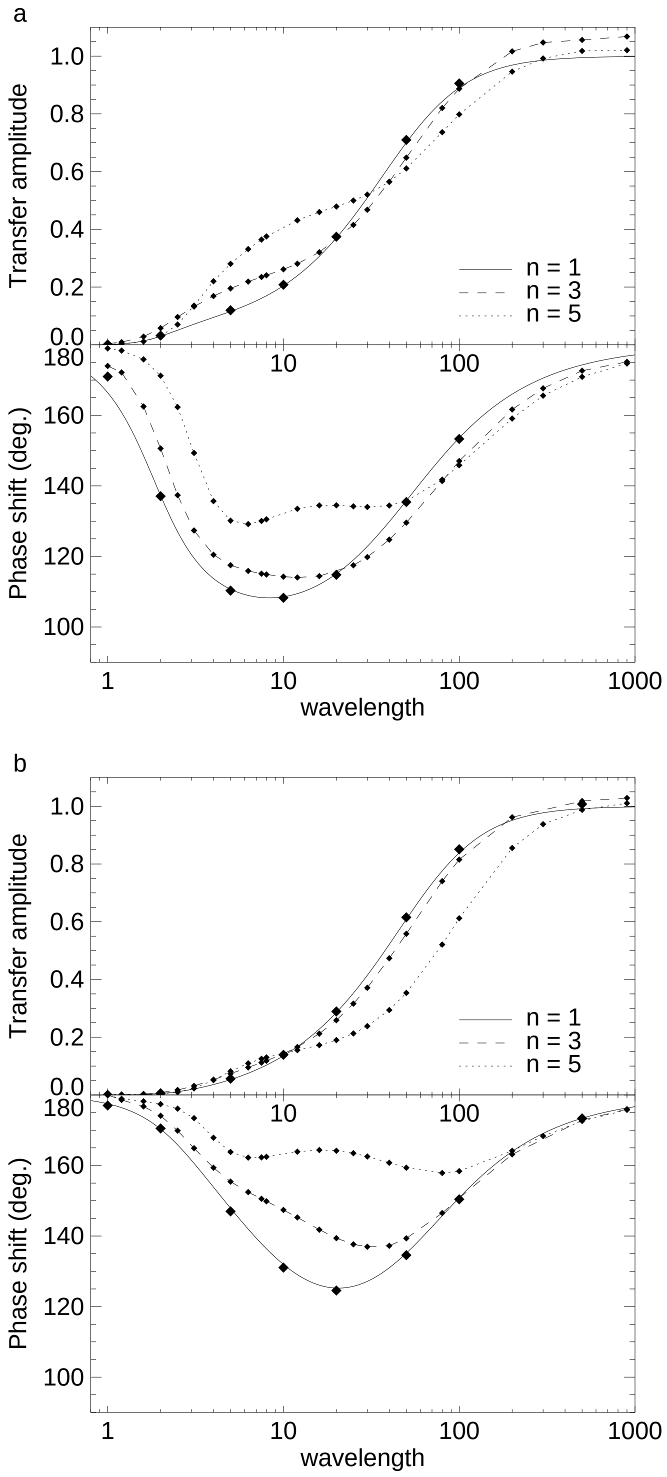

Figure 2.10: Same as Figure 2.9, but for a basal sliding perturbation with $C^{(0)} = 1$ (a) and $C^{(0)} = 10$ (b).

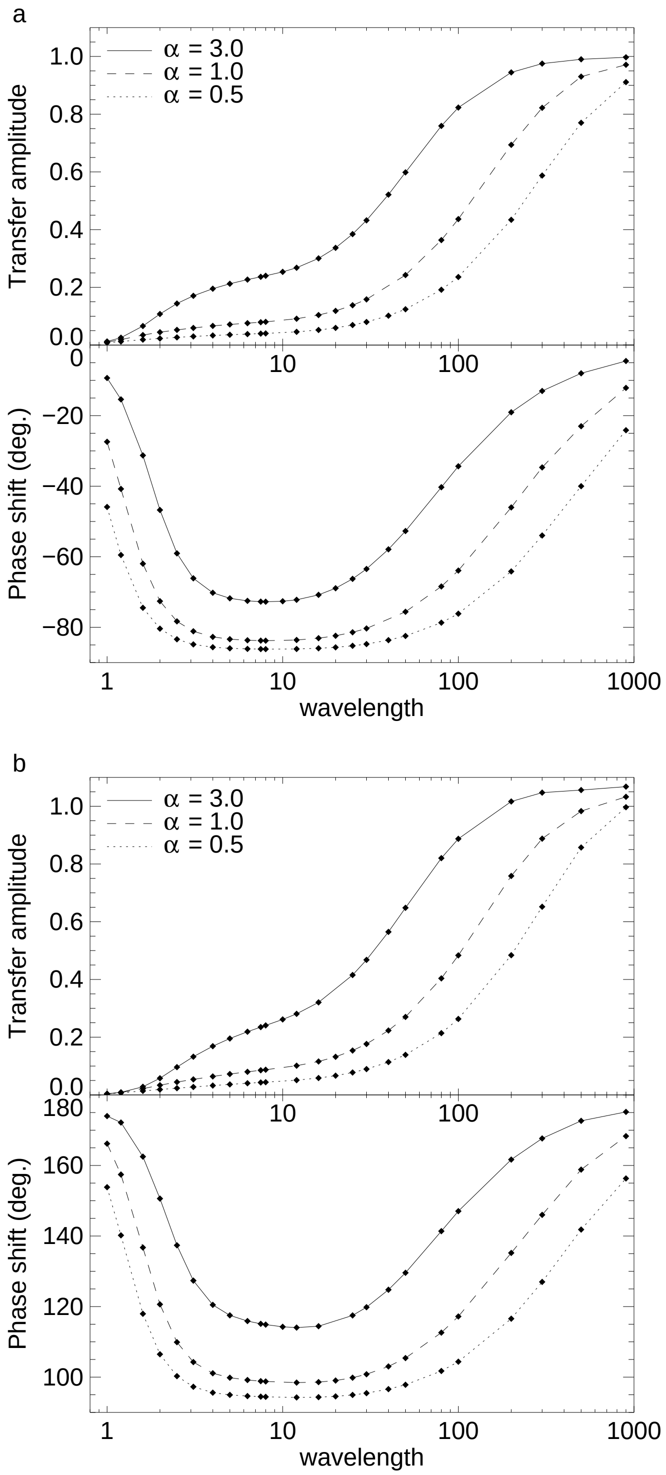

Figure 2.11: $\mathcal{T}_{\mathcal{SB}}$ for $C^{(0)} = 0$ (a) and $\mathcal{T}_{\mathcal{SC}}$ for $C^{(0)} = 1$ (b), both for $n = 3$, $\tau_0 = 0.3$ and different surface slopes α (degrees). All curves are linear interpolations of calculated values (diamonds).

Influence of sliding law exponent

As described above, a Weertman type sliding law is here used as a relationship between the basal sliding velocity u_b and basal shear stress τ_b, that is $u_b = C\tau_b^m$. Observations suggest that the rheology of till under some active ice streams on the Siple Coast, West Antarctica, can be characterized by high values of the sliding law exponent m (Kamb, 2001; Tulaczyk et al., 2000a,b). The transfer characteristics for a high value of the exponent m are therefore of interest with regard to the relationship between bed and surface on fast-flowing ice streams. Figures 2.12a and b show the transfer amplitudes and phase shifts for a bedrock and a basal slipperiness perturbations for $n = 3$ and three different values of 1, 3, and 20 for the sliding law exponent m. As can be seen in these figures increasing m leads to some decrease in transfer amplitudes for both types of basal perturbations. However, no new qualitative features are introduced. The absolute changes in transfer amplitudes as m is increased from 1 to 20 are generally less than 0.1, or in relative terms, for λ larger than about 3, about 10 to 20 percent. We conclude that the transfer characteristics are, in this respect, not fundamentally affected by the degree of rheological non-linearity of till. We emphasize the fact that we have assumed a commonly used form of sliding law. We do not deal here with the important but different issue of understanding under what conditions this kind of sliding law might be realized, nor what might be the limits to its applicability. As has been pointed out by Iken (1981) and recently by Schoof (2005), it is for example likely that in the case of widespread cavitation, sliding velocities become insensitive to changes in basal shear stress.

2.4.3 Surface Velocities

$\mathcal{B}$ perturbation

The steady-state amplitude ratios and phase shifts of surface-parallel (u) and surface-normal (w) surface velocities are shown in Figure 2.13 for a $\mathcal{B}$ perturbation in the absence of basal sliding ($C^{(0)} = 0$). Note that here the terms ‘surface-parallel’ and ‘surface-normal’ refer to the undisturbed plane-slab geometry. Because the surface mass-balance distribution is set to zero, the velocity component normal to the final steady-state geometry is always zero. Analytical amplitude ratios and phase shifts for $n = 1$ are shown as solid lines with diamond symbols representing numerically calculated values. As can be seen the agreement between the analytical and the numerical solutions is good.

In the limits of both short and long wavelengths the perturbations in both surface-parallel and surface-normal velocity components approach zero as expected. This is related to the fact that for $\lambda \to 0$, the anomalous flow field becomes increasingly concentrated at the bed. Slope perturbations calculated on the basis of the shallow-ice approximation, incorrectly, do not approach zero as $\lambda \to 0$ (Gudmundsson, 2004). For long wavelengths the slope perturbations approach zero and with them the amplitude of the velocity perturbations.

For symmetry reasons the phase shift of surface-parallel velocities is zero for $\lambda = 0$ (Gudmundsson, 2003). The surface-parallel velocity is, thus, initially in phase with the bedrock perturbation, with its maximum placed directly over the peak of the sinusoidal bedrock undulation. With the wavelength increasing from zero, the phase shift initially

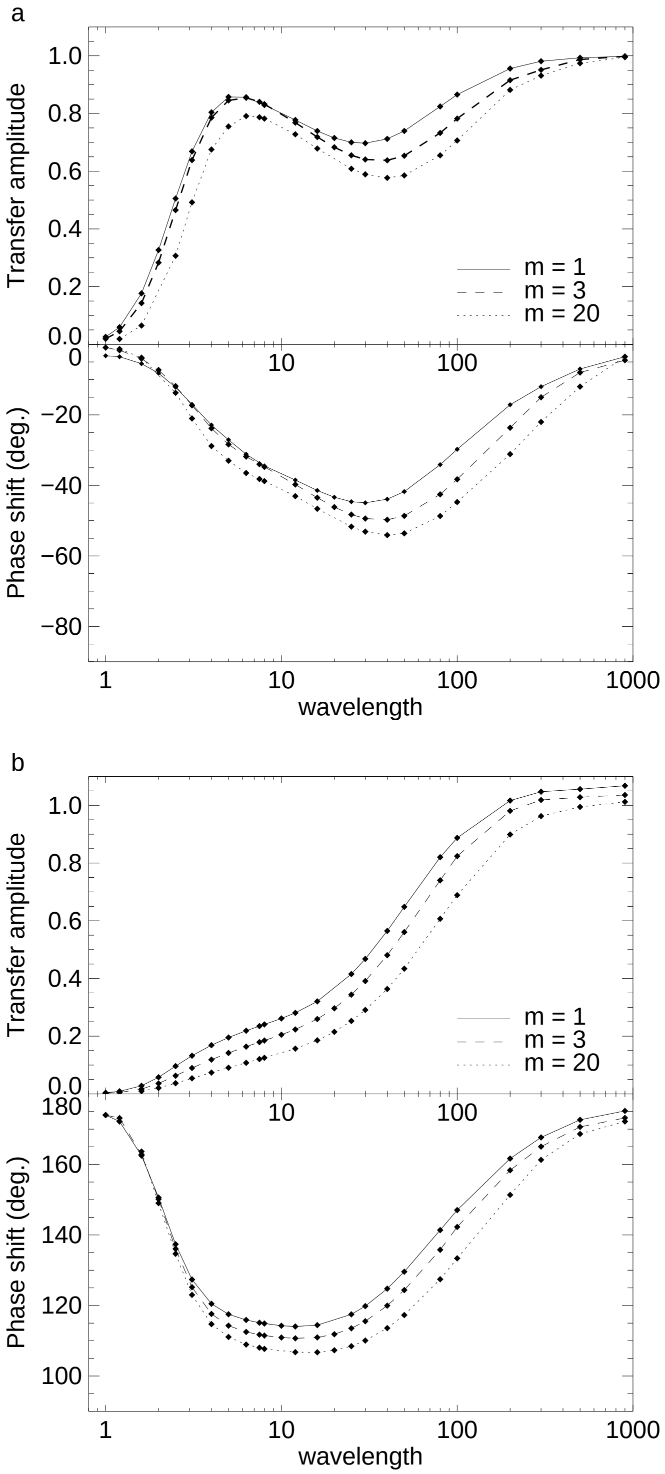

Figure 2.12: $\mathcal{T}_{\mathcal{SB}}$ for $C^{(0)} = 10$ (a) and $\mathcal{T}_{\mathcal{SC}}$ for $C^{(0)} = 1$ (b), for $n = 3$, $\tau_0 = 0.3$ and three different basal sliding law exponents m of 1, 3, and 20. The mean surface slope is $\alpha = 3°$. All curves are linear interpolations of calculated values (diamonds).

decreases and then gradually increases again. As a consequence, a local minimum in phase (maximum negative value) is formed, although for $n = 1$ this minimum can hardly be detected (Figure 2.13a). Note that for negative phase angles, the location of the maximum of the surface-parallel velocity component is upstream of the bedrock peak. As λ is increased towards infinity the relative phase shift approaches $+\pi/2$ with the velocity maximum above the maximum in forward bedrock slope.

Because the phase shift of the surface-parallel velocity remains close to zero, or even becomes somewhat negative, for wavelengths up to about 10 (Figure 2.13a), the maximum of the surface-parallel surface velocity component is almost directly above the peak of the sinusoidal bed-line. This may seem at first sight a somewhat counterintuitive result because a bedrock perturbation might be expected to give rise to a maximum increase in forward surface-parallel velocities downstream of its highest peak. Inspection of the velocity field shows that for this range of wavelengths where the phase shift is negative, a circular motion is set up in the perturbed velocity field. The consequence is reversal in flow direction of the anomalous flow with depth. Balise and Raymond (1985) showed that this type of recirculation within the anomalous velocity field is possible during the initial response to a basal velocity anomaly. The problem considered here is somewhat different from that considered by Balise and Raymond (1985) as the surface is in steady-state and the basal perturbation a geometrical perturbation in the shape of the bed-line rather than a prescribed velocity along an otherwise flat bed. Recirculation is, thus, not just limited to the non steady-state situations considered by Balise and Raymond (1985), but is a general feature of glacier flow at short and intermediate wavelengths. An observation of a decrease in surface velocities over a limited area can, thus, not be taken as indicative of an increase in basal resistance to glacier flow.

Phase shifts for the surface-normal velocity component (w) are equal to $-\pi/2$ for both $\lambda \to 0$ and $\lambda \to +\infty$ (Figure 2.13b) showing that in these limits the maxima in upward and downward velocities are found directly above the steepest upward and downwards slopes of the bed-line, respectively. For all other wavelengths the phase shifts are smaller (larger negative). For wavelengths around 10, the phase shifts in Figure 2.13b are only a few tens of degrees from -180 degrees, and the maximum downward velocity, therefore, situated almost directly above the highest position of the bed-line.

Comparing Figure 2.13 for $C^{(0)} = 0$ to the corresponding Figure 2.14 for $C^{(0)} = 10$ shows that basal motion can give rise to a second local maximum in the $\mathcal{T}_{\mathcal{UB}}$ transfer function. Note that, as discussed above, the appearance of an additional maximum in transfer amplitudes is also observed for $\mathcal{T}_{\mathcal{SB}}$ with increasing $C^{(0)}$ (compare Figures 2.9a and b). Increasing the basal slipperiness from zero to $C^{(0)} = 10$ leads to an increase in the phase shifts of the surface-normal velocity component. Note that for $C^{(0)} = 10$ the maximum in surface-normal transfer amplitude is larger than that of the surface-parallel velocity.

As is the case for the surface topography, the non-linear velocity transfer functions are qualitatively similar to the linear ones. Nevertheless, a number of important differences are observed. All positions of the respective maxima in surface-parallel and surface-normal velocities get shifted to larger wavelengths with increasing n. Maximum transfer amplitudes of the u velocity component are reduced as n is increased, whereas the maximum transfer amplitudes of the w component are, in most cases shown, larger. One of the most interesting effects of non-linear rheology on the velocity transfer characteristics

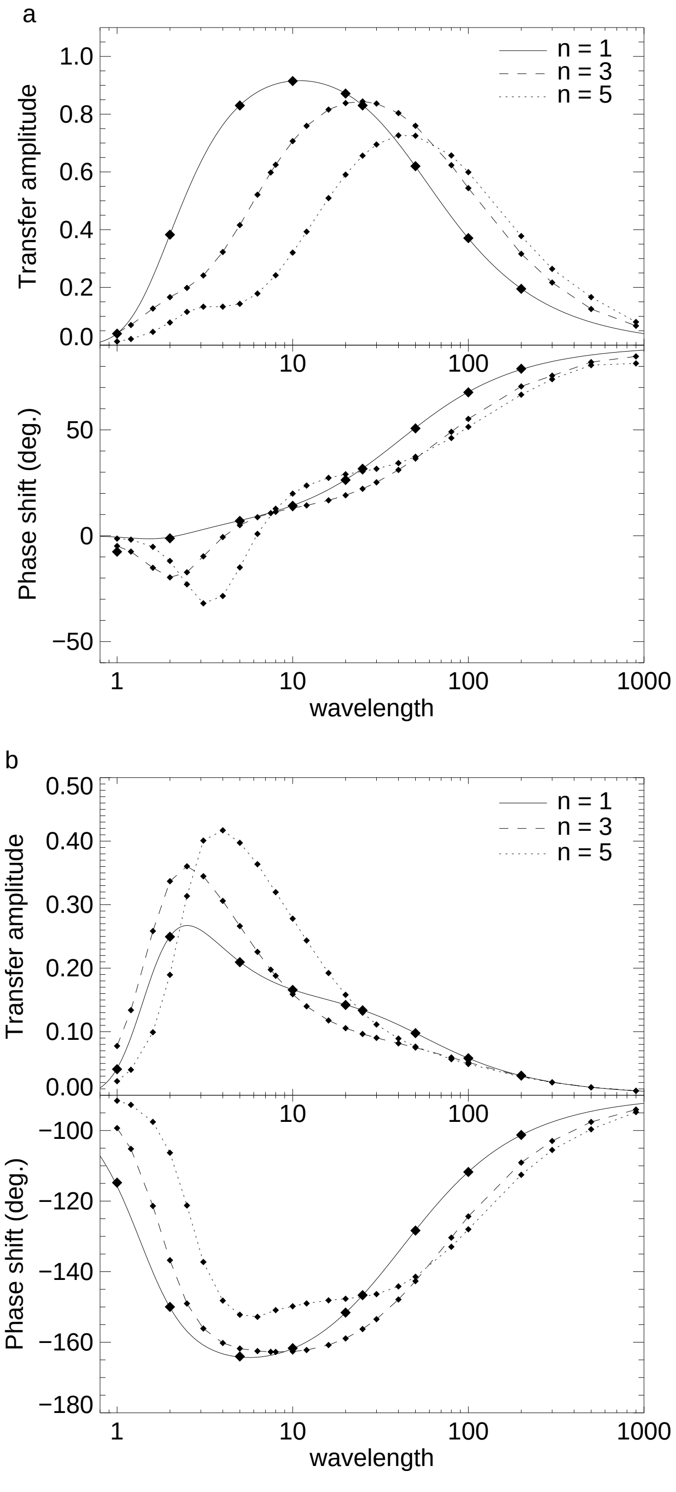

Figure 2.13: Steady-state amplitude ratios and phase shifts of surface-parallel (a) and surface-normal (b) surface velocities for a $\mathcal{B}$ perturbation with $C^{(0)} = 0$. Diamonds indicate calculated values. Solid lines correspond to the analytical solution for $n = 1$. Dashed and dotted lines are linear interpolations of calculated values for $n = 3$ and $n = 5$, respectively. The mean surface slope is $\alpha = 3^\circ$ and $\tau_0 = 0.3$.

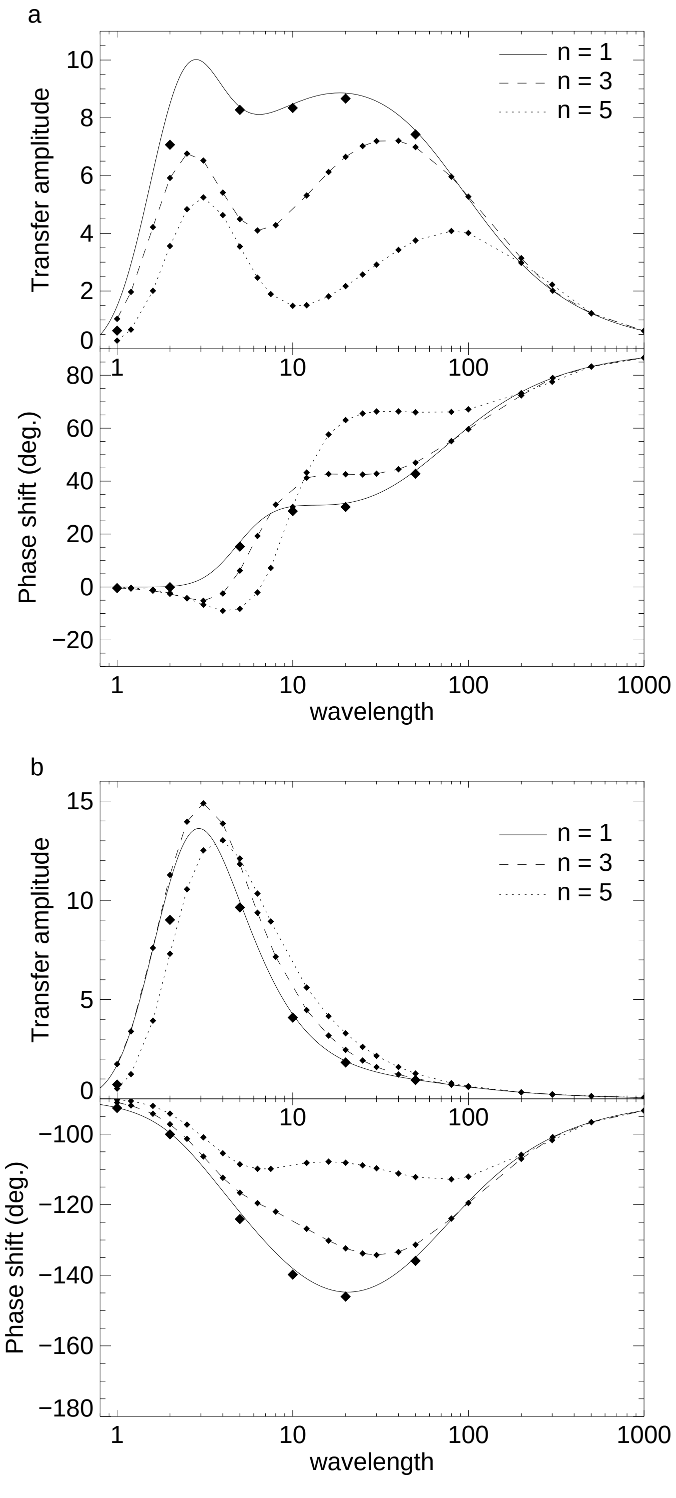

Figure 2.14: Same as Figure 2.13, but for $C^{(0)} = 10$.

is seen in the phase shifts of u over wavelengths less than about 10 (Figures 2.13a and 2.14a) where the phase shifts becomes increasingly negative with n. As discussed above, this implies that the position of maximum surface-parallel velocity is upstream of the peak of the sinusoidal bed-line. Although this is not an entirely non-linear effect (for $n = 1$ the phase shift for $\mathcal{T}_{\mathcal{UB}}$ also does become negative for wavelengths around 2), increasing n leads to considerably smaller (larger negative) phase shifts (Figures 2.13a and 2.14a). Similar to what was observed for the topography, the effects of surface-parallel stress transmission are felt over larger range of wavelengths as n is increased.

$\mathcal{C}$ perturbation

The transfer functions of surface velocities for a basal slipperiness perturbation ($\mathcal{C}$ perturbation) are shown in Figure 2.15 for $C^{(0)} = 1$ and in Figure 2.16 for $C^{(0)} = 10$. The transfer amplitudes of surface-parallel velocities increase monotonically with wavelength from zero towards the maximum of ${C^{(0)}}^2/((n+1) + 2C^{(0)})$ (Gudmundsson, 2004). The phase shift of surface-parallel velocities increases for both values of mean basal slipperiness from $-\pi$ towards zero, showing the same characteristics as the phase shifts of surface-parallel velocities for a $\mathcal{B}$ perturbation. Note that the transfer amplitudes of $\mathcal{T}_{\mathcal{UC}}$ decrease with increasing n. This is similar to Balise (1987) finding that for non-linear rheology the instantaneous transfer of a bed-parallel basal velocity anomaly is less than for a linear rheology. Note also that the transfer amplitudes for the surface-normal velocity components $\mathcal{T}_{\mathcal{WC}}$ increase with n over the shorter range of intermediate wavelengths.

The effects of n on the $\mathcal{T}_{\mathcal{UC}}$ and $\mathcal{T}_{\mathcal{WC}}$ are not dissimilar from those on $\mathcal{T}_{\mathcal{UB}}$ and $\mathcal{T}_{\mathcal{WB}}$. Increasing n causes a reduction in $\mathcal{T}_{\mathcal{UC}}$ amplitudes and the lower limit of the long-wavelength range (for which the shallow-ice approximation can accurately be used), to become shifted to higher wavelengths. Phase angles of surface-parallel velocities initially decrease with λ, and this decrease is more pronounced for higher values of n. There is an overall increase in the phase of the surface-normal velocity component with n.

2.4.4 Discussion and summary

The transfer of finite-amplitude topographic and basal slippery perturbations to the surface of glaciers and ice streams can be broadly summarized as follows. Three different ranges of spatial scales (short, intermediate, and long) can be identified. For each of these spatial scales the transfer characteristics differ in a number of significant aspects.

Over short scale, surface topographic transfer amplitudes ($\mathcal{T}_{\mathcal{SB}}$ and $\mathcal{T}_{\mathcal{SC}}$) are small ($< 0.1$) and the phase shifts for a bedrock and a slipperiness perturbation are within a few tens of degrees of zero and 180 degrees, respectively (Figures 2.9 and 2.10). The range of short scale is from zero to about 3. Increasing n has the effect of reducing the topographic transfer amplitudes. The anomalous flow is concentrated to the vicinity of the bed and surface velocity anomalies are small.

Over intermediate scale, transfer amplitudes of surface-normal velocity components ($\mathcal{T}_{\mathcal{WB}}$ and $\mathcal{T}_{\mathcal{WC}}$) display a pronounced maximum as functions of wavelength (Figures 2.13, 2.14, 2.15, and 2.16). A local maximum in $\mathcal{T}_{\mathcal{SB}}$ transfer amplitudes is formed for $C^{(0)}$ sufficiently large (Figure 2.9). No similar maximum in $\mathcal{T}_{\mathcal{SC}}$ is formed, irrespectively of the

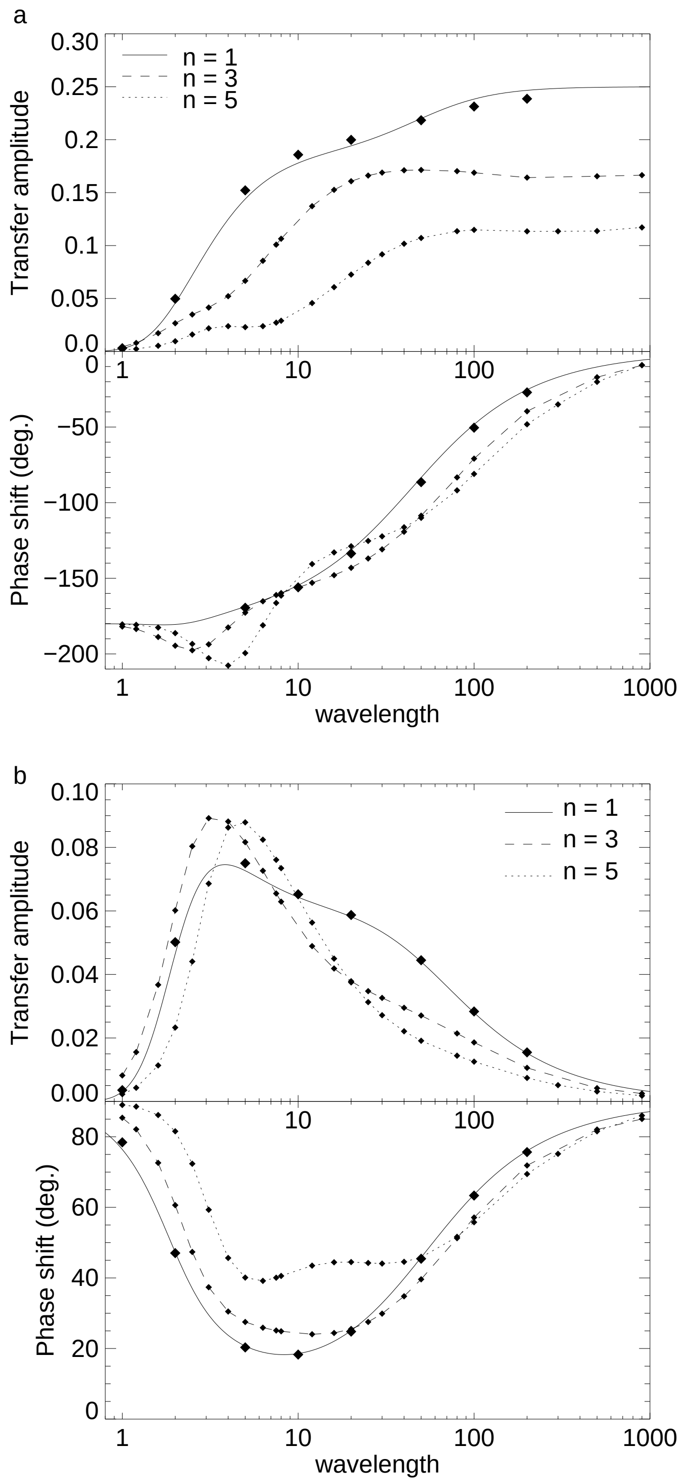

Figure 2.15: Steady-state surface velocity transfer functions for a perturbation in basal slipperiness ($\mathcal{C}$ perturbation); (a) shows the results for the surface-parallel velocity component, while (b) shows those for the surface-normal component. As in other figures, diamonds represent calculated values, the solid line is the analytical solution for $n = 1$, and other curves are linear interpolations of calculated values. The mean surface slope is $\alpha = 3°$, $\tau_0 = 0.3$, and $C^{(0)} = 1$.

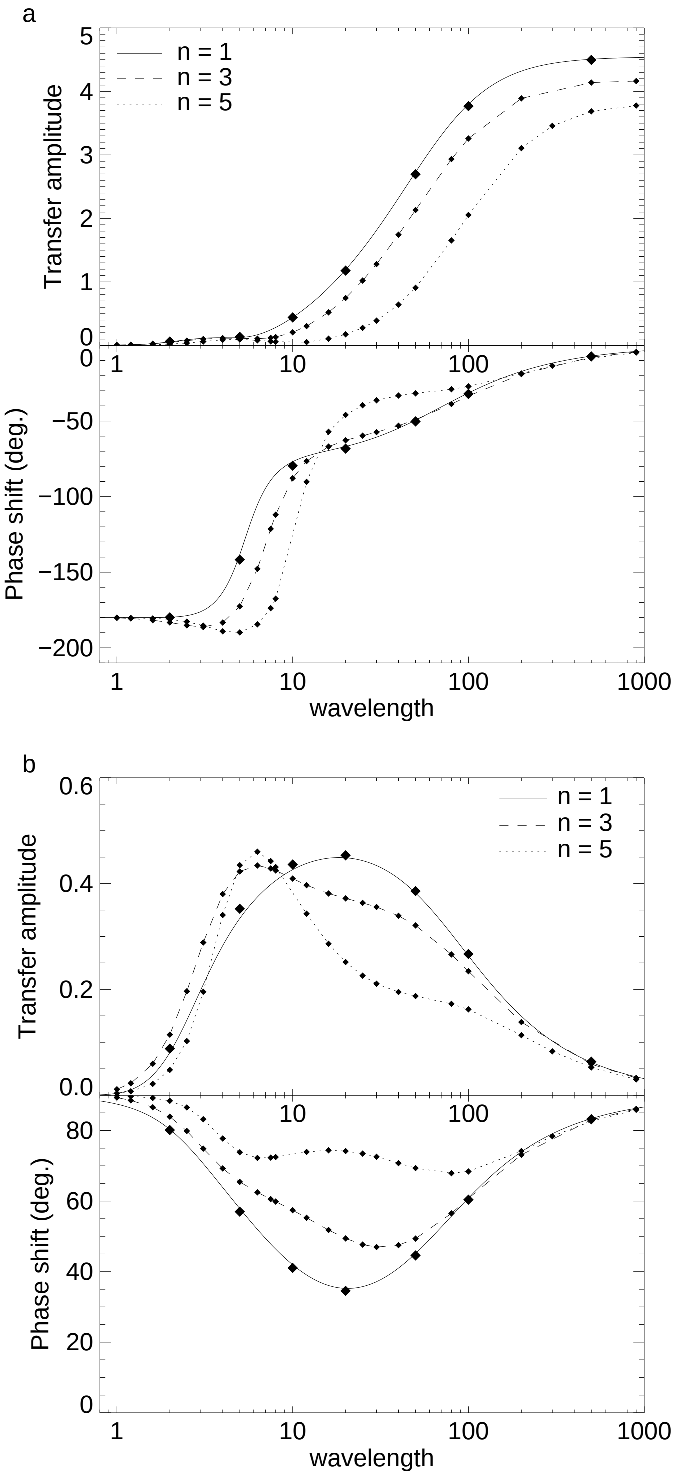

Figure 2.16: Same as Figure 2.15, but for $C^{(0)} = 10$.

value of $C^{(0)}$ (Figure 2.10). Topographic transfer amplitudes increase with n. Intermediate scale ranges from about 1 to 30 for $n = 1$, and from about 2 to 70 for $n = 3$.

By definition of the term ‘long scale’ , the transfer characteristics over this spatial scale can be accurately predicted using the shallow ice approximation. As has been observed by other authors we find that the lower-limit of this range of wavelengths increases markedly with n (e.g., Landon and Raymond, 1978). We also find that the lower limit of the long-wavelength range becomes larger with decreasing surface slope. This implies that the applicability of the shallow ice approximation to problems of glacier flow is markedly more limited for ice sheets with low than high surface slopes. This is an important and interesting point. The main assumption of the shallow ice approximation (SIA) is that the thickness-to-span ratio is small. One might therefore expect that as the overall slope decreases, the accuracy of the SIA improves. This is, however, only correct if no other spatial scales are of importance. In particular, the presence of basal disturbances adds the ratio of their wavelength to thickness as a further non-dimensional parameter. Figure 2.11 shows that the influence of this parameter extends over a larger range of wavelengths as the slope decreases, thereby limiting the applicability of SIA to increasingly larger wavelengths as the overall slope decreases.

The effects of n on transfer characteristics are mainly quantitative. Qualitative aspects, such as the number of local maxima and inflection points, of the bed-to-surface transfer do not change as n is varied. As mentioned above, with increasing n the amplitudes of the topographic transfer functions become smaller over short scale but larger over intermediate scale, and the transition between intermediate and long scale gets shifted to longer wavelengths. The amplitude of the surface-parallel velocity component decreases over intermediate scale with n, while that of the surface-normal component increases somewhat (Figures 2.13, 2.14, 2.15, and 2.16).

The effects of non-linear rheology on bed-to-surface transfer can be understood in terms of how n affects the vertical variation of the effective viscosity distribution of the unperturbed plane slab geometry. For $n = 1$ the viscosity distribution is constant and independent of flow. For $n > 1$ the effective viscosity of the near-surface layer is larger than that of the basal ice, and this stiff upper layer acts as a stress guide. As a consequence, the range of horizontal stress transmission increases with n. This is, as discussed by Landon and Raymond (1978), the reason why the transition between intermediate and long scale shifts to higher wavelengths with n. The stiff upper layer also has the effect of concentrating the anomalous flow towards the bed, leading to smaller topographic transfer amplitudes over short scale, and to a reduction in anomalous surface-parallel velocities. Over intermediate scales, the flow field is considerably more complicated, as it is only over this spatial scale that the perturbations in ice thickness and surface slope are sufficiently large to significantly affect the anomalous flow field (over both short and long spatial scale the thickness and slope perturbations are small and both tend to zero in the limits $\lambda \to 0$ and $\lambda \to +\infty$.) Nevertheless, with regard to non-linear rheological effects, the picture is fairly simple. Because of the stiff upper layer, the amplitude of the surface-parallel surface velocity generally decreases with n, and in order for the net flux perturbation of the anomalous flow field not to be affected — which in steady state must be equal to zero — the surface amplitude must increase at the same time. This same effect of non-Newtonian rheology on transfer characteristics was observed by Jóhannesson (1992, compare for example Figures 4.5.3 and 4.7.1) in his fundamentally different approach to this problem.

The range of longitudinal stress gradients increases with $C^{(0)}$. As a consequence, there are a number of similarities between the effects of n and $C^{(0)}$ on transfer characteristics. Comparing Figure 2.9a with Figure 2.9b, for example, shows that increasing n or $C^{(0)}$ in both cases leads to larger transfer amplitudes over the intermediate scale, and the lower limit of the long scale being shifted to higher wavelengths.

Balise and Raymond (1985) analyzed the transfer of basal velocity anomalies to the surface of a glacier assuming linear Newtonian rheology. They investigated the transfer of basal velocity anomalies to the surface of an undisturbed plane slab and therefore their problem differs from the one considered here. Nevertheless, it is illuminating to consider the differences, and similarities, of these two problems. Balise and Raymond (1985) identified four longitudinal scales of different behavior. Their long scale was defined as the scale where basal velocity anomalies appear at the surface unattenuated. In steady-state, surface velocity anomalies due to bedrock undulations go to zero with $\lambda \rightarrow +\infty$ so this definition of long scale is not applicable to the steady-state problem considered here. We define long scale as the set of wavelengths where the shallow ice approximation gives an accurate description of the flow. Because the shallow-ice approximation predicts a perfect transmission of basal velocity anomalies in the limit $\lambda \rightarrow +\infty$ for the problem considered by Balise and Raymond (1985), our definition, when applied to their problem, matches the definition they use.

Our definition of short scale is also identical to Balise and Raymond's (1985) definition of very short scale, as the scale where there is essentially no surface response. We define the intermediate scale simply as the set of wavelengths not belonging to either short or long wavelengths. But the justification for defining this separate spatial scale is the fact that over this scale the topographic transfer amplitudes are considerably larger than straightforward interpolation from the short and the long-wavelength ranges would suggest. Balise and Raymond (1985) defined a short scale as the scale at which surface velocity perturbations are considerably reduced in amplitude and the surface-parallel component is significantly different from that of the bed. Again, because the problem considered here differs in number of ways from that analyzed by Balise and Raymond (1985), their definition does not directly apply. However, the range of intermediate wavelength for which the phase shift of surface parallel velocity is negative (see Figures 2.13a, 2.14a, 2.15a, and 2.16a) corresponds roughly with the short scale of Balise and Raymond (1985). Furthermore, inspection of the anomalous velocity field reveals that over this range of wavelengths, the anomalous surface velocity is directed roughly in the opposite direction to the velocity directly above the bed-line.

One of the most noteworthy non-linear rheological aspects of the bed-to-surface transfer is the strong increase in the amplitudes of the topographic transfer functions with n across the intermediate spatial scale. Over this scale the flow is strongly affected by horizontal stress-gradients, and the SIA is not valid. In fact, the SIA does not predict this type of an increase in transfer amplitudes. This non-linear effect, in particular when acting in combination with the well-known increase in transfer with $C^{(0)}$, gives rise to considerably larger transfer amplitudes at intermediate scale than predicted by both the SIA and the analytical full-system theory for Newtonian media. With increasing $C^{(0)}$, the reduction over short scale and the increase over intermediate scale with n, progressively gives the $\mathcal{T}_{\mathcal{SB}}$ transfer amplitude $C^{(0)}$ the form of a step-function when plotted as a function of wavelength (see Figure 2.9b). This implies that on active ice streams all Fourier components of topographic disturbances having wavelengths larger than about 3 to 5 are transmitted approximately equally to the surface. This is in marked contrast to the transmission properties of Newtonian medium, where over intermediate wavelengths the medium acts as a band-pass filter predominantly transmitting wavelengths around 3 to 10. Given accurate maps of bed and surface topography this prediction could be tested.

The general increase in transfer amplitudes, and the appearance of a local maximum as a function of wavelength with increasing $C^{(0)}$, are well-known features of the bed-to-surface transfer characteristics of linear fluid (Gudmundsson, 2003). It has been suggested by Gudmundsson et al. (1998, 2003) that the origin of flow-stripes on active ice streams and observed increase in surface roughness during a surge are a consequence of this increase in transfer amplitude. However, this suggestion rested on the assumption that transfer amplitudes for a power-law fluid are not considerably smaller than those of a Newtonian fluid and that they exhibit a similar increase with increasing basal motion. Figure 2.9 now shows this to be the case. In fact, the local maximum in the $\mathcal{T}_{\mathcal{SB}}$ amplitude becomes larger and broader with increasing n (Figure 2.9b). For $n = 3$ up to about 85$\%$ of the amplitude of a sinusoidal bedrock undulation is transferred to the surface. This reaches up to 95$\%$ of the amplitude of the perturbation for $n = 5$ and $C^{(0)} = 10$.

The degree of non-linearity of the basal sliding law does not appear to affect the bed-to-surface transfer characteristics fundamentally (see Figures 2.12a and b). This is of some interest as it has been suggested that appropriate values of m for some active ice streams on Siple Coast, West Antarctica, are most likely rather large (> 20) (Kamb, 2001; Tulaczyk et al., 2000a). It seems likely that other ice streams may be characterized by different and possibly more moderate values of m. The insensitivity of the transfer amplitudes to changes in m shows that high bed-to-surface transfer amplitudes are to be expected for all ice streams irrespectively of what may be the most appropriate value for the sliding law exponent.

Acknowledgments

The authors wish to thank Christian Schoof and Kolumban Hutter for their careful reviews. This work benefited from helpful discussions with Charlie Raymond and Richard Hindmarsh. An earlier draft was improved by comments from Mike Pinnock.

Chapter 3

The influence of basal disturbances on the velocity fields of glaciers and ice streams

This chapter is a draft of a paper to be submitted under the same title to the Journal of Glaciology, with co-authors G. H Gudmundsson from the British Antarctic Survey, Cambridge, UK and M. Vonmoos.

Abstract

The influence of basal disturbances on the velocity fields of glaciers is investigated numerically in two dimensions. This is done for finite-amplitude perturbations in bedrock topography and in basal slipperiness for both linear and non-linear rheology. The effects of nonlinear rheology on the velocity fields are mainly quantitative consisting essentially in a concentration of the anomalous flow near the base and in a reduction of the horizontal velocity perturbation near the surface. At small wavelengths (< 3 ice thicknesses) and small perturbation amplitudes, a recirculation forms in the velocity pattern for both types of perturbations. The anomalous flow increases with the wavelength of the perturbation and reaches a maximum at around 10 ice thicknesses for sufficiently high slip ratios.

3.1 Introduction

Basal disturbances, such as bedrock undulations and spatial variations in resistance to basal sliding, influence both the surface topography and surface velocities as well as the internal flow field of glaciers and ice sheets. Considerable work has been done on the description of the transfer characteristics of basal variability to a glacier surface. Analytical solutions are available for linear rheology (e.g., Hutter et al., 1981; Jóhannesson, 1992; Gudmundsson, 2003) while semi-numerical and numerical solutions exist for nonlinear rheologies (e.g., Hindmarsh, 2004; Raymond and Gudmundsson, 2005). The description of the influence of basal variability on the glacier flow field received, on the other hand far less attention (Balise and Raymond, 1985). In this paper, we investigate numerically how finite amplitude basal disturbances affect the two-dimensional steady-state flow field of glaciers. The analysis include the surface response to basal variability. The glacier velocity fields are computed with a plane-flow finite-element model along flow lines when transverse effects can be ignored. Two types of sinusoidal basal disturbances are considered: (1) bedrock undulations and (2) spatial variations in basal slipperiness along a flat bed. For both types of basal disturbances, the effects of nonlinear rheology and finite-amplitude effects on the flow pattern are examined. Results for linear rheology are compared with relevant analytical solutions (Gudmundsson, 2003). We consider only flow field perturbations, i.e flow deviations from the well-known plane-slab solution. Figure 3.1b shows an example of velocity field perturbation.

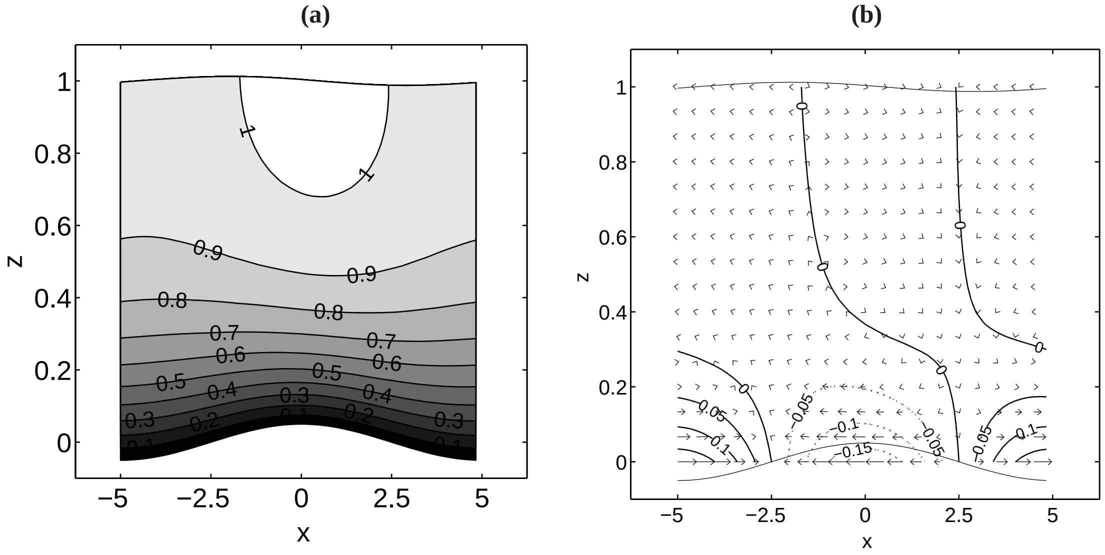

Figure 3.1: (a) Steady-state velocity field in x-direction for flow over a sinusoidal bedrock undulation as in the numerical model. The gray shading corresponds to the different values of horizontal velocities. (b) Velocity field perturbation in reaction to a perturbation in bedrock topography (as shown in panel a)) depicted in undisturbed glacier geometry (rectangle) as explained in section 3.3.1. Solid contour lines denote positive velocity anomalies and dotted lines negative anomalies. Note that the sinusoidal basal perturbation centered at $z = 0$ indicates the position and amplitude of the basal perturbation in disturbed geometry, but has otherwise no direct geometrical relation with the velocity anomalies depicted in undisturbed geometry. Distances along the x and z axis are in units of mean ice thickness $h^{(0)}$.

In this paper, we consider variations in basal properties over both short and long scales with respect to ice thickness, but short with respect to the overall span of the ice sheet, hence allowing us to consider the glacier geometry as corresponding to an inclined plane slab on which perturbations in bed and surface are superimposed. We restrict our investigations to 'small' perturbation amplitudes. By small we mean that the amplitude of the perturbations amount to maximum 10% of the mean ice thickness. This still allows us to determine the amplitude range for which finite amplitude effects can be ignored.

The structure of the paper is as follows. We start be introducing the numerical model in Section 3.2. We describe in Section 3.3 how the perturbations in velocity fields are determined and validate the results by comparison with relevant analytical solutions. We then investigate how the velocity field of glaciers is affected by both types of basal disturbances. The effects of finite amplitude and non-linear rheology are discussed separately.

3.2 Numerical Model

The setup of flow down an infinite plane with a mean inclination α is illustrated in Figure 3.2. The coordinates are ($\tilde{x}$, $\tilde{z}$), where $\tilde{x}$ and $\tilde{z}$ are parallel and perpendicular to the mean slope, respectively. Dimensional variables are denoted with a tilde, nondimensional without. The equation $\tilde{z} = \tilde{s}(\tilde{x}, \tilde{t})$ defines the surface and $\tilde{z} = \tilde{b}(\tilde{x})$ the base of the glacier. The two-dimensional velocity field is represented by the horizontal velocity $\tilde{u}$ and the vertical velocity $\tilde{w}$.

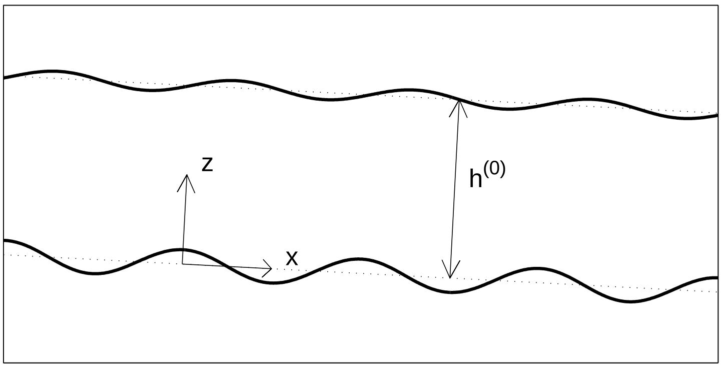

Figure 3.2: Geometry of the glacier and coordinate system as used in the numerical model. Bedrock perturbation and corresponding surface reaction are shown as a black line. The dashed lines show the undisturbed plane slab geometry.

The model is implemented in the commercial finite-element programm MARC. A mixed Lagrangian-Eulerian formulation in two-dimensions (plane strain flow) is employed to calculate the solution (Leysinger Vieli and Gudmundsson, 2004). The numerical model solves the full force-balance equations for which acceleration terms are neglected and the mass-conservation equation for incompressible ice. These equations read $\tilde{\sigma}_{ij,j} = -\tilde{\rho}\tilde{g}_i$ and $\tilde{v}_{i,i} = 0$, respectively. $\tilde{\sigma}_{ij}$ are the components of the Cauchy-stress tensor, $\tilde{\rho}$ is the ice density, $\tilde{g}_i$ the acceleration components due to gravity and $\tilde{v}_i$ are the components of the velocity vector. The constitutive ice flow law is Glen's law (Glen, 1955; Steinemann, 1958), modified according to Hutter (1983) with a linear term to avoid the singularity in viscosity at the surface as the deviatoric stress goes to zero. The constitutive law reads

$$\tilde{\dot{\epsilon}}_{ij} = \tilde{A}(\tilde{\tau}^{n-1} + \tilde{\tau_0}^{n-1})\tilde{\sigma}_{ij}^{(d)}. \tag{3.1}$$

In this equation, $\tilde{A}$ is the rate factor, n the stress exponent, $\tilde{\dot{\epsilon}}_{ij}$, $\tilde{\sigma}_{ij}^{(d)}$ are the strain rate and the deviatoric stress tensors, respectively and $\tilde{\tau}$ the effective shear stress. The parameter $\tilde{\tau}_0$ is the crossover stress at which the linear and exponential terms contribute equally to the total strain rate.

3.2.1 Boundary Conditions

Boundary conditions along the bed are specified by a sliding relation of the form

$$\tilde{u}_b = \tilde{C}(\tilde{x})\tilde{\tau}_b^m, \tag{3.2}$$

where $\tilde{u}_b$ is the sliding velocity tangential to the bed, $\tilde{C}(\tilde{x})$ the sliding coefficient, $\tilde{\tau}_b$ the bed parallel shear stress and m the sliding law exponent. We present only results for $m = 1$. Basal sliding is introduced in the model by adding a uniform thin layer of different viscosity to the base of the glacier such that relation 3.2 is respected. Sinusoidal perturbations in basal slipperiness are introduced by writing

$$\tilde{C}(\tilde{x}) = \tilde{C}^{(0)}(1 + \Delta C \cos \tilde{k}\tilde{x}), \tag{3.3}$$

where $\tilde{C}^{(0)}$ is the mean basal slipperiness and ΔC is the fractional amplitude of the basal slipperiness perturbation. The total amplitude of the basal slipperiness perturbation is given by the product $\tilde{C}^{(0)}\Delta C$. The wave number $\tilde{k} = 2\pi/\tilde{\lambda}$, where $\tilde{\lambda}$ is the wavelength. Similarly, perturbations in bedrock topography are introduced by writing

$$\tilde{b}(\tilde{x}) = \tilde{b}^{(0)}(\tilde{x}) + \Delta\tilde{b} \cos \tilde{k}\tilde{x}, \tag{3.4}$$

where $\tilde{b}^{(0)}$ is the mean bedrock elevation and $\Delta\tilde{b}$ the amplitude of the bedrock perturbation. The superscript $^{(0)}$ indicates averages values and Δ deviations from the mean (perturbation). This notation is used because when comparing numerical results with relevant perturbations theories, these correspond to zeroth-order quantities. The ice surface is stress-free and allowed to evolve according to the kinematic boundary condition until steady-state is reached. The kinematic boundary condition reads

$$\tilde{s}_{\tilde{t}} + \tilde{u}\tilde{s}_{\tilde{x}} = \tilde{w}, \qquad \tilde{z} = \tilde{s}(\tilde{x}, \tilde{t}). \tag{3.5}$$

Accumulation and ablation are not taken into account. The kinematic boundary condition is integrated forward in time with an unconditionally stable implicit Crank-Nicholson scheme (Raymond and Gudmundsson, 2005).

Periodic boundary conditions are imposed along the upstream and downstream glacier model boundaries.

3.2.2 Non-dimensionalization

The variables are non-dimensionalized by choosing their typical values. For example, spatial scales are non-dimensionalized with a typical thickness. We will write $\psi = \tilde{\psi}/[\tilde{\psi}]$; the quantities in square brackets represent the respective typical values, and those without tilde are the corresponding dimensionless quantities. The variables are non-dimensionalized as follows; thickness $\tilde{h}$, elevations $\tilde{z}, \tilde{s}, \tilde{b}$ and horizontal position $\tilde{x}$ are scaled with a typical mean ice thickness $[\tilde{h}^{(0)}]$. The velocity components $\tilde{u}, \tilde{w}$ are scaled with a typical contribution of internal deformation to the mean surface-parallel velocity $[\tilde{u}_d]$. Pressures and stresses are scaled by a typical bed parallel shear stress $[\tilde{\tau}_b] = \tilde{\rho}\tilde{g}\tilde{h}\sin(\alpha)$, where $\tilde{\rho}$ is the ice density and $\tilde{g}$ the acceleration due to gravity. Time is scaled by $[\tilde{h}/\tilde{u}_d]$. In scaled units, the glacier thickness is equal to unity and the mean surface parallel deformational velocity $u_d = 1$. The coordinate system is defined so that $z = s^{(0)} = 1$ and $z = b^{(0)} = 0$.

3.2.3 Model Characteristics

Four-node, isoparametric, quadrilateral Hermann elements are used. The model length correspond to the wavelength of the basal perturbation. The computational grid comprises 60 elements in x-direction and 30 elements in z-direction. The basal layer comprises two elements in z-direction.

3.3 Model Results

$\mathcal{B}$ perturbation refer to perturbations in basal topography while $\mathcal{C}$ perturbation to perturbations in basal slipperiness. Model results are discussed separately for both types of disturbances. We report results for steady-state flows only. The mean surface slope is always 3 °. All results are presented in nondimensional form. For model runs with $n = 3$, the cross-over stress is set to $\tau_0 = 0.3$ according to Raymond and Gudmundsson (2005) (see also Chapter 2). The discussion focuses mainly on horizontal velocity perturbations.

3.3.1 Determination of the velocity field perturbations

The velocity field perturbations are presented in the same form as analytical results from perturbation theories (Gudmundsson, 2003), allowing to compare results for different perturbation wavelengths and amplitudes and to validate the numerical results by comparison with analytical solutions. The velocities at the actual deformed coordinates (x, z) have to be transferred to the undeformed zeroth-order coordinates $(x, z^{(0)})$ using a first order Taylor approximation. Note that z and $z^{(0)}$ are located at the same relative vertical position with respect to the actual glacier thickness and undeformed slab thickness, respectively. The perturbation in horizontal velocity $\Delta u(x, z^{(0)})$ is thus obtained by subtracting from the horizontal velocity $u(x, z)$ the value of the mean horizontal velocity of the undisturbed plane slab $u^{(0)}(x, z^{(0)})$ and the product of the vertical derivative of the mean horizontal velocity for the undisturbed plane slab $\frac{\partial u^{(0)}}{\partial z}$ with the difference between the vertical node coordinates and the mean vertical elevation for that level $\Delta z = z - z^{(0)}$, i.e.,

$$\Delta u(x, z^{(0)}) = u(x, z) - u^{(0)}(x, z^{(0)}) - \frac{\partial u^{(0)}}{\partial z} \Delta z. \tag{3.6}$$

The mean horizontal velocity at the zeroth order level $u(x, z^{(0)})$, i.e. the zeroth-order infinite plane-slab solution, reads for linear rheology

$$u^{(0)}(x, z^{(0)}) = 1 - (1 - {z^{(0)}}^2) + C^{(0)}, \tag{3.7}$$

whereas for non-linear rheology and modified Glen's law, it is given by

$$u^{(0)}(x, z^{(0)}) = \frac{\frac{2(1-(1-z^{(0)})^{(n+1)})}{\tau_0^{(n-1)}} + (n+1)(1-(1-z^{(0)})^{(n-1)})}{\frac{2}{\tau_0^{(n-1)}+n+1}} + C^{(0)}. \tag{3.8}$$

The perturbation in vertical velocity $\Delta w(x, z^{(0)})$ equals the vertical velocity $w(x, z)$ since the zeroth order vertical velocity is zero ($w^{(0)}(x, z^{(0)}) = 0$).

For notational compactness, we refer in the following with velocity field (u, w) to the velocity field perturbations $(\Delta u, \Delta w)$.

3.3.2 Validation

Steady-state numerical results for linear rheology were compared with analytical solutions for linear rheology and small amplitude perturbations (Gudmundsson, 2003). Figure 3.3 shows examples of the absolute difference between steady-state numerical and analytical solution for both sinusoidal bedrock and slipperiness perturbations. The wavelength $\lambda = 100$ and the amplitudes of the perturbations $\Delta b = \Delta C = 0.05$ or 5 $\%$ ice thickness. As can be seen, the absolute difference is small and the agreement between the numerical and analytical solution good. The numerical solution has also been validated by comparing numerical transient and steady-state surface-to-bed amplitude ratios and phase shifts for sinusoidal bedrock and basal slipperiness perturbations with analytical solutions (Raymond and Gudmundsson, 2005). As the agreement was excellent, we have a high confidence in the correctness of the numerical solution.

3.3.3 Nonlinear Finite Amplitude Effects

A property of the analytical solution for linear rheology (Gudmundsson, 2003) is that the magnitude of the velocity perturbations increases proportionally to the amplitude of the basal perturbations. Theoretically, this is correct to first order in Δbk and ΔCk, respectively, where k is the wave number, and the analytical solution should be accurate whenever $\Delta bk \ll 1$ or $\Delta Ck \ll 1$ and $\Delta b/h^{(0)} \ll 1$ or $\Delta C/h^{(0)} \ll 1$, where $h^{(0)}$ is the mean slab thickness. We therefore start by examining the validity of this property, i.e we determine for which range of basal amplitudes finite amplitude effects can be ignored.

$\mathcal{B}$ perturbation

Figure 3.4 shows the difference between numerical and analytical solutions for $C^{(0)} = 0$, $\lambda = 1$ (a, b) and $\lambda = 50$ (c, d) for two different amplitudes of the sinusoidal bedrock perturbation of $\Delta b = 0.05, 0.1$. In the figure, the sinusoidal bedrock undulation centered at $z = 0$ indicates the position and amplitude of the perturbation in disturbed geometry, but has otherwise no direct geometrical relation with the velocity anomalies depicted in undisturbed glacier geometry. Contour lines show the magnitude of the difference in surface-parallel velocity. Note that the term surface-parallel refer to the undisturbed plane-slab geometry. Since the numerical solution is accurate, we consider differences between numerical and analytical solution to be due to nonlinear finite amplitude effects not accounted for in the analytical perturbation solution. As can be seen, the differences increase with the amplitude of the perturbation and decrease with wavelength. This is due to the fact that at small wavelengths, the slope perturbations are more pronounced; for $\Delta b = 0.1$ and $\lambda = 1$, $\Delta bk = 0.62 \not\ll 1$, whereas for $\lambda = 50$, $\Delta bk = 0.01 \ll 1$. For $\lambda = 50$, the analytical solution is accurate for both $\Delta b = 0.05$ and $\Delta b = 0.1$. These results are consistent with those from Raymond and Gudmundsson (2005) showing that the analytical solution for $\mathcal{B}$ perturbation and no basal sliding is accurate for perturbation amplitudes up to $\Delta b = 0.3$ for $\lambda = 25$.

Interestingly, in all cases shown in Figure 3.4, the difference in horizontal velocity is negative over the whole computational domain except at the bed, where it becomes negligible.

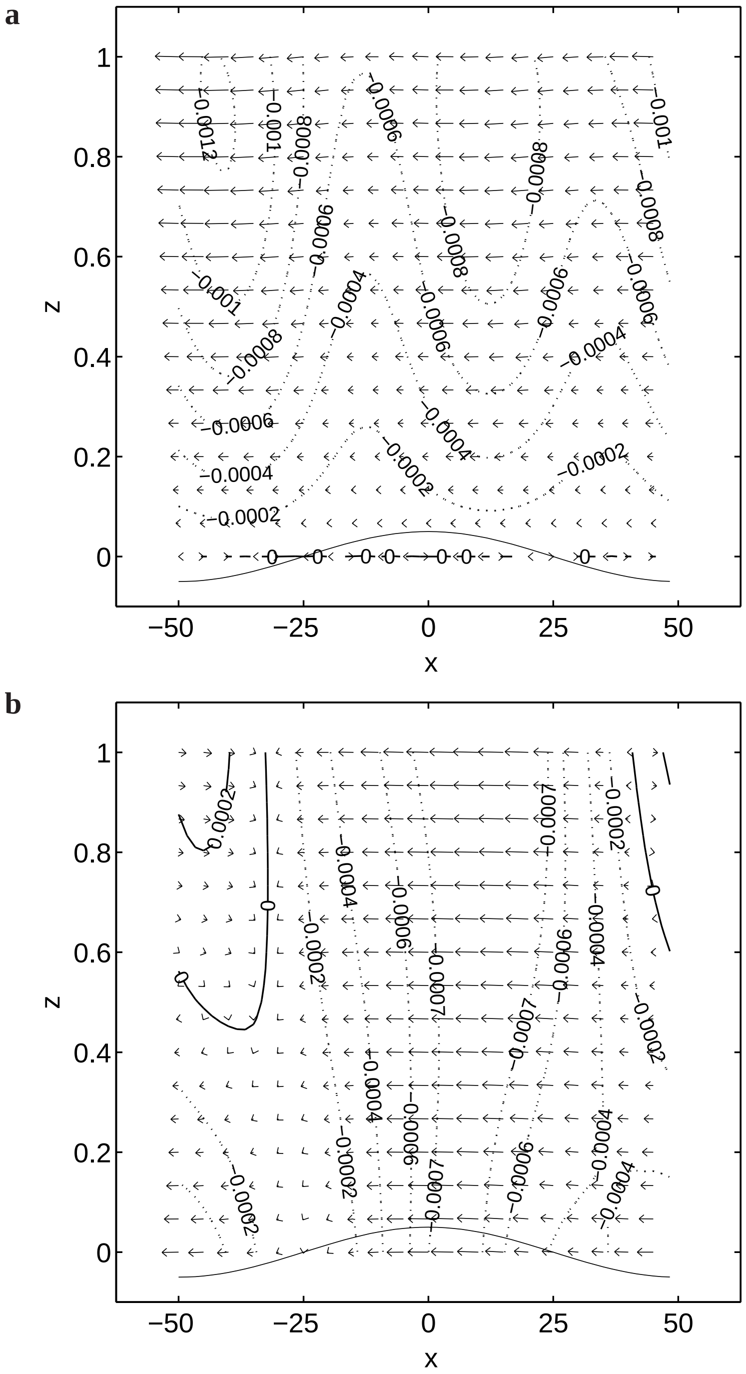

Figure 3.3: Absolute difference between numerical and analytical velocity fields for (a) a sinusoidal bedrock perturbation with amplitude $\Delta b = 0.05$ and no basal sliding ($C^{(0)} = 0$) and (b) a basal sliding perturbation with a fractional amplitude $\Delta C = 0.05$ and a mean basal slipperiness $C^{(0)} = 1$. The wavelength is $\lambda = 100$ and the mean surface slope is $\alpha = 3°$. The basal perturbations centered at $z = 0$ show the position and amplitude of the perturbations in disturbed geometry, but have otherwise no direct geometrical relation with the velocity anomalies depicted in undisturbed geometry. Solid contour lines are positive differences in horizontal velocity and dotted contour lines are negative differences in horizontal velocity.

This shows that in the numerical model, the bed obstacle slows down the flow, i.e., reduces the mean velocity. This effect becomes progressively stronger with the amplitude of the perturbation. The difference between the numerical and analytical solution increases faster than linearly with increasing amplitude. At the bed, the difference is zero since the horizontal velocity perturbation $\Delta u(x, z^{(0)})$ corresponds to the prescribed basal boundary condition in the analytical solution ($\frac{\partial u^{(0)}}{\partial z}\Delta z$ in Eq. 3.6) by Gudmundsson (2003) for $C^{(0)} = 0$. Almost no difference in vertical velocity can be observed.

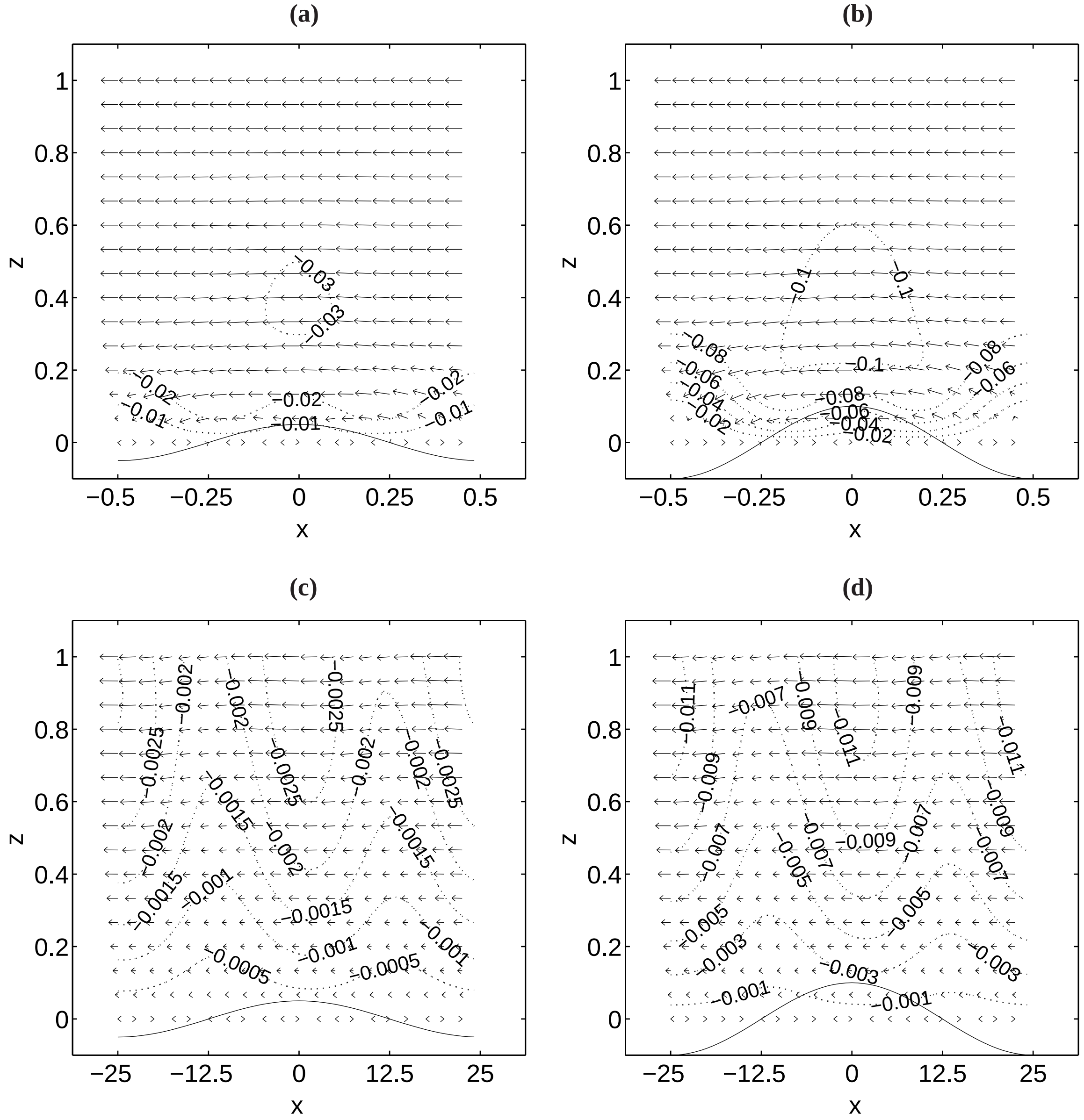

Figure 3.4: Difference between numerical and analytical velocity fields for a bedrock perturbation with $C^{(0)} = 0$, (a and b) $\lambda = 1$ and (c and d) $\lambda = 50$. The amplitude of the perturbation is (a and c) 5%, and (b and d) 10%. The surface slope is 3°. Contour plots are of the surface-parallel velocity.

The difference between numerical and analytical solution for a bedrock perturbation with basal sliding is shown in Figure 3.5. At the bed, the difference is not zero as was the case for no basal sliding. The difference is due to the fact that in the numerical model, basal sliding is sensitive to the bedrock perturbations. In the model, the sliding velocity equals the required velocity (for example $u_b^{(0)} = 10$ for $C^{(0)} = 10$) as long as no basal perturbations are introduced or if the slope perturbation, i.e Δbk is small. At small wavelength and large amplitudes the slope perturbation induces a form resistance to basal sliding, which is not accounted for in the analytical solution. The resulting sliding velocity at the top of the basal layer is therefore smaller all along the bed than the theoretical value. This effect is particularly pronounced at small wavelengths, for $\lambda = 1$ and $\Delta b = 0.05$ the mean basal sliding velocity reduces from $u_b^{(0)} = 10$ to $u_b^{(0)} = 3.3$ whereas for $\lambda = 10$ and $\Delta b = 0.05$, $u_b^{(0)} = 9.92$. Therefore, as was the case for $C^{(0)} = 0$, the difference between the numerical and analytical solution is negative over the whole computational domain.

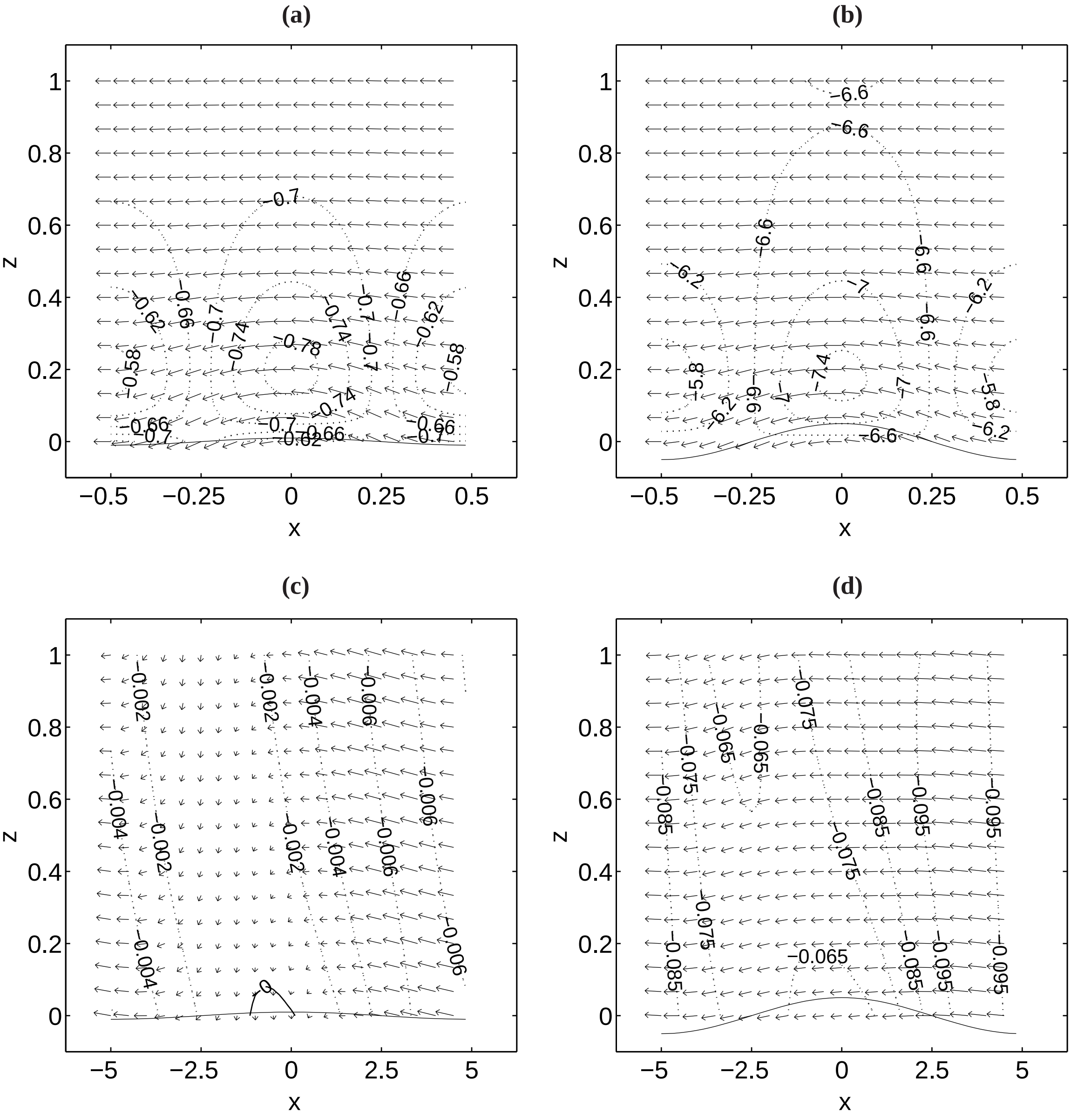

Figure 3.5: Difference between numerical and analytical velocity fields for a bedrock perturbation with $C^{(0)} = 10$, (a and b) $\lambda = 1$ and (c and d) $\lambda = 10$. The amplitude of the perturbation is (a and c) 1%, and (b and d) 5%. The surface slope is 3°. Contour lines are of the surface-parallel velocity.

For $n = 3$, finite amplitude effects are very similar to those observed for linear rheology as long as Glen's flow law is modified with a crossover stress term (Eq. 3.1). If this is not done, finite amplitude effects become particularly strong at small amplitudes, as the ice becomes very viscous near the surface due to the low stresses and strains. Because these finite amplitude effects are caused by physically unrealistic aspects of Glen's flow law, we present, in the following, only results for $n = 3$ with $\tau_0 = 0.3$. For $n = 3$ and $\tau_0 = 0.3$, numerical simulations not presented here show that finite amplitude effects can be ignored for the amplitude range $\Delta b, \Delta C < 0.1$ for wavelengths $\lambda > 5$ ice thicknesses. Below this value, finite amplitude effects modify the internal flow pattern significantly as will be shown in section 3.3.4. In terms of transfer amplitudes however, finite amplitude effects can be ignored for smaller wavelengths. These results are consistent with those from Raymond and Gudmundsson (2005) (see also Chapter 2).

$\mathcal{C}$ perturbation

In Figure 3.6 the difference between numerical and analytical solution is shown for a basal slipperiness perturbation with $C^{(0)} = 1$ for wavelengths of $\lambda = 1$ and $\lambda = 50$. As was the case for $\mathcal{B}$ perturbations, the difference increases with the amplitude and diminishes with the wavelength, but the difference still remains very small. At small wavelength ($\lambda = 1$), the slope perturbation in ΔCk introduces at the bed a vertical velocity which is not present in the analytical case since the basal boundary condition

$$\Delta w = u\frac{\partial \Delta b}{\partial x} \tag{3.9}$$

implies that the vertical velocity is zero at the bed since Δb is zero (the bed is flat).

3.3.4 Velocity fields

$\mathcal{B}$ perturbation

We present in this section numerical velocity fields for sinusoidal perturbations in basal topography for both no basal sliding and constant basal sliding. Results for both linear and non-linear rheology are discussed. We focus on situations where geometrical non-linearities play a minor role except at small wavelengths ($\lambda < 5$), where finite-amplitude effects modify the flow fields. For this wavelength range ($\lambda < 5$), we present the results for different perturbation amplitudes. Figure 3.7 shows the velocity fields for a wavelength $\lambda = 1$ and two different basal amplitudes for both linear and non-linear rheologies in the absence of basal sliding ($C^{(0)} = 0$). Contour plots show the horizontal velocity. The sinusoidal bedrock perturbations and corresponding steady-state surface responses centered at $z = 0$ and $z = 1$, respectively, indicate the position and amplitude of the perturbations in disturbed geometry, but have otherwise no direct geometrical relation with the velocity anomalies depicted in undisturbed geometry. At small perturbation amplitude ($\Delta b = 0.01$) (Figure 3.7a and c), we observe a reversal in the direction of the anomalous flow with depth. At the bed, over the peak of the undulation, negative surface-parallel velocities are observed, whereas over the low of the undulation, positive velocities. The reversal in velocity takes place at about $z = 0.2$. Above this depth, positive velocities are observed over the peak of the sinusoidal bed line, and negative velocities over the

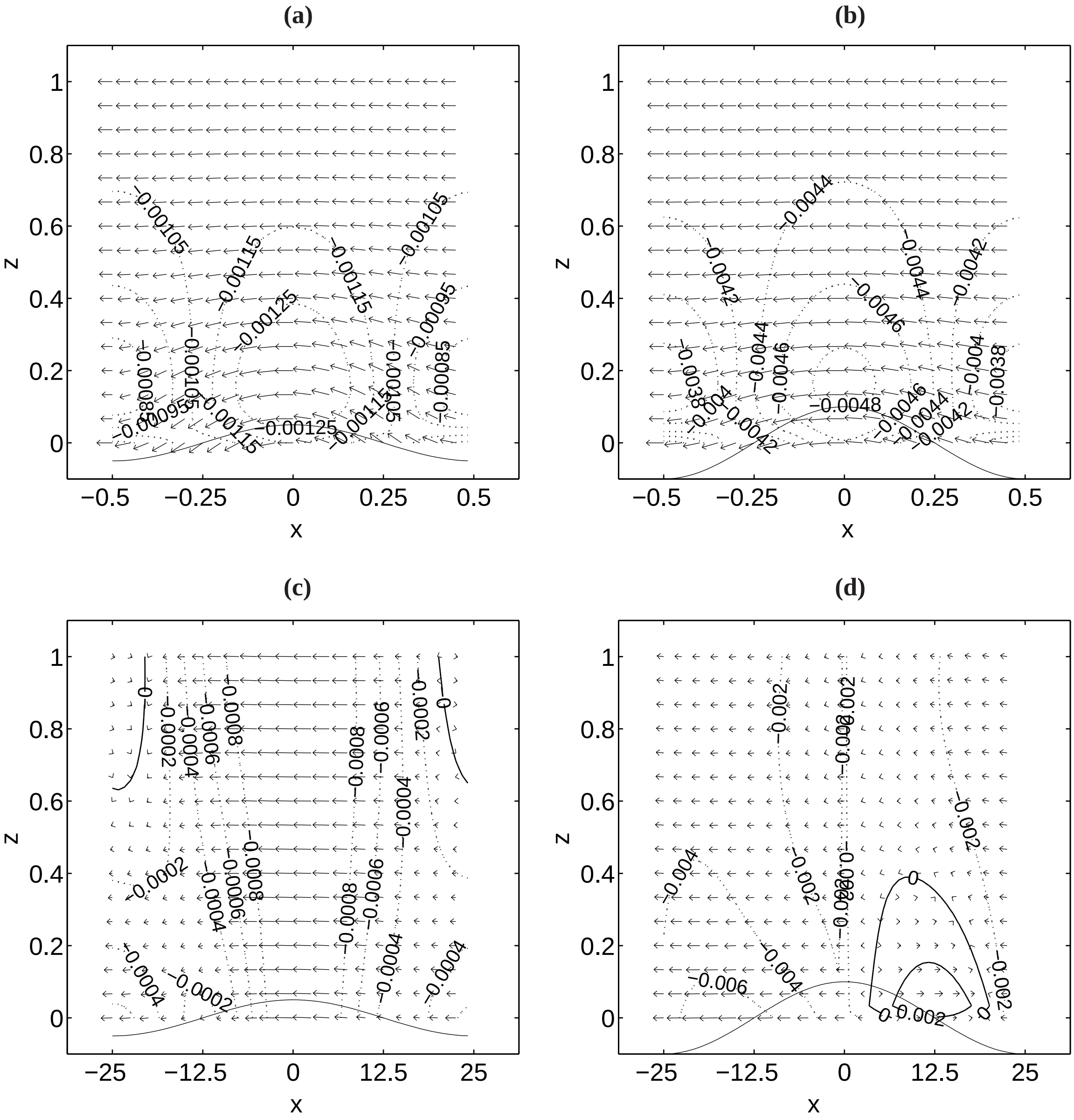

Figure 3.6: Difference between numerical and analytical velocity fields for a perturbation in resistance to basal sliding with $C^{(0)} = 1$. (a, b) $\lambda = 1$. (c, d) $\lambda = 50$. The amplitude of the perturbation is (a, c) 5%, and (b, d) 10%. The surface slope is 3°. Contour plots show the surface-parallel velocity.

low. Note that above $z > 0.6$ for the linear rheology case and above $z > 0.25$ for the non-linear rheology case, the flow perturbation is almost zero. The velocity field for non-linear rheology is qualitatively similar to the linear one. However, as compared to the velocity field for linear rheology (Figure 3.7a), in the nonlinear case (Figure 3.7c), most of the anomalous flow is concentrated in the vicinity of the bed. This is to be expected since for non-Newtonian ice, most of the internal deformation takes place in a narrow region near the glacier base. If we consider the perturbations in flux, the need for this circular motion

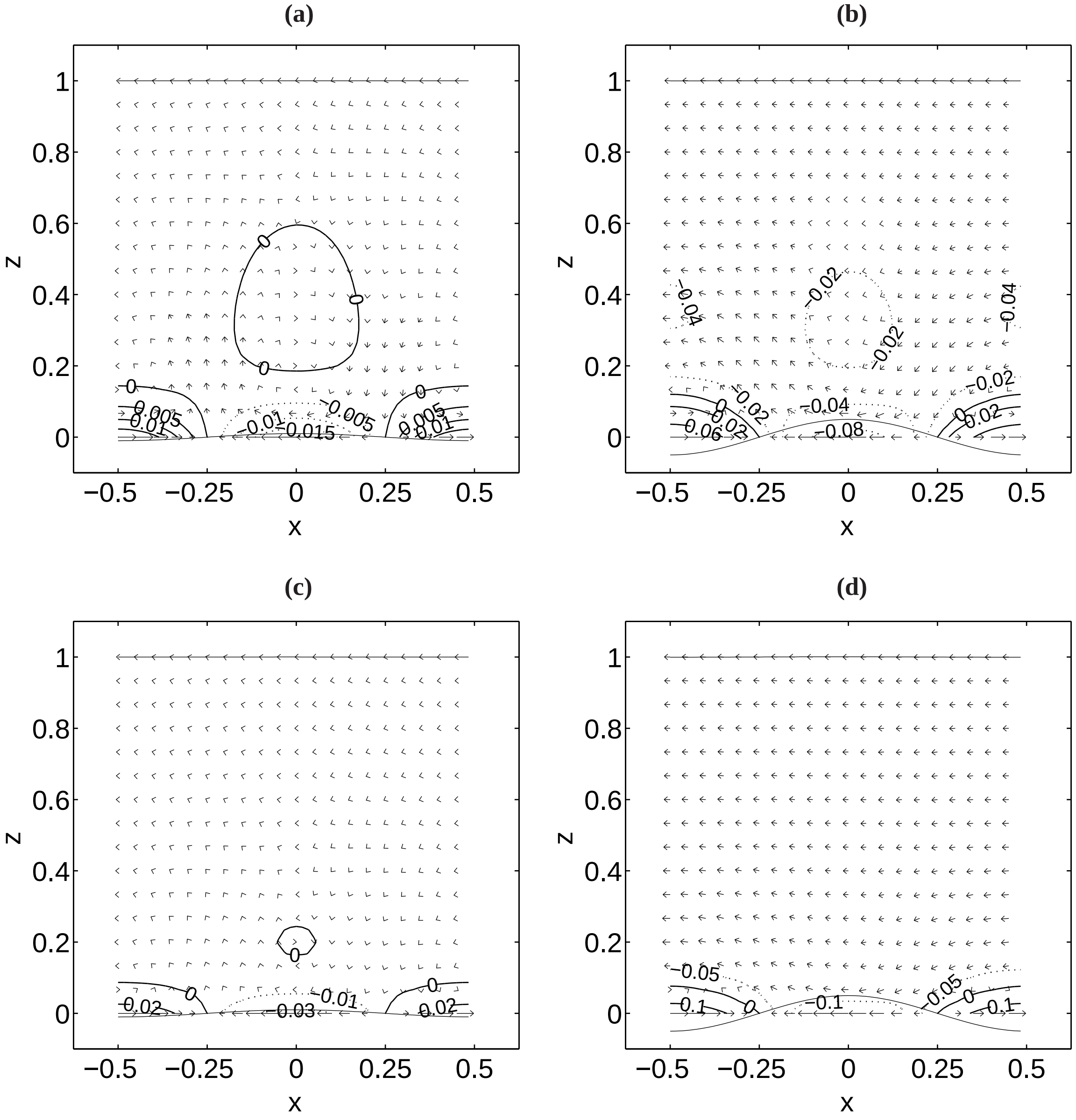

Figure 3.7: Numerical velocity fields with contour plots of horizontal velocity for a perturbation in basal topography with $C^{(0)} = 0$. The wavelength $\lambda = 1$ and the amplitude of perturbation is (a, c) $\Delta b = 0.01$ and (b, d) $\Delta b = 0.05$. (a, c) for linear rheology ($n = 1$) and (b, d) for nonlinear rheology with $n = 3$ and $\tau_0 = 0.3$. The surface slope is 3°.

in the velocity field becomes clear. To first oder, the flux q can be written as

$$q(x) = \int_{b(x)}^{s(x)} u(x, z)\, dz = q^{(0)} + \Delta q, \tag{3.10}$$

where $q^{(0)}$ is the flux for the unperturbed flow and Δq is the first order flux perturbation, which is defined as

$$\Delta q = u_s^{(0)} \Delta s - u_b^{(0)} \Delta b + \int_{b^{(0)}}^{s^{(0)}} \Delta u(x,z)\, dz. \tag{3.11}$$

$u_s^{(0)}$ and $u_b^{(0)}$ are the zeroth order surface and bed velocity, respectively, Δs and Δb the surface and bed perturbation, respectively and Δu the horizontal velocity perturbation as determined in Eq. 3.6. Equation 3.11 holds only as long as nonlinear finite-amplitude effects can be ignored. Finite-amplitude effects introduce higher order terms which must be considered to ensure mass conservation. In steady-state, the flux perturbation must be equal to zero, that is $\Delta q = 0$. For no basal sliding, $u_b^{(0)} = 0$, hence the vertical integral over the surface-parallel velocity must balance $u_s^{(0)} \Delta s$. As for small wavelength the surface reaction Δs is very weak ($\Delta s \approx 0$), the integral over Δu must also vanish. For a non-zero perturbation in velocity the integral can only be made zero if Δu changes direction with depth, forming a recirculation. A very similar type of recirculation has been shown by Balise and Raymond (1985) to be able to form in a Newtonian media during the initial response to a perturbation in basal velocities. In a similar manner, Gudmundsson (1997b) showed that the surface-near flow field in a confluence area of two glaciers can also be considered to be affected by anomalous surface-parallel circular motion in the horizontal plane. With increasing amplitude of the bedrock perturbation, the circular motion disappears (Figure 3.7b and d). This difference is due to finite-amplitude effects not accounted for in the analytical solution. A recirculation can be observed for wavelengths up to 3 ice thicknesses.

With increasing λ, the velocity perturbation extends towards the surface and the surface geometry starts to react to the bedrock perturbation. The velocity fields for a wavelength $\lambda = 10$ for linear (a) and non-linear (b) rheology are shown in Figure 3.8. The flow pattern is very similar in both cases. Negative horizontal velocities are located at the bed above the peak of the undulation and shifted upstream of the glacier with height to the surface. A similar pattern can be observed for positive horizontal velocities located at the bed above the low of the undulation. As was the case for $\lambda = 1$, the magnitude of the perturbation increases in the vicinity of the bed with the nonlinear rheology. In order to keep the flux perturbation zero, the vertical integral over the surface-parallel velocity Δu must compensate for the surface reaction. As for $\lambda = 10$ the surface reaction is almost identical for linear and non-linear rheology (Raymond and Gudmundsson, 2005), the vertical integral over the surface-parallel velocity must amount the same value for both $n = 1$ and $n = 3$. Since the magnitude of the perturbation in horizontal velocity is bigger near the base for $n = 3$, the reversal in flow direction over depth takes place closer to the base for $n = 3$ to compensate a bigger flux near the base. This can be observed by looking at the curvature of the zero contour lines in Figure 3.8a and b.

As λ increases towards infinity, the slope perturbations approach zero and with them the amplitude of the velocity perturbations at the surface (Figure 3.9a and b for $\lambda = 300$ ice thicknesses). The flow pattern becomes uniform; negative and positive velocities extend respectively from the peak and the low of the undulation to the surface. Almost no vertical velocities can be observed. Again, the flow perturbation for non-linear rheology is more concentrated towards the bed. Bedrock perturbations become gradually transmitted entirely to the surface and are in phase with the surface perturbations. In terms of mass

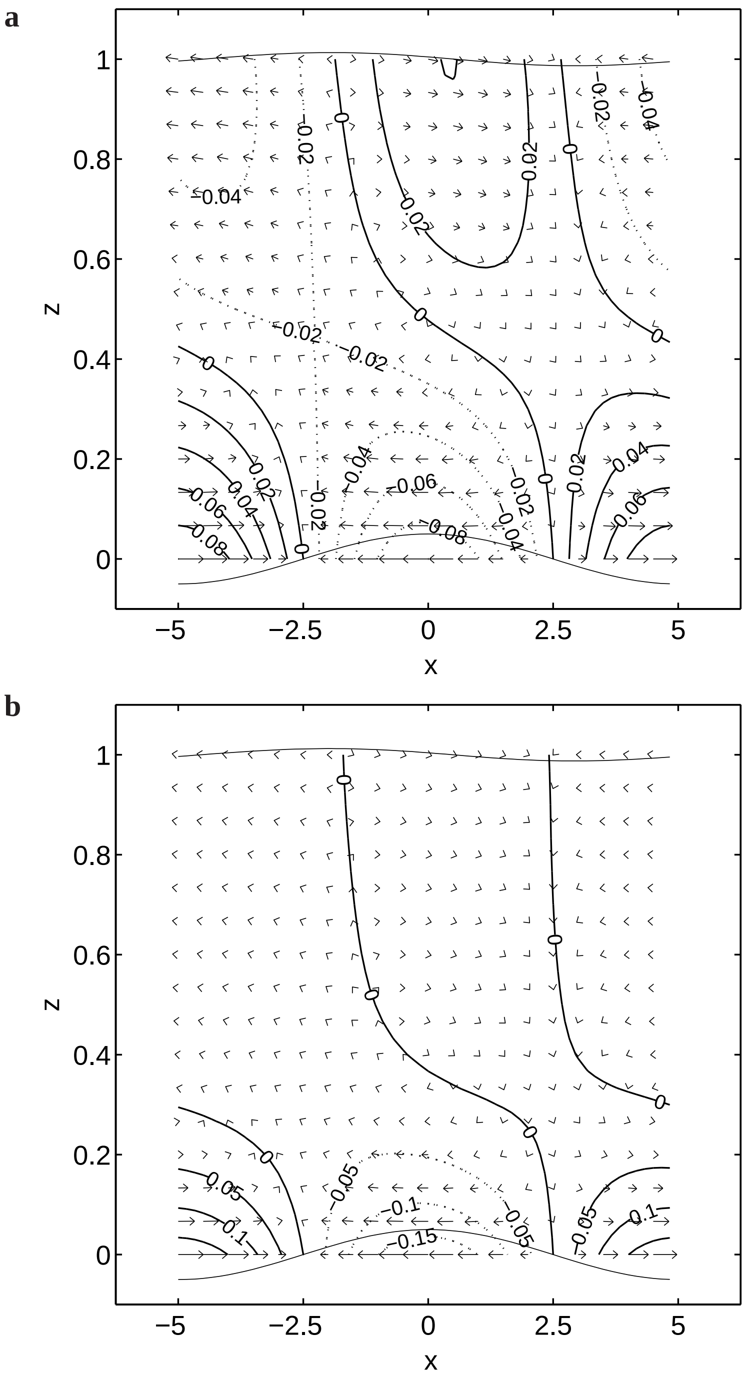

Figure 3.8: Numerical velocity fields for a perturbation in basal topography with no basal sliding ($C^{(0)} = 0$). The wavelength $\lambda = 10$ and the perturbation amplitude $\Delta b = 0.01$. (a) for linear rheology ($n = 1$) and (b) for nonlinear rheology with $n = 3$ and $\tau_0 = 0.3$. The surface slope is 3°. Contour plots refer to the horizontal velocity. Bedrock and corresponding surface perturbation centered at $z = 0$ and $z = 1$, respectively, indicate the position and amplitude of the perturbations in disturbed geometry, but have otherwise no direct geometrical relation with the velocity anomalies depicted in undisturbed geometry.

conservation, this means that $u_s^{(0)}\Delta s$ is positive and maximum over the peak of the sinusoidal bedrock and must therefore be compensated by a negative vertical integral of Δu. The contrary prevails over the low of the sinusoidal bed line. Note that at the surface, the maximum of the horizontal velocity is located above the maximum in forward bedrock slope.

Figure 3.10 shows the velocity fields for a perturbation in basal topography with constant basal sliding ($C^{(0)} = 10$) and a wavelength of $\lambda = 10$. Two main zones of positive and negative horizontal velocities extending from the glacier bed to the surface may be distinguished. Positive horizontal velocities are located downstream of the peak of the undulation, while negative horizontal velocities upstream. As compared to the same perturbation wavelength and no basal sliding, the amplitude of the flow perturbation in both horizontal and vertical velocity increases markedly. The perturbation in the flow field extends noticeably further towards the surface, particularly for the vertical flow component. As a result, the surface reaction to the bedrock undulation is much stronger than for no basal sliding and increases with n. A local maximum in bed-to-surface and bed-to-surface velocity transfer amplitude forms for $n = 1$ and $n > 1$ at sufficiently high slip ratios (Raymond and Gudmundsson, 2005). Gudmundsson et al. (1998) and Gudmundsson (2003) give a simple physical explanation for the appearance of the local maximum as being the result of a competition between two processes as the wavelength is increased: the increase of the vertical extent of the anomalous flow as measured from the bed line and the decrease of the strength of the anomalous flow as the slope perturbation Δbk diminishes. Thus, while with increasing λ the flow perturbation affects progressively more the surface geometry, the overall strength of the perturbations decreases. Hence there must be some intermediate wavelength at which the transfer and the anomalous flow field reaches a local maximum. The velocity fields for linear and nonlinear rheology are again very similar with one noticeable difference in the position of the global maxima in horizontal velocity. This maxima reaches the surface for linear rheology, whereas for nonlinear rheology it is located in the lower half of the glacier. This difference explains the reduction in transfer amplitudes of the u velocity component as n is increased (Raymond and Gudmundsson, 2005).

As for no basal sliding condition, the flow pattern becomes homogeneous with increasing wavelength (Figure 3.11 for $\lambda = 100$ ice thicknesses). The perturbation in vertical velocity diminishes towards zero and the horizontal surface velocity slowly as well.

$\mathcal{C}$ perturbation

Figure 3.12 shows the velocity field for a sinusoidal perturbation in basal slipperiness with wavelength $\lambda = 1$ ice thickness and perturbation amplitude $\Delta C = 0.05$ for both linear (a) and non-linear rheology (b). The mean basal slipperiness $C^{(0)} = 1$ and $\alpha = 3°$. In both linear and nonlinear cases, the induced perturbation in the flow field is very weak and mostly concentrated at the bed. At the bed, positive velocities are observed directly above the peak of the sinusoidal basal sliding perturbation (with enhanced basal sliding) and negative velocities above the low of the perturbation (with reduced basal sliding). Above the peak of the perturbation, the horizontal velocity changes direction with depth and becomes negative above $z \approx 0.1$ to the surface. As was the case for $\mathcal{B}$ perturbation and no basal sliding, for both linear and nonlinear rheologies the change of flow direction with depth sets up a circular motion. The center of the circular motion lies closer to the

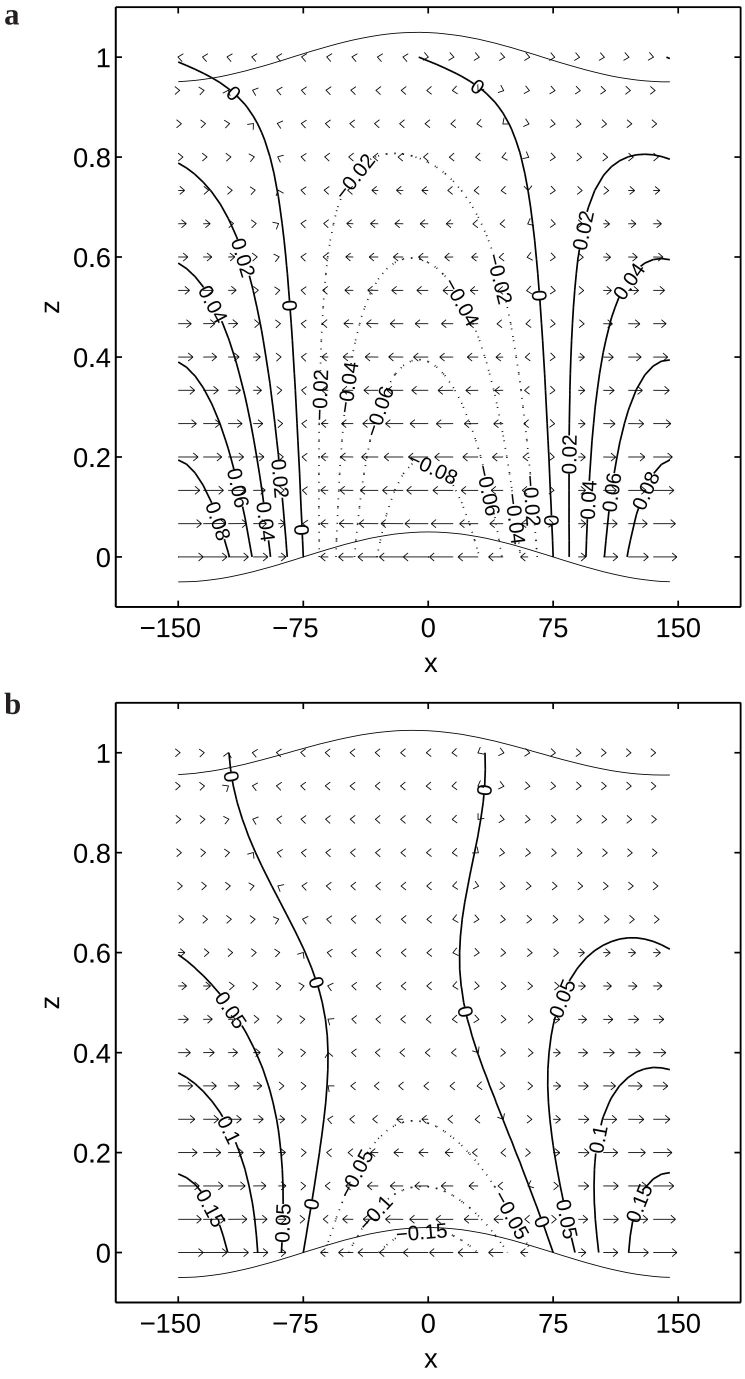

Figure 3.9: Same as Figure 3.8, but for $\lambda = 300$.

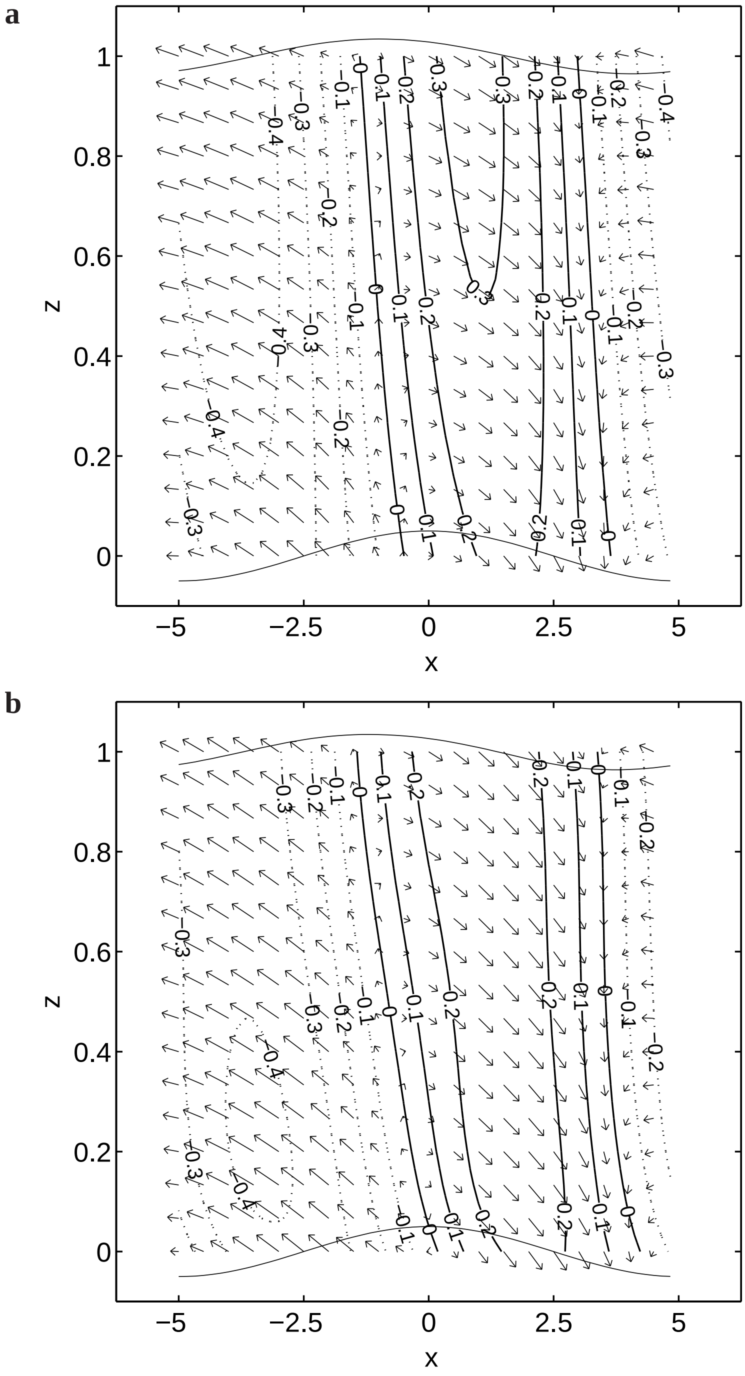

Figure 3.10: Numerical velocity fields for a perturbation in basal topography with basal sliding ($C^{(0)} = 10$. The wavelength $\lambda = 10$ and the perturbation amplitude $\Delta b = 0.05$. (a) for linear rheology ($n = 1$) and (b) for nonlinear rheology with $n = 3$ and $\tau_0 = 0.3$. The surface slope is 3°. Contour plots refer to the horizontal velocity. Bedrock and corresponding surface perturbation centered at $z = 0$ and $z = 1$, respectively, indicate the position and amplitude of the perturbations in disturbed geometry, but have otherwise no direct geometrical relation with the velocity anomalies depicted in undisturbed geometry.

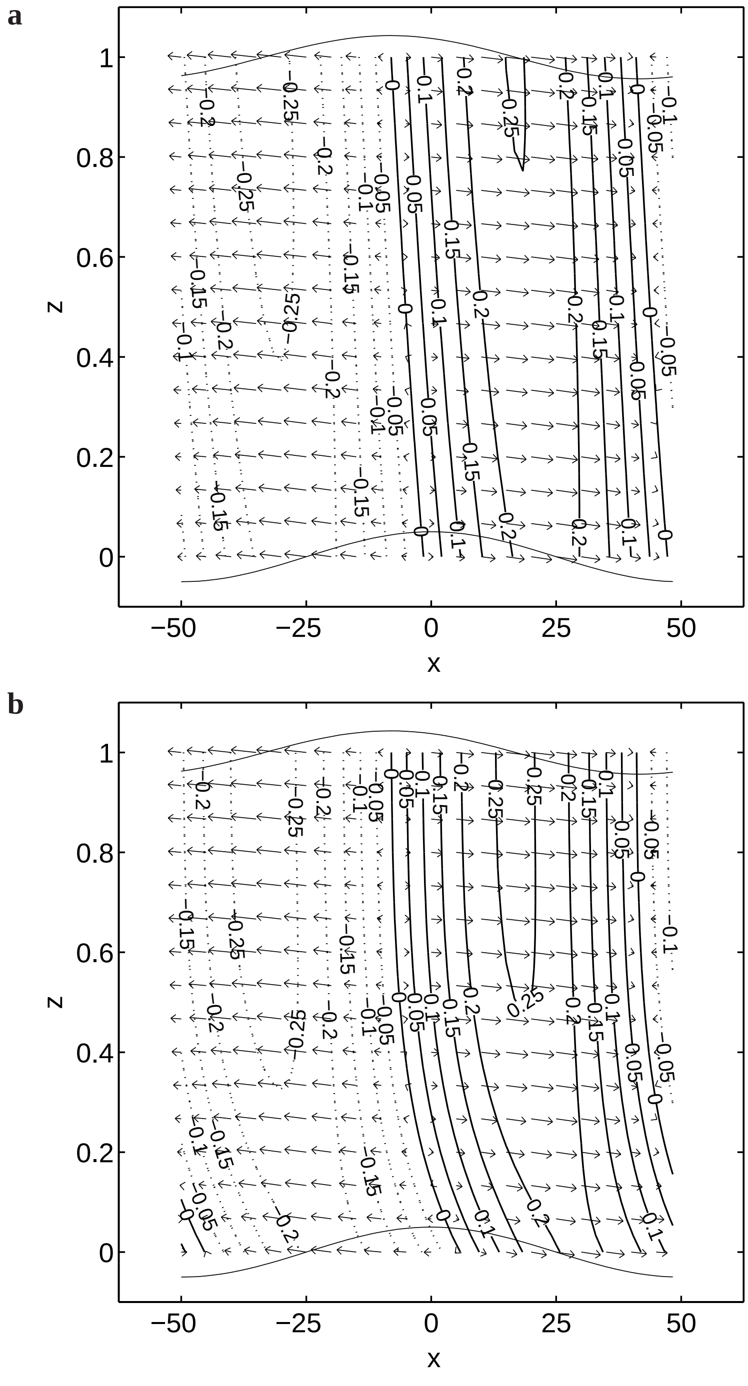

Figure 3.11: Same as Figure 3.10, but for $\lambda = 100$.

bed and the anomalous field is more concentrated near the bed for nonlinear rheology than for linear rheology. Note that for $n = 3$, the anomalous flow field approaches zero in the upper half of the ice thickness. As for $\mathcal{B}$ perturbation, the observed circular motion can be explained by the perturbation in flux (Eq. 3.11). For basal slipperiness perturbations, the second term $u_b^{(0)} \Delta b$ of Eq. 3.11 is always zero since $\Delta b = 0$ (the bed is flat). Again, as there is almost no surface reaction to the applied perturbation ($\Delta s \approx 0$), the vertical integral over the surface-parallel velocity must remain equally small and this can only be if Δu changes direction with depth. (How do you explain q at x = -0.5? all negative??)

Figure 3.13 shows the velocity field for a wavelength of the basal slipperiness perturbation equals to 10 ice thicknesses for linear (a) and nonlinear rheology (b). As for $\mathcal{B}$ perturbation, the vertical extent of the perturbation increases with the wavelength and the surface starts to react to the basal perturbation. The flow pattern is very similar to that for $\mathcal{B}$ perturbation with no basal sliding and a wavelength of $\lambda = 10$ (Figure 3.8) except that the sign of the horizontal velocity perturbation is reversed: velocities are positive there where basal sliding is enhanced (above the peak of the sinusoidal basal slipperiness perturbation) and negative where basal sliding is reduced. Note that the magnitude of the perturbations is much smaller than for perturbations in bed topography.

As λ increases towards infinity, the phase shift in horizontal surface velocities goes to zero for all n's. Figure 3.14a and b shows that for $\lambda = 300$ positive velocities reaches from the bed to the surface of the glacier above the peak of the perturbation and negative velocities above the low. The vertical velocity is almost zero from the base to the surface. The surface topography reaction increases towards the maximum value of transfer amplitude of $C^{(0)}/(n + 1 + 2C^{(0)})$ with a phase shift of 180 °. As the minimum of the surface perturbation is now located more or less directly above the peak of the sinusoidal basal sliding perturbation, the term $u_s^{(0)} \Delta s$ in Eq. 3.11 is thus everywhere negative and compensates for the positive vertical integral over the horizontal velocity perturbation above the peak of the perturbation. Since the surface perturbation goes through zero exactly there where the basal perturbation is zero, no perturbation in velocity field is to be observed at $x = -\lambda/4$ and $x = \lambda/4$.

3.4 Discussion and Summary

The effects of finite amplitude bedrock and basal slipperiness perturbations on the flow field of glaciers are broadly summarized referring to the three different ranges of spatial scales introduced in Raymond and Gudmundsson (2005) (Chapter 2 in this thesis): short, intermediate and large wavelengths. For each of these spatial scales, the velocity fields differ in a number of significant aspects. Raymond and Gudmundsson (2005) define short scale as the scale at which there is essentially no surface response to the basal perturbation. Long scale is the scale at which the transfer characteristics can be accurately described by the shallow ice approximation. The intermediate scale covers the wavelengths not belonging to either short or long scale.

Over a short scale, the anomalous flow field is concentrated in the vicinity of the bed and the perturbed velocities are small. With increasing n the anomalous flow gets shifted towards the bed and the perturbed velocities reduced towards the surface. At small amplitude perturbations (< 0.05), a circular motion sets up in the perturbed velocity field. This

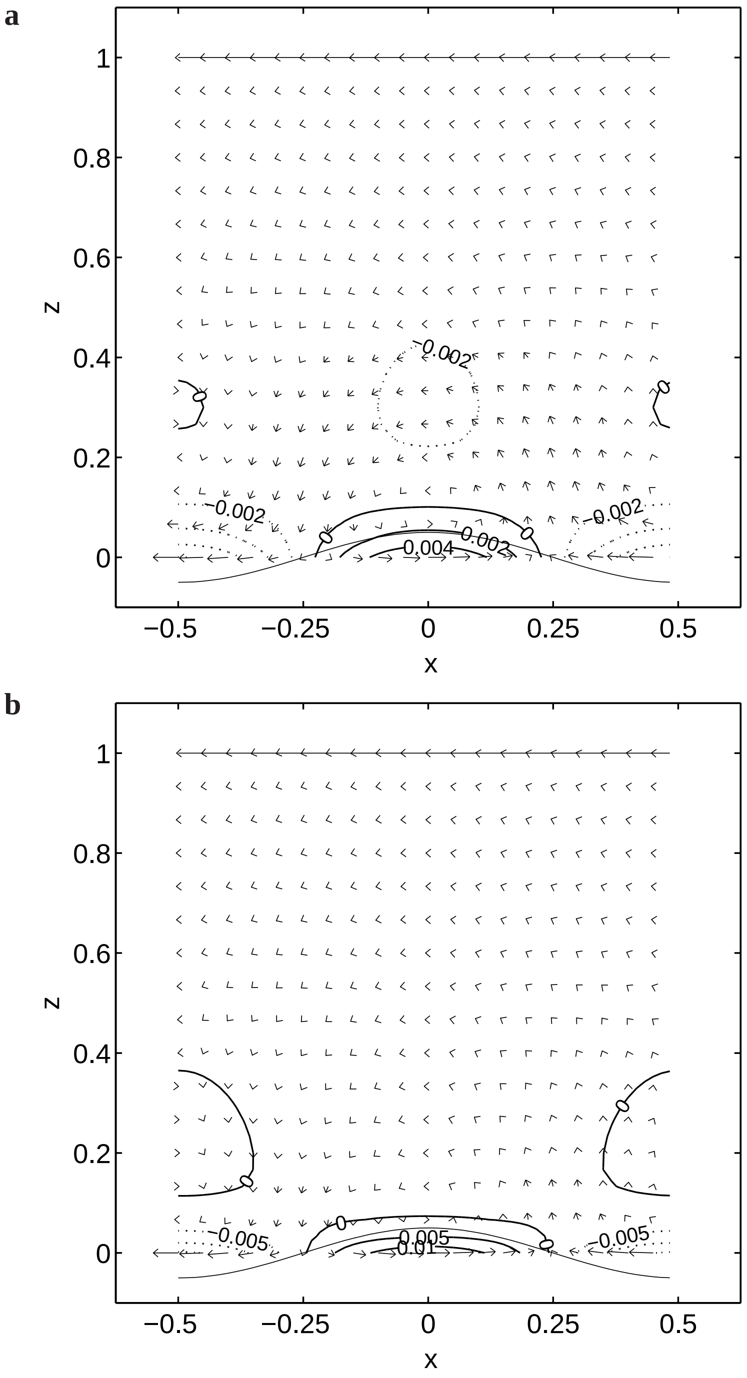

Figure 3.12: Numerical velocity fields with contour plots of horizontal velocity for a basal slipperiness perturbation with $C^{(0)} = 1$. The wavelength $\lambda = 1$ and the fractional perturbation amplitude $\Delta C = 0.05$. (a) for linear rheology ($n = 1$) and (b) for nonlinear rheology with $n = 3$ and $\tau_0 = 0.3$. The surface slope is 3°.

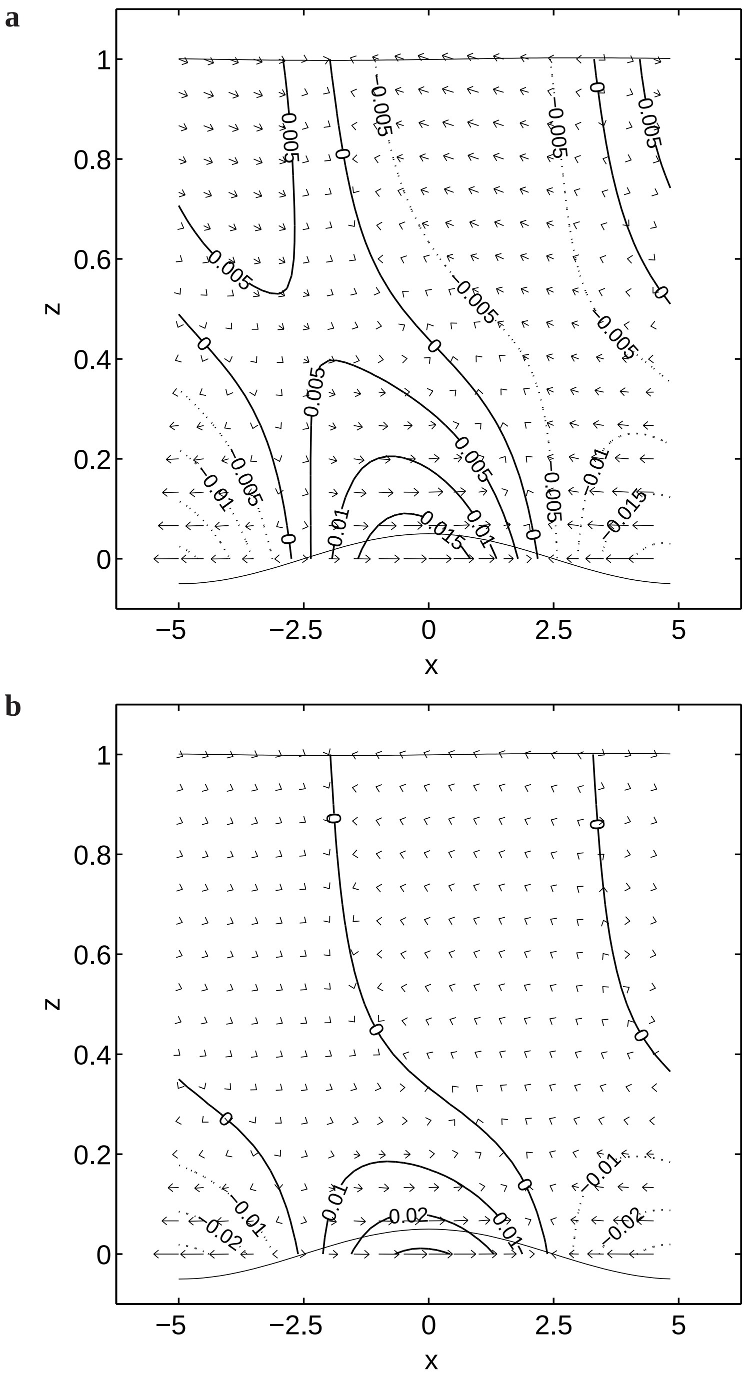

Figure 3.13: Same as Figure 3.12 but for $\lambda = 10$.

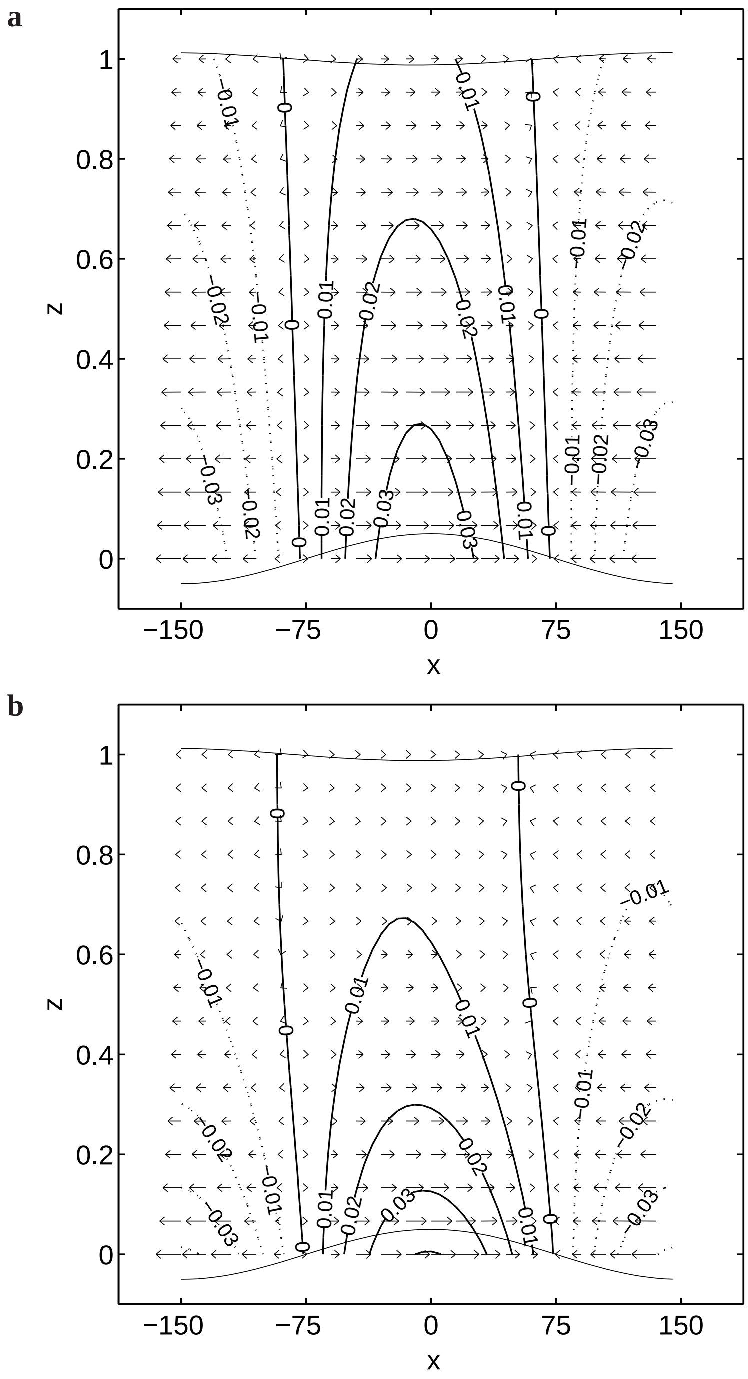

Figure 3.14: Same as Figure 3.12 but for $\lambda = 300$.

circular motion disappears with increasing amplitude and with increasing n. The range of short scale is from zero to about 3.

Over intermediate scale, the velocity field is strongly affected by the basal perturbations, as the anomalous flow increases with the wavelength and the thickness and slope perturbations are still sufficiently large. At sufficiently high slip ratios, the anomalous flow reaches a local maximum for perturbations in basal topography. This maximum coincides with a local maximum in surface transfer amplitudes. Increasing n has the effect of concentrating the anomalous flow in the vicinity of the bed, while reducing the amplitudes of the horizontal velocity perturbations near of the surface. Hence, the transfer amplitudes of surface-parallel surface velocity are smaller for nonlinear than for linear rheology. However, for bedrock perturbations and no basal sliding, the amplitude of the surface-parallel velocity increases with n for wavelengths larger than 30 ice thicknesses. The intermediate scale ranges from about 3 to 70.

Over long scale, as the thickness and slope perturbations decrease, the strength of the perturbation diminishes. The flow pattern becomes uniform with depth. Two zones of positive and negative horizontal velocities extending from the glacier base to the surface can be distinguished. The perturbations decrease strongly towards the surface. There is almost no perturbation in vertical velocities.

The effects of nonlinear rheology on the velocity fields are mainly quantitative and do not affect the overall flow pattern significantly. The magnitude of horizontal velocity perturbations increases strongly with n in the vicinity of the bed and the anomalous flow concentrates near the base for both $\mathcal{B}$ and $\mathcal{C}$ perturbations.

Part II

Inverse problem

Chapter 4

Bayesian inference

This chapter is intended as a short introduction to Bayesian inference. The Bayesian approach is illustrated with a simple linear problem.

4.1 Bayesian inference: an introduction

As any inverse method, the goal of Bayesian inference is to make quantitative inferences about Earth characteristics from remote observations (Gouveia and Scales, 1998). The Bayesian approach to inversion is named after Thomas Bayes as it makes use of Bayes theorem on conditional probability. In Bayesian inference, probability is not interpreted as the outcome of repeated random trials, but as a measure of knowledge about the true value of a given physical parameter (Tarantola, 2005). Thus, any prior understanding or expectation about some quantity to be retrieved may be incorporated in the solution. This information is expressed as a prior probability distribution. In the same way, experimental errors contained in the measurements can be quantified as a probability distribution. Once we have set up a forward function describing the physics of the measurement process, Bayes theorem allows us to combine the a priori with the measurements and produce a posterior probability density function for the quantities we wish to retrieve. In this context, Bayes theorem is used as a rule to infer or update prior knowledge in the light of new information. Summarizing:

- Prior knowledge available before the measurement is expressed as a prior probability density function (*pdf*)
- Experimental errors contained in the measurement is described statistically and the measurement process is expressed as a forward function
- Bayes'theorem provides a formalism for combining the a priori information with the information contained in the data and calculate a posterior *pdf* by updating the prior *pdf* with the measurement *pdf*

We emphasize here that the posterior probability density function does not produce an 'answer' for the retrieved quantities, but describes how the measurements improve knowledge of the model parameters. To obtain an explicit answer for the model parameters, it may be appropriate to single out from the ensemble described by the *pdf* the solution with the most probable value, i.e the one for which the *pdf* is maximum, which is referred to as the maximum a posteriori solution (Rodgers, 2000).

In the following, we will denote the quantities we want to retrieve by a model parameter vector $\boldsymbol{m}$. The quantities actually measured in order to retrieve $\boldsymbol{m}$ will be assembled into a data vector $\boldsymbol{d}$. The process of measurement will be described by a forward function which encapsulates our understanding of the measurement. Bayes theorem generalized for the vector case reads

$$P(\boldsymbol{m}|\boldsymbol{d}) = \frac{P(\boldsymbol{d}|\boldsymbol{m})P(\boldsymbol{m})}{P(\boldsymbol{d})}. \tag{4.1}$$

$P(\boldsymbol{m}|\boldsymbol{d})$ is the conditional probability density function of the model parameters $\boldsymbol{m}$ given the measurements $\boldsymbol{d}$. This *pdf* is the solution to the inverse problem and is generally referred to as the posterior distribution as it describes what we know after we have assimilated the data and prior information.

$P(\boldsymbol{m})$ is the prior distribution for the model parameters $\boldsymbol{m}$ expressing our knowledge of $\boldsymbol{m}$ obtained independently of the measurements.

$P(\boldsymbol{d})$ is the prior *pdf* of the measurements. This *pdf* can be shown to be a normalizing factor and therefore Eq. (4.1) is sometimes written as

$$P(\boldsymbol{m}|\boldsymbol{d}) = P(\boldsymbol{d}|\boldsymbol{m})P(\boldsymbol{m}). \tag{4.2}$$

$P(\boldsymbol{d}|\boldsymbol{m})$ is the conditional probability distribution describing the likelihood that, given a particular model parameter vector $\boldsymbol{m}$, a data vector, $\boldsymbol{d}$, will be observed. This *pdf* quantifies the misfit between the observed data $\boldsymbol{d}$ and the modeled or synthetic data generated by a suitable forward function $\mathbf{G}(\boldsymbol{m})$. This *pdf* is generally referred to as the likelihood function.

With these definitions, the theorem may be paraphrased as

$$\text{posterior} = \frac{\text{likelihood} \times \text{prior}}{\text{normalizing constant}}.$$

Generally, both the likelihood and prior probability density distributions are taken to be Gaussian. For a scalar measurement, the Gaussian distribution $P(d)$ with mean d and variance σ^2 reads

$$P(d) = \frac{1}{(2\pi)^{\frac{1}{2}}\sigma} \exp\left[-\frac{(d-\bar{d})^2}{2\sigma^2}\right]. \tag{4.3}$$

The probability that d lies in $(d, d+\delta d)$ is $P(d)\delta d$. The Gaussian distribution for a vector is of the form

$$P(\boldsymbol{d}) = \frac{1}{(2\pi)^{\frac{n}{2}}\mathbf{C_D}^{\frac{1}{2}}} \exp\left[-\frac{1}{2}(\boldsymbol{d}-\bar{\boldsymbol{d}})^T \mathbf{C_D}^{-1}(\boldsymbol{d}-\bar{\boldsymbol{d}})\right], \tag{4.4}$$

4.2 Application example: a linear problem with Gaussian statistics

In the following, an illustration of the Bayesian approach is given for a linear problem. For a linear problem, the forward function describing the relationship between the measurement vector and the model parameters can be expressed as

$$\boldsymbol{d} = \mathbf{G}\boldsymbol{m} + \boldsymbol{\epsilon}, \tag{4.5}$$

where $\mathbf{G}$ is the vector-valued forward function and $\boldsymbol{\epsilon}$ the measurement error.

We consider in the following that all uncertainties can be described by multivariate Gaussian distributions. The Gaussian distribution is commonly used to describe probability density functions as many processes are well described by it and it is algebraically convenient (Rodgers, 2000).

Thus, the a priori probability distribution can be expressed as

$$P(\boldsymbol{m}) = \exp\left[-\frac{1}{2}(\boldsymbol{m} - \boldsymbol{m}_{\text{prior}})^T \mathbf{C_M}^{-1}(\boldsymbol{m} - \boldsymbol{m}_{\text{prior}})\right], \tag{4.6}$$

where $\boldsymbol{m}_{\text{prior}}$ is the a priori value of $\boldsymbol{m}$ and $\mathbf{C_M}$ is the associated covariance matrix. The likelihood function $P(\boldsymbol{d}|\boldsymbol{m})$ reads

$$P(\boldsymbol{d}|\boldsymbol{m}) = \exp\left[-\frac{1}{2}(\boldsymbol{d} - \mathbf{G}\boldsymbol{m})^T \mathbf{C_D}^{-1}(\boldsymbol{d} - \mathbf{G}\boldsymbol{m})\right], \tag{4.7}$$

with $\mathbf{C_D}$ the covariance matrix for the measurement errors. The product of those two distributions yields the following expression the a posteriori probability density function $P(\boldsymbol{m}|\boldsymbol{d})$

$$P(\boldsymbol{m}|\boldsymbol{d}) = \exp\left[(\boldsymbol{d} - \mathbf{G}\boldsymbol{m})^T \mathbf{C_D}^{-1}(\boldsymbol{d} - \mathbf{G}\boldsymbol{m}) + (\boldsymbol{m} - \boldsymbol{m}_{\text{prior}})^T \mathbf{C_M}^{-1}(\boldsymbol{m} - \boldsymbol{m}_{\text{prior}})\right]. \tag{4.8}$$

Taking the minus logarithm of the above expression and maximizing with respect to $\boldsymbol{m}$ defines a maximum a posteriori solution for the estimates $\hat{\boldsymbol{m}}$

$$\hat{\boldsymbol{m}} = \boldsymbol{m}_{\text{prior}} + \mathbf{C_M}\mathbf{G}^T(\mathbf{G}\mathbf{C_M}\mathbf{G}^T + \mathbf{C_D})^{-1}(\boldsymbol{d} - \mathbf{G}\boldsymbol{m}_{\text{prior}}). \tag{4.9}$$

Chapter 5

Estimating basal properties of glaciers from surface measurements: a non-linear Bayesian inversion approach applied to synthetic data

This chapter is a draft of a paper to be submitted under the same title in the Journal of Geophysical Research, with co-author G. H Gudmundsson from the British Antarctic Survey, Cambridge, UK.

Abstract

We introduce a non-linear Bayesian inference approach to estimate the basal properties of a glacier, i.e. bedrock topography and basal slipperiness from observations of surface topography and surface velocities. The inverse procedure is based on an iterative Newtonian optimization of a cost function involving a forward step solved with a numerical finite-element model. The first order forward model derivatives needed for inversion are approximated by analytical linear transfer functions (Gudmundsson, 2003). Using synthetic surface data generated with a forward finite-element model, we show that the inversion procedure resolves accurately the perturbations and converges quickly to the correct solution. The number of iterations needed for convergence increases with the amplitude of the basal perturbations.

5.1 Introduction

The goal of geophysical inverse problems is to make quantitative inferences about Earth characteristics from remote observations (e.g., Gouveia and Scales, 1998). Estimating basal properties of glaciers from surface measurements presents an example of an inverse problem. In this paper, we use a probabilistic Bayesian inference approach (e.g., Rodgers, 2000; Tarantola, 2005) to estimate bedrock topography and basal slipperiness from surface velocities and surface geometry. In Bayesian inference, a priori information about the basal properties is expressed as a probability density function and combined with the surface measurements to give an a posteriori probability distribution which describes the final uncertainty of the estimates. The solution of the inverse problem, i.e. the a posteriori probability distribution, provides an ensemble of solutions from which we single out the most likely one corresponding to the maximum of the a posteriori probability.

The forward function describing the relationship between the model parameters, i.e. bedrock topography and basal slipperiness, and the observations, i.e. surface topography and surface velocities, is solved numerically with a plane-strain finite-element model. This allows to consider both the rheological nonlinearity of the ice and nonlinear finite-amplitude effects of basal perturbations. As there exist no explicit solutions for the inversion of this non-linear forward function, the solution of the inverse problem must be sought numerically and iteratively. Hence, the a posteriori probability distribution for the model parameters is optimized via a nonlinear Gauss-Newton procedure to find the maximum of the a posteriori probability. A key issue in the derivation of the solution is the determination of the first order derivatives of the forward function. These can be evaluated numerically, but as the computational time involved for this is long relative to the original forward model computation, it is preferable to evaluate the algebraic derivatives of the forward function (Rodgers, 2000). Thus, we choose to approximate the first order derivatives of the forward model with analytical transfer functions (Gudmundsson, 2003). These transfer functions correspond effectively to the first order forward function derivatives only in the case where the ice rheology is linear and in the case where finite-amplitude effects are absent. This approximation is a crucial feature of the proposed method, as it would greatly enhance its numerical efficiency. The main concern of this paper is therefore to determine whether this approximation is adequate when nonlinear effects are present.

In this paper, no assumptions need be made about the strength of the finite-amplitude effects. This can only be ensured by the fully nonlinear treatment proposed here. Inverse methods making use of a forward function approximated directly by the analytical theory developed by (Gudmundsson, 2003) as done by Thorsteinsson et al. (2003) will on the other hand always be inherently restricted to small variations about the mean conditions since the perturbation theory relies on a number of small-amplitude assumptions about the strength of the perturbations. Thorsteinsson et al. (2003) applied a linear least-square inversion to infer both bed elevation and basal lubrication from surface observations on Ice Stream E, West Antarctica.

Further examples of inversion of surface observations to determining basal conditions under glaciers can be found in e.g. Van der Veen and Whillans (1989); MacAyeal (1992); MacAyeal et al. (1995); Vieli and Payne (2003); Joughin et al. (2004); Truffer (2004). MacAyeal (1992) and MacAyeal et al. (1995) applied control theory to determine the basal shear stress under ice streams from ice velocity data, ice thickness and surface elevation. Joughin et al. (2004) modified the method to yield a direct inversion for the basal stress corresponding to a weak plastic bed. Truffer (2004) inverted a linearized one-dimensional forward model to calculate the basal velocity of a valley glacier.

The purpose of this paper is to introduce and test the suitability of a non-linear Bayesian inference approach to determine the bedrock undulations and basal lubrication under ice streams from observations of surface topography, horizontal and vertical surface velocity. The inference approach is applied along flow lines when transverse effects can be ignored. We restrict the observations to noise-degraded synthetic surface data generated with a forward numerical model for different types of basal disturbances. The amplitude of the applied basal disturbances is varied such that the influence of the finite-amplitude effects on the inversion can be investigated. These nonlinear finite-amplitude effects are investigated first separately for linear rheology. They are then combined with the rheological nonlinearity of the ice. The influence of the temperature-dependence of the flow on the inversion is also examined. The case studies presented allow us to explore the capabilities of the inverse procedure and in particular to assess the suitability of the approximation of the first order derivatives of the forward function by linear transfer functions. We determine to what extent the inverse procedure converges to the true solution and how many iterations are needed.

The structure of the paper is as follows. We start by describing in Section 5.2 the forward theory, i.e the numerical model. We then introduce the non-linear Bayesian inference method in Section 5.3. The results of the proposed inversion method are presented in Section 5.4, where the suitability of the method is discussed.

5.2 Bed-to-surface transfer and forward model

The ’forward problem’ consists in calculating the steady-state surface topography and surface velocities of glaciers from bedrock topography and basal slipperiness distributions. This problem is non-linear because the ice rheology is nonlinear and because the surface reacts in a nonlinear fashion to finite amplitude basal perturbations. Defining a vector $\boldsymbol{d}$ which contains all available surface quantities and a vector $\boldsymbol{m}$ containing the basal properties, we can write the relation between bed and surface as

$$\boldsymbol{d} = \boldsymbol{g}(\boldsymbol{m}), \tag{5.1}$$

where $\boldsymbol{g}$ is the forward function. We use as forward function a nonlinear finite-element model that allows us to deal with both types of nonlinearities mentioned above. We refer in the following to the forward function $\boldsymbol{g}$ as the forward model. The numerical model is two-dimensional, plane-strain. Four-nodes, isoparametric, quadrilateral Hermann elements are used. A mixed Lagrangian-Eulerian approach is employed in determining the position of the steady-state surface (Leysinger Vieli and Gudmundsson, 2004). The numerical model solves the full force-balance equations for which acceleration terms are neglected and the mass-conservation equation for incompressible ice. These equations read $\sigma_{ij,j} = -\rho g_i$ and $v_{i,i} = 0$, respectively, where σ_{ij} are the components of the Cauchy-stress tensor, ρ is the ice density, g the acceleration due to gravity and v_i are the components of the velocity vector $\boldsymbol{v} = (u, w)$. The glacier geometry corresponds to a uniformly inclined plane slab of constant thickness on which perturbations in bed and surface topography are superimposed. Figure 5.1 illustrates the problem geometry. The coordinates are (x, z), where x is parallel and z perpendicular to the mean slope. The equation $z = s(x, t)$ defines the surface and $z = b(x)$ the base of the glacier. The constitutive law is Glen’s flow law, extended, following Hutter (1983), with a linear term to avoid the singularity in viscosity as the deviatoric stress goes to zero

$$\dot{\epsilon}_{ij} = A(\tau^{n-1} + {\tau_0}^{n-1})\sigma_{ij}^{(d)}. \tag{5.2}$$

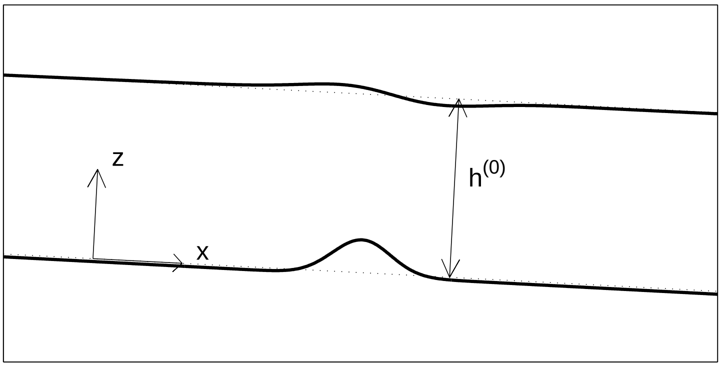

Figure 5.1: Illustration of the problem geometry and coordinate system. Gaussian-shape bedrock perturbation and corresponding surface reaction are shown as a black line. The dashed lines show the undisturbed glacier geometry.

In this equation, A is the rate factor, n the stress exponent, $\dot{\epsilon}_{ij}$, $\sigma_{ij}^{(d)}$ and τ are the strain rate, the deviatoric stress tensors and the effective shear stress, respectively. The parameter τ_0 is the crossover stress at which the linear and power terms contribute equally to the total strain rate. This parameter has been introduced only in model runs where the model geometry did not give rise to a sufficiently big mean longitudinal strain rate to avoid a large effective viscosity at the surface. Else, its influence is negligible. In nondimensional form, the rate factor A equals to $A = (n+1)/2$. In dimensional units and isothermal conditions, the rate factor A follows the value from Paterson (1994). The numerical model has also been run under cold temperatures conditions with a linear increase of temperature with depth from minus 25° C at the surface to 0° C at the bottom. The temperature-dependent rate factor has been introduced in the numerical model following Smith and Morland (1981).

Boundary conditions along the bed are specified by a sliding relation of the form

$$u_b = C(x)\tau_b^m, \tag{5.3}$$

where u_b is the sliding velocity tangential to the bed, $C(x)$ the sliding coefficient, and τ_b the bed parallel shear stress. Basal sliding is introduced in the finite-element model by adding a uniform thin layer of different viscosity to the base of the glacier such that relation (5.3) is respected. The function describing the basal topography $b(x)$ is defined as

$$b(x) = b^{(0)} + \Delta b(x), \tag{5.4}$$

where $b^{(0)}$ is the mean bedrock elevation and $\Delta b(x)$ the variation around this mean value. Similarly, the function describing the mean basal slipperiness $C(x)$ reads

$$C(x) = C^{(0)}(1 + \Delta C(x)), \tag{5.5}$$

with $C^{(0)}$ the mean basal slipperiness and $\Delta C(x)$ the fractional amplitude of the basal slipperiness perturbation. Note that the total amplitude of the basal slipperiness perturbation is given by the product $C^{(0)}\Delta C$. The mean basal slipperiness $C^{(0)}$ corresponds to the ratio of sliding velocity to the surface-parallel deformational velocity, i.e. the slip ratio. Perturbations in bedrock topography are referred to in the following as $\mathcal{B}$ perturbations and perturbations in basal slipperiness as $\mathcal{C}$ perturbations.

The ice surface ($z = s(x, t)$) is stress-free and evolves with time according to the kinematic boundary condition until steady-state is reached. The kinematic boundary condition reads

$$s_t + us_x = w, \tag{5.6}$$

where $s(x, t)$ describes the surface elevation, t is the time, and u and w are the horizontal and vertical velocities, respectively. Accumulation and ablation are not taken into account. The kinematic boundary condition (5.6) is integrated forward in time with an implicit Crank-Nicholson scheme. To speed up the evolution of the free surface towards steady-state, we initialize the computations with the analytical steady-state surface profile for linear rheology and respective basal perturbations (Gudmundsson, 2003). Periodic displacement boundary conditions are imposed along the upstream and downstream glacier model boundaries, i.e. both horizontal and vertical velocities of the upstream model boundary are constrained to be equal to those of the downstream boundary at all times. Hence, the flow section is repeated infinitely in x-direction. Periodic boundary conditions can only be imposed in cases where the glacier thickness is the same at both boundaries. If the glacier thickness is not the same, pressures must be prescribed at the edges.

The size of the mesh in the x-direction follows a Gaussian repartition centered around the middle of the prescribed perturbations where we expect the largest deformations. This allows to reduce the total amount of elements and computational time. The results of the numerical model have been validated by comparison with relevant perturbation theories (Raymond and Gudmundsson, 2005; Chapter 2 in this thesis).

Similarly to the basal perturbations, the steady-state surface topography, horizontal velocity and vertical velocity can be partitioned as $s(x) = s^{(0)} + \Delta s(x), u(x) = u^{(0)} + \Delta u(x), w(x) = w^{(0)} + \Delta w(x)$, respectively. In the following, we focus on the relationship between basal and surface perturbations and for notational compactness we refer with s, u, w to the surface perturbations and with b, C to the basal perturbations.

5.3 Non-linear Bayesian Inversion

Notation

Vectors will be denoted by bold face italic letters (e.g. $\boldsymbol{d}$) and matrices by bold uppercase letters (e.g. $\mathbf{C}$). The notation $P(\boldsymbol{m}|\boldsymbol{d})$ indicates the probability density function (*pdf*) of $\boldsymbol{m}$ conditional on $\boldsymbol{d}$. In $\boldsymbol{d} = \boldsymbol{g}(\boldsymbol{m})$, the forward function $\boldsymbol{g}$ is vector-valued and returns the vector $\boldsymbol{d}$ for a given value of the vector $\boldsymbol{m}$. Retrieved values are denoted by a circumflex (e.g. $\hat{\boldsymbol{m}}$) which indicates an estimated quantity and are the result of operating on the measurement with some inverse or retrieval method $\mathbf{R}$ ($\hat{\boldsymbol{m}} = \mathbf{R}(\boldsymbol{d})$) (Rodgers, 2000).

5.3.1 Formulation of the Problem

To estimate the basal properties of a glacier from surface measurements, we will consider the unknowns assembled into a so called model parameter vector $\boldsymbol{m}$, and the measured quantities into a data vector $\boldsymbol{d}$. In Bayesian inference, the notion of knowledge and uncertainty about data and model parameters is expressed in terms of probability distributions. In the Bayesian inference approach, the solution of the inverse problem is an a posteriori probability distribution for the model parameters $\boldsymbol{m}$. This posterior probability density results from the combination of prior information $\boldsymbol{m}_{\text{prior}}$ with the data $\boldsymbol{d}$ using Bayes theorem

$$P(\boldsymbol{m}|(\boldsymbol{d},\boldsymbol{m}_{\text{prior}})) = \frac{P(\boldsymbol{m}|\boldsymbol{m}_{\text{prior}})P(\boldsymbol{d}|(\boldsymbol{m},\boldsymbol{m}_{\text{prior}}))}{P(\boldsymbol{d}|\boldsymbol{m}_{\text{prior}})}, \tag{5.7}$$

where the data $\boldsymbol{d}$, model parameter $\boldsymbol{m}$ and a priori vectors

$$\begin{aligned} \boldsymbol{d} &= (\boldsymbol{s},\boldsymbol{u},\boldsymbol{w})^T & (5.8)\\ \boldsymbol{m} &= (\boldsymbol{b},\boldsymbol{C})^T, & (5.9)\\ \boldsymbol{m}_{\text{prior}} &= (\boldsymbol{b}_{\text{prior}},\boldsymbol{C}_{\text{prior}})^T, & (5.10) \end{aligned}$$

consist of surface topography $\boldsymbol{s}$, horizontal and vertical velocities $\boldsymbol{u}$, $\boldsymbol{w}$, bedrock topography $\boldsymbol{b}$, basal slipperiness $\boldsymbol{C}$, and a priori values of $\boldsymbol{b}$, $\boldsymbol{C}$, respectively. The superscript ^{T} means transposition, here to column vectors. Note that $\boldsymbol{s} = (s_1, s_2, \ldots, s_N)$, with N the number of discretization points for inversion. These points do not correspond to the discretization points of the finite-element model. The vectors $\boldsymbol{u},\boldsymbol{w},\boldsymbol{b},\boldsymbol{C}$ are of the same length as $\boldsymbol{s}$. Hence, the length of the measurement vector $\boldsymbol{d}$ and model parameter vector $\boldsymbol{m}$ is $3 \times N$ and $2 \times N$, respectively. Moreover, $P(\boldsymbol{m}|(\boldsymbol{d},\boldsymbol{m}_{\text{prior}}))$ denotes the posterior probability density function (*pdf*) for the model parameters $\boldsymbol{m}$ conditional on $\boldsymbol{d}$ and prior information $\boldsymbol{m}_{\text{prior}}$ and $p(\boldsymbol{m}|\boldsymbol{m}_{\text{prior}})$ is the prior *pdf* for the model parameters $\boldsymbol{m}$. This *pdf* incorporates prior information on the model parameters that is known independently of the measurements. As an example, the bed topography could be known independently from radio-echo sounding measurements. The a priori information may also arise from theoretical considerations (e.g., bedrock perturbation must be smaller than ice thickness), or from a definition (e.g., basal speed is not negative). $P(\boldsymbol{d}|(\boldsymbol{m},\boldsymbol{m}_{\text{prior}}))$ refers to the likelihood function. The likelihood function describes the probability of observing the data $\boldsymbol{d}$ if the model parameters were $\boldsymbol{m}$. The denominator $P(\boldsymbol{d}|\boldsymbol{m}_{\text{prior}})$ in expression (5.7) can be shown to be a normalizing factor for the posterior *pdf* $P(\boldsymbol{m}|(\boldsymbol{d},\boldsymbol{m}_{\text{prior}}))$ since

$$P(\boldsymbol{d}|\boldsymbol{m}_{\text{prior}}) = \int P(\boldsymbol{d}|(\boldsymbol{m},\boldsymbol{m}_{\text{prior}}))P(\boldsymbol{m}|\boldsymbol{m}_{\text{prior}})dm. \tag{5.11}$$

For simplicity, the posterior *pdf* (5.7) is commonly redefined as

$$P(\boldsymbol{m}|(\boldsymbol{d},\boldsymbol{m}_{\text{prior}})) = P(\boldsymbol{m}|\boldsymbol{m}_{\text{prior}})P(\boldsymbol{d}|(\boldsymbol{m},\boldsymbol{m}_{\text{prior}})). \tag{5.12}$$

Equation (5.12) measures how well the model parameters agree with the prior knowledge updated in the light of the measurements. It describes the final uncertainty of the estimates. The solution presented here has been derived using Bayes theorem (e.g., Rodgers, 2000; Jeffreys, 1939). Solutions derived from the notion of the conjunction of probabilities as done by Tarantola and Valette (1982) and Tarantola (2005), although more general than the one presented here, reduce to the same conclusions in all particular cases.

Equation (5.12) is general. In this study, we assume that both data and modeling uncertainties can be described by Gaussian distributions. This assumption is very common since many processes can be described by the Gaussian distribution and it is algebraically convenient (Rodgers, 2000). The a priori probability density function therefore reduces to

$$P(\boldsymbol{m}|\boldsymbol{m}_{\text{prior}}) = \exp\left[-\frac{1}{2}(\boldsymbol{m}-\boldsymbol{m}_{\text{prior}})^T\mathbf{C_M}^{-1}(\boldsymbol{m}-\boldsymbol{m}_{\text{prior}})\right], \tag{5.13}$$

where $\mathbf{C_M}$ is the a priori covariance matrix describing the uncertainties in the prior model parameters. The likelihood function is given by

$$P(\boldsymbol{d}|(\boldsymbol{m},\boldsymbol{m}_{\text{prior}})) = \exp\left[-\frac{1}{2}(\boldsymbol{d}-\boldsymbol{g}(\boldsymbol{m}))^T\mathbf{C_D}^{-1}(\boldsymbol{d}-\boldsymbol{g}(\boldsymbol{m}))\right]. \tag{5.14}$$

Here, $\mathbf{C_D}$ is the covariance matrix of the noise in the data and $\boldsymbol{g}(\boldsymbol{m})$ is the forward modeling operator encapsulating the relevant physics in the relation between surface data $\boldsymbol{d}$ and model parameters $\boldsymbol{m}$ as described thoroughly in Section 5.2.

Defining the cost function by $J(\boldsymbol{m}) = -2\ln P(\boldsymbol{m}|(\boldsymbol{d},\boldsymbol{m}_{\text{prior}}))$ and substituting (5.13) and (5.14) into (5.12) we obtain

$$J(\boldsymbol{m}) = [(\boldsymbol{d}-\boldsymbol{g}(\boldsymbol{m}))^T\mathbf{C_D}^{-1}(\boldsymbol{d}-\boldsymbol{g}(\boldsymbol{m}))+(\boldsymbol{m}-\boldsymbol{m}_{\text{prior}})^T\mathbf{C_M}^{-1}(\boldsymbol{m}-\boldsymbol{m}_{\text{prior}})]. \tag{5.15}$$

We solve Eq. (5.15) for the minimum of $J(\boldsymbol{m})$ corresponding to the maximum of the posterior probability distribution $P(\boldsymbol{m}|(\boldsymbol{d},\boldsymbol{m}_{\text{prior}}))$, that is, we single out the most likely model parameters $\hat{\boldsymbol{m}}$ from the ensemble described by the *pdf*. This solution is referred to as the maximum a posteriori solution (MAP). Because the forward modeling operator $\boldsymbol{g}(\boldsymbol{m})$ is non-linear, there is no explicit solution to Eq. (5.15). We therefore perform a nonlinear optimization to find the maximum a posteriori solution $\hat{\boldsymbol{m}}$ that maximizes $P(\boldsymbol{m}|(\boldsymbol{d},\boldsymbol{m}_{\text{prior}}))$. To find the minimizers of $J(\boldsymbol{m})$ we equate the derivative of Eq. (5.15) to zero.

Defining

$$\boldsymbol{\phi}(\boldsymbol{m}) = \nabla_m J(\boldsymbol{m}) = -\mathbf{K}^T(\boldsymbol{m})\mathbf{C_D}^{-1}[\boldsymbol{d}-\boldsymbol{g}(\boldsymbol{m})] + \mathbf{C_M}^{-1}(\boldsymbol{m}-\boldsymbol{m}_{\text{prior}}), \tag{5.16}$$

where $\mathbf{K}(\boldsymbol{m}) = \nabla_m\boldsymbol{g}(\boldsymbol{m})$ is the Jacobian or the Fréchet derivative matrix, the solution of the optimization problem is given by $\boldsymbol{\phi}(\hat{\boldsymbol{m}}) = 0$.

The value of $\hat{\boldsymbol{m}}$ is found using Newton's method via the iteration

$$\boldsymbol{m}_{i+1} = \boldsymbol{m}_i - [\nabla_m\boldsymbol{\phi}(\boldsymbol{m}_i)]^{-1}\boldsymbol{\phi}(\boldsymbol{m}_i), \tag{5.17}$$

where the subscript i denotes the i-th iteration, the inverse is a matrix inverse and

$$\nabla_m\boldsymbol{\phi}(\boldsymbol{m}) = \mathbf{C_M}^{-1} + \mathbf{K}(\boldsymbol{m})^T\mathbf{C_D}^{-1}\mathbf{K}(\boldsymbol{m}) - [\nabla_m\mathbf{K}^T(\boldsymbol{m})]\mathbf{C_D}^{-1}[\boldsymbol{d}-\boldsymbol{g}(\boldsymbol{m})]. \tag{5.18}$$

$\nabla_m\boldsymbol{\phi}(\boldsymbol{m})$ is the second derivative of the cost function also called its Hessian. Equation (5.18) involves both the first derivative $\mathbf{K}(\boldsymbol{m})$ and the second derivative $\nabla_m\mathbf{K}(\boldsymbol{m})$ of the forward model, whose resulting product is small in the moderately non-linear case

(Rodgers, 2000). Ignoring this term and substituting (5.16) and (5.18) into the Newtonian iteration (5.17) gives the $\boldsymbol{m}_{i+1}$ iteration according to the Gauss-Newton method, namely

$$\boldsymbol{m}_{i+1} = \boldsymbol{m}_i + (\mathbf{C_M}^{-1} + \mathbf{K}_i^T \mathbf{C_D}^{-1} \mathbf{K}_i)^{-1} [\mathbf{K}_i^T \mathbf{C_D}^{-1} (\boldsymbol{d} - \boldsymbol{g}(\boldsymbol{m}_i)) - \mathbf{C_M}^{-1} (\boldsymbol{m}_i - \boldsymbol{m}_{\text{prior}})], \tag{5.19}$$

where $\mathbf{K}_i = \mathbf{K}(\boldsymbol{m}_i)$. The first derivatives of the forward model $\mathbf{K}_i$, are approximated using linear transfer functions, i.e

$$\mathbf{K}_i = \begin{pmatrix} \frac{\partial \boldsymbol{g}(\boldsymbol{m})_s}{\partial \boldsymbol{b}} & \frac{\partial \boldsymbol{g}(\boldsymbol{m})_s}{\partial \boldsymbol{C}} \\ \frac{\partial \boldsymbol{g}(\boldsymbol{m})_u}{\partial \boldsymbol{b}} & \frac{\partial \boldsymbol{g}(\boldsymbol{m})_u}{\partial \boldsymbol{C}} \\ \frac{\partial \boldsymbol{g}(\boldsymbol{m})_w}{\partial \boldsymbol{b}} & \frac{\partial \boldsymbol{g}(\boldsymbol{m})_w}{\partial \boldsymbol{C}} \end{pmatrix} \approx \begin{pmatrix} \mathcal{T}_{\mathcal{SB}} & \mathcal{T}_{\mathcal{SC}} \\ \mathcal{T}_{\mathcal{UB}} & \mathcal{T}_{\mathcal{UC}} \\ \mathcal{T}_{\mathcal{WB}} & \mathcal{T}_{\mathcal{WC}} \end{pmatrix}. \tag{5.20}$$

The transfer functions $\mathcal{T}$ are analytical solutions for linear rheology and small amplitude variations of the bed topography and basal slipperiness solved using perturbation methods (Gudmundsson, 2003). The transfer functions describe the relationship between basal and surface perturbations in terms of transfer amplitudes (the ratio of surface and basal amplitudes for sinusoidal perturbations) and phase shifts, given as functions of wavelength. They depend on the glacier slope α and the slip ratio $C^{(0)}$. The transfer functions $\mathcal{T}$ have a two letter suffix. The first suffix denotes the effect and the second one the cause. $\mathcal{T}_{\mathcal{SB}}$ describes a change in surface topography caused by a perturbation in bedrock topography, whereas $\mathcal{T}_{\mathcal{UC}}$ describes a change in surface-parallel velocity caused by a spatial variation in basal slipperiness. Figure 5.2 shows examples of analytical transfer functions as functions of the perturbation wavelength for both types of sinusoidal perturbations $\mathcal{B}$ and $\mathcal{C}$ for $C^{(0)} = 200$ and a surface slope of $\alpha = 0.5°$.

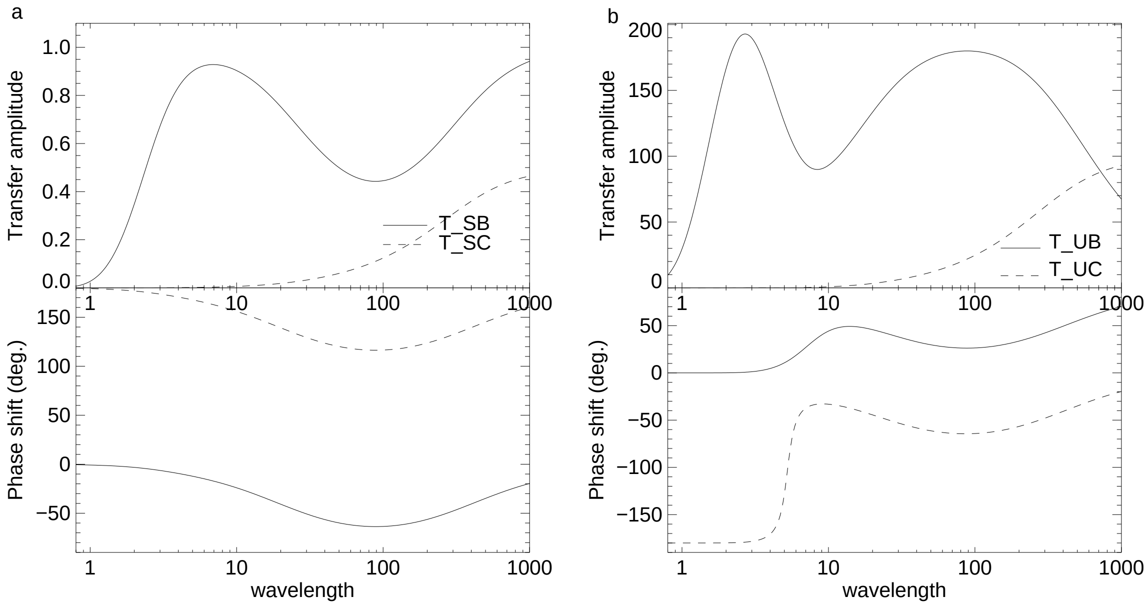

Figure 5.2: (a) Steady-state amplitude ratios and phase shifts for both bedrock ($\mathcal{T}_{\mathcal{SB}}$) and basal slipperiness perturbations ($\mathcal{T}_{\mathcal{SC}}$). (b) Steady-state amplitude ratios and phase shifts of surface-parallel velocities for a bedrock ($\mathcal{T}_{\mathcal{UB}}$) and basal slipperiness perturbation ($\mathcal{T}_{\mathcal{UC}}$). The medium is Newtonian. The mean surface slope is $0.5°$ and mean basal slipperiness is $C^{(0)} = 200$.

To use the transfer function formulation for $\mathbf{K}_i$, the inversion must be done in Fourier space. In (5.19) all vector components, i.e, surface fields, a priori and basal perturbations are therefore transformed into frequency space. The covariance matrices for the data and model parameters $\mathbf{C_D}$ and $\mathbf{C_M}$ are transformed into the Fourier space by the relation $\mathbf{FCF}^H$ where $\mathbf{F}$ is the discrete Fourier transform matrix, $\mathbf{C}$ the matrix to be transformed and ^{H} the Hermitian transpose. The transpose ^{T} in Eq. (5.19) is substituted with the Hermitian transpose ^{H}.

Covariance matrices

The covariance matrix for the noise in the data $\boldsymbol{d}$ is defined as

$$\mathbf{C_D} = \begin{pmatrix} \mathbf{C_s} & \mathbf{0} & \mathbf{0} \\ \mathbf{0} & \mathbf{C_u} & \mathbf{0} \\ \mathbf{0} & \mathbf{0} & \mathbf{C_w} \end{pmatrix}. \tag{5.21}$$

The matrix $\mathbf{C_D}$ is a block diagonal matrix consisting of the matrices describing the uncertainties in the surface topography $\mathbf{C_s}$, horizontal velocity $\mathbf{C_u}$ and vertical velocity $\mathbf{C_w}$ along the main diagonal. The off-diagonal blocks are zero matrices, since no cross-correlation between errors in surface topography, horizontal and vertical velocity is considered. Note the data covariance matrix can easily be modified to describe the correlation between some surface fields, as would be required for example using SAR interferometry data where surface velocity errors depend on surface elevation errors.

The covariance matrix for the noise in surface topography $\mathbf{C_s}$ takes the form

$$\mathbf{C_s} = \begin{pmatrix} \sigma^2_{s_1 s_1} & \sigma^2_{s_1 s_2} & \cdots & \sigma^2_{s_1 s_N} \\ \sigma^2_{s_2 s_1} & \sigma^2_{s_2 s_2} & \cdots & \sigma^2_{s_2 s_N} \\ \vdots & \vdots & \ddots & \vdots \\ \sigma^2_{s_N s_1} & \sigma^2_{s_N s_2} & \cdots & \sigma^2_{s_N s_N} \end{pmatrix},$$

where N is the number of discretization points. The matrix element ${\sigma^2}_{s_i s_j}$ is the covariance of s_i and s_j, with $1 \leq i, j \leq N$. If the noise in the data is uncorrelated, the corresponding covariance matrix is of diagonal form. $\mathbf{C_u}$ and $\mathbf{C_w}$ are of the same form but with the indices s replaced by u and w, respectively.

The covariance matrix for $\boldsymbol{m}_{\text{prior}}$ is defined as

$$\mathbf{C_M} = \begin{pmatrix} \mathbf{C_B} & \mathbf{0} \\ \mathbf{0} & \mathbf{C_C} \end{pmatrix}, \tag{5.22}$$

in which $\mathbf{C_B}$ and $\mathbf{C_C}$ have the same structure as $\mathbf{C_s}$. No a priori cross-correlation between the two model parameters is considered.

The correlation between off-diagonal elements is assumed to follow a Gaussian distribution

$$\mathbf{C_B}[i, j] = \sigma_B \exp\left(-\frac{(x_i - x_j)^2}{l_B^2} \right). \tag{5.23}$$

σ_B describes the variance of the fluctuation about the mean $\boldsymbol{m}_{\text{prior}}$ of the Gaussian probability density that characterizes the uncertainty of the a priori estimate, l_B is the correlation length and x the position.

First guess

To start the Newtonian iteration we need an initial guess for $\boldsymbol{m}_{i=0}$ in Eq. (5.19). The initial guess generally corresponds to the a priori values for the model parameters $\boldsymbol{m}_{\text{prior}}$ (Rodgers, 2000). As stated above, we consider here that little is known a priori and set deliberately $\boldsymbol{m}_{\text{prior}} = 0$. To define $\boldsymbol{m}_{i=0}$, we assume that the relationship between basal and surface properties is linear (i.e the ice rheology is linear and the amplitude of the basal perturbation is small) and can be completely described using the perturbation theory of Gudmundsson (2003). Thus, the forward relation (5.1) simplifies to $\boldsymbol{d} = \mathbf{K}\boldsymbol{m} + \boldsymbol{\epsilon}$, where $\mathbf{K}$ is a matrix of transfer functions. As all pdf's are still Gaussian, the cost function is of same form as (5.15) but with $\boldsymbol{g}(\boldsymbol{m})$ replaced by $\mathbf{K}$. Taking the minus logarithm of this new expression and maximizing with respect to $\boldsymbol{d}$, the maximum a posteriori solution is given by

$$\hat{\boldsymbol{m}}_{\text{linear}} = \boldsymbol{m}_{\text{prior}} + (\mathbf{C_M}^{-1} + \mathbf{K}^T\mathbf{C_D}^{-1}\mathbf{K})^{-1}\mathbf{K}^T\mathbf{C_D}^{-1}(\boldsymbol{d} - \mathbf{K}\boldsymbol{m}_{\text{prior}}). \tag{5.24}$$

Hence, we start the optimization of the objective function $J(\boldsymbol{m})$ by setting $\boldsymbol{m}_{i=0} = \hat{\boldsymbol{m}}_{\text{linear}}$.

Convergence

The convergence of the Gauss-Newton iteration is second order (Rodgers, 2000). The convergence analysis is required to determine when the optimization of the objective function (5.15) is reached. The convergence test is based on the function $J(\boldsymbol{m})$ being minimized such that

$$J(\boldsymbol{m}_i) - J(\boldsymbol{m}_{i-1}) \ll (3 \times N) \tag{5.25}$$

at the minimum, with $3 \times N$ the length of the measurement vector $\boldsymbol{d}$. At the minimum, $3 \times N$ corresponds theoretically to the expected value of $J(\hat{\boldsymbol{m}})$ (Tarantola, 2005).

Inverse procedure

In summary, the different steps involved in the iterative optimization by which the objective function $J(\boldsymbol{m})$ is minimized, are:

i Define a first guess for $\boldsymbol{m}_{i=0}$

ii Calculate the steady-state surface response $\boldsymbol{g}(\boldsymbol{m}_i)$ for the given bedrock and the distribution of the basal slipperiness with the forward finite-element model

iii Test for convergence using (5.25). Once the stopping criterion is satisfied, stop the iteration procedure, else

iv Determine incremental corrections to the bedrock profile and the distribution of the basal slipperiness using (5.19). Return to step (ii)

5.4 Numerical simulations

All synthetic surface data sets (i.e. surface topography, horizontal and vertical velocity) have been generated with the finite-element forward model described in Section 5.2. The perturbations in bedrock and basal slipperiness correspond either to Gaussian peak distributions or to step functions. Different slopes and slip ratios have been used. The synthetic surface data set was corrupted by uncorrelated Gaussian noise. The forward relation (5.1) hence modifies to

$$\boldsymbol{d} = \boldsymbol{g}(\boldsymbol{m}) + \boldsymbol{\epsilon}, \tag{5.26}$$

where ϵ are the measurement errors. Fourier transformation of the surface fields requires them to be interpolated onto an equidistant grid. Two different interpolation methods were used for this purpose on different data sets. First, a simple linear interpolation was applied. The covariance matrix for the noise in the data followed then a Gaussian distribution,

$$C_s[i,j] = \sigma_{si}\sigma_{sj} \exp\left(-\frac{(x_i - x_j)^2}{l_s^2}\right), \tag{5.27}$$

with σ_{si} the standard deviation of each point and l_s the correlation length. Secondly, the observations were interpolated using the geostatistical interpolation method of universal kriging (Kitanidis, 1997). The method makes use of the experimental variogram to describe the spatial variability of the measurements. The structure of the data as described by the variogram is then approximated with an isotropic Gaussian model. The covariance matrix for the noise in the data results directly from the interpolation method. The noise-degraded, interpolated surface fields are considered to be the observed data for the inversions. The results presented in the figures of this section focus on the perturbations. The total model length varies, however, between 400 and 700 mean ice thicknesses depending on the model geometry. All results are presented in non-dimensional form. The dimensional variables entering the problem are substituted through scalings by nondimensional variables (Raymond and Gudmundsson, 2005; Chapter 2 in this thesis). The spatial variables x, z, s, b are scaled with the mean ice thickness $h^{(0)}$ and the velocity components u, w with the mean surface-parallel deformational velocity u_d. The stresses and the pressure are scaled by the mean basal shear stress τ_b. Results for linear rheology are presented first, followed by results for non-linear rheology. In both cases, we distinguish between small and large ($\geq$ 0.1) perturbation amplitudes.

5.4.1 Linear rheology

All calculations for linear rheology are isothermal. The surface data were corrupted by uncorrelated Gaussian noise with zero mean and standard deviation equal to 5x10^{-4} for the surface topography, 10^{-3} and 3x10^{-3} for the horizontal and vertical velocity components, respectively. This noise-level corresponds to the expected surface measurement errors when performed with GPS. The prior *pdf* used in the inversions was set by assuming that little was known *a priori*; the prior model $\boldsymbol{m}_{\text{prior}}$ was set to zero (dotted lines in Figures 5.4, 5.6 and 5.8). The standard deviation of the prior was 0.25 of the ice thickness with a correlation length of 10 ice thicknesses.

Small amplitude perturbations

Figure 5.3 illustrates a synthetic surface data set generated with the numerical forward model for Gaussian peak distributions for both bedrock and basal slipperiness perturbations. The interpolation was done with the method of best linear unbiased estimator (BLUE). The amplitude of both basal disturbances amounts to 5% of the mean ice thickness.

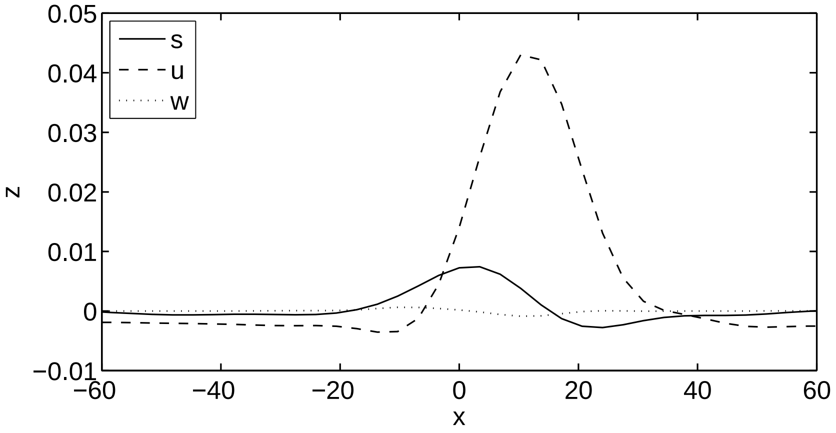

Figure 5.3: Steady-state surface topography $\boldsymbol{s}$, horizontal $\boldsymbol{u}$ and vertical $\boldsymbol{w}$ velocity components generated for Gaussian peak distributions for $\boldsymbol{b}$ and $\boldsymbol{C}$ as shown in Figure 5.4 (solid lines with circles). The medium is Newtonian. The mean surface slope $\alpha = 0.5^\circ$ and mean basal slipperiness $C^{(0)} = 200$. Note that for this illustration, the surface velocities are normed with the slip ratio $C^{(0)}$.

Figure 5.4 shows the inferred bed topography and basal slipperiness distribution for the inversion of the surface perturbations shown in Figure 5.3. The first guess and subsequent iterations are shown as well as the maximum a posteriori solution (MAP) obtained with two iterations. The true basal disturbances (solid lines with circles) are shown for comparison. As can be seen in Figure 5.4, the first guess (dash-dotted lines), obtained by assuming a linear relationship between basal and surface properties, already resolves accurately both basal perturbations. This is to be expected since the ice rheology is linear and for small perturbation amplitudes, non-linear finite-amplitude effects not accounted for in the analytical perturbation theory, are particularly weak (Raymond and Gudmundsson, 2005). Interestingly, through non-linear optimization, we are able to improve the estimates such that the maximum a posteriori solution for the forward model parameters $\hat{\boldsymbol{m}}$ is almost identical to the true value of the basal disturbances $\boldsymbol{m}$. The $\mathcal{B}$ perturbation is better resolved than the $\mathcal{C}$ perturbation in the first guess as well as at the end of the iteration process. We will see below that this is generally the case. This feature can be explained by looking at the sensitivity of the retrieval to the true basal perturbation, i.e. the averaging kernel. This shows that information about the basal slipperiness perturbations is transmitted at longer wavelengths than the bedrock perturbations (Gudmundsson and Raymond, in preparation).

Figure 5.5 shows the residuals between observations and FE-model predictions for, (a) the surface topography $\Delta \boldsymbol{s}$, (b) the horizontal velocity $\Delta \boldsymbol{u}$ and, (c) the vertical velocity $\Delta \boldsymbol{w}$ for iteration number 0 and 2. The residuals are defined as $\Delta \boldsymbol{d}_i = \boldsymbol{d} - \boldsymbol{g}(\boldsymbol{m}_i)$ where

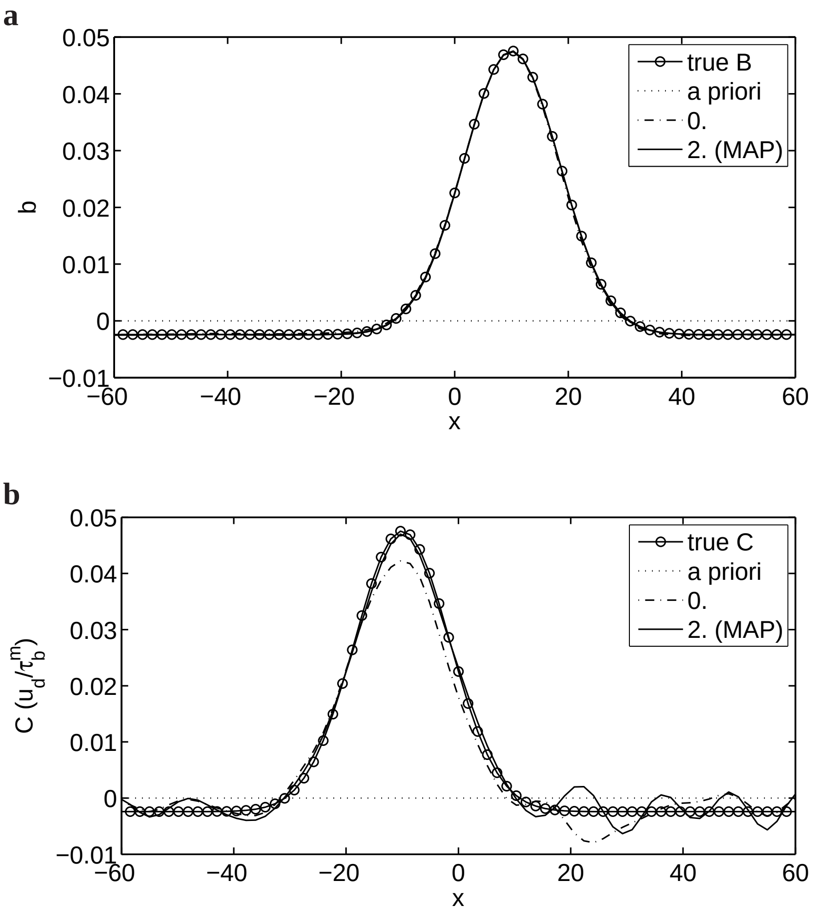

Figure 5.4: Inferred, (a) bed topography and, (b) basal slipperiness distributions estimated from the surface data set shown in Figure 5.3. The true basal perturbations are the solid lines with circle, and the iterations are labeled with iteration number. The maximum a posteriori solution (MAP) is the solid line. The a priori was set to zero. The medium is Newtonian, mean surface slope is $0.5°$ and mean basal slipperiness $C^{(0)} = 200$. Note that the 0th iteration and the MAP virtually coincide with the true bedrock perturbation in panel (a).

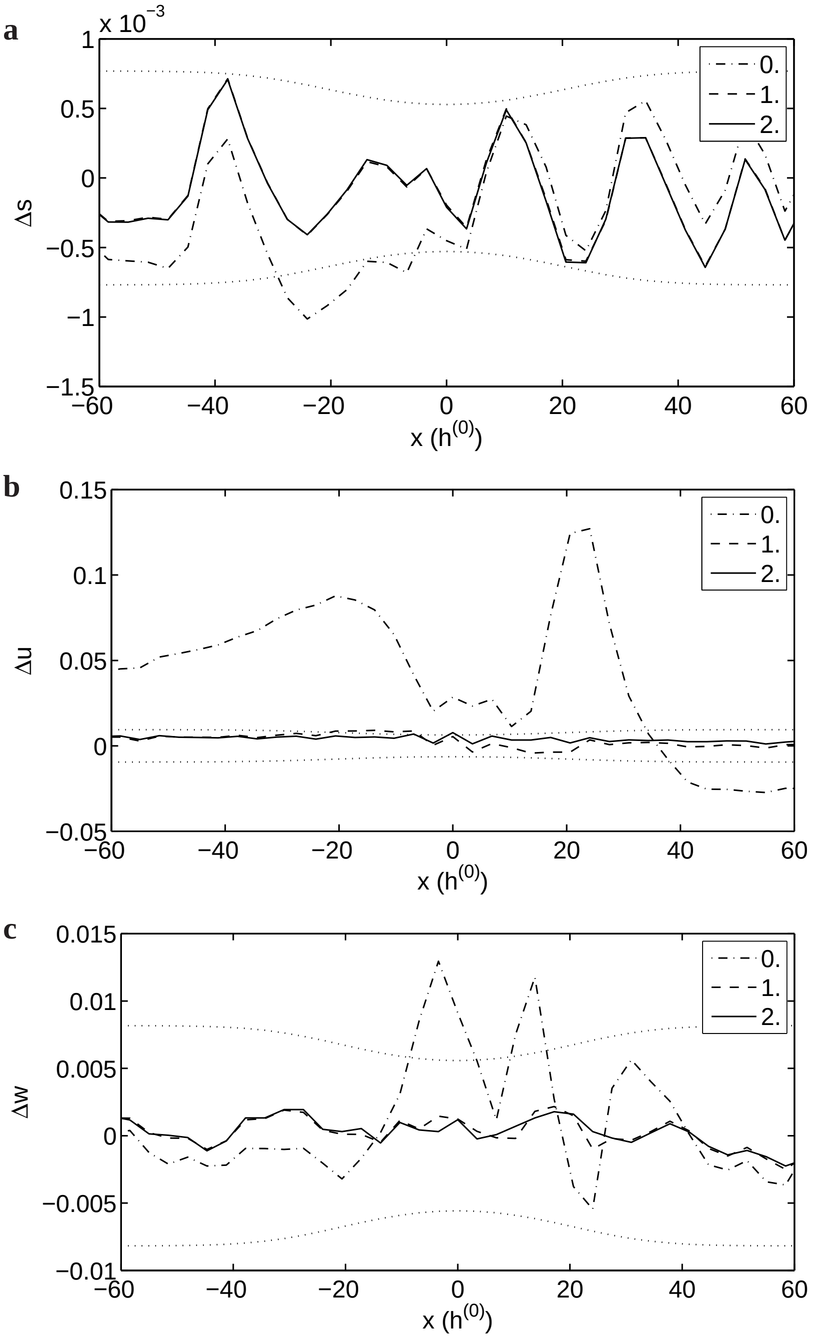

Figure 5.5: Residuals between observations and FE-model predictions for (a) surface topography, (b) horizontal and (c) vertical velocity. The residuals are defined as $\Delta \boldsymbol{d}_i = \boldsymbol{d} - \boldsymbol{g}(\boldsymbol{m_i})$ with i the iteration number. The dotted lines correspond to the square-roots of the main diagonal of the data covariance matrix $\mathbf{C_D}$ determined with the optimal interpolation method BLUE. Note that the first and second iteration lines are almost superimposed in panel (a).

$\Delta \boldsymbol{d}_i$ is the vector of residuals and $\boldsymbol{g}(\boldsymbol{m}_i)$ the forward finite-model prediction for the model parameters $\boldsymbol{m}_i$ at iteration numbers $i = 0, 2$. The optimization procedure has been carried out until the model fits the observed data to one noise standard deviation (dotted lines). As can be seen, only the horizontal velocity is poorly predicted by the FE-model for the first guess. The finite-element model predicts with some phase shifts smaller horizontal velocities for the regions where the slipperiness perturbation has been underestimated and larger horizontal velocities in regions where the perturbation has been overestimated.

Figure 5.6 shows the inferred bedrock and basal slipperiness perturbations for step perturbations and perturbation amplitudes of 0.05 ice thickness. The mean surface slope is 1° and mean basal slipperiness $C^{(0)} = 40$. The noise-degraded surface data have been linearly interpolated. Since the transfer function theory describing the forward model derivatives treats the model boundary as periodic, we need to alleviate the discontinuities introduced by the step function at the edges. The periodicity of the inverse model is ensured by returning the perturbations to zero with a sine function over a distance of about 10 ice thicknesses at both sides.

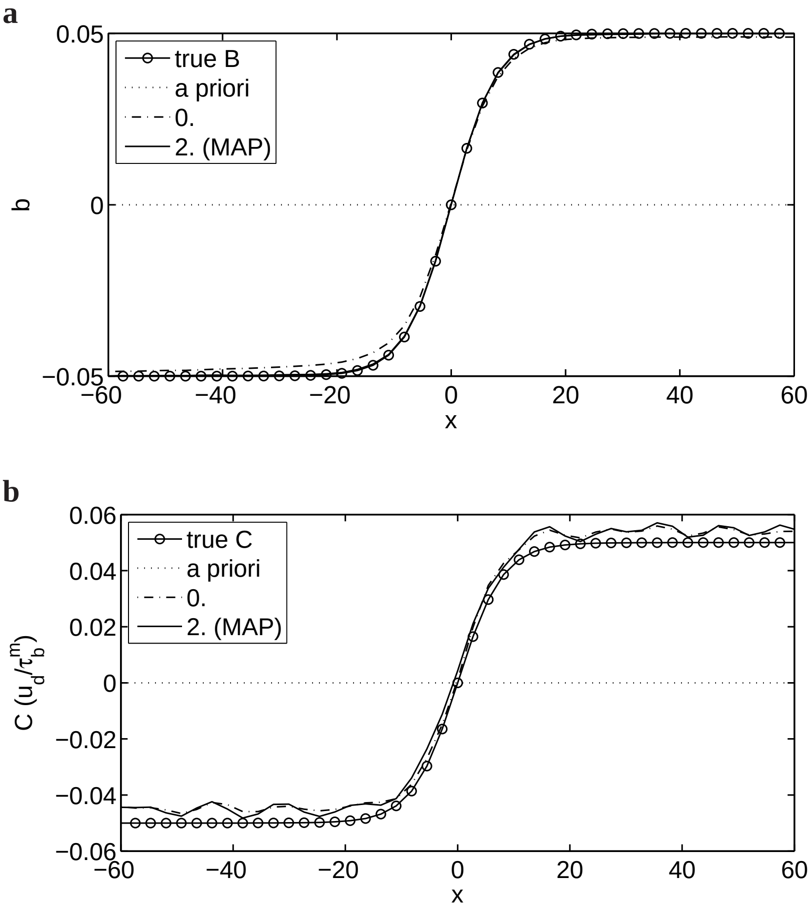

Figure 5.6: Inferred, (a) bed topography and, (b) basal slipperiness distributions. The true basal perturbations are shown for comparison (solid lines with circles). The a priori was set to zero (dotted lines). The medium is Newtonian, the mean surface slope is 1° and mean basal slipperiness $C^{(0)} = 40$. Note superimposing of MAP line with true bedrock line in panel (a).

As was the case in the previous example, the inferred $\mathcal{B}$ and $\mathcal{C}$ perturbations with the analytical solution (first guess) are very close to the true perturbations. Here again, the non-linear finite-amplitude effects are very limited and in fact, only two iterations are needed to compute the MAP. The bedrock perturbation is excellently recovered, whilst the basal slipperiness perturbation remains somewhat overestimated over the whole domain shown. Figure 5.7 shows that primarily the horizontal velocity is poorly reproduced by the forward finite-element prediction of the first guess retrieval. The negative variation in $\Delta \boldsymbol{u}$ is mainly the reaction to the underestimated $\mathcal{B}$ perturbation between $x = -60$ and $x = 0$.

Large amplitude perturbations

Figure 5.8 shows the inferred bedrock and basal slipperiness perturbations for the same Gaussian peak distributions as shown in Figure 5.4, but for perturbation amplitudes of 20%. The surface data have been interpolated using BLUE. The mean surface slope $\alpha = 0.5^\circ$ and the mean basal slipperiness $C^{(0)} = 200$. With increasing amplitude of the basal perturbations, the problem becomes increasingly non-linear and finite-amplitude effects can no longer be ignored. The surface perturbations do no longer correspond to the sum of the effects of the individual sinusoidal components of the basal perturbations and the relationship between bed and surface can no longer be completely described by a linear forward relation as assumed for the first guess retrieval. As expected, the first guess retrieval is poorer than it was for small amplitude perturbations; still, the bedrock perturbation is only somewhat overestimated around the perturbation center. The first guess retrieval locates a peak in the basal slipperiness at the right position ($x \approx -10$). However, it also produces a negative peak at $x = 10$ with a considerable amplitude of more than 10 ice thicknesses. This negative peak becomes positive at iteration number 1 in order to compensate for the too small horizontal velocities at the surface (Figure 5.9). The retrieval converges then quickly to the true solution. Two more iterations are needed as compared to the case with perturbation amplitude of 5% to reduce the residuals to one noise standard deviation (Figure 5.9). A total of four iterations is needed to compute the MAP.

These three examples of Bayesian inversion of noise-degraded surface data for linear rheology show accurate retrievals for both Gaussian-shaped and step perturbations. Interestingly, for small amplitudes perturbations, although a single linear inverse step is sufficient to predict the basal properties accurately, a few iterations still improve the estimates. The results show that with increasing amplitude of the perturbations, a single linear inversion step does not suffice any more to determine accurately the basal properties and particularly the basal slipperiness distribution. The method is capable of separating the effects of $\mathcal{B}$ and $\mathcal{C}$ perturbations, although $\mathcal{C}$ perturbations generally have less influence on the surface characteristics than $\mathcal{B}$ perturbations.

5.4.2 Non-linear rheology

All calculations for non-linear rheology have been performed with a value of the stress exponent n in the constitutive equation (5.2) of $n = 3$. Here, both non-dimensional and dimensional models have been run. Isothermal conditions prevail unless otherwise stated. As for linear rheology, results for small amplitude perturbations are presented first

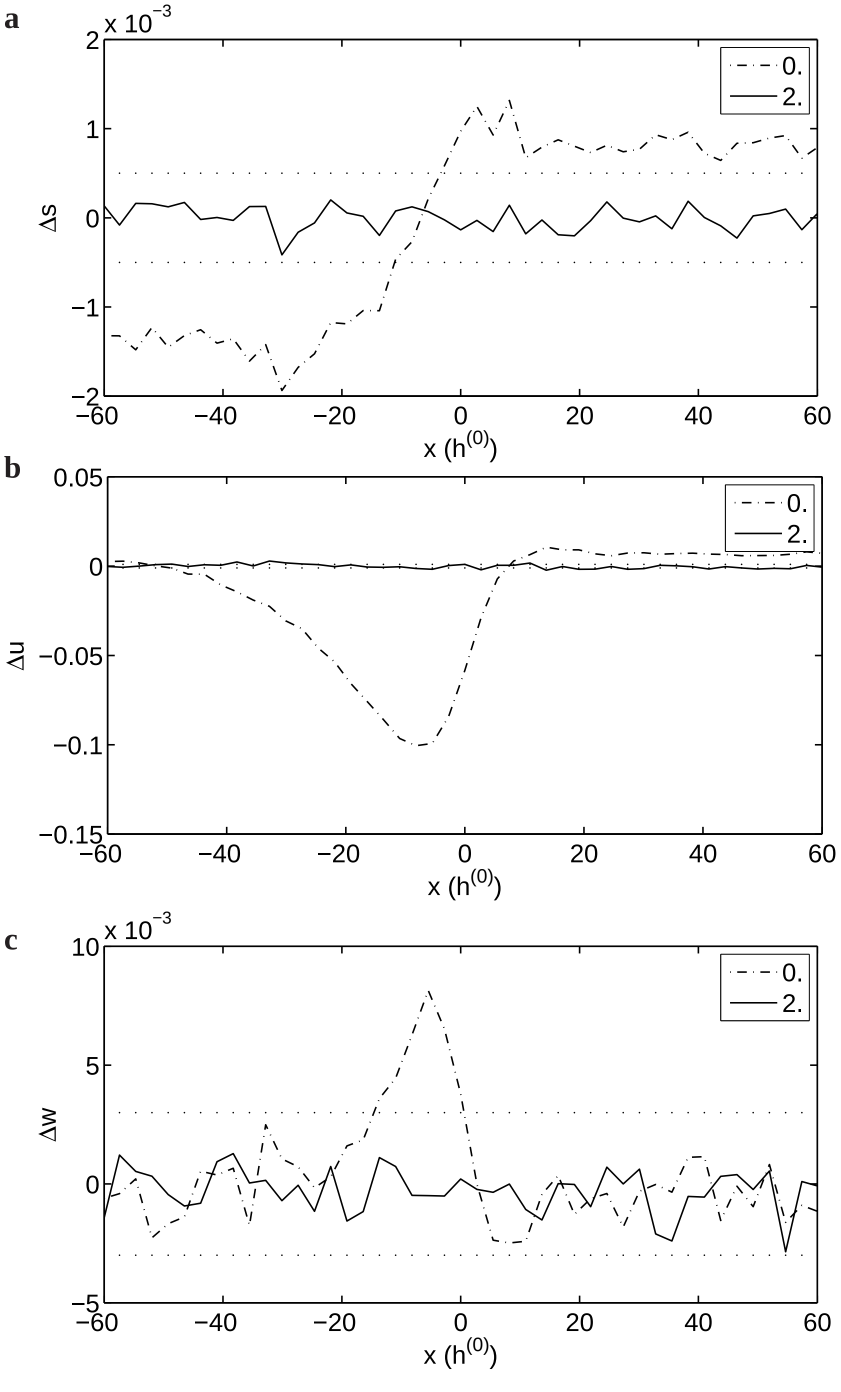

Figure 5.7: Residuals between observations and FE-model predictions for (a) surface topography, (b) horizontal and (c) vertical velocity. The dotted lines correspond to the square-roots of the main diagonal of the data covariance matrix $\mathbf{C_D}$.

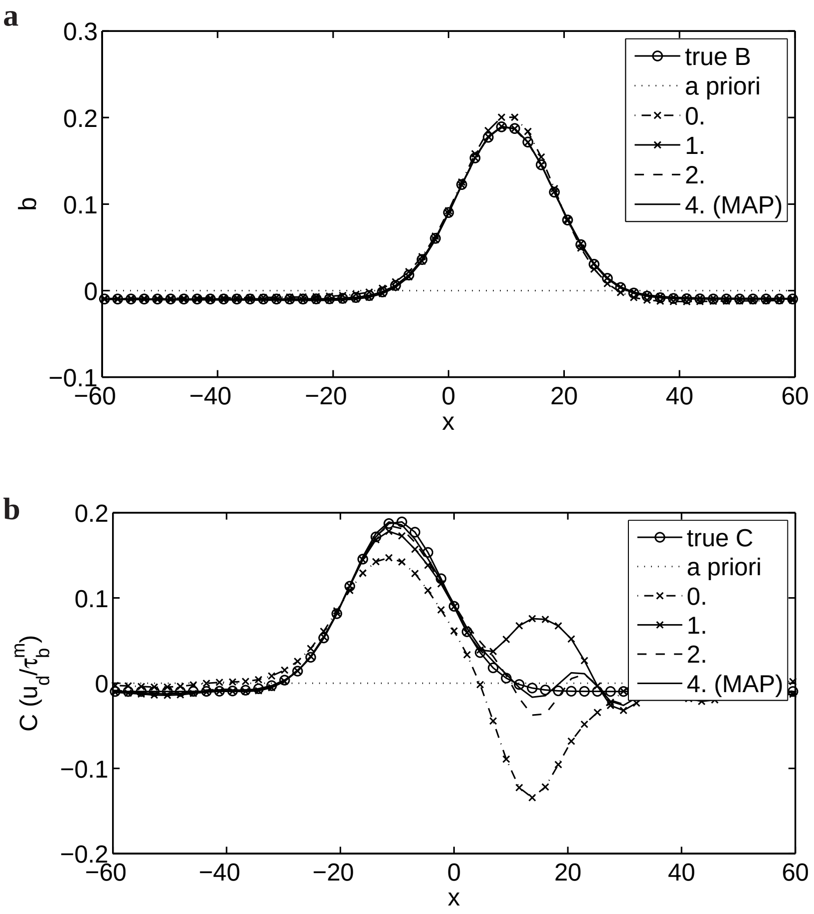

Figure 5.8: Same as Figure 5.4 but for basal perturbation amplitudes of 0.2. Note extensive superimposing of different lines with true bedrock topography for iterations ≥1 in panel (a).

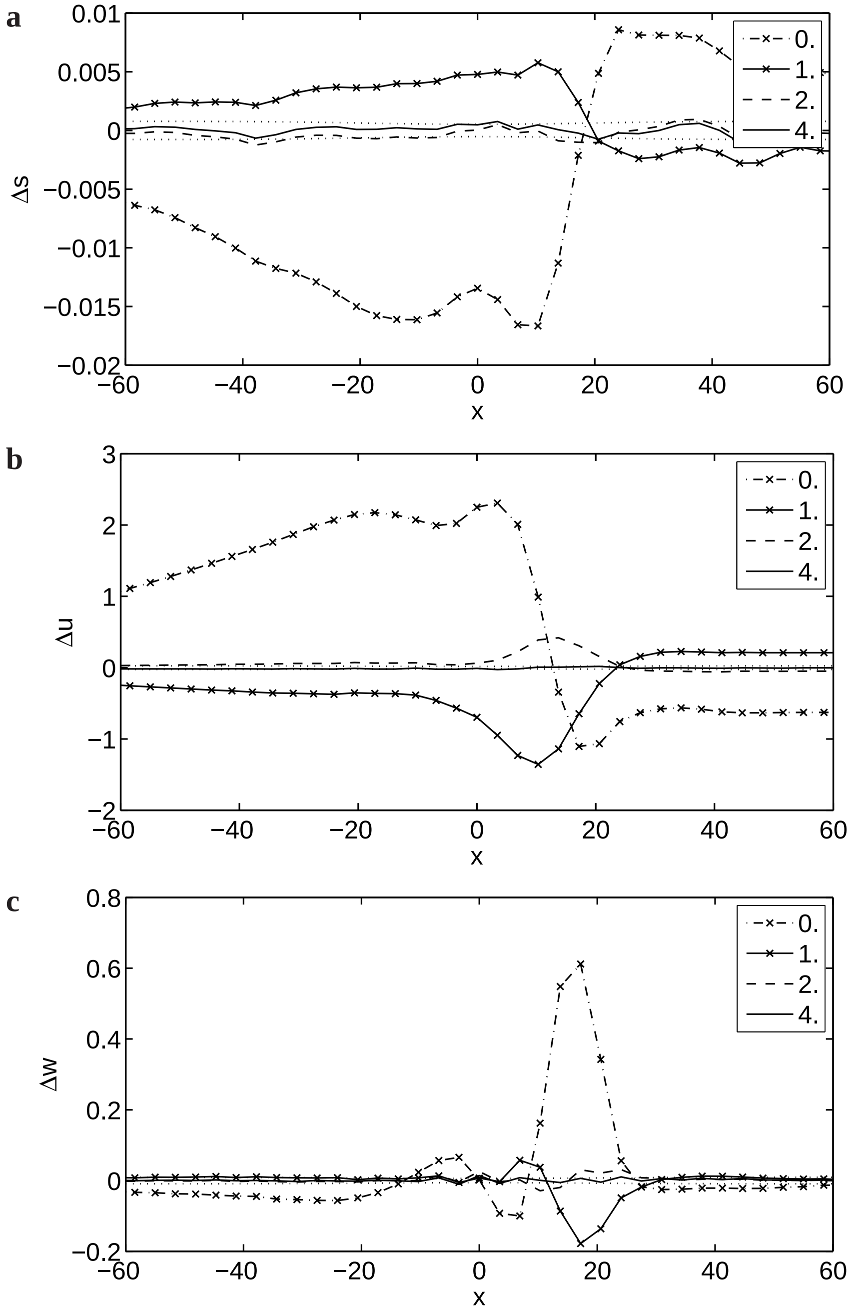

Figure 5.9: Residuals $\Delta \boldsymbol{d}_i$ between observations and FE-model predictions for (a) surface topography, (b) horizontal and (c) vertical velocity. The dotted lines correspond to the square-roots of the main diagonal of the data covariance matrix $\mathbf{C_D}$ determined with the optimal interpolation method BLUE.

followed by results for large amplitude perturbations. Finally, case studies involving ice temperature effects on the flow, differing value of the sliding law exponent or less surface data points for inversion are presented. In all cases presented, the prior model $\boldsymbol{m}_{\text{prior}}$ was set to zero as was the case for linear rheology.

Small amplitude perturbations

Figure 5.10 presents the estimated $\mathcal{B}$ and $\mathcal{C}$ perturbations obtained by inversion of the noise-degraded surface data generated for Gaussian peak distributions with perturbation amplitudes of 5 $\%$. The true perturbations are the solid lines with circles. The surface observations have been interpolated with BLUE. The mean ice thickness is $h^{(0)} = 1000$ m, the surface slope is $\alpha = 0.2^\circ$ and the mean sliding velocity amounts to 200 times the mean surface-parallel deformational velocity $u_d = 4.03$ m a^{-1}, i.e the slip ratio $C^{(0)} = 200$. The cross-over stress $\tau_0 = 10$ kPa lies within the range of values suggested by Pettit and Waddington (2003). The maximum a posteriori solution $\hat{\boldsymbol{m}}$ has been obtained with 7 iterations (solid lines) and reproduces well the true perturbations. As for linear rheology and small-amplitude perturbations, finite-amplitude effects are here particularly weak. Nonlinear effects arise primarily from the nonlinearity of the ice rheology. The first guess retrieval obtained by assuming linear rheology and small amplitude perturbations does not capture the whole basal slipperiness perturbation and predicts some oscillations over a horizontal distance covering about twice the extent of the true perturbation. On the other hand, the $\mathcal{B}$ perturbation is estimated very well by the first guess. Through non-linear optimization, the amplitude of the oscillations of the $\mathcal{C}$ perturbation is reduced iteratively to settle around the true perturbation.

The residuals between surface observations and FE-model predictions are shown in Figure 5.11. Mainly the FE-model prediction of the horizontal and vertical surface velocity deviate from the observations at iteration 0. The residuals for the surface topography (Figure 5.11a) already almost fall into one noise standard deviation.

Figure 5.12 shows the estimated bed topography and basal slipperiness for step perturbations of relative amplitude of 5%. The observations were computed for a mean ice thickness $h^{(0)} = 300$ m, a surface slope $\alpha = 1^\circ$ and a slip ratio $C^{(0)} = 40$. The cross-over stress $\tau_0 = 0$ kPa and the mean surface deformational velocity $u_d = 3.36$ m a^{-1}. Five iterations are needed for convergence (solid lines). As for linear rheology, the $\mathcal{B}$ perturbation is resolved more accurately than the $\mathcal{C}$ perturbation. The first guess retrieval predicts for the basal slipperiness perturbation, in addition to the step perturbation, a peak at $x = -3$ km. This peak is reduced continuously towards the true $\mathcal{C}$ perturbation as are the residuals towards the noise level (Figure 5.13).

Large amplitude perturbations

We now consider the inversion of noise-degraded synthetic data generated for non-linear rheology and relative amplitudes of the basal perturbations of 20 $\%$. Both types of nonlinearities are thus combined and affect the surface response. The calculations are nondimensional, the cross-over stress $\tau_0 = 0.3$, the mean surface slope $\alpha = 0.25^\circ$ and slip ratio $C^{(0)} = 200$. The surface observations have been interpolated with BLUE. The maximum a posteriori solution, computed with 11 iterations is shown in Figure 5.14 along with

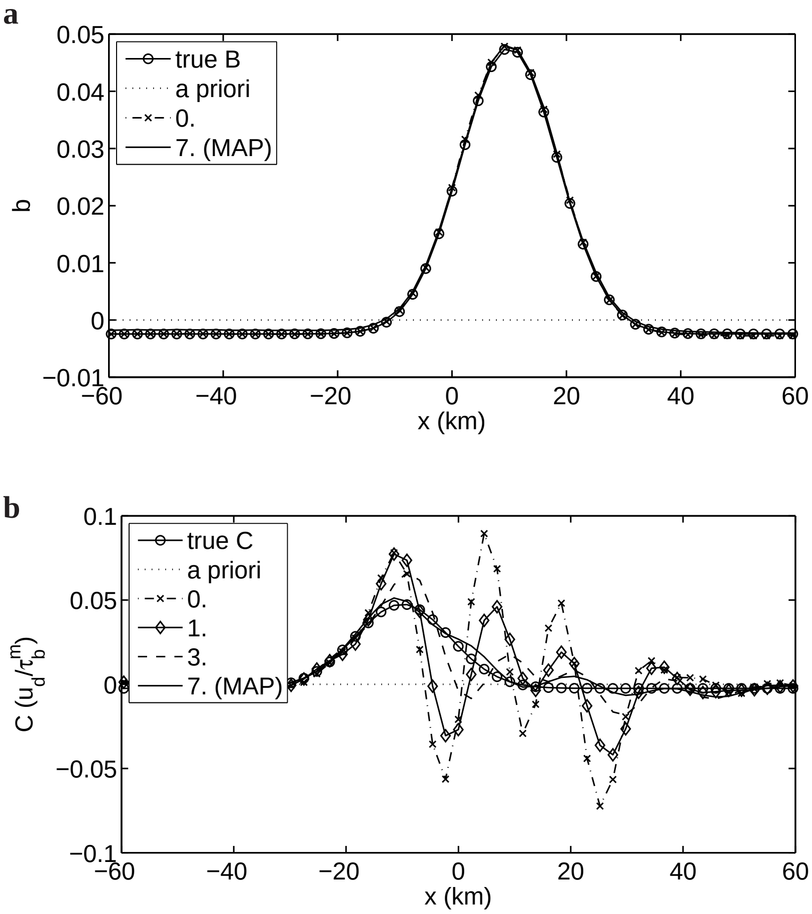

Figure 5.10: Inferred (a) bed topography and (b) basal slipperiness distributions. The true basal perturbations are the solid lines with circles. The a priori was set to zero. The ice rheology is non-linear, $n = 3$, $\tau_0 = 10$ kPa, the mean surface slope $\alpha = 0.2^\circ$ and the slip ratio $C^{(0)} = 200$. Note superimposing of 0th and 7th iteration line with true bedrock line in panel (a).

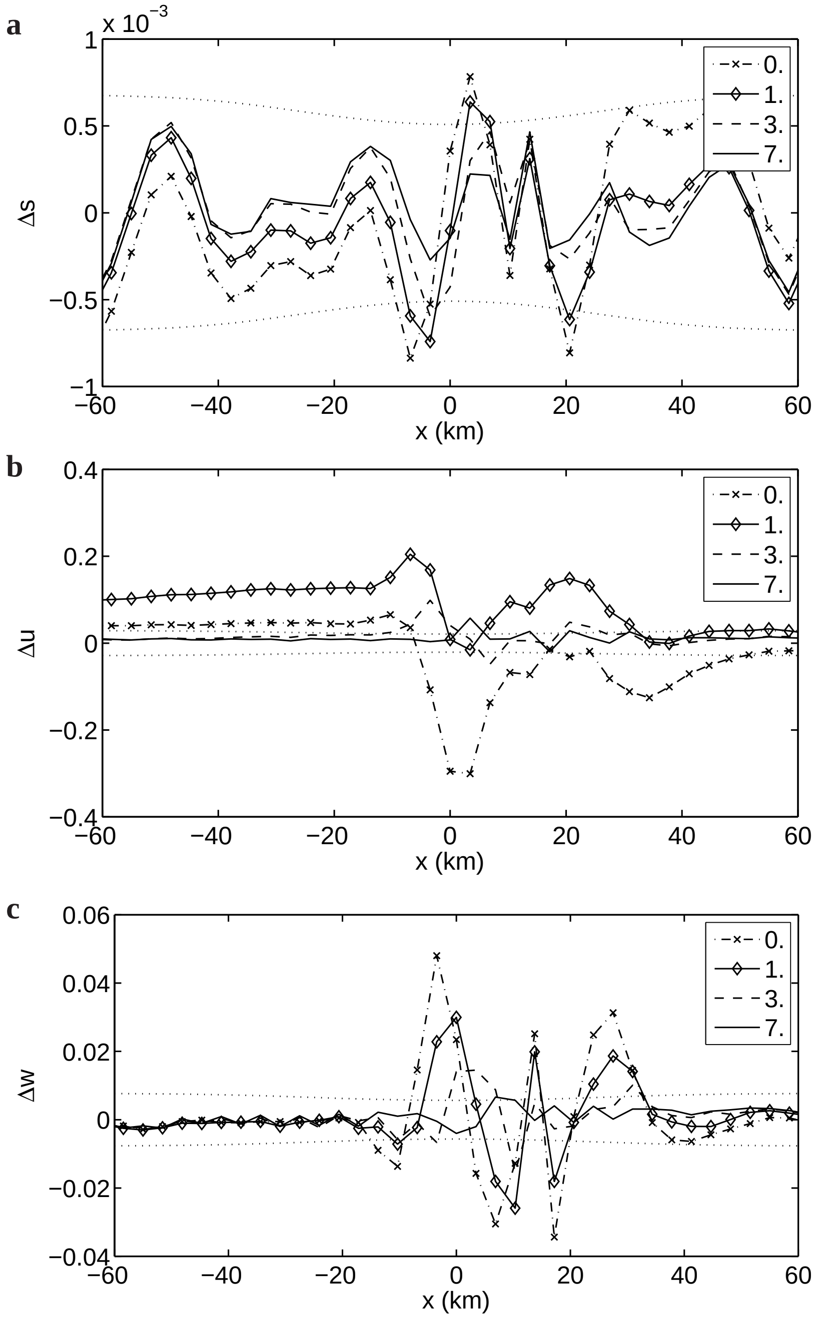

Figure 5.11: Residuals between observations and FE-model predictions for (a) surface topography, (b) horizontal and (c) vertical velocity. The dotted lines correspond to the square-roots of the main diagonal of the data covariance matrix $\mathbf{C_D}$.

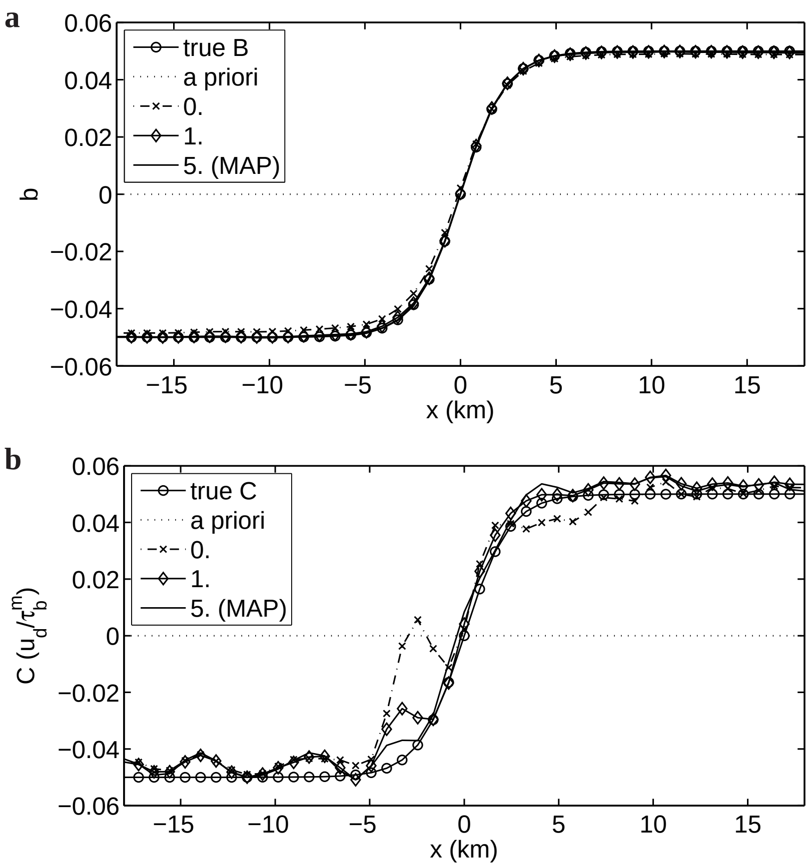

Figure 5.12: Inferred (a) bed topography and (b) basal slipperiness distributions. The true basal perturbations are shown for comparison (solid lines with circles). The a priori was set to zero. The ice rheology is non-linear, $n = 3$, $\tau_0 = 0$ kPa. The mean ice thickness is 300 m, $\alpha = 1°$, $C^{(0)} = 40$. Note extensive superimposing of different lines with true bedrock topography in panel (a).

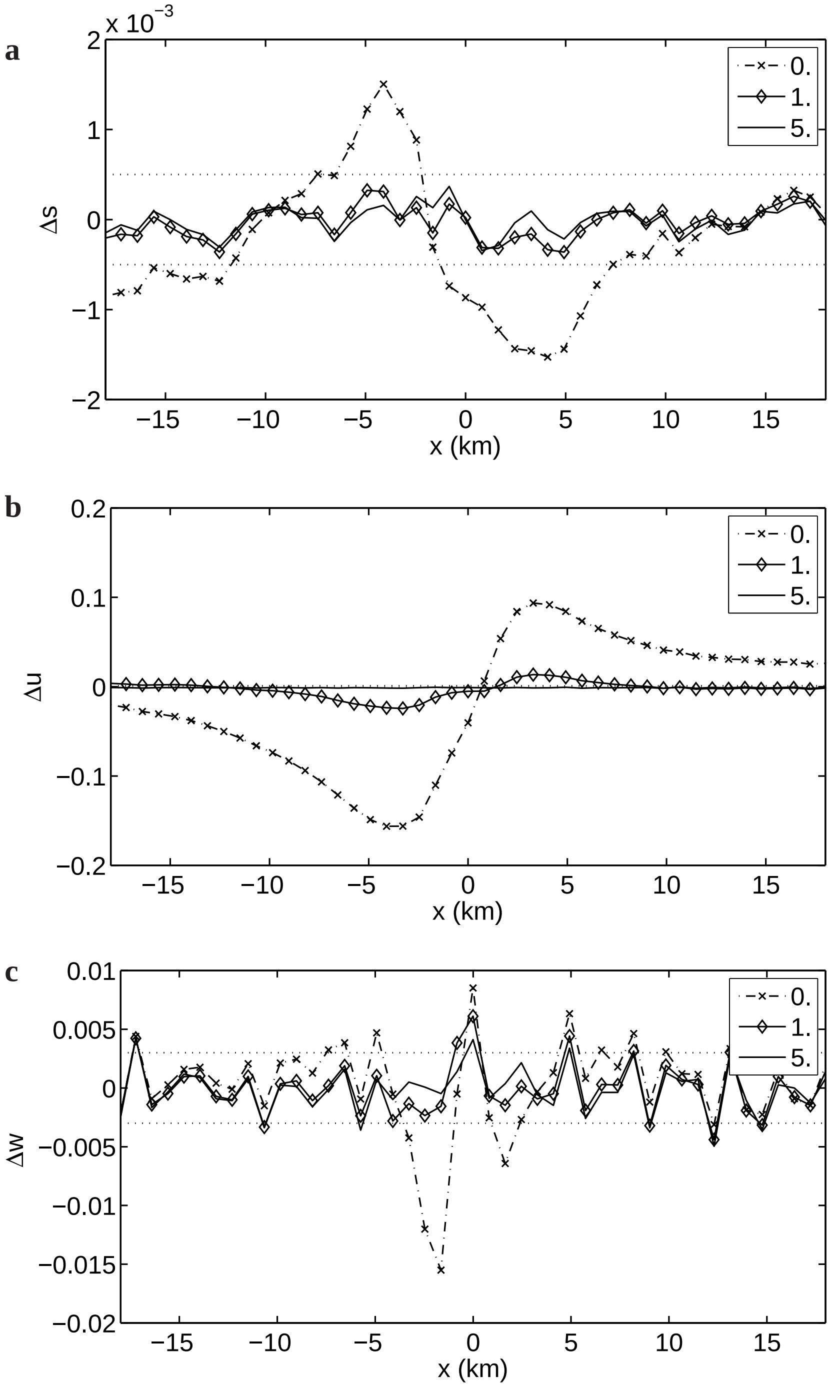

Figure 5.13: Residuals between observations and FE-model predictions for (a) surface topography, (b) horizontal and (c) vertical velocity. The dotted lines correspond to the square roots of the main diagonal of the data covariance matrix $\mathbf{C_D}$.

the true basal disturbances (solid lines with circles). As can be seen, the MAP solution converged to the correct solution and reproduces well the prescribed basal disturbances. This is a very good result as it shows that the approximation of the first order derivatives of the forward model with analytical linear transfer function in the optimization procedure (Eq. 5.19) is adequate to determine the basal properties even when both nonlinear rheology and finite-amplitude effects are combined. The amplitude of the initial guess was enforced to remain smaller than 0.3 and the variations were chosen to be smooth in order to ensure a quick convergence of the solution. The initial estimate (iteration 0) for $\mathcal{C}$ captures no effect directly under the true perturbation, but introduces a broad Gaussian-peak disturbance at $x \approx 10$ ice thicknesses (dash-dotted lines with crosses in Figure 5.14b).

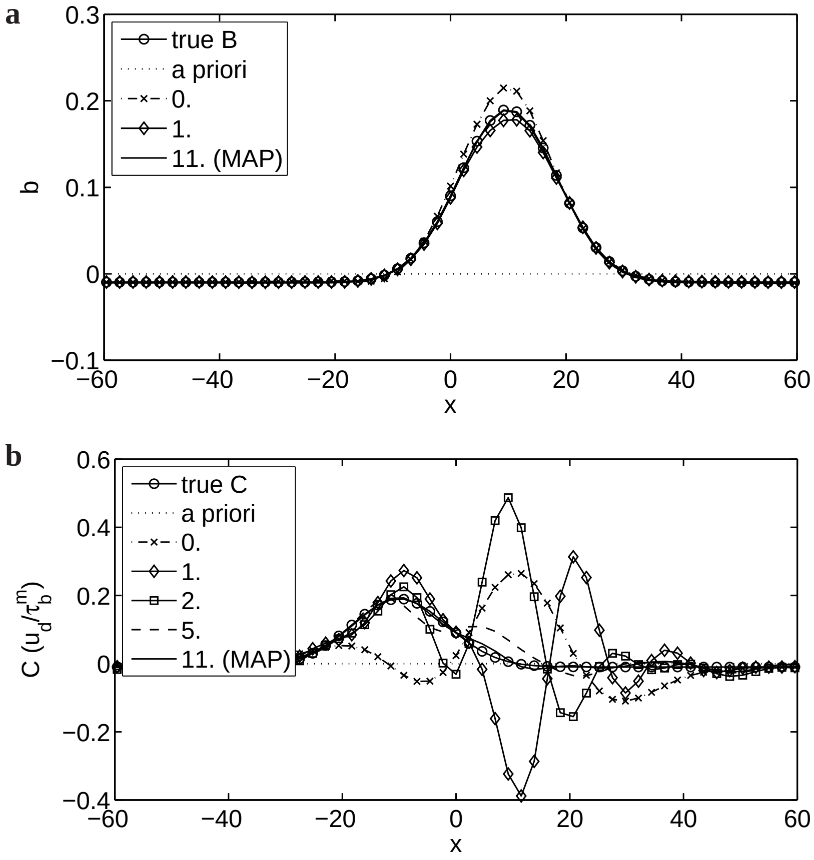

Figure 5.14: Inferred (a) bed topography and (b) basal slipperiness distributions for nonlinear rheology and perturbation amplitudes of 0.2. $\alpha = 0.25°$, $C^{(0)} = 200$, $n = 3$ and $\tau_0 = 0.3$. Note superimposing of MAP line with true bedrock topography in panel (a).

The combination of this feature with a slightly stronger $\mathcal{B}$ perturbation at $x \approx 10$ ice thicknesses leads to higher horizontal surface velocities than measured in the domain $-10 < x < 20$ (Figure 5.15b, dash-dotted lines with crosses). At iteration 1, the $\mathcal{C}$ estimate is more or less reversed; its amplitude becomes positive at $x \approx -10$, respectively negative at $x \approx 10$ (solid line with diamonds). The amplitude of the $\mathcal{B}$ perturbation is reduced. This time, the horizontal surface velocities predicted for these model parameters by the forward finite-element model are smaller than those of the measurements for $x < -15$. This is again compensated for at iteration 2 with an inverse higher and shallower peak at $x = 10$. This oscillating behavior disappears at iteration 3.

As compared with the non-linear inversion of surface data generated for the same

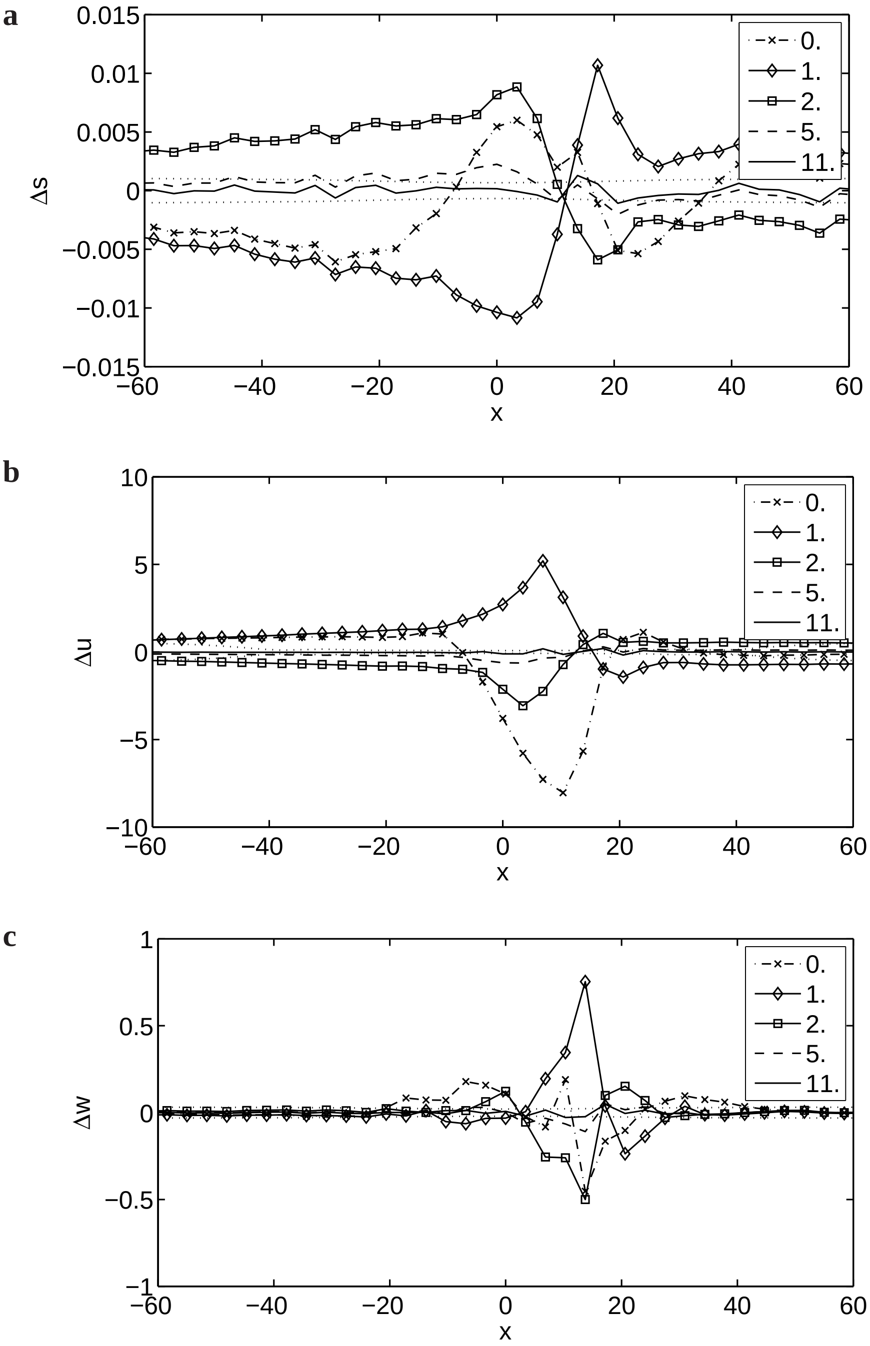

Figure 5.15: Residuals between observations and FE-model predictions for (a) surface topography, (b) horizontal and (c) vertical velocity. The dotted lines show the standard deviation (square roots of the diagonal elements of the data covariance matrix).

Gaussian-peak disturbances but for linear rheology (Figure 5.8), we see that twice as many iterations are needed in order to fit the surface data up to the noise level.

Temperature-dependent ice rheology

Starting from the same basal disturbances as shown in Figure 5.12, the surface data used for the inversion presented in Figure 5.16 have been generated for the same forward model characteristics as described above (small amplitude perturbations, step perturbation; $h^{(0)}$ = 300 m, $\alpha = 1°$, $C^{(0)} = 40$, $\tau_0 = 0$ kPa), but for a temperature-dependent ice rheology. The ice temperature is -25° at the surface and 0° at the bottom. The temperature gradient is linear. The rate factor A is determined from a double exponential fit derived by Smith and Morland (1981). The surface-parallel deformational velocity amounts in this case to $u_d = 1.27$ m a^{-1}. As can be seen in Figure 5.16, even for a non-linear temperature-dependent ice rheology, the linear initial guess (dash-dotted lines with crosses) captures a step perturbation for both $\mathcal{B}$ and $\mathcal{C}$ perturbations (margins in Figure 5.16). The perturbation in basal topography is resolved by the first guess as accurately as it was for isothermal conditions (Figure 5.12a).

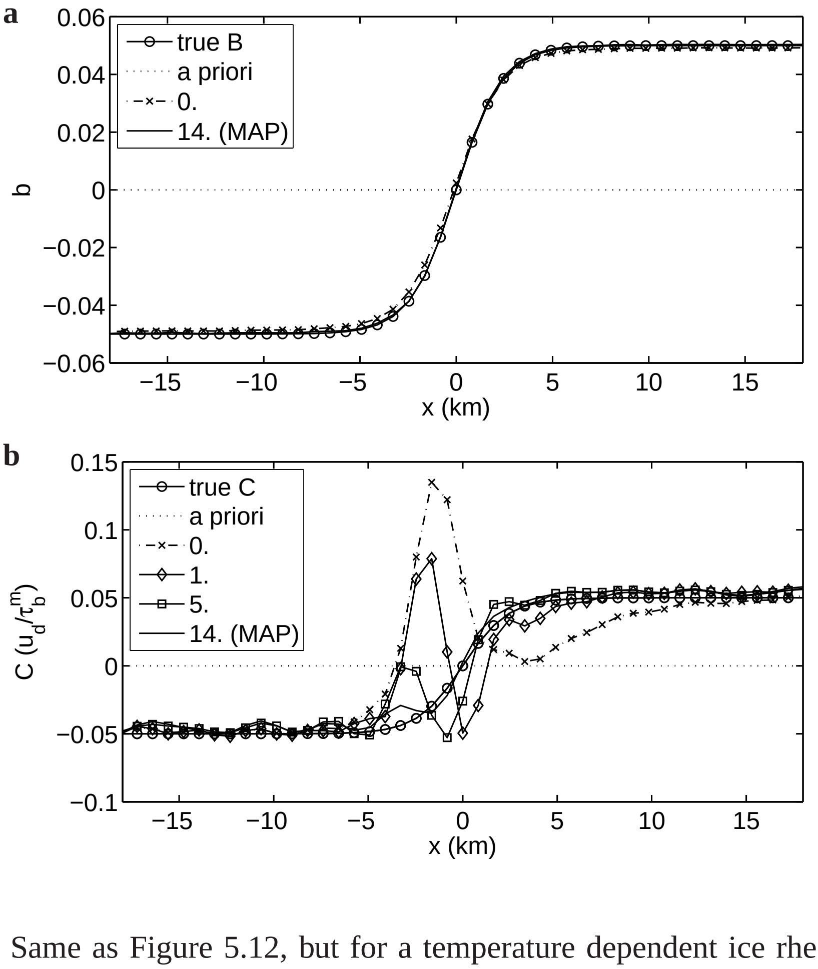

Figure 5.16: Same as Figure 5.12, but for a temperature dependent ice rheology. $n = 3, \tau_0 = 0$. The temperature profile is linear with surface temperature = -25° and bottom temperature 0°.

A substantial information loss around the center of the basal slipperiness perturbation can be observed for the first guess as compared with the isothermal case (Figure 5.12b). The

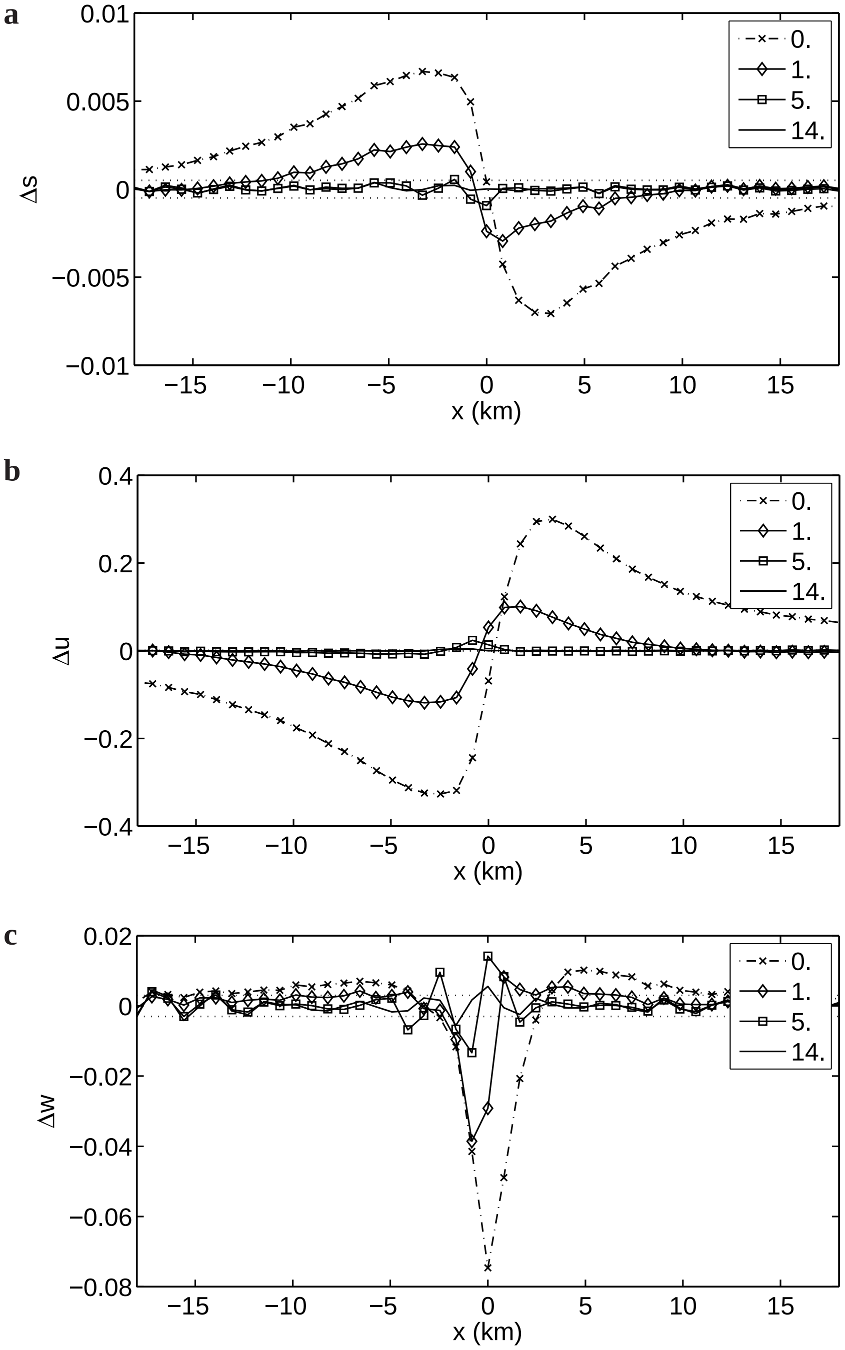

Figure 5.17: Residuals between observations and FE-model predictions for (a) surface topography, (b) horizontal and (c) vertical velocity for two iterations. The dotted lines show the standard deviation.

maximum a posteriori model has been computed with 14 iterations (solid lines in Figure 5.16). In contrast to Figure 5.14, the estimates converge towards the solution without oscillations and the residuals (Figure 5.17) diminish continuously toward the noise-level. About 4 times as many iterations are needed as compared with the corresponding isothermal case to fit the observed data up to the noise level. Still, the MAP model estimates are as good as the corresponding estimates for isothermal conditions. This is an encouraging result for the application of this inverse procedure on real ice streams as long as the forward model characteristics are accurately known.

Sliding Law Exponent

As stated above, we use a Weertman type sliding law, which relates the basal shear stress τ_b to the basal sliding velocity u_b, $u_b = C(x)\tau_b^m$. Observations suggest that the rheology of till under some ice streams on the Siple Coast, West Antarctica, may be characterized by high values of the sliding law exponent m (Kamb, 2001; Tulaczyk et al., 2000a,b). It is hence important to investigate the influence of the sliding law exponent on the proposed inverse method. The surface data were computed for Gaussian peak distributions with perturbation amplitudes of 5%. The sliding law exponent $m = 3$, $\tau_0 = 10$ kPa, the mean ice thickness $h^{(0)} = 1000$ m, the surface slope $\alpha = 0.2°$, the deformational surface velocity $u_d = 4.03$ and the slip ratio $C^{(0)} = 200$. The surface observations have been interpolated with BLUE. Figure 5.18 shows the inferred bed topography and basal slipperiness distributions. The corresponding residuals are shown in Figure 5.19.

The maximum a posteriori estimates have been computed with 10 iterations (solid lines) and reproduces well the prescribed basal disturbances. This demonstrates that the approximation of the forward model derivatives by linear transfer functions for higher values of the sliding law exponent still gives remarkably accurate estimates of the basal perturbations.

Sparse surface observations

We now turn to the problem of estimating the basal properties of glacier when only sparse observations are available. To this end we rejected randomly 70% of the surface data generated with the forward numerical model for the same basal perturbations and model characteristics as described above (Section sliding law exponent), but for $m = 1$. The remaining surface data points were corrupted by uncorrelated Gaussian-noise and subsequently interpolated with BLUE. Hence, the number of discretization points for inversion is the same as in all previous examples. As can be seen in Figure 5.21 the variances of the individual elements of $\boldsymbol{s}$, $\boldsymbol{u}$ and $\boldsymbol{w}$ (diagonal elements of the data covariance matrices) are larger than in Figure 5.19 and vary along x depending on the number of observations available in the neighborhood. Thus, in regions where the standard deviation is larger than the residuals between observations and FE-model prediction, no more information can be gained from the observations for inversion. The optimization of the objective function has been stopped after 6 iterations. The inferred basal properties capture the basal disturbances particularly well between $-20 < x > 20$ km. This zone is characterized by the smallest variances of the surface observations. The MAP predicts on the other hand a negative bump in basal topography at $x = -40$ km and a positive bump in basal

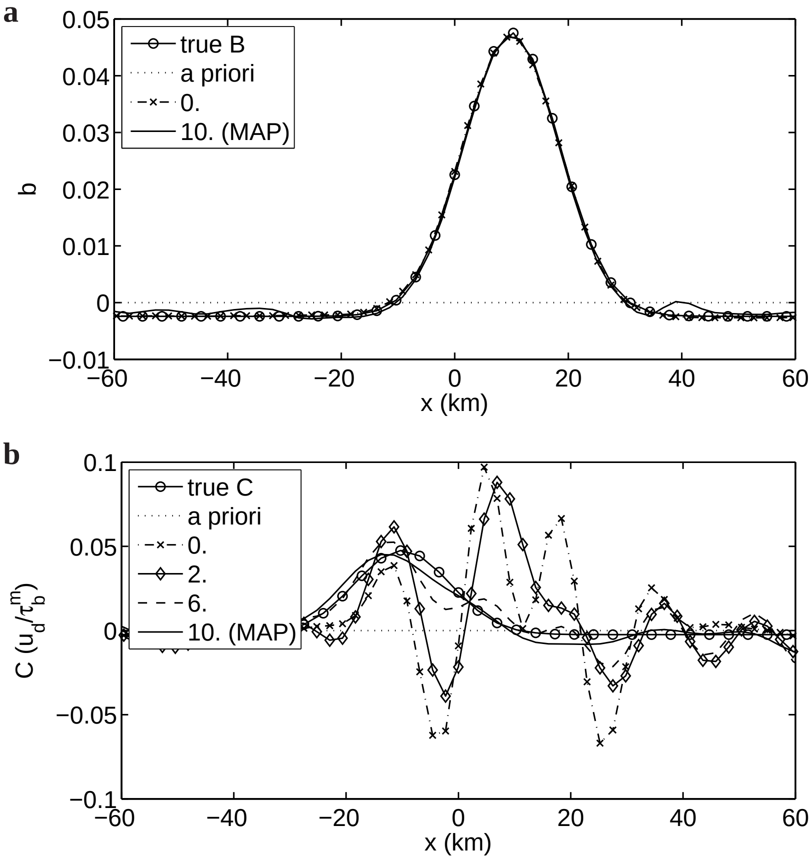

Figure 5.18: Inferred (a) bed topography and (b) basal slipperiness distributions for a basal sliding exponent m of 3.

slipperiness distribution at $x = -35$ km. Both features are not present in the prescribed basal disturbances, but are as probable as any other feature, since no information can be obtained from the surface observations in these regions. This case study show that regular and dense surface measurements are needed in order to perform an accurate retrieval.

5.4.3 Modeling errors

Until now, the model characteristics entering the forward numerical model for generation of the synthetic surface data were the same as those used for inversion (e.g. mean ice thickness $h^{(0)}$, slip ratio $C^{(0)}$). The artificial noise introduced in the data and the interpolation of the surface fields were the only sources of errors. As the success and accuracy of any retrieval depend on the forward model and on the forward model characteristics, we now investigate the effects of modeling errors on the estimates. Only errors in the forward model characteristics will be considered. The physics entering the forward model will be kept unchanged. By forward model characteristics we mean surface slope α , mean ice thickness $h^{(0)}$, slip ratio $C^{(0)}$, mean surface-parallel deformational velocity u_d and temperature distribution in the ice. For real data, the forward model characteristics are not known *a priori* but have to be estimated from the surface observations or from other sources of informations such as radar or ice temperature measurements. In the following, we assume that both surface slope α and mean ice thickness $h^{(0)}$ are known. This

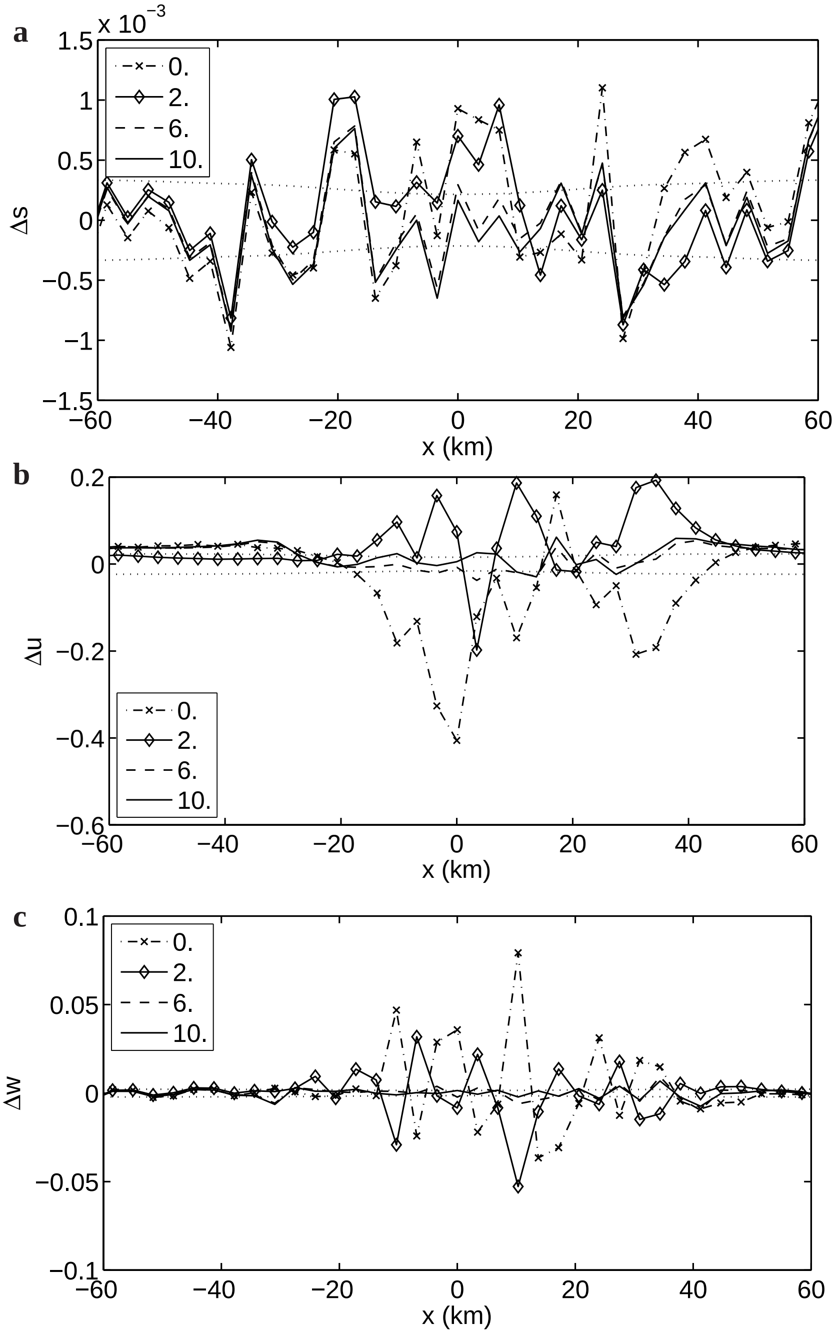

Figure 5.19: Residuals between observations and FE-model predictions for (a) surface topography, (b) horizontal and (c) vertical velocity for two iterations. The dotted lines show the standard deviation.

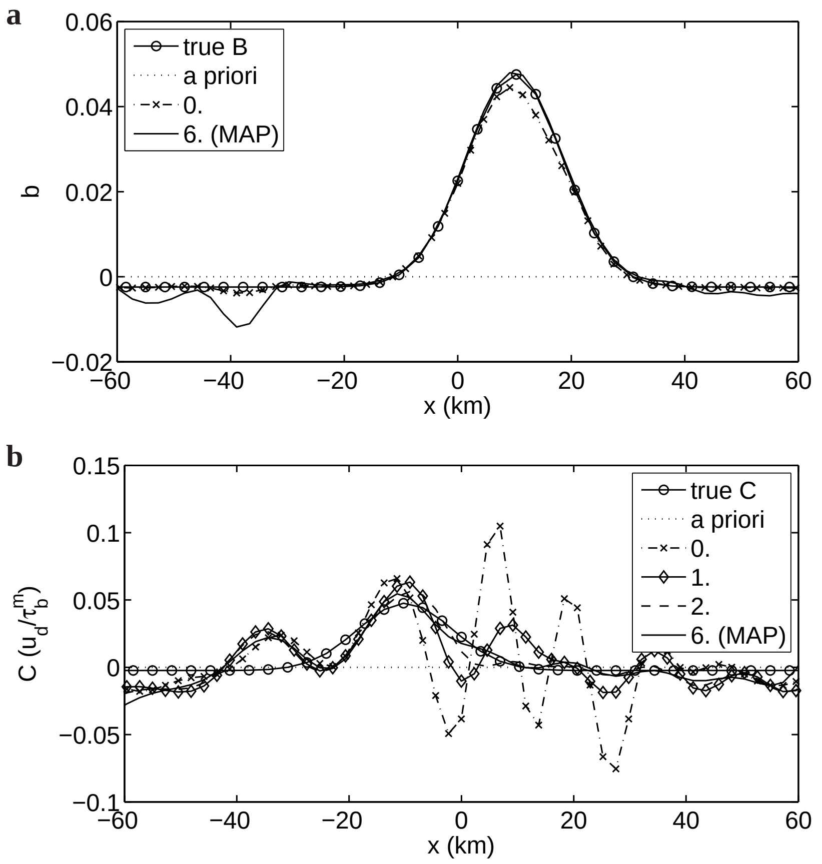

Figure 5.20: Same as Figure 5.18, but for $m = 1$. 70 $\%$ of the surface data generated with the forward numerical model have been rejected randomly before interpolation and inversion.

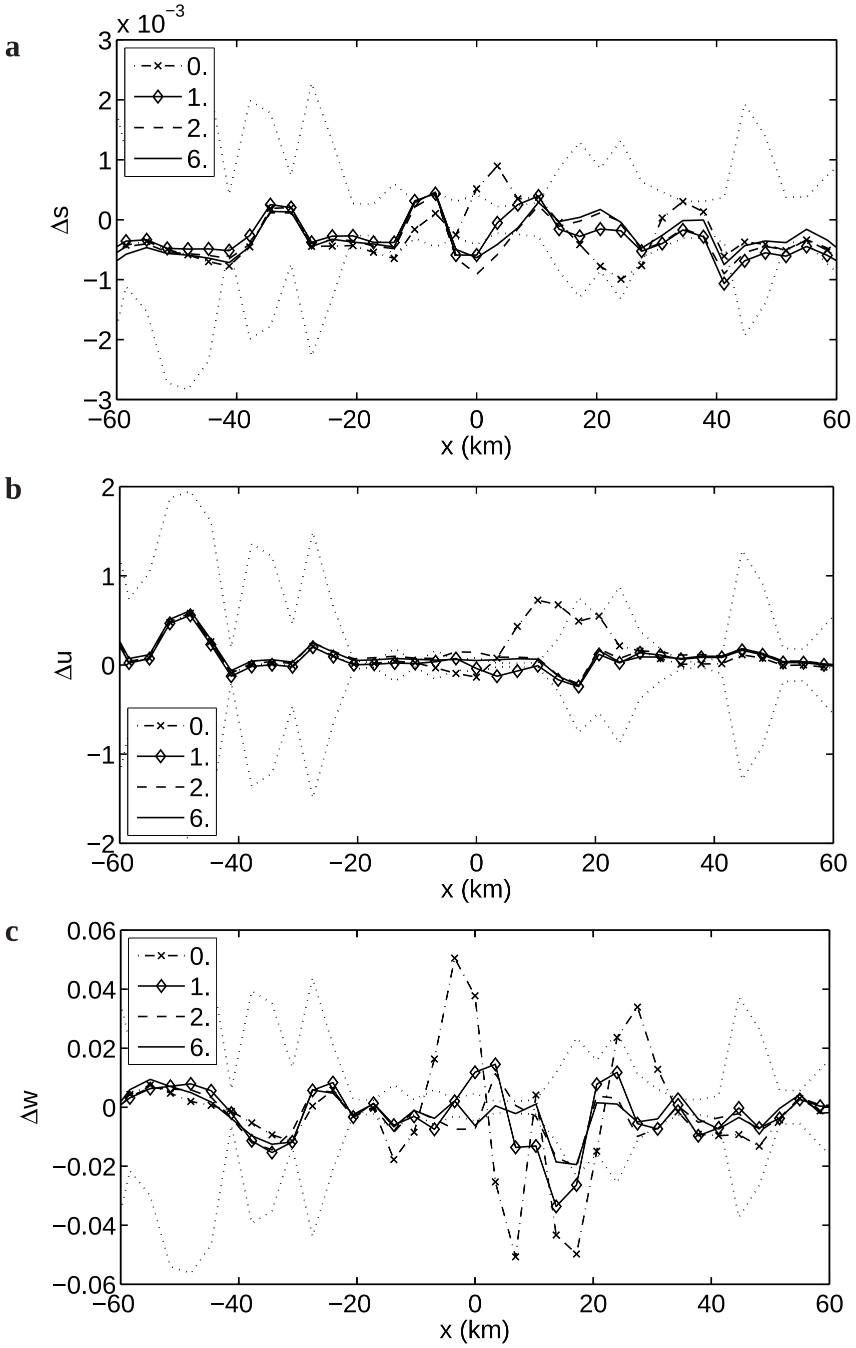

Figure 5.21: Residuals between observations and FE-model predictions for (a) surface topography, (b) horizontal and (c) vertical velocity for two iterations. The dotted lines show the standard deviation.

will generally be the case in areas where such an inversion procedure might be applied. The slip ratio $C^{(0)}$ will have to be estimated from the measured mean longitudinal surface velocity and from the estimated contribution of deformational velocity u_d to the surface velocity. Since u_d is itself sensitive to the chosen value of the rheological parameters A, n, τ_0 and to the temperature distribution in the ice, there will generally exist a range of plausible values for u_d and $C^{(0)}$ that equally describes the surface observations. For now, only the temperature profile will be estimated, the same rheological parameters as used for the generation of the synthetic surface data will be used. We expect to be able to isolate the nearest to the true model characteristics by looking at the value of the maximum a posteriori solution at the minimum.

Let us consider the synthetic surface data generated for step perturbations with linear temperature profile increasing from -25° at the surface to 0° at the bottom (see the case for temperature-dependent ice rheology in Subsection 5.4.2). The true deformational velocity amounts to 1.27 m a^{-1} and the corresponding slip ratio is $C^{(0)} = 40$. As the temperature profile is not known, we start by estimating a linear temperature profile with surface temperature -20° and bottom temperature 0°. The mean surface deformational velocity u_d is estimated to be 1.45 m a^{-1} using the standard temperature-dependent flow law for ice. The slip ratio is then estimated from the mean longitudinal surface speed to $C^{(0)} = 35$. These estimated values of the forward model characteristics are subsequently introduced in the inverse calculations as well as in the forward finite-element model.

Figure 5.22 shows a comparison of the maximum a posteriori model as obtained with the true model characteristics and with the modeling errors. The true basal properties are also shown for comparison. In both cases, the basal topography perturbation is completely recovered. The basal slipperiness perturbation is, on the other hand, resolved less accurately for the case with the wrong estimated model characteristics than with the true ones. The inversion procedure has been stopped after 7 iterations for the wrong model and after 14 iterations for the true one. The value of the maximum a posteriori solution $J(\hat{\boldsymbol{m}})$ at the minimum for the case with the wrong model characteristics is 8 times bigger than for the true model and also about 8 times bigger than the theoretically expected value of $J(\hat{\boldsymbol{m}}) = 3 \times N$ at the minimum. Thus, if we were to select a forward model characteristics set best describing the observations, we would choose the one for which the value of the maximum a posteriori solution $J(\hat{\boldsymbol{m}})$ is closest to the theoretical one. The MAP solution for the wrong model characteristics would obviously be discarded.

5.5 Conclusions

Using a non-linear Bayesian inference approach applied to synthetic surface data generated with a finite-element numerical model, we have shown that the inverse method gives remarkably accurate estimates of the basal perturbations. We could demonstrate that the first order derivatives of the forward model entering the Gauss-Newton retrieval method can be adequately approximated by linear transfer functions (Gudmundsson, 2003) even when the relationship between basal and surface properties is nonlinear. This approximation is attractive as it greatly enhances the numerical efficiency of the method by sparing the time-consuming evaluation of numerical derivatives. The proposed method is capable of dealing with both non-linear finite-amplitude effects and rheological nonlinearities.

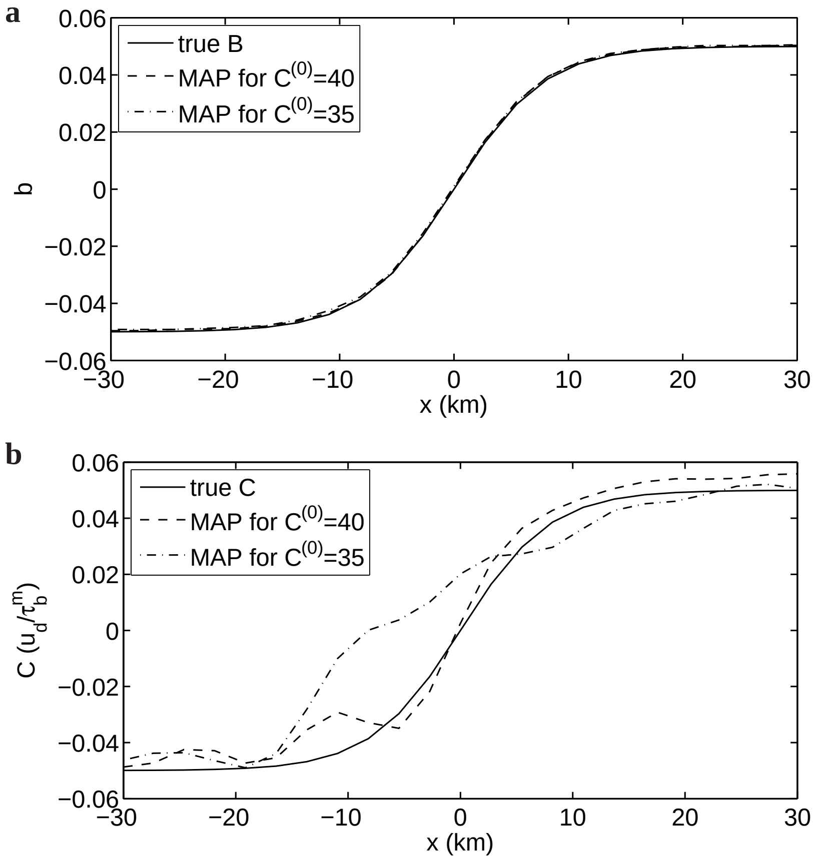

Figure 5.22: Comparison between MAP (a) bed topography and (b) basal slipperiness as obtained with the true model characteristics ($u_d = 1.27$ m a^{-1}, $C^{(0)} = 40$; dashed lines) and with the wrong estimated model characteristics ($u_d = 1.45$ m a^{-1}, $C^{(0)} = 35$; dashed-dotted lines). The true basal perturbations are also shown for comparison (solid lines).

In all case studies considered, the inversion procedure converged quickly and to the correct solution. Examples of inversion of noise-degraded surface data for linear rheology and small amplitude perturbations show that although a single linear inverse step is sufficient to predict the basal properties accurately, the Gauss-Newton method nevertheless improves the estimates. With increasing amplitudes of the perturbations and for nonlinear rheology, the results show that a single linear inverse step does not provide accurate estimates of the basal perturbations, particularly of the basal slipperiness perturbation. Bedrock perturbations required generally only two to three iterations to be fully recovered, whereas perturbations in basal slipperiness needed up to 15 iterations to converge. This difference in convergence speed between the two types of basal disturbances considered can be explained by looking at the averaging kernel, i.e. the sensitivity of the retrieval to the true perturbations. This shows that information about the basal slipperiness is transmitted at longer wavelengths than bedrock disturbances and that the information transfer is weaker than for topographic perturbations. Rheological nonlinearities require generally more iterations to convergence than non-linear finite-amplitude effects.

We did not investigate the sensitivity of the maximum a posteriori solution to the initial guess used in the optimization of the objective function $J(\boldsymbol{m})$. In nonlinear optimization, there might be multiple minima and the solution might converge to the local minimum closest to the initial guess.

By applying the procedure to real data, modeling errors will have to be inevitably considered. We showed that amongst a range of plausible model characteristics entering the forward model, it is possible to select those approaching best to the true parameters as long as the model physics remains unchanged. We did not investigate the implications of incomplete or incorrect model physics. Modeling errors such as incomplete or incorrect model physics might also be accounted for by considering in the objective function a probability density function describing the modeling uncertainties (Tarantola, 2005).

Chapter 6

Estimating glacier basal properties from surface measurements: a non-linear inversion approach applied to the Rutford Ice Stream, West Antarctica

This chapter is a draft of a paper to be submitted under the same title in the Journal of Geophysical Research, with co-author G. H Gudmundsson from the British Antarctic Survey, Cambridge, UK.

Abstract

We introduce a non-linear Bayesian inversion approach (e.g., Tarantola, 2005; Rodgers, 2000) to estimate the basal properties, that is bedrock topography and basal slipperiness, along a flow line of Rutford ice stream from observations of surface topography and surface velocities. The forward function describing the relationship between the basal properties and the observations is solved numerically with a plane-strain finite-element model. As there exist no explicit solution for the inversion of this non-linear forward function, the solution of the inverse problem is sought numerically and iteratively by using a nonlinear Gauss-Newton procedure. The first order forward model derivatives needed for inversion are approximated by analytical linear transfer functions (Gudmundsson, 2003). This approximation is attractive as it greatly enhances the numerical efficiency of the method by sparing the time-consuming evaluation of the numerical derivatives (Chapter 5 in this thesis; Raymond and Gudmundsson (2007)).

Inversions performed with synthetic data showed that the inversion procedure behaves correctly and converges to the correct solution. The basal properties we compute for Rutford ice stream are consistent both with the surface observations and the radar measurements of bedrock topography.

6.1 Introduction

Ice streams of the West Antarctic Ice Sheet exhibit high flow velocities despite small gravitational driving stresses (Whillans et al., 2001). Several studies have shown that these high velocities are enabled by an efficient basal lubrication (e.g., Alley et al., 1986; Blankenship et al., 1986; Kamb, 2001). In many cases, extensive and fine-grained tills contribute to the extreme lubrication (Alley et al., 1987). In this paper, we introduce a nonlinear Bayesian inversion approach to estimate the basal properties from surface data along a flow line under Rutford Ice Stream, West Antarctica. Available data consists of recently acquired Global Positioning System (GPS) observations as well as airborne radar data combined with velocities observations from Frolich et al. (1987). Rutford ice stream flows southeast into the Ronne Ice Shelf. It is bounded on its west flank by the Ellsworth Mountains and on its east by the Fletcher Promontory and in this sense it shares both the attribute of an ice stream and of an outlet glacier. It varies in width from 20 to 30 km and is over 2000 m thick along most of its length (Doake et al., 2001).

The proposed inversion method uses observations of surface elevations and surface velocities to infer both bedrock topography and basal lubrication. In Bayesian inference, probability is interpreted as a measure of knowledge and the solution to the inverse problem is a probability distribution for the model parameters, i.e the basal properties we seek to estimate. Any information about the basal conditions available prior to the measurements may be incorporated into the solution as a prior probability density function. Bayes theorem then allows us to combine this prior distribution with the measurements to produce a posterior probability density function for the quantities we wish to retrieve.

The forward model describing our understanding of the physics of the relationship between basal and surface properties is a numerical finite-element model for ice stream flow including all terms of the momentum balance equations. This model allows us to calculate the transient evolution of the free surface.

The structure of the paper is as follows. We start by describing the forward ice stream model in Section 6.2. We then introduce the non-linear Bayesian inference method in Section 6.3 and show results for synthetic data in Section 6.4. The inversion results for Rutford Ice Stream are presented in Section 6.5, followed by a discussion.

6.2 Forward Ice Stream Model

We use a commercial finite-element program MARC to model the ice dynamics along the flow line on Rutford Ice Stream shown in Figure 6.7. The forward model is two-dimensional and plane-strain. Four-nodes, isoparametric, quadrilateral Hermann elements are used. A mixed Lagrangian-Eulerian approach is employed in determining the position of the steady-state surface (Leysinger Vieli and Gudmundsson, 2004). The coordinates are (x, z), where x is taken in the direction of the flow line and z is the vertical. The surface and the bed are given by $z = s(x, t)$, $z = b(x)$, respectively, and t represents time. u denotes the horizontal velocity and w the vertical velocity.

The numerical model solves the full force-balance equations for which acceleration terms are neglected and the mass-conservation equation for incompressible ice. These equations read $\sigma_{ij,j} = -\rho g_i$ and $v_{i,i} = 0$, respectively, where σ_{ij} are the components of the

Cauchy-stress tensor, ρ is the ice density, g the acceleration due to gravity and v_i are the components of the velocity vector. The glacier geometry is constrained by surface and bed topography measurements. The constitutive law is Glen's flow law, extended following Hutter (1983) with a linear term to avoid the singularity in viscosity as the deviatoric stress goes to zero

$$\dot{\epsilon}_{ij} = A(\tau^{n-1} + {\tau_0}^{n-1})\sigma_{ij}^{(d)}. \tag{6.1}$$

In this equation, A is the rate factor, n the stress exponent, $\dot{\epsilon}_{ij}$, $\sigma_{ij}^{(d)}$ and τ are the strain rate, the deviatoric stress tensors and the effective shear stress, respectively. The parameter τ_0 is the crossover stress at which the linear and exponential terms contribute equally to the total strain rate. In this study, $n = 3$ and the rate factor $A = A_0 B(T)$ is temperature dependent. The rate factor is expressed as the product of a constant rate factor A_0 at a reference temperature and a parameter $B(T)$ describing the temperature dependence. The parameter $B(T)$ follows a double exponential fit derived by Smith and Morland (1981)

$$B(T) = 0.9316\exp(0.32769T) + 0.0686\exp(0.07205T), \quad T \geq -7.65°C, \tag{6.2}$$

$$B(T) = 0.7242\exp(0.69784T) + 0.3438\exp(0.14747T), \quad T \leq -7.65°C, \tag{6.3}$$

where T is the Celsius temperature. The temperature profile is assumed to increase linearly from a mean surface temperature of $T_s = -25$ ° C to $T_b = 0°$ C at the bed.

6.2.1 Boundary Conditions

At the upstream and downstream model ends, velocities are prescribed. Along the bed, we prescribe a sliding relation of the form $u_b = C(x)\tau_b^m$, which relates the basal shear stress τ_b to the basal sliding velocity u_b. $C(x)$ is the sliding coefficient and m the sliding law exponent. The sliding law exponent is $m = 1$ in this study. Basal sliding is introduced in the numerical model by adding a uniform thin layer with the right viscosity to give a surface-parallel velocity at its top equal to the required sliding velocity.

The ice surface is stress free and evolves with time according to the kinematic boundary condition. The kinematic boundary condition reads

$$s_t + u_s s_x - w_s = \dot{b}(x), \tag{6.4}$$

where $s(x,t)$ describes the surface elevation, t is the time, and u_s and w_s are the horizontal and vertical surface velocity, respectively and $\dot{b}(x)$ is the accumulation rate function.

6.2.2 Parameterization of the Shear Margins

Several studies of West Antarctic ice streams indicate that most of the resistance to ice stream flow originate at the bed and at the lateral margins (Echelmeyer et al., 1994; Whillans et al., 2001, e.g). In our FE two-dimensional plane-strain model the lateral shear cannot be physically considered. It will be parameterized based on the theory by Van der Veen and Whillans (1996) for force balance in ice streams. In their theory, the force balance in the flow line direction, integrated in the vertical and lateral directions, reads

$$-2\frac{\partial h\sigma_{xx}^{(d)}}{\partial x} + \frac{h}{W}\tau_l + \tau_b = -\rho g h\frac{\partial s}{\partial x}, \tag{6.5}$$

where h and W are the ice thickness and the ice stream width, respectively. $\sigma_{xx}^{(d)}$ is the deviatoric part of the longitudinal stress, τ_b is the basal shear stress and τ_l is the lateral shear stress expressed as

$$\tau_l = \left(\frac{2u_c}{AW}\right)^{\frac{1}{n}}, \tag{6.6}$$

with n and A the exponent and the rate factor of Glen's flow law and u_c the velocity in x-direction in the center of the ice stream. In our two-dimensional model, the first two terms of the left-hand side of (6.5) (variation of longitudinal stress and basal shear) balance the term on the right-hand side (body force). Since our model does not account for shear effect, we rewrite (6.5) as

$$-2\frac{\partial h\sigma_{xx}^{(d)}}{\partial x} + \tau_b = -\rho^* g^* h\frac{\partial s}{\partial x}, \tag{6.7}$$

where $\rho^* g^*$ plays the role of an effective body force defined as

$$\rho^* g^* = \rho g + \frac{1}{W}\left(\frac{2u_c}{AW}\right)^{\frac{1}{n}}\left[\frac{\partial s}{\partial x}\right]^{-1}. \tag{6.8}$$

Hence, ρg is reduced by the effect of the shear margins ($\frac{\partial s}{\partial x}$ is negative). In the finite-element model, the prescribed body force ρg is replaced by the effective body force $\rho^* g^*$. The value of the centerline velocity u_c in (6.8) is determined from velocity measurements on Rutford Ice Stream.

6.3 Non-linear Bayesian Inversion

Notation

Vectors will be denoted by bold face italic letters (e.g. $\boldsymbol{d}$) and matrices by bold uppercase letters (e.g. $\mathbf{C}$). The notation $P(\boldsymbol{m}|\boldsymbol{d})$ indicates the multidimensional probability density function (*pdf*) of the vector $\boldsymbol{m}$ conditional on $\boldsymbol{d}$. In $\boldsymbol{d} = \boldsymbol{g}(\boldsymbol{m})$, the forward function $\boldsymbol{g}$ is vector-valued and returns the vector $\boldsymbol{d}$ for a given value of the vector $\boldsymbol{m}$.

6.3.1 Formulation of the problem

To estimate the basal properties under Rutford Ice Stream, we perform a nonlinear Bayesian inverse calculation consisting in determining $P(\boldsymbol{m}|\boldsymbol{d})$, the probability density for the model parameters $\boldsymbol{m}$, i.e the basal properties, conditional on the surface measurements $\boldsymbol{d}$. This probability distribution is termed the a posteriori distribution and can be written using Bayes'rule as

$$P(\boldsymbol{m}|(\boldsymbol{d}, \boldsymbol{m}_{\text{prior}})) = \frac{P(\boldsymbol{m}|\boldsymbol{m}_{\text{prior}})P(\boldsymbol{d}|\boldsymbol{m})}{P(\boldsymbol{d})}. \tag{6.9}$$

The denominator of Eq. 6.9 can be shown to be a normalizing factor and will therefore be ignored. Hence, the a posterior distribution reduces to the product of two terms, i.e the likelihood function and the a priori distribution. The likelihood function $P(\boldsymbol{d}|\boldsymbol{m})$ measures the probability of observing the data $\boldsymbol{d}$ if the model parameters were $\boldsymbol{m}$, while the a priori probability density $P(\boldsymbol{m}|\boldsymbol{m}_{\mathbf{prior}})$ incorporates information that is known independently of the data.

We assume in the following that both the measurements errors and the prior estimate can be described by multidimensional Gaussian distributions, i.e the likelihood function is given by

$$P(\boldsymbol{d}|\boldsymbol{m}) = \exp\left[-\frac{1}{2}(\boldsymbol{d}-\boldsymbol{g}(\boldsymbol{m}))^T \mathbf{C_D}^{-1}(\boldsymbol{d}-\boldsymbol{g}(\boldsymbol{m}))\right], \tag{6.10}$$

while the a priori probability distribution is given by

$$P(\boldsymbol{m}|\boldsymbol{m}_{\text{prior}}) = \exp\left[-\frac{1}{2}(\boldsymbol{m}-\boldsymbol{m}_{\text{prior}})^T \mathbf{C_M}^{-1}(\boldsymbol{m}-\boldsymbol{m}_{\text{prior}})\right]. \tag{6.11}$$

$\boldsymbol{g}(\boldsymbol{m})$ represents the numerical forward ice stream model that calculates the surface components given a discretized model $\boldsymbol{m} = [\boldsymbol{b}\ \boldsymbol{C}]^T$, with $\boldsymbol{b}$ and $\boldsymbol{C}$ the basal topography and basal slipperiness vectors, respectively. The observed surface data $\boldsymbol{d} = [\boldsymbol{s}\ \boldsymbol{u}\ \boldsymbol{w}]^T$ consists of the surface topography $\boldsymbol{s}$, horizontal surface velocity $\boldsymbol{u}$ and vertical surface velocity $\boldsymbol{w}$. $\mathbf{C_D}$ is the data covariance matrix, $\mathbf{C_M}$ is the model covariance matrix and $\boldsymbol{m}_{\text{prior}}$ the center of the a priori probability density.

Taking twice the minus of the logarithm of the product of Eq. 6.10 and Eq. 6.11, defines the following cost function $J(\boldsymbol{m}) = -2\ln P(\boldsymbol{m}|(\boldsymbol{d},\boldsymbol{m}_{\text{prior}}))$

$$J(\boldsymbol{m}) = [(\boldsymbol{d}-\boldsymbol{g}(\boldsymbol{m}))^T \mathbf{C_D}^{-1}(\boldsymbol{d}-\boldsymbol{g}(\boldsymbol{m})) + (\boldsymbol{m}-\boldsymbol{m}_{\text{prior}})^T \mathbf{C_M}^{-1}(\boldsymbol{m}-\boldsymbol{m}_{\text{prior}})] \tag{6.12}$$

from which we single out the model with the largest probability, referred to as the maximum a posteriori model (MAP). The maximum a posteriori model is derived from an iterative optimization process of the objective function (6.12) that minimizes $J(\boldsymbol{m})$.

We have used a nonlinear Gauss-Newton method in the minimization. The Fréchet derivatives, which are the first derivatives of the forward model with respect to the model parameters, are approximated with analytical transfer functions (Gudmundsson, 2003). These transfer functions are valid for linear rheology and small amplitude variations of the basal disturbances. They are complex functions of the wavenumber vector $\boldsymbol{k}$ and of a set of zeroth-order parameter that describe the mean state of the glacier, i.e surface slope α, slip ratio $C^{(0)}$, mean ice thickness $h^{(0)}$ and mean deformational surface velocity u_d. This approximation is very convenient since it avoids having to evaluate the first derivatives of the forward model numerically. This greatly enhances the numerical efficiency of the method. Raymond and Gudmundsson (2007) show that this approximation is suitable for large amplitudes of the basal perturbations as well as for non-linear ice rheology and non-linear sliding law.

The use of the analytical transfer functions for the Fréchet derivatives involves respecting the geometrical assumptions for which they are valid. In Gudmundsson's (2003) theory, derived using perturbation methods, the glacier geometry is a parallel-sided slab of thickness $h^{(0)}$, with slope α, on which small perturbations in basal properties are superimposed. The Rutford ice stream geometry cannot be approximated to a parallel-sided slab at global scale. At small scale, however, the ice stream can be considered as a parallel-sided slab for which a set of zeroth-order parameter describing the mean state of the glacier can be determined. By small scale we mean here approximately 20 ice thicknesses. Hence, the minimization of the objective function (6.12) is repeated for each point along the profile.

To use the transfer function formulation, the minimization of the objective function (6.12) has to be done in Fourier space. Thus, all vector components entering the objective function (6.12), i.e surface fields, a priori and covariance matrices, are transformed into frequency space. The transpose ^{T} is substituted with the Hermitian transpose ^{H}. The covariances matrices for the data and model parameters $\mathbf{C_D}$ and $\mathbf{C_M}$ are sent to the Fourier space by the relation $\mathbf{FCF^H}$ where $\mathbf{F}$ is the discrete Fourier transform matrix, $\mathbf{C}$ the matrix to be transformed and ^{H} the Hermitian transpose. The transformation of the above components into frequency space requires them to be first interpolated onto an equidistant grid. This gives rise to interpolation errors and some spatial correlation between interpolated values, both of which can be estimated using geostatistical interpolation method.

The optimization of the objective function 6.12 starts with the a priori values for the model parameters $\boldsymbol{m}_{\text{prior}}$.

Inverse procedure

The different steps involved in the iterative optimization by which the objective function $J(\boldsymbol{m})$ is minimized, are:

i Define an a priori $\boldsymbol{m}_{\text{prior}}$ for the bedrock topography and basal slipperiness distribution to start the optimization of the objective function.

ii Calculate the steady-state surface response $\boldsymbol{g}(\boldsymbol{m}_i)$ for the given bedrock and the distribution of the basal slipperiness with the forward finite-element model. i indicates the i-th iterate with $\boldsymbol{m}_{i=0} = \boldsymbol{m}_{\text{prior}}$.

iii Test for convergence using (5.25). Once the stopping criterion is satisfied, stop the iteration procedure, else

iv Determine incremental corrections to the prior bedrock profile and distribution of the basal slipperiness by inversion. Return to step (ii)

6.3.2 Quantifiying uncertainties

Data Uncertainties

The covariance matrix for the noise in the data $\mathbf{C_D}$ defines the uncertainties in the data. The matrix $\mathbf{C_D}$ is a block diagonal matrix consisting of the matrices describing the uncertainties in the surface topography $\mathbf{C_s}$, horizontal velocity $\mathbf{C_u}$ and vertical velocity $\mathbf{C_w}$ along the main diagonal. The off-diagonal blocks are zero matrices, since no cross-correlation between the surface fields is considered. The elements along the main diagonal of the block matrices are the variances of the individual measurements about the mean of the multidimensional Gaussian probability and the off-diagonal elements show to what extent these individual measurements are correlated. The means of these probability densities are defined by the observed data $\boldsymbol{d}$.

$$\mathbf{C_D} = \begin{pmatrix} \mathbf{C_s} & \mathbf{0} & \mathbf{0} \\ \mathbf{0} & \mathbf{C_u} & \mathbf{0} \\ \mathbf{0} & \mathbf{0} & \mathbf{C_w} \end{pmatrix}. \qquad (6.13)$$

The covariance matrices for $\mathbf{C_s}$, $\mathbf{C_u}$ and $\mathbf{C_w}$ result from the geostatistical interpolation method of best linear unbiased estimator (BLUE) (Kitanidis, 1997) , where we follow the assumption that the measurement errors have a Gaussian distribution.

Uncertainties in the model parameters

The prior probability (6.11) is represented by a multidimensional Gaussian probability density, characterized by the mean $\boldsymbol{m}_{\text{prior}}$ and covariance matrix $\mathbf{C_M}$. The mean $\boldsymbol{m}_{\text{prior}}$ contains both a priori bed topography and basal slipperiness ($\boldsymbol{m}_{\text{prior}} = [\boldsymbol{b}_{\text{prior}}\ \boldsymbol{C}_{\text{prior}}]^T$). We describe in Section 6.5.2 how those priors are computed for the Rutford inversion.

The covariance matrix $\mathbf{C_M}$ is of block diagonal form and consists of the matrix $\mathbf{C_B}$ describing the uncertainties in the prior bedrock topography and $\mathbf{C_C}$ in the prior basal slipperiness along the main diagonal. No cross-correlation between bed topography and basal slipperiness is considered so that the off-diagonal blocks of $\mathbf{C_M}$ are zero matrices.

$$\mathbf{C_M} = \begin{pmatrix} \mathbf{C_B} & \mathbf{0} \\ \mathbf{0} & \mathbf{C_C} \end{pmatrix}. \qquad (6.14)$$

As a first approximation, the variances of the prior (diagonal elements of $\mathbf{C_B}$ and $\mathbf{C_C}$) about the mean $\boldsymbol{m}_{\text{prior}}$ are taken to be of constant values and the correlation between the individual points is assumed to decrease with the distance following a Gaussian distribution.

6.4 Inversions with synthetic data

As stated above, the inversion procedure applied to perturbations superimposed on a parallel sided slab has been tested thoroughly in Chapter 5. Here we test whether the inversion procedure modified for the case that the ice stream cannot be approximated to a parallel sided slab at global scale, still converges and to the correct solution. The synthetic surface data used for inversion are generated with the forward ice stream model described above. These surface data are corrupted with uncorrelated Gaussian noise to simulate measurement errors. The noisy data are taken to be the observed data in the inverse calculation. We present two examples of inversions with two different set of basal properties to illustrate the capabilities and limitations of the inverse procedure. In both cases, the initial surface topography of the finite-element model, used to start the forward calculations until steady-state, is obtained by applying a 40 km Lanczos filter (Emery and Thomson, 2001, p.533-539) to the measured surface topography along the flow line on Rutford Ice Stream. The Lanczos filter filters the data in frequency space by removing all frequencies greater than the cut-off frequency. The zeroth-order parameters entering the transfer function calculations, i.e slip ratio, surface slope, surface deformational velocity and ice thickness are determined from the finite-element model result for the prior $\boldsymbol{g}(\boldsymbol{m}_{\text{prior}})$ and filtered with a 40 km Lanczos filter, such that these mean values do not vary too fast along the flow line. The finite-element model length corresponds to the length of the selected flow line on Rutford Ice Stream. The finite-element mesh has a spatial resolution of 1 km in x-direction and 200 m in z-direction.

6.4.1 Simple geometry

The first inversion experiment uses a simplified bedrock geometry of that measured on Rutford Ice Stream. This choice is arbitrary and only designed to test whether the inversion procedure behaves correctly when there is a strong gradient in ice thickness and surface slope in flow direction. The synthetic bedrock topography and basal slipperiness distribution used to generate the synthetic surface data are obtained as follows. The bedrock topography is computed by applying a 100 km Lanczos filter to the measured bedrock topography along the flow line and by adding a sinusoidal perturbation of wavelength 40 km to the filtered data. The amplitude of the perturbation varies along the profile following a Gaussian distribution and amounts to a maximum of 10 $\%$ of the mean ice thickness in the middle. The resulting bedrock topography ($\boldsymbol{b}_{\text{true}}$) is shown in Figure 6.1a (solid line). The basal slipperiness distribution ($\boldsymbol{C}_{\text{true}}$) is chosen such as to produce horizontal surface velocities of the order of magnitude of those measured on Rutford ice stream. To that end, $\boldsymbol{C}_{\text{true}}$ was estimated from the basal shear stress $\boldsymbol{\tau}_b$ computed from the local ice thickness and surface slope and from the basal velocity on Rutford Ice Stream by the relation $\boldsymbol{C}_{\text{true}} = \boldsymbol{u}_b/\boldsymbol{\tau}_b$, where $\boldsymbol{u}_b$ is approximated with the measured horizontal surface velocity. A sinusoidal perturbation was also added on this distribution. The resulting basal slipperiness distribution can be seen in Figure 6.1b (solid line). The prior distribution $\boldsymbol{B}_{\text{prior}}$ and $\boldsymbol{C}_{\text{prior}}$ needed to start the optimization procedure consists of the true distributions without sinusoidal perturbations (dashed-dotted lines with crosses in Figure 6.1a and b). The zeroth-order parameter entering the transfer functions are shown in Figure 6.3. Starting from the prior distributions, 8 iterations have been needed to compute the maximum a posteriori solution (dashed line in Figure 6.1). The maximum a posteriori solution reproduces both bedrock topography and basal slipperiness distribution very well, except in the region $275 < x < 300$ km. The residuals between observations and finite-element predictions are presented in Figure 6.2 and show that the inverse procedure is capable of reducing the difference between measured and inferred data up to the noise level in the data (dotted lines in Figure 6.2).

6.4.2 Rutford bedrock topography

In this subsection, we use as synthetic bedrock topography the measured bedrock geometry along the selected flow line on Rutford Ice Stream. This permits to examine the capabilities of the inversion procedure when short-scale basal perturbations (of the order of 2-5 mean ice thicknesses) are present. The measured bedrock geometry was interpolated using BLUE to define the basal topography of the forward finite-element model. As

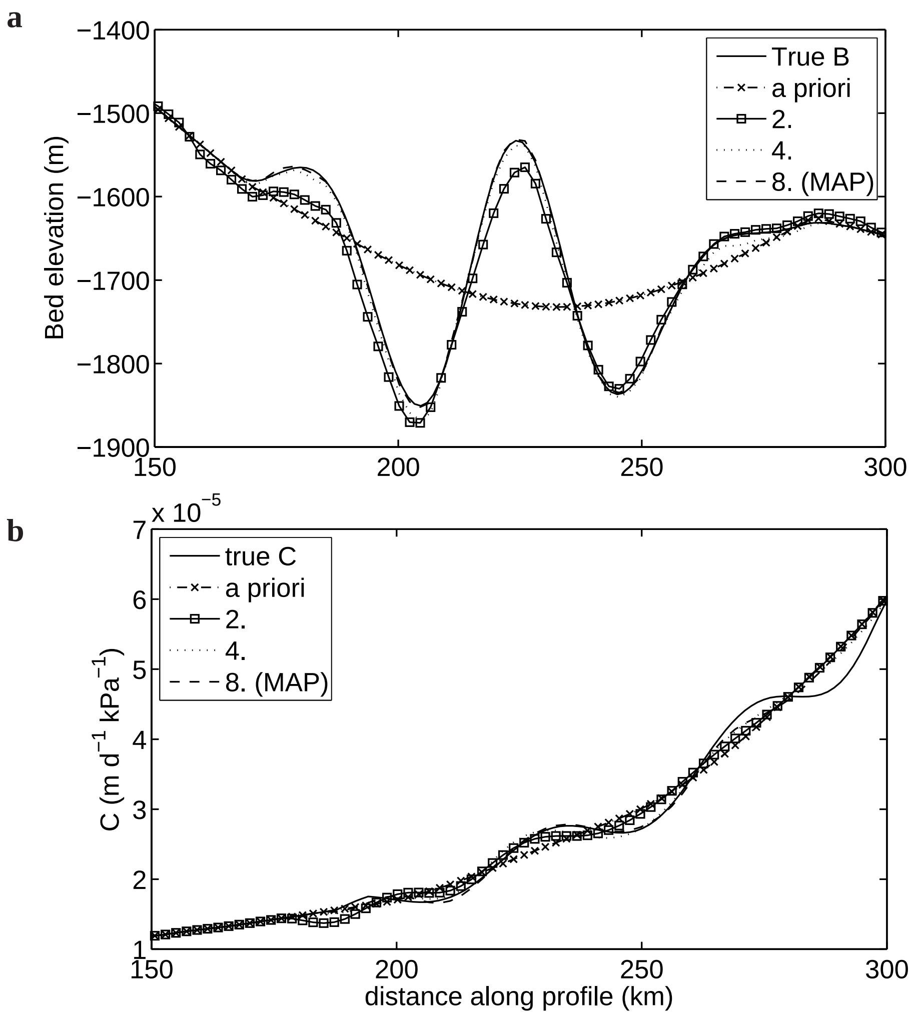

Figure 6.1: Estimated (a) bedrock topography and (b) basal slipperiness distribution from synthetic surface data generated with the finite-element model for the true distributions (solid lines). The dashed lines show the prior distributions used to start the optimization procedure. The maximum a posteriori solution (dashed lines (MAP)) has been reached after 8 iterations. The other lines show intermediate iteration results.

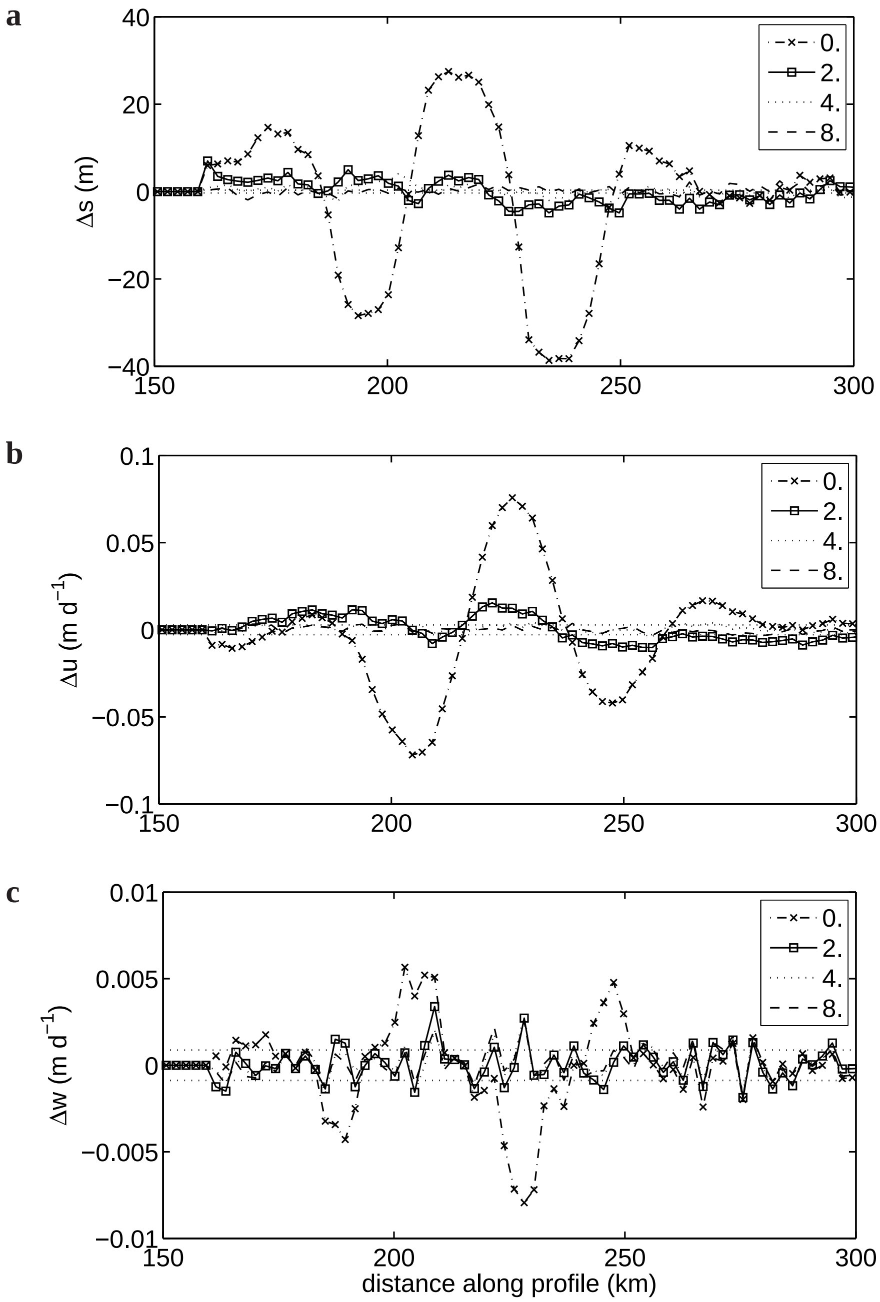

Figure 6.2: Residuals between observations and FE-model predictions for (a) surface topography, (b) horizontal and (c) vertical velocity. The dotted lines correspond to the square roots of the main diagonal of the data covariance matrix $\mathbf{C}_D$.

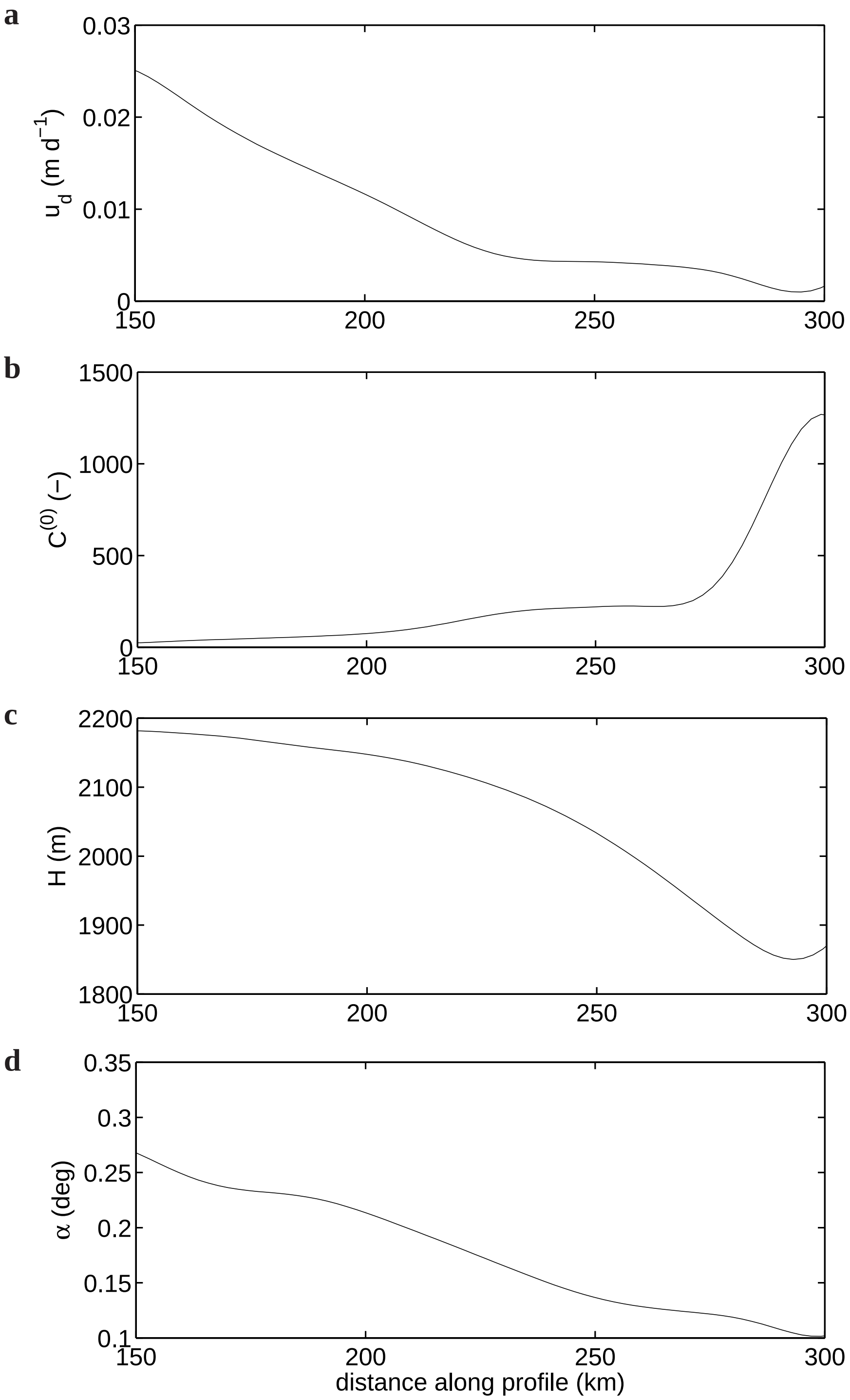

Figure 6.3: Zeroth-order parameter entering the transfer functions determined from the finite-element results for the prior ($\boldsymbol{g}(\boldsymbol{m}_{\text{prior}})$) by applying a Lanczos filter of 40 km, which corresponds to removing all frequencies greater than approximately 20 mean ice thicknesses. (a) Mean surface deformational velocity u_d, (b) slip ratio $C^{(0)}$, (c) mean ice thickness and (d) mean surface slope.

in Section 6.4.1, the basal slipperiness distribution is chosen such as to produce horizontal surface velocities of the order of magnitude of those measured on Rutford Ice Stream by applying the same method as described above. The prior distribution for the bedrock topography consists of the true bedrock smoothed with a Lanczos filter of 30 km. The prior basal slipperiness distribution is estimated from the horizontal surface velocity, local ice thickness and basal shear stress as explained in subsection 6.4.1. The set of zeroth-order parameters entering the transfer functions and calculated from the finite-element model result for the prior $\boldsymbol{g}(\boldsymbol{m}_{\text{prior}})$ are shown in Figure 6.4.

Figure 6.5 shows the inferred bedrock and basal slipperiness distributions (dashed lines). Interestingly, most of the bed features are very well recovered after only 2 iterations (dashed-dotted line). The maximum a posteriori solution is obtained with 12 iterations. The estimated basal slipperiness distribution is very similar to the true distribution, except that the amplitude of the peak of the basal slipperiness distribution ($x = 250$ km) is overestimated. The width of the peak is on the other hand reproduced correctly. As can be seen in Figure 6.6, the estimated surface topography and surface velocities fit the observed data up to the noise level.

6.5 Rutford Ice Stream Inversion

In the following, we present the results obtained for the selected flow line on Rutford Ice Stream. The basal properties are first inferred from surface measurements without integration of the surface evolution with time in the forward model. The surface geometry of the forward finite-element model is imposed throughout the optimization (at each iteration of the inversion procedure) by the measured surface topography on Rutford Ice Stream. The inversion produces estimates of the basal properties that best reproduce the measured surface velocities for the given surface topography at the measurement moment. This ’snapshot’ approach corresponds to what has been used so far in all other treatments of the problem (e.g., MacAyeal et al., 1995). However, comparison between measured and calculated rates of surface elevation changes reveal large and significant differences. Therefore, in a second step, the surface topography is allowed to evolve with time in the forward model until steady state is reached according to Eq. 6.4. The glacier surface geometry of the forward finite-element model is no longer imposed, but results, similarly to the surface velocities, from the inferred basal conditions. This second approach allows to determine basal conditions that are consistent both with observations of surface topography and surface velocities and with observed rates of surface elevation changes.

6.5.1 Data

The selected flowline on Rutford Ice Stream is shown in Figure 6.7. The corresponding surface and bedrock topography data come from airborne radar sounding and were provided by H. Corr from the British Antarctic Survey, UK. The horizontal and vertical velocity data are a combination of Global Positioning System (GPS) observations collected continuously from late December 2003 until mid-February 2004 from G. H. Gudmundsson and of observations of stake movement from aluminum poles surveyed in 1984/85 and 1985/86 from R. M Frolich (Frolich et al., 1987). We assume that the flow regime of

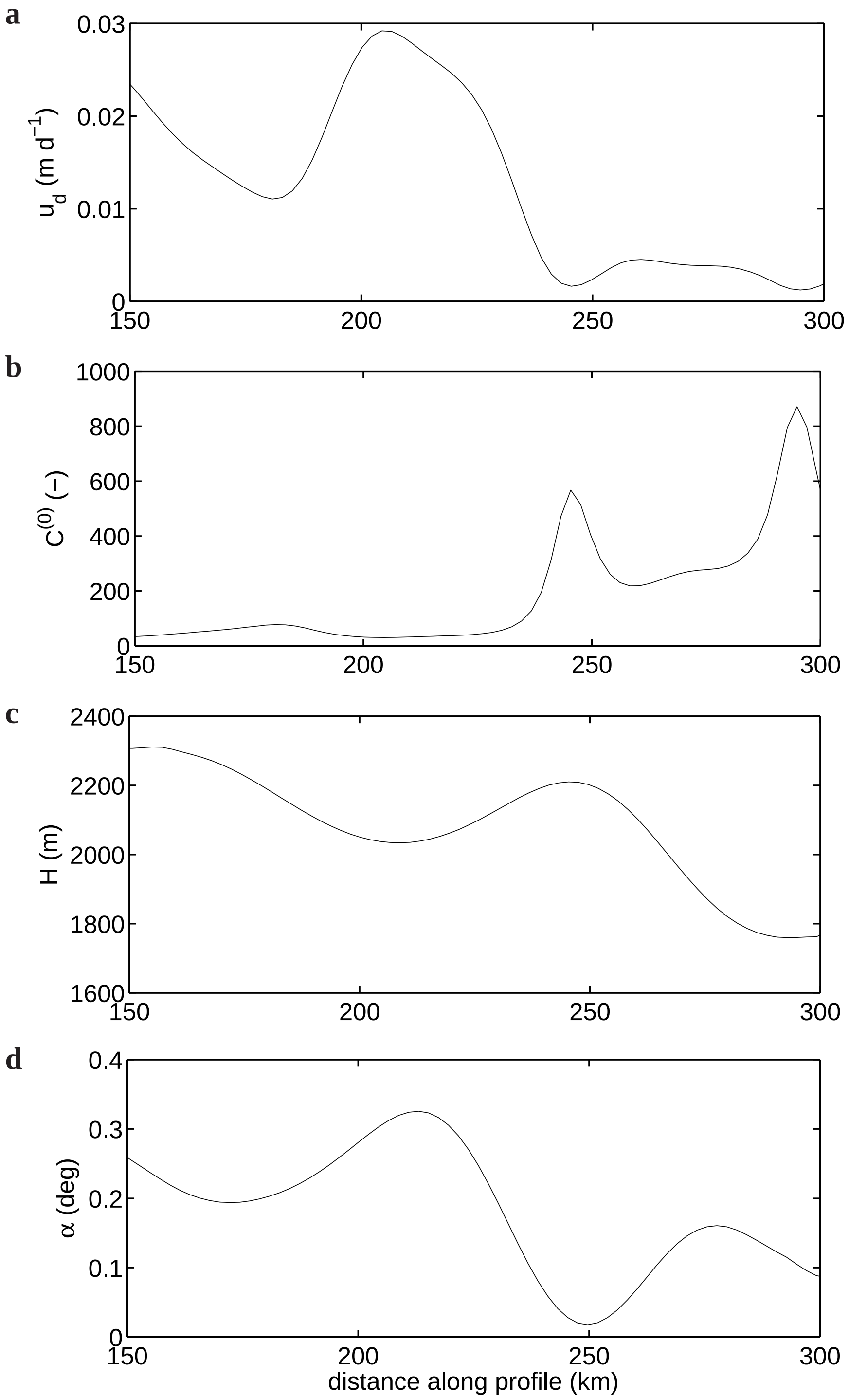

Figure 6.4: Zeroth-order parameter entering the transfer functions determined from the finite-element results for the prior ($\boldsymbol{g}(\boldsymbol{m}_{\mathrm{prior}})$) by applying a Lanczos filter of 40 km which corresponds to removing all frequencies greater than approximately 20 mean ice thicknesses. (a) Mean surface deformational velocity u_d, (b) slip ratio $C^{(0)}$, (c) mean ice thickness and (d) mean surface slope.

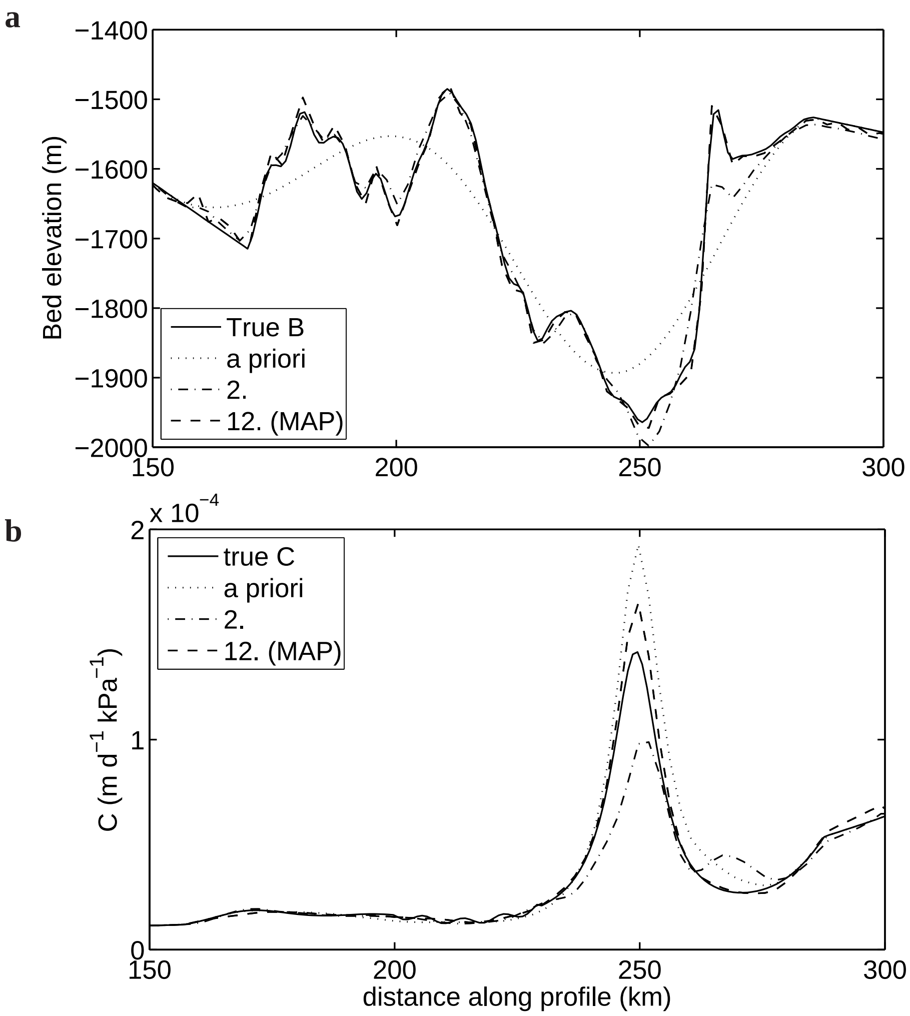

Figure 6.5: Estimated (a) bedrock topography and (b) basal slipperiness distribution from synthetic surface data generated with the finite-element model for the true distributions (solid lines) and added noise. The maximum a posteriori solution reproduces the true bedrock topography very accurately. The basal slipperiness distribution is recovered well, but overestimated at $x = 250$ km.

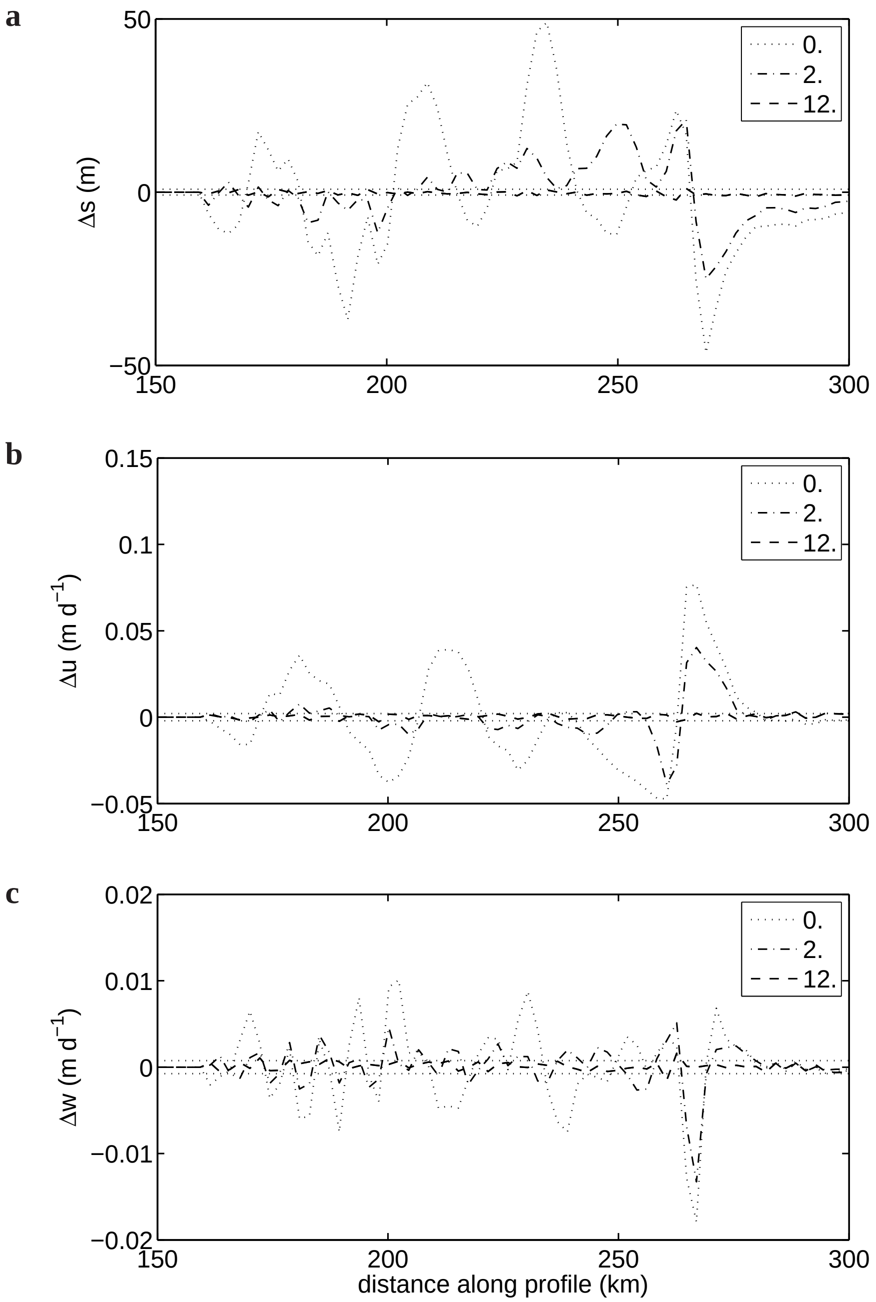

Figure 6.6: Residuals between observations and FE-model predictions for (a) surface topography, (b) horizontal and (c) vertical velocity. The dotted lines show the standard deviation of the surface data (square roots of the main diagonal of the data covariance matrix $\mathbf{C}_D$).

Rutford Ice Stream did not change significantly over the last two decades. By comparing ground-based GPS measurements, Gudmundsson and Jenkins (2007) found no significant decadal-scale velocity changes of Rutford Ice Stream. Surface accumulation data were computed by R. Arthern from the British Antarctic Survey, UK, using polarization of 4.3-cm wavelength microwave emission (Arthern et al., 2006). All raw data are presented in Figure 6.8. Horizontal surface velocities increase from 0.8 m per day at the beginning of the flow line to 1.1 m per day at the grounding line. There is a gap in vertical surface velocity between 180 km and 230 km. The data were interpolated for inversion using BLUE. The interpolated data are shown in Figure 6.9. The dotted lines in Figure 6.9a show the standard deviation of the bedrock topography, which amounts to 30 m. This error is bigger than the measurement errors. The errors bars plotted on the velocities in Figures 6.9b and c correspond to the square roots of the main diagonal elements of the data covariance matrix $\mathbf{C_D}$. As can be seen, the standard deviation of the velocities increases in regions where no or only few data points are available.

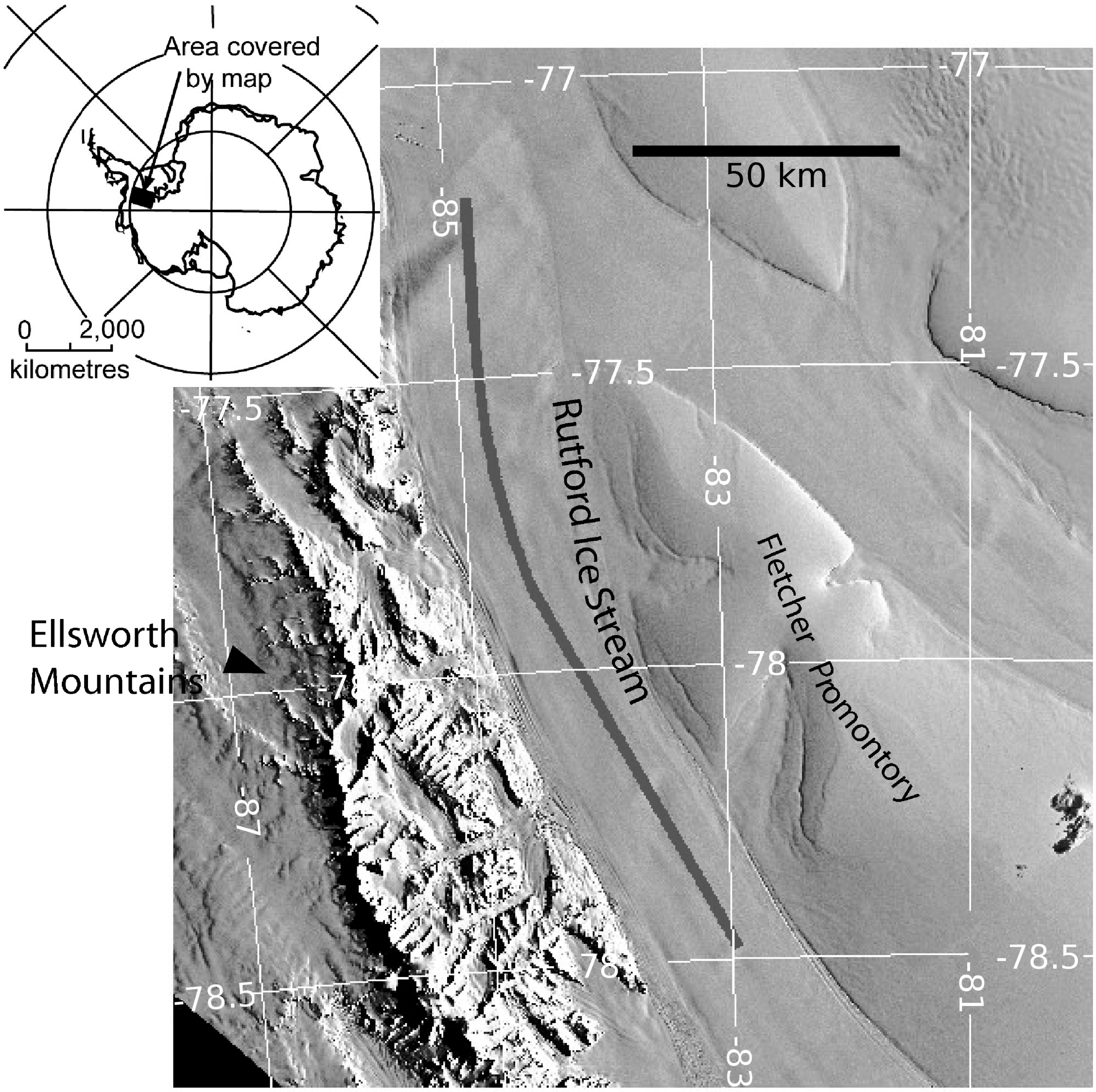

Figure 6.7: Selected flow line on Rutford Ice Stream, West Antarctica.

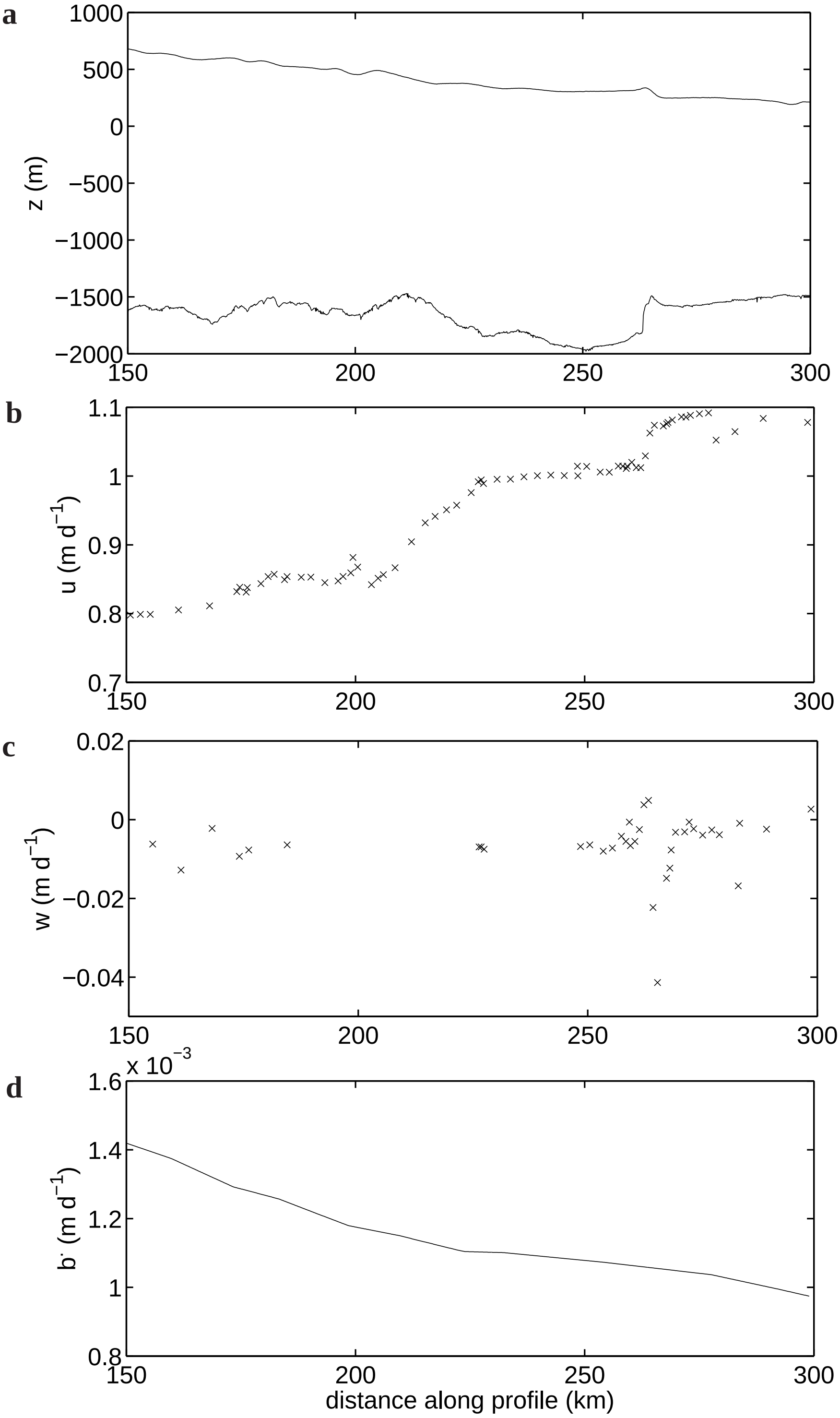

Figure 6.8: Rutford Ice Stream data. (a) Surface and bedrock topography as measured from airborne radar, (b) horizontal surface velocity, (c) vertical surface velocity and (d) ice equivalent accumulation rate along the profile shown in Figure 6.7. Velocities are in meters per day. The grounding line is located at $x = 299$ km.

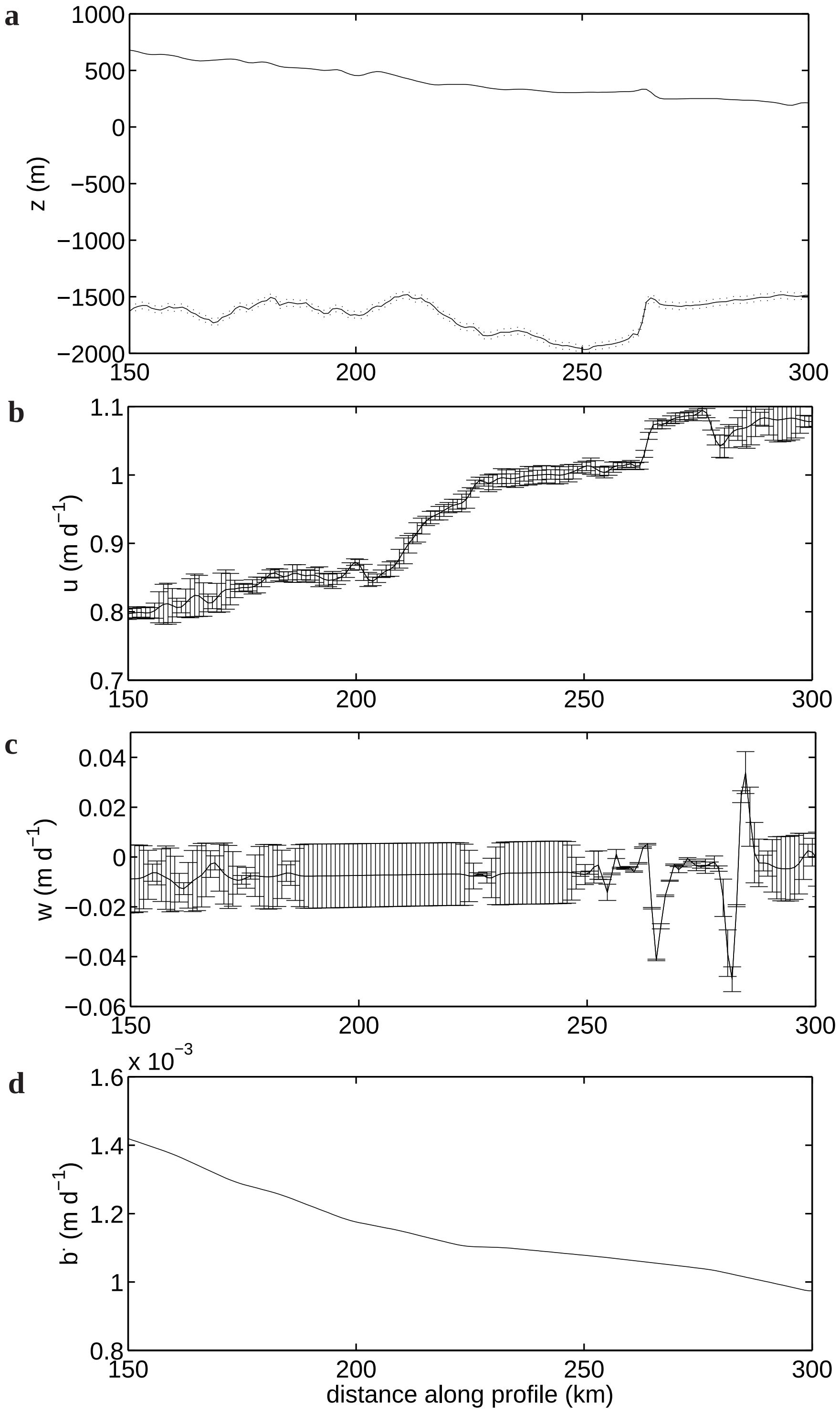

Figure 6.9: Rutford Ice Stream interpolated data. (a) Surface and bedrock topography, (b) horizontal and (c) vertical surface velocities with error bars and (d) ice equivalent accumulation rate along the profile shown in Figure 6.7. Velocities are in meters per day. The grounding line is located at $x = 299$ km.

6.5.2 Prior model parameters

For the inversion of the Rutford surface data, the prior for the bedrock topography $\boldsymbol{b}_{\text{prior}}$ was obtained by interpolating the radar measurements shown in Figure 6.8a onto an equidistant grid using BLUE. The resulting $\boldsymbol{b}_{\text{prior}}$ is shown in Figures 6.9a and 6.12a (solid line). The prior basal slipperiness $\boldsymbol{C}_{\text{prior}}$ (Figure 6.10) was estimated from the basal shear stress $\boldsymbol{\tau}_b$ computed from the local ice thickness and surface slope and from the basal velocity on Rutford Ice Stream by the relation $\boldsymbol{C}_{\text{prior}} = \boldsymbol{u}_b/\boldsymbol{\tau}_b$. The basal velocity is taken here to be the surface velocity, since the deformational ice velocity is generally small on Rutford ice stream. The prior distribution for the basal lubrication can be seen in Figure 6.10. $\boldsymbol{C}_{\text{prior}}$ increases from the upstream end of the flow line to the grounding line. A large peak in basal slipperiness centered at 245 km coincide with a deep through in basal topography. This peak in basal slipperiness is needed to reproduce more or less the measured horizontal surface velocity as the surface slope is locally reversed.

The set of zeroth-order parameters entering the transfer functions are determined by applying a 40 km Lanczos filter on the finite-element model results for the prior ($\boldsymbol{g}(\boldsymbol{m}_{\text{prior}})$) obtained without calculating the forward transient surface evolution in time. These parameters are shown in Figure 6.11. In the numerical model, we observe extrusion flow in the region $240 < x < 260$ km, as the surface slope is locally reversed (negative). By applying the 40 km Lanczos filter described above on the deformational velocity, we get negative deformational velocities in this region. In the determination of the zeroth-order deformational velocity u_d, we combine a 60 km Lanczos filter with the 40 km filter in the region $230 < x < 270$ km in order to enforce a positive u_d in this region. We emphasize here that the cut-off frequency of the Lanczos filter, e.g., 40 km, does not have to correspond to an exact spatial scale, but should be of several ice thicknesses such that the filtered data reflect the general trend of the zeroth-order ice stream geometry. Figure 6.11a shows that the deformational velocity diminishes from 0.03 m per day at the upstream end of the flow line to 0.002 m per day at the grounding line. Hence, the basal sliding velocity increases towards the grounding line. This can be seen in Figure 6.11b as the slip ratio increases from 40 to 500 at the downstream end of the flow line. The ice thickness varies from 2300 m at the upstream end to 1700 m at the grounding line with a peak of 2230 m at 250 km. The surface slope diminishes from $\approx$ 0.3° to 0.1 ° at the grounding line. At around 250 km, a small surface slope coincides with small deformational velocity and a high slip ratio.

6.5.3 Inversion without surface evolution

In this section we estimate the basal properties along the selected flow line without calculating the transient evolution of the free surface with time in the forward model (Eq. 6.4 is not used). As we invert for the differences between observed data and finite-element predictions ($\boldsymbol{d} - \boldsymbol{g}(\boldsymbol{m}_i)$ in Eq. 6.12), and the surface remains unchanged throughout the optimization, $\Delta \boldsymbol{s}$ remains identically zero and does not provide any information for inversion. This represents an important information loss. In this case, the basal conditions are determined from the differences between observed and finite-element predictions of horizontal and vertical velocities. Figure 6.12 shows the maximum a posteriori solution for the bedrock and basal slipperiness distribution for the selected flow line on Rutford Ice Stream. The prior distributions are shown for comparison. Figure 6.12a shows that the

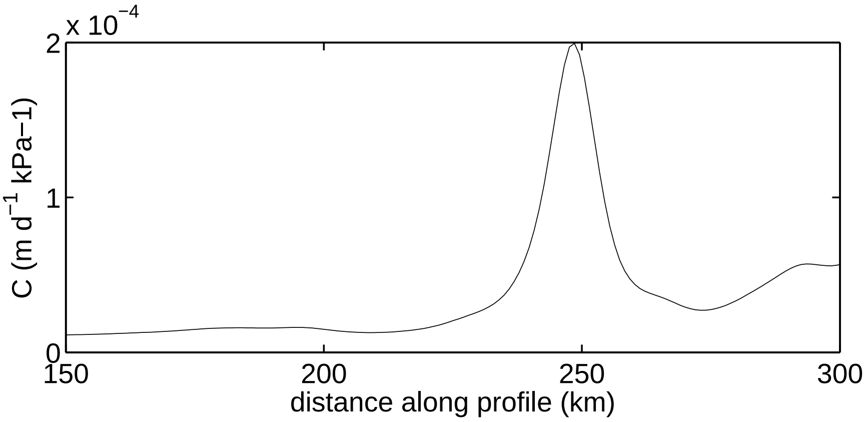

Figure 6.10: Prior distribution for the basal slipperiness along a flow line on Rutford Ice Stream determined from the estimated basal shear stress and basal velocity by the relation $\boldsymbol{C}_{\text{prior}} = \boldsymbol{u}_b/\boldsymbol{\tau}_b$.

overall estimated bedrock shape is consistent with the radar measurements. Over the first half of the flow line, the estimated bedrock topography is very similar to the measured bed but some estimated peaks become more pronounced. Over the second half of the flow line, the estimated bed differs more from the measured bedrock topography and becomes less deep. We observe also some peaks which are not present in the radar data.

Figure 6.12b shows the estimated basal slipperiness distribution as compared to the prior distribution. The estimated basal slipperiness does not change much over the first half of the flow line, but detects some small features. From $x = 220$ to the grounding line, the estimated basal slipperiness differs more in amplitude from the a priori.

The residuals between observations and finite-element predictions are shown in Figure 6.13. The non-zero Δs residuals (Figure 6.13) are due to interpolation errors, since the grid for inversion is not exactly the same as in the forward model. The differences in horizontal velocity diminishes towards the noise in the data over the first half of the profile, then increases in the region $230 < x < 270$ and are reduced again at the downstream end. The increase in the residuals for the horizontal surface velocity in the region $230 < x < 270$ can be explained by the fact that in this region, the surface slope is locally reversed and produces extrusion flow.

Figure 6.14 shows a comparison between observed and inferred data along the flow line. The surface agreement is excellent as the prescribed surface in the finite-element model is the measured surface topography interpolated to the finite-element model grid. The finite-element model reproduces the horizontal velocity pretty well except in the region $220 < x < 260$. The vertical velocities are reproduced less precisely and are often over- or underestimated.

Figure 6.15 shows the calculated rates of surface elevation changes for the inferred surface data. The calculated rates of surface elevation changes are large and vary strongly along the profile between -0.04 m d^{-1} and 0.04 m d^{-1}. These calculated rates differ significantly from the measured rates of surface elevation changes on Rutford Ice Stream which amount approximately to 0.1 m y^{-1}.

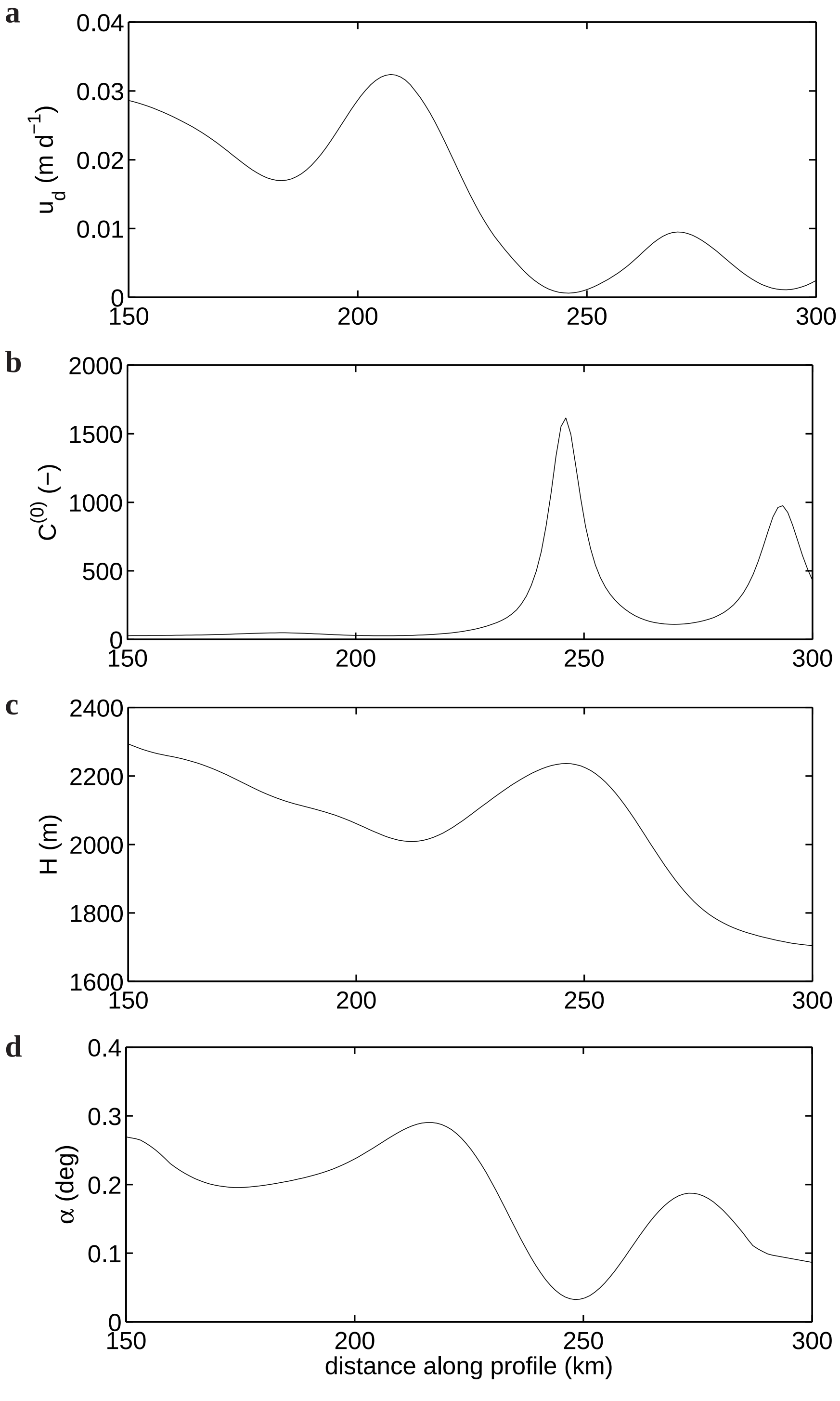

Figure 6.11: Zeroth-order parameter entering the transfer functions determined from the finite-element results for the prior ($\boldsymbol{g}(\boldsymbol{m}_{\text{prior}})$) by applying a Lanczos filter of 40 km which corresponds to removing all frequencies greater than approximately 20 mean ice thicknesses. (a) Mean surface deformational velocity u_d, (b) slip ratio $C^{(0)}$, (c) mean ice thickness and (d) mean surface slope.

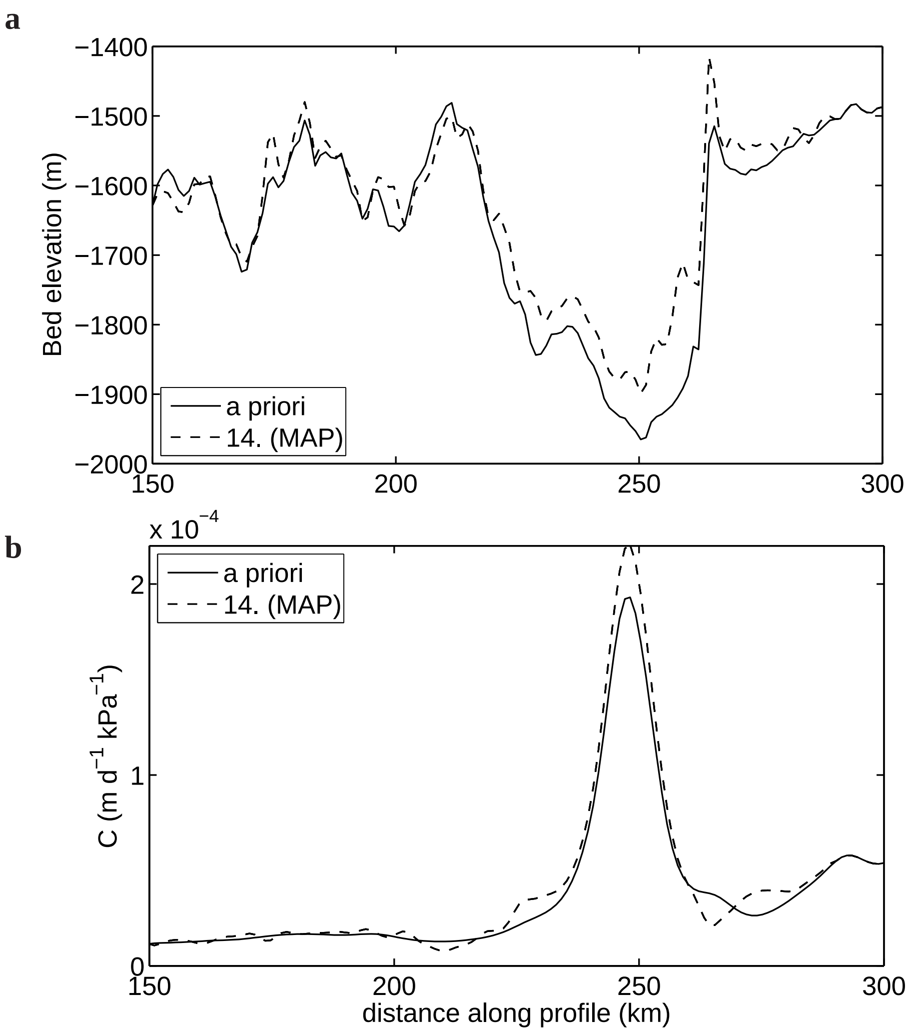

Figure 6.12: Inferred (a) bedrock topography and (b) basal slipperiness distribution for the selected flow line on Rutford Ice Stream for the case without surface evolution in the forward finite-element model. The solid lines correspond to (a) the prior bedrock distribution obtained by interpolating the airborne radar data using BLUE to the forward finite-element grid and (b) the prior basal lubrication distribution. The maximum a posteriori solution is shown as a dashed line.

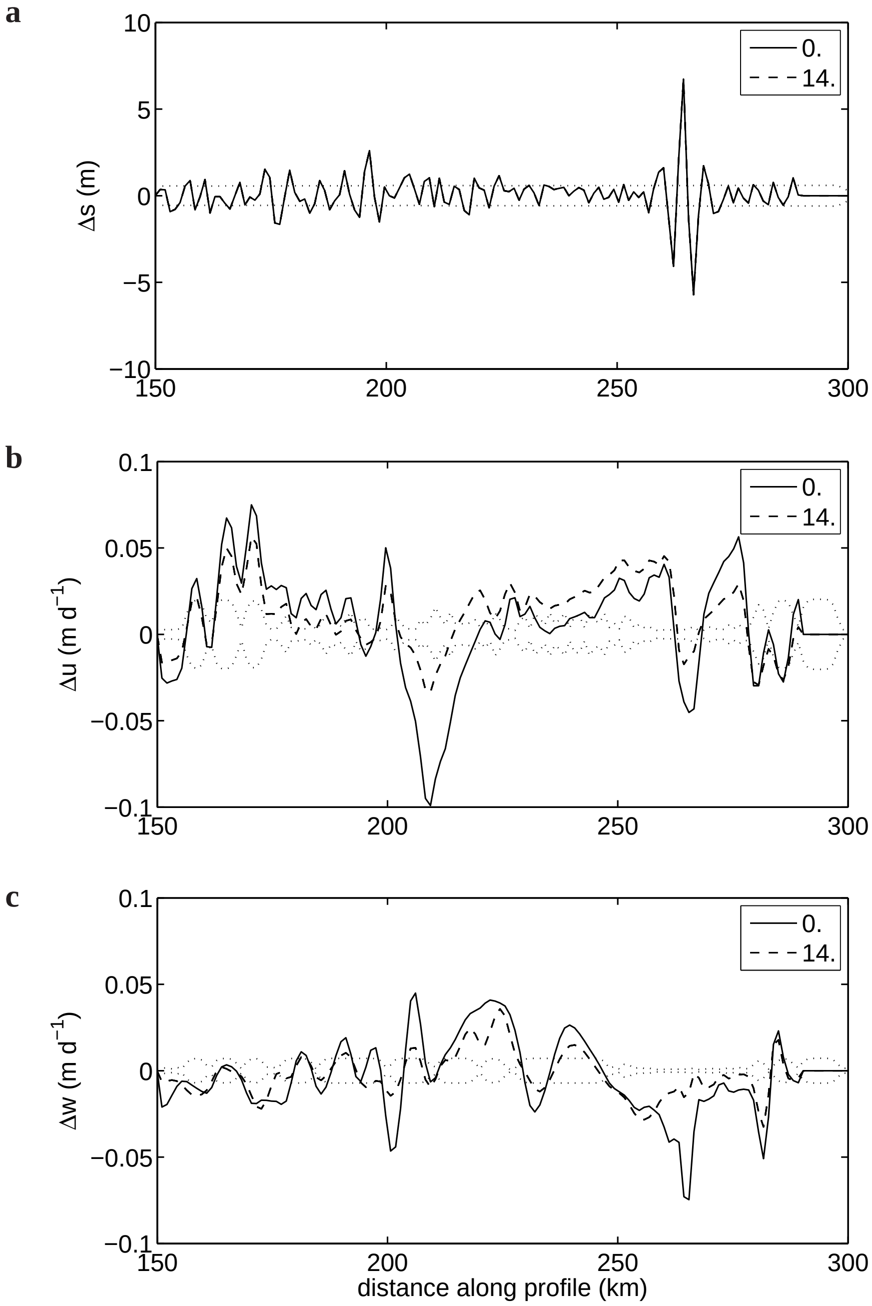

Figure 6.13: Residuals between observations along the selected flow line on Rutford Ice Stream and FE-model predictions for (a) surface topography, (b) horizontal and (c) vertical velocity. The solid lines show the residuals for the prior distribution and the dashed lines for the maximum a posteriori solution. The dotted lines correspond to the standard deviation of the observed data, corresponding to the square roots of the main diagonal elements of the data covariance matrix $\mathbf{C}_D$. Note that the Δs residuals (panel (a)) are coincident since the surface is not evolved with time. Note 0th and 14th iteration residual lines are superimposed in panel (a).

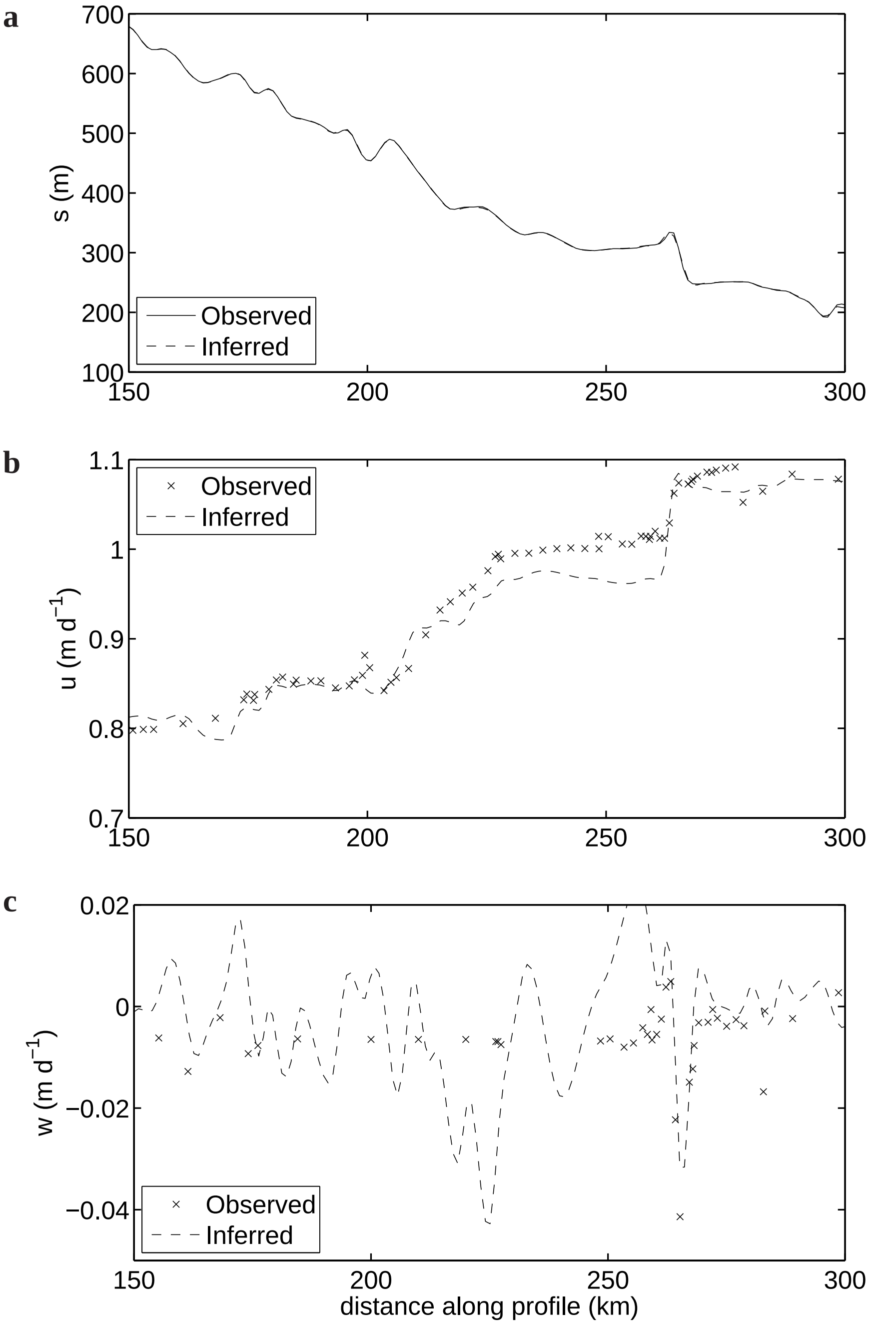

Figure 6.14: Comparison between observed (solid line in (a) and crosses in (b) and (c)) and inferred data (dashed lines) along the flow line on Rutford Ice Stream. (a) surface topography, (b) horizontal and (c) vertical velocity. The inferred data correspond to the finite-element prediction for the maximum a posteriori solution shown in Figure 6.16. The surface fit is excellent as the surface is not evolved with time in the forward model.

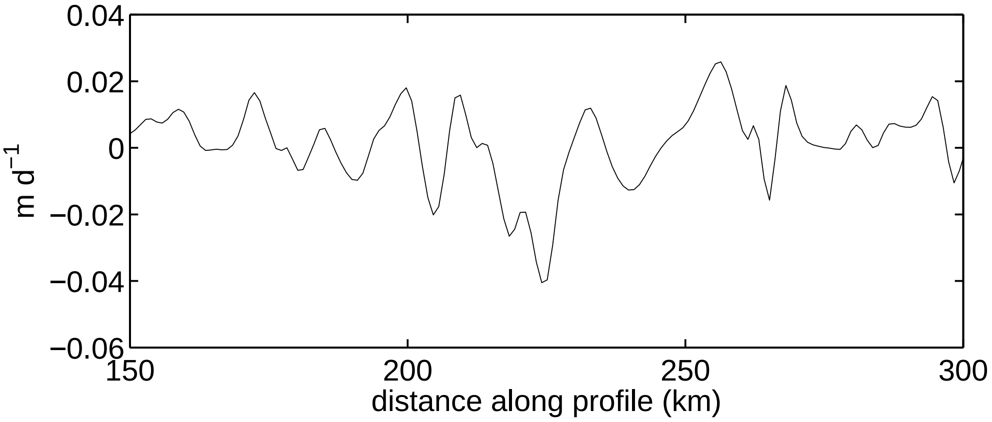

Figure 6.15: Calculated rates of surface elevation changes for the inferred surface data along the flow line.

6.5.4 Inversion with surface evolution

In this section, the surface of the forward finite-element model is evolved with time until steady-state with the basal conditions is reached (Eq. 6.4). Hence, we look for basal conditions that not only reproduces the measured surface topography and surface velocities as close as possible, but also the measured rates of surface elevation changes. The forward calculations of the free surface with time in the forward finite-element model started from the interpolated measured surface topography. Steady-state is defined to be reached as soon as the change in vertical displacement between two consecutive time steps is less than 0.05 cm. The difference between the observations and the steady-state surface fields, i.e surface topography, horizontal and vertical velocity, of the finite-element model is then calculated in Eq. 6.12 for inversion.

Figure 6.16 shows the estimated bedrock topography and basal slipperiness distribution along the flow line. The a priori distributions are shown for comparison. From the upstream end of the profile to the grounding line, the overall shape of the bed is similar to the measured bedrock. From the upstream end to 220 km, the amplitude and widths of several peaks and troughs differ from those measured. Note that some of the estimated troughs are deeper. For the region $170 < x < 220$ km, the estimated bed lies always deeper than the measured bedrock. From 220 km to the grounding line, the estimated bed is less deep, but this estimate feature may not be reliable. The step in the bed at position $x = 270$ km is maintained by the inversion.

The estimated basal slipperiness C is shown in Figure 6.16b. As compared to the a priori, the maximum a posteriori solution predicts small scale features from the upstream end of the profile to $x = 220$ km. The peak in the basal slipperiness at $x = 250$ km is increased as well as much of the a priori down to the grounding line.

The residuals between observations and finite-element predictions are shown in Figure 6.17. For the maximum a posteriori solution, the differences between observed and inferred data is almost reduced to the noise level in the data from the upstream end of the selected profile to 220 km. Downstream from 220 km to the grounding line, the finite-element results deviate systematically from the measured data. This shows that in this region, the model assumptions must be questioned.

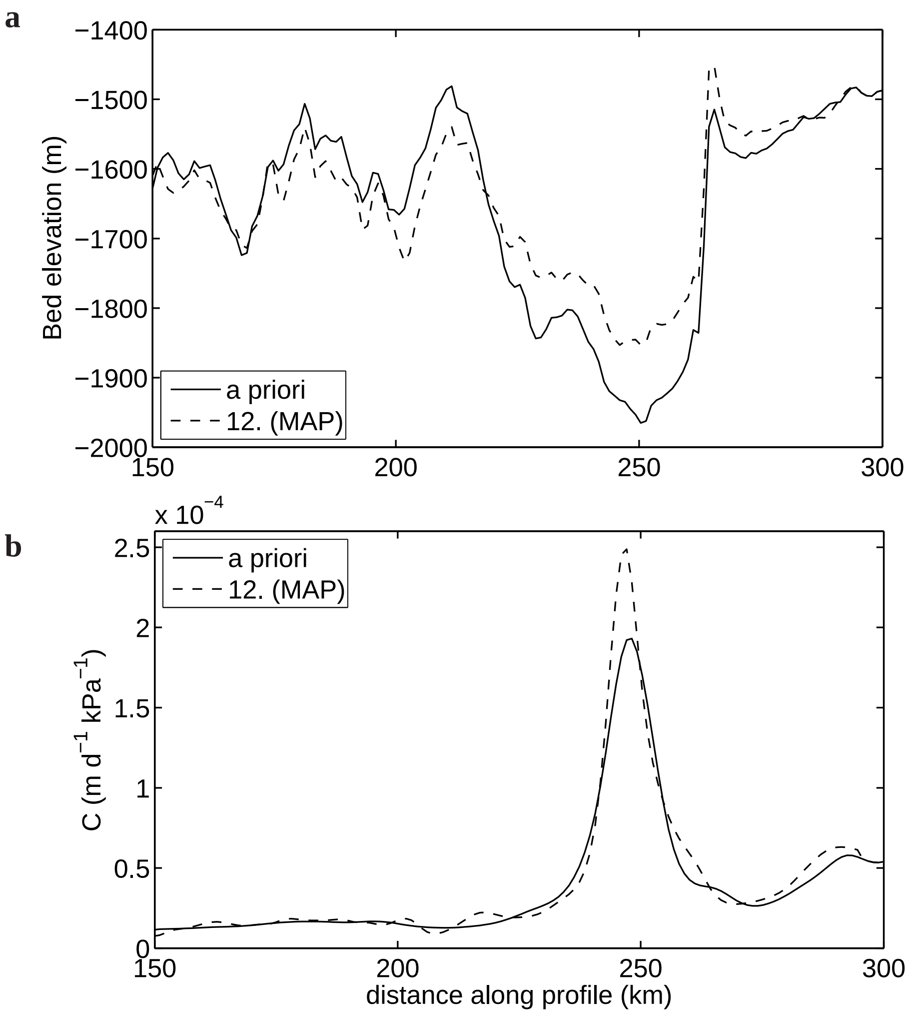

Figure 6.16: Estimated (a) bedrock topography and (b) basal slipperiness distribution for the selected flow line on Rutford Ice Stream for the case that the surface is evolved until steady-state is reached. The solid lines correspond to (a) the prior bedrock distribution and (b) the prior basal lubrication distribution. The maximum a posteriori solution is shown as a dashed line.

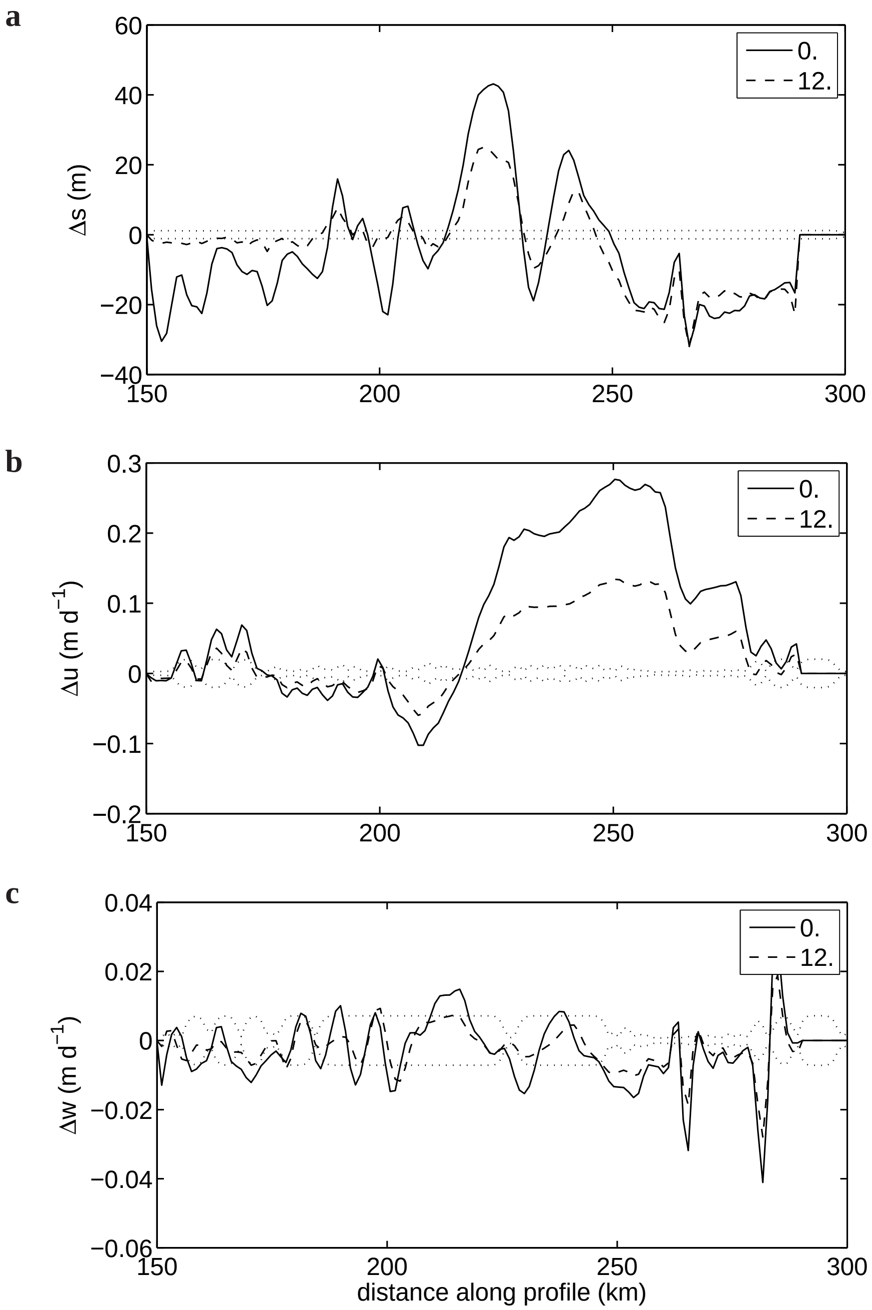

Figure 6.17: Residuals between observations along a flow line on Rutford Ice Stream and FE-model predictions for (a) surface topography, (b) horizontal and (c) vertical velocity. The solid lines show the residuals for the prior distribution and the dashed lines for the maximum a posteriori solution.

Figure 6.18 provides a comparison of observed and inferred surface data along the flow line. As can be seen, the agreement between the observed and inferred surface topography (Figure 6.18a) is very good from the upstream end of the profile down to 220 km. From 220 km down to the grounding line, the agreement is poor because of the influence of the reverse surface slope between $240 < x < 260$ km as explained above. The figure shows nicely how the surface gets more reversed in this region with the forward calculation in time. For the horizontal and vertical velocity (panels b and c in Figure 6.18), the agreement between observed and estimated surface data is also good from the upstream end of the profile to 220 km. Interestingly, at $x = 270$ km, the observed trough in vertical velocity is reproduced by the finite-element model but with reduced amplitude.

Figure 6.19 shows the calculated rates of surface elevation changes for the inferred surface data. The rates of changes are generally small and exceed only in a few places along the profile -0.005 m d^{-1} or 0.005 m d^{-1}. The calculated rates of changes are compatible with measurements of surface elevation changes on Rutford Ice Stream (approximately 0.1 m y^{-1}).

6.6 Discussion

The inversion results presented above are consistent both with the surface observations and the radar measurements of bedrock topography. Especially in the case that the surface is evolved with time to steady-state, over the upper half of the profile to 220 km, the fit between measured and inferred surface topography is very good (Figure 6.17a). This shows that the assumption that the surface data are in steady-state with the basal conditions must be correct. Over the lower part of the profile, the bedrock differs significantly more from the radar measurements than over the upper part of the profile. One observes a systematic deviation of the finite-element predictions from the measured data. In the numerical model, we observe a reverse surface slope in the region $240 < x < 260$ km which produces locally extrusion flow. As the surface evolves towards steady-state, this reverse slope gets more and more negative and has the effect of slowing down the flow of a large part of the ice stream (from $220 < x < 280$ km). The horizontal surface velocity diminishes continuously starting from a velocity of $\approx$ 1 m d^{-1} to $\approx$ 0.75 m d^{-1} in steady-state. This systematic deviation indicates that the model assumptions, i.e two dimensional, must be questioned. Indeed, in this region, transverse radar measurements showed the presence of a broad channel from which we expect three-dimensional effects. Transverse effects may also play a dominant role in carrying down the ice to the ice shelf. In this respect, the estimated basal conditions over the lower half of the profile may be regarded as effective basal conditions in line with the model assumptions.

6.6.1 Comparison between inversion results with and without surface evolution

Figure 6.20 compares the estimated bedrock topography and basal slipperiness distribution for both types of inversions. The solid line correspond to the inversion without forward calculation of the surface with time and the dashed line to the inversion with surface evolution. The deep bedrock through located at $x = 160$ km coincide for both

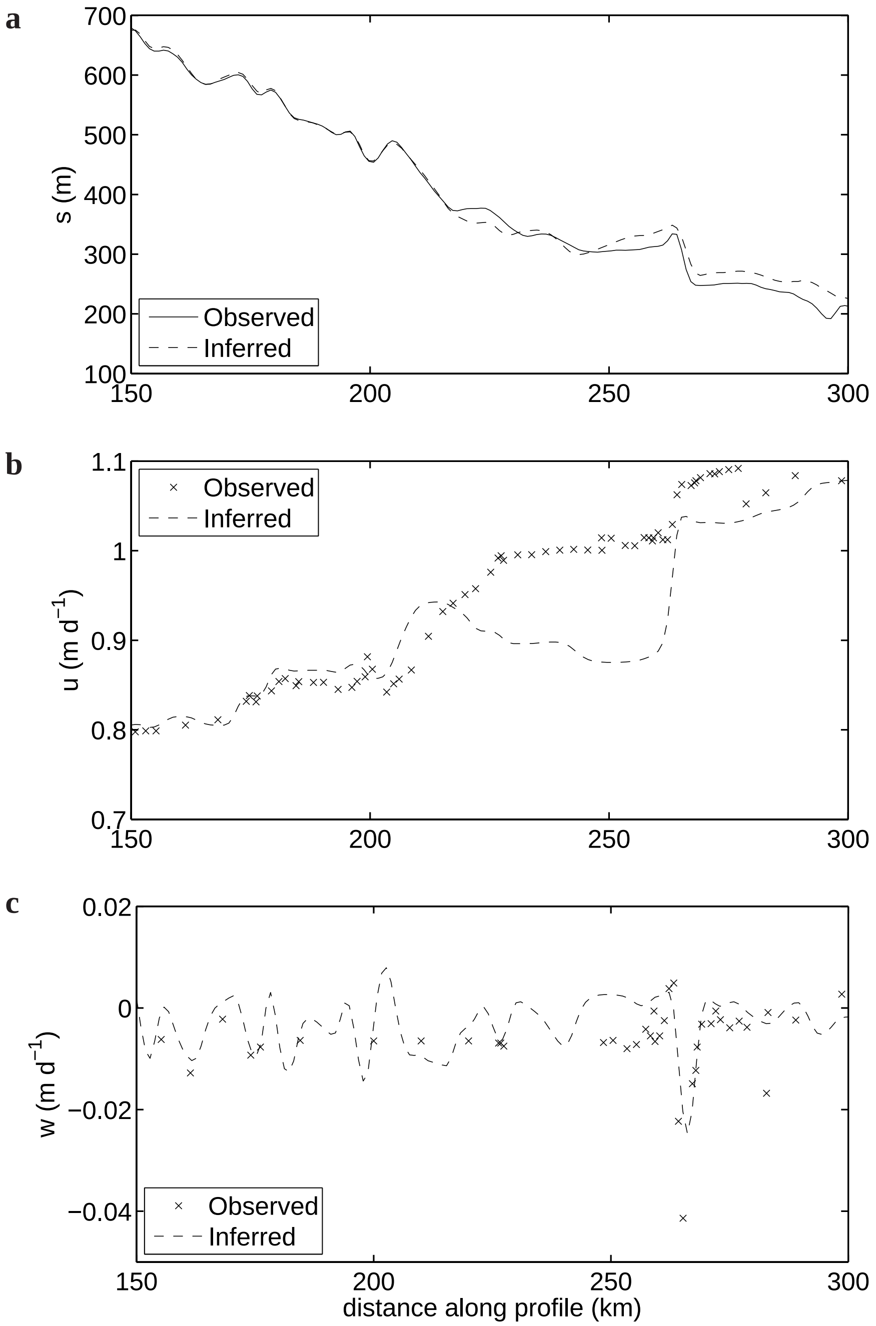

Figure 6.18: Comparison between observed (solid line in (a) and crosses in (b) and (c)) and inferred data (dashed lines) along the flow line on Rutford Ice Stream. (a) surface topography, (b) horizontal and (c) vertical velocity. The inferred data correspond to the finite-element prediction for the maximum a posteriori solution shown in Figure 6.16.

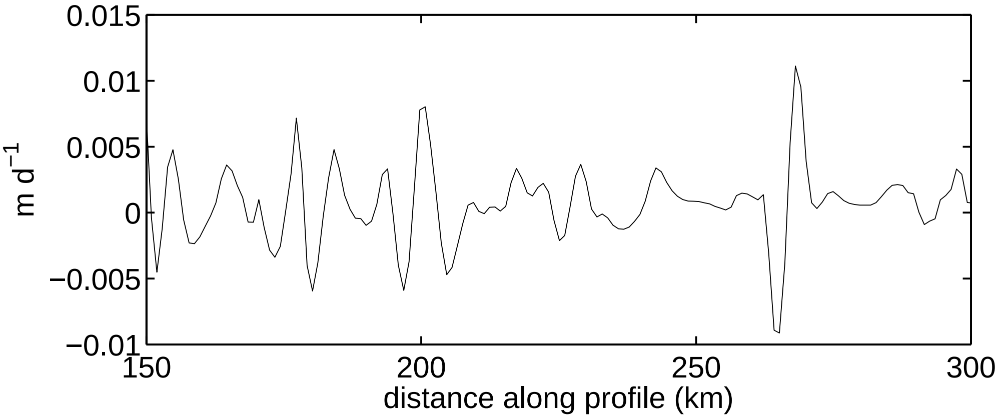

Figure 6.19: Calculated rates of surface elevation changes for the inferred surface data along the flow line.

inversions. The horizontal position of much of the peaks and troughs are the same. The inversion with surface evolution tends to predict a deeper bed over the first half of the profile. Note that the position of the step in the bed is the same for both inversions as well as the amplitude of the peak of the step. The inversion without surface evolution predicts some peaks at the bottom of the step.

The basal slipperiness distribution is very similar for both inversions over the first half of the profile, but some small scale features differ. Over the lower half of the profile to the grounding line, a large peak in basal slipperiness is estimated in both cases, but with different widths and maximum amplitude.

Figure 6.21 shows a comparison of the residuals between observations and finite-element model predictions for the maximum a posteriori solution of both inversions. The residuals for the horizontal and vertical velocity (Figure 6.21b and c) show that over the upper half of the profile, the inversion with surface evolution reproduces somewhat better the measured data. Over the lower half of the profile, the horizontal velocity is clearly better reproduced by the inversion without surface evolution for the reasons discussed above. Hence, for the upper part of the profile where the model assumptions are generally correct, we would select the inversion results with surface evolution.

Figure 6.22 shows a comparison between the calculated rates of surface elevation changes for the inferred surface data for both inversion approach. The calculated rates of surface elevation changes are clearly much smaller over the whole profile for the inversion with surface evolution than without. The calculated rates of changes for the inversion with surface evolution are compatible with observations of surface elevation changes on Rutford Ice Stream.

6.7 Conclusions

Using a nonlinear Bayesian inversion method, we have shown that it is possible to estimate both bedrock topography and basal slipperiness along a flow line on Rutford Ice Stream from observed surface topography and surface velocities.

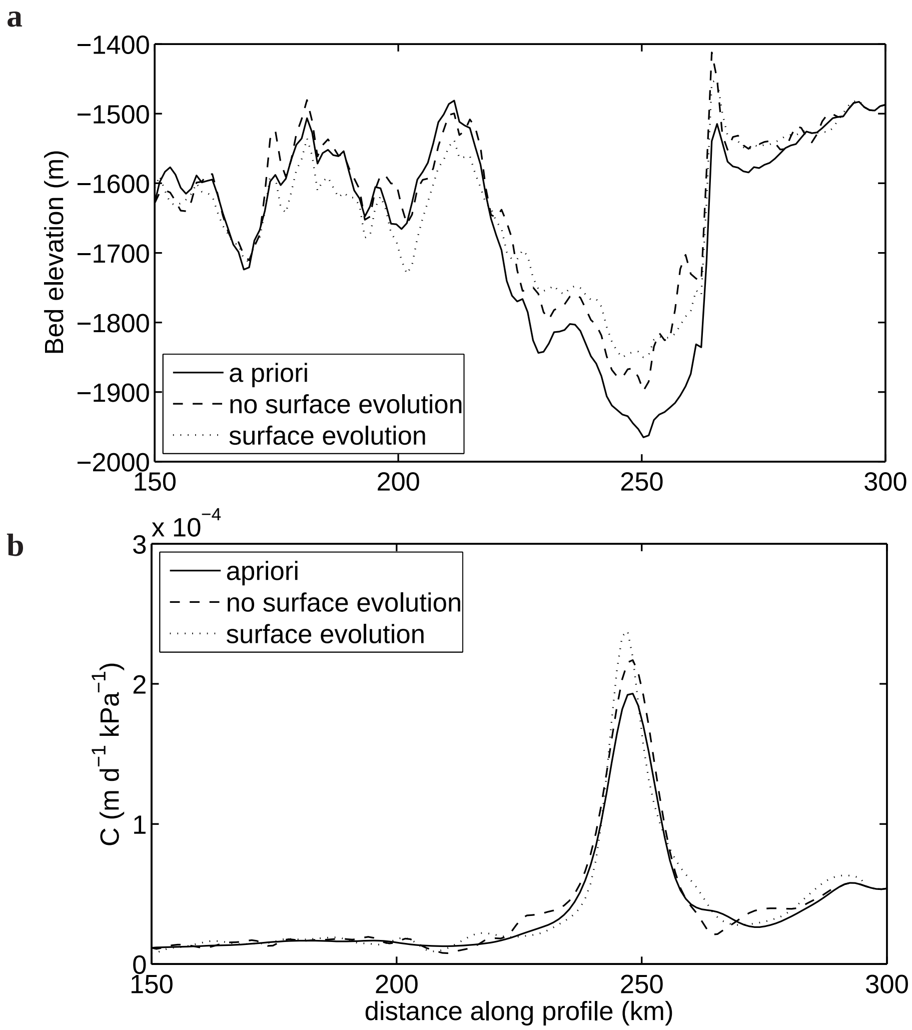

Figure 6.20: Comparison between inferred (a) bedrock topography and (b) basal slipperiness distribution for the inversion without ('no surface evolution', solid line) and with surface evolution until steady-state is reached ('surface evolution', dashed line).

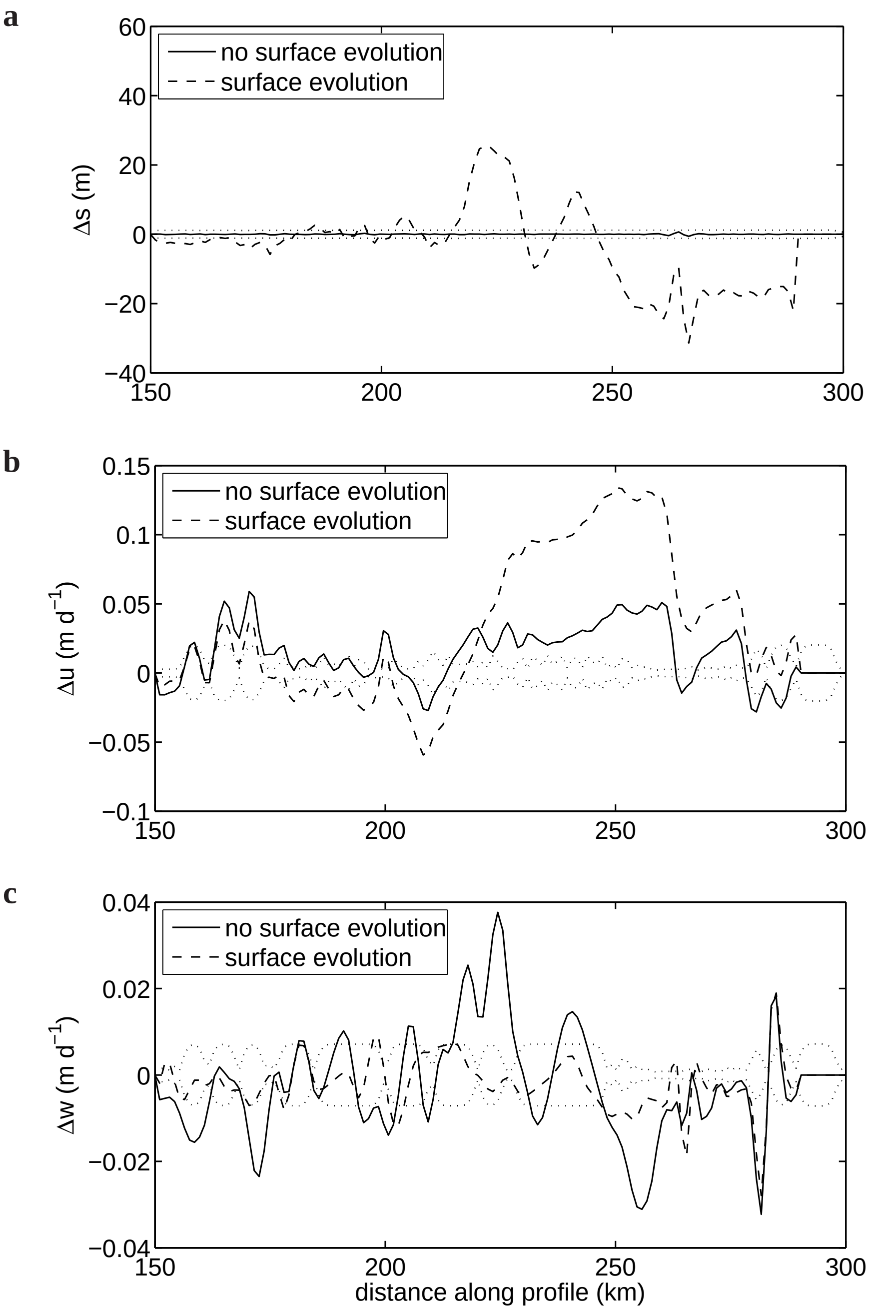

Figure 6.21: Comparison of the residuals between observations and finite-element prediction for the maximum a posteriori solution for (a) surface topography, (b) horizontal and (c) vertical velocity for the inversion without ('no surface evolution', solid line) and with surface evolution until steady-state ('surface evolution', dashed line).

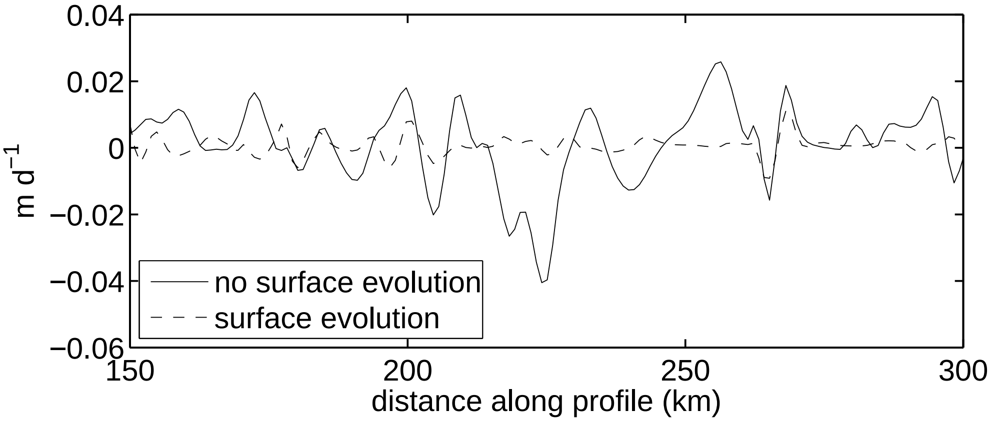

Figure 6.22: Calculated rates of surface elevation changes for the inferred surface data along the flow line.

We first inferred basal properties from surface measurements without calculating the evolution of the surface with time in the finite-element model. This 'snapshot' inversion corresponds to the approach used so far in all other treatments of this problem (e.g., MacAyeal et al., 1995). However, comparison between measured and calculated rates of surface elevation changes revealed large and significant differences. Therefore, in a second step, the surface topography was allowed to evolve until steady-state in the finite-element model. The steady-state finite-element predictions for the surface data were then used for inversion. With this inversion, we could determine basal conditions that are consistent with all surface observations, i.e., surface topography, surface velocities and rates of surface elevation changes.

For both inversions, the estimated bedrock topography is consistent with radar measurements of the bed and vary from the measurements approximately 40 m up to 100 m locally. Over the first half of the selected flow line, the estimated basal slipperiness is very similar for both inversions. By inverting the surface data without forward calculation of the surface evolution in time, we lose informations on surface topography. This may explain some of the differences observed between the results of both types of inversions performed. The inversion results of the second half of the profile (from $220 < x < 280$ km) are limited by the influence of a reverse surface slope on the modeled ice stream dynamics. These limitations could be overcome by introducing a correction term for the ignored transverse effects.

The Bayesian inversion method introduced allowed to include a priori informations about the model parameters known independently of the surface measurements. For the selected flow line, we incorporated in the inversion the measured bedrock topography from airborne radar as well as an a priori for the basal lubrication determined such as to produce horizontal surface velocities of the order of magnitude of those measured on Rutford Ice Stream.

Chapter 7

General Conclusions

This chapter provides a general conclusion, an overview of the results as well as an outlook.

This thesis aimed at estimating the basal properties under ice streams by means of inverse modeling of surface data. A nonlinear Bayesian inference approach was developed for this purpose. In Bayesian inference, information about the basal properties is quantified in term of probabilities. By doing so, the uncertainties associated with the inverse calculation due to data errors and due to our prior understanding or expectation about the basal conditions are formally incorporated into the calculation. Those probabilities are combined using Bayes theorem to derive a final a posteriori probability distribution, from which we extract the most likely estimates corresponding the maximum of the probability. In this thesis, both uncertainties in surface measurements and prior estimates have been characterized by Gaussian probability distributions. A key issue of the proposed method was to determine whether the first order derivatives of the forward model can be adequately approximated by linear transfer functions or not.

As any inverse method, the Bayesian inversion method introduced requires the construction of a forward function describing the relevant physics of the relationship between surface and basal properties. This forward problem consists in calculating the steady-state surface geometry and surface velocities of ice streams and glaciers for a given bedrock topography and basal slipperiness. The forward problem is solved with a numerical finite-element model allowing to consider the nonlinear ice rheology and the nonlinear effects of finite-amplitude basal perturbations on the surface. Both the forward and inverse models are two-dimensional and can be applied along flow lines when transverse effects are of small importance.

This forward function was used in a first step to investigate the effects of basal disturbances on the steady-state surface topography and surface velocities (Chapter 2) as well as the internal flow field of glaciers (Chapter 3). Two types of sinusoidal basal disturbances were considered; (1) bedrock undulations and (2) spatial variations in basal slipperiness. This contributes to the understanding of the relationship between basal and surface conditions, i.e how and if basal disturbances are transmitted to the surface of glaciers, for nonlinear rheology and finite-amplitude effects and allows to determine, at least in principle, if inferences on the nature of basal conditions from surface observations have some chance of success or not.

The proposed inverse method was first applied to synthetic data to test the suitability of the method to determine the bedrock perturbations and basal slipperiness under ice streams from observations of surface topography, horizontal and vertical velocity. The inversion of the non-linear forward function, i.e forward finite-element model, is accomplished by a nonlinear Gauss-Newton method (Rodgers, 2000). The Fréchet derivatives are approximated by linear transfer functions (Gudmundsson, 2003). This approximation is a key issue of the proposed method as it greatly enhances the numerical efficiency of the method by sparing the time-consuming evaluation of the numerical derivatives. The main concern of Chapter 5 was therefore to determine whether this approximation is adequate or not.

The inversion method was then extended such that it can be applied to real data. The proposed inversion method was applied along a selected flow line on Rutford Ice Stream, West Antarctica and showed that it is possible to estimate both bedrock topography and basal slipperiness from observed surface topography and surface velocities. The inversion results were consistent with both surface observations and radar measurements of bedrock topography. Over the upper half of the profile, relatively small perturbations in basal slipperiness are necessary to fit the surface data. Over the lower half of the profile to the grounding line, a large peak in basal slipperiness is estimated. In this region, transverse effects are known to play an important role and in this respect, the model assumptions must be questioned.

In the following we give a short overview of the achieved results. Detailed summaries of the results and conclusions have been provided at the end of each chapter.

7.1 Overview of the results

7.1.1 Forward problem

The effects of varying the exponent n in Glen's flow law on transfer characteristics are mainly quantitative and do not affect qualitative aspects of the transfer amplitude and phase shifts such as the number of maxima and inflection points when plotted as a function of wavelength.

Qualitatively, the information transfer from the basal boundary towards the surface increases with the wavelength of the basal perturbations for both linear and non-linear rheology. The transfer also increases with increasing slip ratio and with increasing mean surface slope.

Transfer amplitudes generally becomes smaller with increasing n for wavelengths less than about 3 times the mean ice thickness. For larger wavelength, the situation is reversed and transfer amplitudes increase with n. A strong increase in the amplitudes of the topographic transfer functions with n can be observed for wavelength from 3 to 70 ice thicknesses.

The degree of nonlinearity of the basal sliding law does not appear to affect the bed-to-surface transfer characteristics fundamentally.

For active ice streams, characterized by high basal slipperiness, low surface slope (<0.5 °) topographic transfer amplitudes are generally large (> 0.5) and fairly constant for all wavelengths longer than about 3 to 5 ice thicknesses.

As for transfer characteristics, the effects of nonlinear rheology on the internal flow field of glacier are mainly quantitative and do not affect the overall flow pattern significantly. Increasing n has the effect of concentrating the anomalous flow towards the bed. For wavelength shorter than about 3 ice thicknesses and small amplitude perturbations (< 0.05), the perturbed velocities are small and a circular motion sets up in the perturbed velocity field.

7.1.2 Inverse problem

The synthetic surface data inversion experiments showed that the inversion procedure converges quickly and to correct solution, giving remarkably accurate estimates of the basal perturbations for both non-linear rheology and finite-amplitude effects. In all case studies considered, the first order derivatives of the forward model entering the Gauss-Newton retrieval method could be adequately approximated by linear transfer functions, in the sense that the method converged quickly and to the correct solution.

Bedrock perturbations generally require two to three iterations to be fully recovered, whereas perturbations in basal slipperiness need up to 15 iterations to converge.

In the case where the glacier geometry cannot be approximated to a parallel sided slab at global scale, the inversion procedure has to be applied iteratively along a flow line. Inversions performed using synthetic data show that in this case as well, it is possible to retrieve much of the basal features and that convergence is quick.

We have shown that it is possible to estimate both bedrock topography and basal lubrication along a flow line on Rutford Ice Stream from observed surface topography and surface velocities. The basal properties we compute for Rutford ice stream are consistent both with the surface observations and the radar measurements of bedrock topography. Over the second half of the profile to the grounding line, the inversion results are limited by the influence of a reverse surface slope on the modeled ice stream dynamics. Here, transverse effects play likely a dominant role and should be included in the numerical model.

7.2 Outlook

The non-linear Bayesian inference method as developed in this thesis represents a very promising approach to estimate the basal properties under ice streams from surface data along flow lines. As such, the method could be applied to other ice streams flow lines where transverse effects are believed to play a minor role.

The proposed inversion procedure is not adequate for problems where transverse effects are important. For such cases, an expansion of the method to three dimensions should be considered and should be fundamentally possible. In three-dimensions also, the first order derivatives of the forward model could probably be approximated by analytical linear transfer functions (Gudmundsson, 2003), but this should be tested. As the number of unknowns in the inverse problem will increase considerably in three dimensions, the computational cost of the procedure proposed here will increase significantly.

As our inversion experiments showed, the accuracy of the inversion estimates depends on the accuracy of the surface observations as well as on the number and spatial repartition of the surface observations. In order to obtain accurate estimates of the basal properties under ice streams regularly spaced surface measurements are an indispensable condition. A separation distance between surface measurements of approximately one ice thickness would be optimal.

Bibliography

Alley, R. B. (1993). In search of ice-stream sticky spots. *J. Glaciol.*, 39(133):447–545.

Alley, R. B., Blankenship, D. D., Bentley, C. R., and Rooney, S. T. (1986). Deformation of till beneath Ice Stream B, West Antarctica. *Nature*, 322:57–59.

Alley, R. B., Blankenship, D. D., Bentley, C. R., and Rooney, S. T. (1987). Till beneath Ice Stream B 3. Till deformation: Evidence and implications. *J. Geophys. Res.*, 92(B9):8921–8929.

Arthern, R. J., Winebrenner, D. P., and Vaughan, D. G. (2006). Antarctic snow accumulation mapped using polarization of 4.3-cm wavelength microwave emission. *J. Geophys. Res.*, 111(D06107). doi:10.1029/2004JD005667.

Balise, M. J. (1987). The relation between surface and basal velocity variations in glaciers, with application to the mini-surges of Variegated Glacier. *Unpublished PhD Thesis, University of Washington*.

Balise, M. J. and Raymond, C. F. (1985). Transfer of basal sliding variations to the surface of a linearly viscous glacier. *J. Glaciol.*, 31(109):308–318.

Bamber, J. L., Vaughan, D. G., and Joughin, I. (2000). Widespread Complex Flow in the Interior of the Antarctic Ice Sheet. *Science*, 287:1248–1250.

Bentley, C. R. and Giovinetto, M. B. (1990). Mass balance of Antarctica and sea level change. In Weller, G., Wilson, C. L., and Sevberin, B. A. B., editors, *International Conference on the Role of Polar Regions in Global Change*, pages 481–488, University of Alaska, Fairbanks, Geophysical Institute/Center for Global Change and Arctic Systems Reseach.

Blankenship, D. D., Bentley, C. R., Rooney, S. T., and Alley, R. B. (1986). Seismic measurements reveal a saturated porous layer beneath an active Antarctic ice stream. *Nature*, 322 (6074):54–57.

Doake, C. S. M., Corr, H. F. J., Jenkins, A., Makinson, K., Nicholls, K. W., Nath, C., Smith, A. M., and Vaughan, D. G. (2001). Rutford Ice Stream, Antarctica. In Alley, R. and Bindschadler, R., editors, *The West Antarctic ice sheet: Behavior and Environment*, volume 77 of *Antarctic Research Series*, pages 221–235. American Geophysical Union.

Duval, P. (2003). Rheology of glacier ice; role of the liquid phase and recrystallization. In *Milestones in Physical Glaciology: From the Pioneers to a Modern Science*, volume 180 of *Mitteilungen*, pages 9–10. VAW, ETH-Zürich.

Duval, P., Arnaud, L., Brissaud, O., Montagnat, M., and de la Chapelle, S. (2000). Deformation and recrystallization processes of ice from polar ice sheets. *Ann. Glaciol.*, 30:83–87.

Echelmeyer, K. A., Harrison, W. D., Larsen, C., and Mitchell, J. E. (1994). The role of the margins in the dynamics of an active ice stream. *J. Glaciol.*, 40(136):527–538.

Emery, W. J. and Thomson, R. E. (2001). *Data Analysis Methods in Physical Oceanography*. Elsevier, 2d edition.

Fahnestock, M. and Bamber, J. (2001). Morphology and surface charcteristics of the West Antarctic Ice Sheet. In Alley, R. and Bindschadler, R., editors, *The West Antarctic ice sheet: Behavior and Environment*, volume 77 of *Antarctic Research Series*, pages 13–27. American Geophysical Union.

Fahnestock, M. A., Scambos, T. A., Bindschadler, R. A., and Kvaran, G. (2000). A millennium of variable ice flow recorded by the Ross Ice Shelf, Antarctica. *J. Glaciol.*, 46(155):652–664.

Frolich, R. M., Mantripp, D. R., Vaughan, D. G., and Doake, C. S. M. (1987). Force balance of Rutford Ice Stream, Antarctica. In *The Physical Basis of Ice Sheet Modelling*, volume 170, pages 323–331, Vancouver. International Association of Hydrological Sciences.

Gades, A. M., Raymond, C. F., Conway, H., and Jacobel, R. W. (2000). Bed properties of Siple Dome and adjacent ice streams, West Antarctica, inferred from radio-echo sounding measurements. *J. Glaciol.*, 46(152):88–94.

Glen, J. W. (1955). The creep of polycrystalline ice. *Proceedings of the Royal Society of London, Ser. A*, 228(1175):519–538.

Goldsby, D. L. and Kohlsted, D. L. (2001). Superplastic deformation of ice: Experimental observations. *J. Geophys. Res.*, 106(B6):11017–11030. 10.1029/2000JB900336.

Gouveia, W. P. and Scales, J. A. (1998). Bayesian seismic waveform inversion: Parameter estimation and uncertainty analysis. *J. Geophys. Res.*, 103(B2):2759–2780. 10.1029/97JB02933.

Gudmundsson, G. H. (1997a). Basal-flow characteristics of a non-linear flow sliding frictionless over strongly undulating bedrock. *J. Glaciol.*, 43(143):80–89.

Gudmundsson, G. H. (1997b). Ice deformation at the confluence of two glaciers investigated with conceptual map-plain and flow-line models. *J. Glaciol.*, 43(145):537–547.

Gudmundsson, G. H. (2003). Transmission of basal variability to a glacier surface. *J. Geophys. Res.*, 108(B5). 10.129/2002JB002107.

Gudmundsson, G. H. (2004). The relationship between surface and basal perturbations on glaciers and ice sheets in the long-wavelength limit. *Unpublished report, British Antarctic Survey*.

Gudmundsson, G. H., Aðalgeirsdóttir, G., and Björnsson, H. (2003). Observational verification of predicted increase in bedrock-to-surface amplitude transfer during a surge. *Ann. Glaciol.*, 36:91–96.

Gudmundsson, G. H. and Jenkins, A. (2007). Decadal invariability in the flow of Rutford Ice Stream, West Antarctica. *Geophysical Research Abstracts*, 9:06614. SRef-ID: 1607-7962/gra/EGU2007-A-06614.

Gudmundsson, G. H., Raymond, C. F., and Bindschadler, R. (1998). The origin and longevity of flow-stripes on Antarctic ice streams. *Ann. Glaciol.*, 27:145–152.

Hindmarsh, R. C. A. (2004). A numerical comparison of approximations to the Stokes equations used in ice sheet and glacier modeling. *J. Geophys. Res.*, 109. 10.1029/2003JF000065, F01012.

Hutter, K. (1983). *Theoretical glaciology; material science of ice and the mechanics of glaciers and ice sheets*. D. Reidel Publishing Company/Tokyo, Terra Scientific Publishing Company.

Hutter, K., Legerer, F., and Spring, U. (1981). First-order stresses and deformations in glaciers and ice sheets. *J. Glaciol.*, 27(96):227–270.

Iken, A. (1981). The effect of the subglacial water pressure on the sliding velocity of a glacier in an idealized numerical model. *J. Glaciol.*, 27(97):407–421.

Jeffreys, H. (1939). *Theory of Probablility*. Oxford: Clarendon Press.

Jóhannesson, T. (1992). Landscape of Temperate Ice Caps. *Unpublished PhD Thesis, University of Washington*.

Johnson, R. E. and McMeeking, R. M. (1984). Near-surface flow in glaciers obeying Glen's law. *Quarterly Journal of Mechanics and Applied Mathematics*, 37(2):273–291. A correction contained in a corrigendum published in the issue 37(4),.p. 632.

Joughin, I., Fahnestock, M., and Bamber, J. L. (2000). Ice flow in the northeast Greenland ice stream. *Ann. Glaciol.*, 31:141–146.

Joughin, I., MacAyeal, D. R., and Tulaczyk, S. (2004). Basal shear stress of the Ross ice streams from control method inversions. *J. Geophys. Res.*, 109(B09405). 10.1029/2003JB002960.

Joughin, I. and Tulaczyk, S. (2002). Positive mass balance of the Ross Ice Streams, West Antarctica. *Science*, 295(5554):476–480.

Joughin, I., Tulaczyk, S., Bindschadler, R., and Price, S. F. (2002). Changes in West Antarctic ice stream velocities: Oberservation and analysis. *J. Geophys. Res.*, 107(B11).

Kamb, B. (2001). Basal zone of the West Antarctic Ice Sheet and its role in lubrication of their rapid motion. In Alley, R. and Bindschadler, R., editors, *The West Antarctic ice sheet: Behavior and Environment*, volume 77 of *Antarctic Research Series*, pages 157–199. American Geophysical Union.

Kitanidis, A. K. (1997). *Introduction to geostatistics: applications to hydrogeology*. Cambridge University Press.

Landon, J. and Raymond, C. F. (1978). Chislenniy raschet reaktsii poverkhnosti lednika na izmeneniya tolshchîny l'da [Numerical calculation of adjustment of a glacier surface to pertubations of ice thickness]. *Mater. Glyatsiol. Issled. Khron. Obsuzhdeniya*, 32:123–133 (in Russian); 233–239 (in English).

Leysinger Vieli, G. J.-M. C. and Gudmundsson, G. H. (2004). On estimating length fluctuations of glaciers caused by changes in climatic forcing. *J. Geophys. Res.*, 109(F1). 10.1029/2003JF000027, F01007.

MacAyeal, D. R. (1992). The basal stress distribution of Ice Stream E, Antarctica, inferred by control methods. *J. Geophys. Res.*, 97(B1):596–603.

MacAyeal, D. R., Bindschadler, R. A., and Scambos, T. A. (1995). Basal friction of Ice Stream E, West Antartica. *J. Glaciol.*, 41:247–262.

Morland, L. W. (2001). Influence of bed topography on steady plane ice sheet flow. In Greve, B., Ehrentraut, H., and Wang, Y., editors, *Continuum Mechanics and Applications in Geophysics and the Environment*, pages 276–304. Springer, New York.

Paterson, W. S. B. (1994). *The physics of glaciers*. Butterworth-Heinemann, Oxford, third edition.

Pettit, E. C. and Waddington, E. D. (2003). Ice flow at low deviatoric stress. *J. Glaciol.*, 49(166):359–369.

Raymond, M. J. and Gudmundsson, G. H. (2005). On the relationship between surface and basal properties on glaciers, ice sheets, and ice streams. *J. Geophys. Res.*, 110(B08411). 10.1029/2005JB003681.

Raymond, M. J. and Gudmundsson, G. H. (2007). Estimating basal properties of glaciers from surface measurements: a non-linear bayesian inversion approach applied to synthetic data. *J. Geophys. Res.* in preparation.

Reeh, N. (1987). Steady-state three-dimensional ice flow over an undulating base: first-order theory with linear ice rheology. *J. Glaciol.*, 33(114):177–185.

Retzlaff, R. and Bentley, C. R. (1993). Timing of stagnation of Ice Stream C, West Antarctica, from short-pulse radar studies of buried surface crevasses. *J. Glaciol.*, 39(133):553–561.

Rodgers, C. D. (2000). *Inverse Methods for Atmospheric Sounding. Theory and Practice*. World Scientific Publishing Co. Pte. Ltd. Singapore.

Schoof, C. (2002). Basal perturbations under ice streams: form drag and surface expression. *J. Glaciol.*, 48(162):407–416.

Schoof, C. (2003). The effect of basal topography on ice sheet dynamics. *Continuum Mech. Thermodyn.*, 15(3):295–307.

Schoof, C. (2004). Bed topography and surges in ice streams. *Geophys. Res. Lett.*, 31. L06401.

Schoof, C. (2005). The effect of cavitation on glacier sliding. *Proceedings of the Royal Society of London, Ser. A*, 461:609–627.

Schweizer, J. and Iken, A. (1992). The role of bed separation and friction in sliding over an undeformable bed. *J. Glaciol.*, 38(128):77–92.

Smith, G. D. and Morland, L. W. (1981). Viscous relations for the steady creep of polycrystalline ice. *Cold Regions Science and Technology*, 5:141–150.

Steinemann, S. (1958). Experimentelle Untersuchungen zur Plastizität von Eis. Geotechnische Serie Nr. 10, Beiträge zur Geologie der Schweiz.

Tarantola, A. (2005). *Inverse Problem Theory and Methods for Model Parameter Estimation*. Society for Industrial and Applied Mathematics.

Tarantola, A. and Valette, B. (1982). Inverse problems = quest for information. *Journal of Geophysics*, 50:159–170.

Thorsteinsson, T., Raymond, C. F., Gudmundsson, G. H., Bindschadler, R. B., Vornberger, P., and Joughin, I. (2003). Bed topography and lubrication inferred from surface measurements on fast flowing ice streams. *J. Glaciol.*, 49(167):481–490.

Truffer, M. (2004). The basal speed of valley glaciers: an inverse approach. *J. Glaciol.*, 50(169):236–242.

Tulaczyk, S., Kamb, W. B., and Engelhardt, H. F. (2000a). Basal mechanics of Ice Stream B, West Antarctica 1. Till mechanics. *J. Geophys. Res.*, 105(B1):463–482. 10.1029/1999JB900329.

Tulaczyk, S., Kamb, W. B., and Engelhardt, H. F. (2000b). Basal mechanics of Ice Stream B, West Antarctica 2. Undrained plastic bed model. *J. Geophys. Res.*, 105(B1):483–494. 10.1029/1999JB900328.

Van der Veen, C. J. and Whillans, I. M. (1989). Force Budget: I. Theory and Numerical Methods. *J. Glaciol.*, 35(119):53–60.

Van der Veen, C. J. and Whillans, I. M. (1996). Model experiments on the evolution and stabiliity of ice streams. *Ann. Glaciol.*, 23:129–137.

Vieli, A., Funk, M., and Blatter, H. (2000). Tidewater glaciers: frontal flow acceleration and basal sliding. *Ann. Glaciol.*, 31:217–221.

Vieli, A. and Payne, A. J. (2003). Application of control methods for modelling the flow of pine island glacier, west antarctica. *Ann. Glaciol.*, 36:197–204.

Whillans, I. M., Bentley, C. R., and van der Veen, C. J. (2001). Ice Streams B and C. In Alley, R. and Bindschadler, R., editors, *The West Antarctic ice sheet: Behavior and Environment*, volume 77 of *Antarctic Research Series*, pages 13–27. American Geophysical Union.

Whillans, I. M. and Johnsen, S. J. (1983). Longitudinal variations in glacial flow: theory and test using data from the Byrd Station strain network, Antarctica. *J. Glaciol.*, 29(101):78–97.

Acknowledgements

I am greatly indebted to my supervisor, Dr. Hilmar Gudmundsson, for his continuous guidance and stimulating scientific discussions. His enthusiasm for science and glaciology in particular, were essential to keep my motivation high. He has always offered wise advice and sharp insights, and I have learned a lot from him. Moreover, the time spent with him in Cambridge (thank you Hilmar for hosting me in your various homes) or Zurich was always very pleasant. Thank you very much for everything, Hilmar!

I wish to express my gratitude to Prof. Martin Funk, head of the Section of Glaciology at VAW, for giving me the opportunity to work on this subject. He not only co-initiated the project with Dr. Hilmar Gudmundsson, but has kept his door open to any of my questions, and has provided valuable suggestions for further research whenever needed. When the project funding ran out and my thesis was not yet finished, he found the means to extend my salary. Merci, Martin, pour ton amitié, ton soutien et la confiance dont tu m'as témoigné tout au long de la thèse.

I am indebted to Prof. Hans-Erwin Minor, head of the Laboratory of Hydraulics, Hydrology and Glaciology (VAW) of ETH Zurich for being my advisor. His support, particularly during the evaluative stages of the work, is greatly appreciated. I am further grateful to Prof. Douglas MacAyael from University of Chicago, who kindly agreed to serve on my committee. His insightful comments and suggestions greatly improved the manuscript.

I had the opportunity to work several times at the British Antarctic Survey in Cambridge. Sincere thanks are due to Dr. Richard Hindmarsh for the encouragement on my research and fruitful collaboration and to Dr. Robert Arthern for providing me accumulation data along a flow line on Rutford Ice Stream.

Dr. Gwendolyn Leysinger Vieli introduced me to MARC/MENTAT and provided me programs, while finishing her PhD in Bristol. Thank you Gwendo for your assistance that made my work considerably easier at the beginning!

I am grateful to Prof. Kolumban Hutter for his thorough review of Chapter 5 of this thesis.

I would like to thank my colleagues at VAW for their friendship: Andreas Bauder, Hermann Bösch, Olaf Eisen, Jérôme Faillettaz, Urs Fischer, Jakob Helbing, Matthias Huss, Martin Lüthi, Bruno Nedela, Christoph Ortmanns, Antoine Pralong, Marie Rousselot, Thomas Schuler, Markus Schatzmann, Aurel Schwerzmann, Tetsuo Sueyoshi, Shin Sugiyama, Fabian Walter, Mauro Werder and Thomas Wyder (in alphabetical order) and many others. Merci à Andreas pour les sympathiques travaux-sorties-balades au glacier du Giétro. Vielen Dank an Bruno für die netten Diskussionen und die schönen Zeichnungen.

This work was supported by ETH research grant No 0-20054-02.

Last but not least, I am thankful to Antoine for his unlimited patience with me during these four years. His love and tenderness gave me the strength that I needed to accomplish this dissertation. His continuous support was essential for the successful completion of this work. Merci, Antoine, d’avoir partagé avec moi les joies et les affres des doutes. Merci d’avoir été là, et d’être là avec moi...